EXPERIMENTAL INVESTIGATION OF THE THERMO-MECHANICAL BEHAVIOUR AND THERMAL PROPERTIES OF LONDON CLAY

A thesis submitted to Imperial College London in partial fulfilment of the requirements

for the degree of Doctor of Philosophy

by

Daniel Martinez Calonge

Department of Civil and Environmental Engineering

Imperial College London

London SW7 2AZ

June 2017

In memory of Isabel

Declaration

I hereby declare that this thesis is the result of my own work and that any quotation from, or description of, the work of others has been appropriately referenced, whether published or unpublished. This thesis is not the same as any that I have submitted for any degree, diploma or other qualification at any other university.

The copyright of this thesis rests with the author and is made available under a Creative Commons Attribution Non-Commercial No Derivatives licence. Researchers are free to copy, distribute or transmit the thesis on the condition that they attribute it, that they do not use it for commercial purposes and that they do not alter, transform or build upon it. For any reuse or redistribution, researchers must make clear to others the licence terms of this work.

Daniel Martinez Calonge

June 2017

“The aim of science is not to open the door to infinite wisdom, but to set a limit to infinite error.”

- Bertold Brecht, *Life of Galileo*

Abstract

In recent years, the study of the thermo-hydro-mechanical behaviour of soils has been a growing area within the geotechnical community due to its importance to a wide range of civil engineering applications and activities which involve the ground as a heat source, sink or medium for heat storage. This thesis reports an experimental study of the thermo-mechanical behaviour and thermal properties of London clay and is structured in three blocks as follows.

The first part of the thesis describes the development of new experimental capabilities in the Imperial College Geotechnics Laboratory and the methodology of the thermo-mechanical and thermal properties tests. A new temperature-controlled apparatus capable of testing saturated soils at pressures up to 800 kPa and temperatures ranging from ambient to 85 ºC is presented. The thermal performance of the cell is thoroughly assessed, as well as the calibration of the different components. Furthermore, the use of needle techniques, single and dual probe, for the measurement of the thermal properties of soils is investigated.

The second part reports a laboratory programme of thermo-mechanical tests on reconstituted London clay samples. The thermally-induced volumetric strains during drained heating and cooling cycles in samples with different stress histories are investigated, showing similitudes and discrepancies with other clays. The nature of the measurement of thermal deformations in this study, as well as on published work, is discussed in detail. Moreover, the temperature effects on the compression behaviour, strength and stiffness of the material are also investigated.

Finally, the measurements of the thermal properties (thermal conductivity, diffusivity and volumetric heat capacity) performed on reconstituted and intact London clay samples using the single needle and dual-probe heat-pulse tests are presented, discussing the influence of the state and nature of the sample (porosity, water content, mineralogy), direction of measurement and the appropriateness of the instruments used.

Acknowledgements

First of all, I would like to thank Prof. Lidija Zdravkovic for her immense expertise, guidance and support throughout this project. Working with her has been a splendid experience and I particularly appreciated her constant availability and eagerness to discuss any scientific ideas or difficulties whenever they came up. I would also like to thank Dr. Way Way Sim for her enormous support and guidance since the MSc dissertation which lead to this thesis. I would like to express my gratitude for giving me the opportunity to undertake this research at Imperial College London

Special thanks go to Steve Ackerley and Duncan Parker, because this thesis would have not been possible without their constant technical support, interest and enthusiasm. The gratitude is also extended to Alan Bolsher and Graham Keefe for all their assistance in the laboratory.

I would like to extend my sincerest thanks and appreciation to the rest of the staff and PhD colleagues in the Geotechnics section for the many valuable discussions and the great time we have had together. In particular, I would like to thank Dr. Jamie Standing for his help obtaining the material used in this project and to Masahide, Emil, Ilias, Tingfa, Vasilis and Wenjie for their assistance and support during my research.

The financial support by the Engineering and Physical Sciences Research Council (EPSRC) and the Geotechnical Consulting Group (GCG) is also greatly acknowledged.

Very special thanks also go to my amazing friends who managed to stick with me during these years and be very supportive, each in its own way.

My most special recognition goes to my brother Javi, my dad David, as well as my girlfriend Katerina for their love, encouragement, patience and belief in me. Without their unconditional support, I would not have been able to complete the PhD.

Last but not least, no words suffice to describe my late mother's contribution to my life. I owe her everything and this thesis is dedicated to her memory.

Table of contents

List of Tables

List of Figures

List of Symbols

Latin characters

A_0	Cross-sectional area of the sample prior to testing stage
A_c	Current cross-sectional area of the sample
A_{ce}	Cross-sectional area of the sample at the end of shearing
A_{peak}	Cross-sectional area of the sample at peak strength
B	Coefficient of saturation
C	Volumetric heat capacity
C_f	Needle calibration factor
E_{tan}^{u}	Undrained tangent stiffness
G_s	Specific gravity of the solids
K_i	Intrinsic permeability
I	Current
L	Length of heating element
M	Stress ratio q/p' at critical state
M_i	Initial tangent Modulus of the membrane
M_s	Secant modulus of the membrane at 10% strain
N	Specific volume on the NCL for $p' = 1$ kPa
Q	Heat input
R	Resistance
R_c	Specific gas constant
R_s	Radius of sample in thermal properties tests
S	Gradient of the linear part of temperature-log time plots
S_s	Specific surface of the clay mineral
T	Temperature
T_h	Average temperature of the heating elements
T_m	Temperature maximum (dual-probe heat-pulse test)
T_{mn}	Annual mean air temperature
T_p	Annual amplitude of the monthly average air temperature
T_s	Temperature of the sample
T_{soil}	Temperature of the soil
V_0	Volume of the sample prior to testing stage

V_{dr}	Volume of drained water
V_s	Volume of solids in the sample
V_w	Volume of water in the sample
c	Specific heat capacity
d_a & d_b	Major and minor axes of the ellipse surface
e	Void ratio
d_0	Diameter of the sample at the end of consolidation
d_{im}	Initial upstretched diameter of the membrane
k	Hydraulic conductivity
m	Coefficient multiplying the pressure in Baldi et al.(1988) (see Eq.[5.7])
n	Porosity
p	Pressure
p_0	Atmospheric pressure
p_{0m}	Initial confining pressure applied by the membrane
p'	Mean effective stress
p'_c	Maximum mean effective stress applied to the sample
p'_e	p' in the NCL at the same v
q	Deviatoric stress
q_{max}	Maximum mobilised deviatoric stress
r	Radial distance away from line heat source
t	Time
t_m	Time of temperature maximum (dual-probe heat-pulse test)
t_0	Heating duration
u	Pore pressure
x_i	Volume fractions of each of the soil constituents
w	Water content (gravimetric)
z	Depth

Greek characters

Ω	Soil fabric parameter
α_e & α_p	Gradients of the volumetric strain vs temperature plots
α_e^* & α_p^*	Gradients of the void ratio vs temperature plots
α_s	Thermal expansion coefficient of the solids

α_w	Thermal expansion coefficient of water
ε_a	Axial strain
ε_e	Axial strain at the end of the test
ε_{peak}	Axial strain at peak strength
ε_r	Radial strain
ε_v	Volumetric strain
$\varepsilon_{v,T}$	Thermal volumetric strain
κ	Thermal diffusivity (in the context of thermal properties)
κ	Gradient of the swelling lines in the $v - \ln(p')$ plane
λ	Thermal conductivity (in the context of thermal properties)
λ	Gradient of the NCL in the $v - \ln(p')$ plane
μ	Viscosity
ν	Specific volume
ρ	Density
ρ_d	Dry density
σ_{3m}	Correction to the minor principal stress
φ	Phase shift
ω	Angular frequency

Acronyms

AD	Air-dried
GLY	Glycolated
HP	Hyde Park site
ICGL	Imperial College Geotechnics Laboratory
NC	Normally consolidated
NCL	Normal compression line
OC	Overconsolidated
OCR	Overconsolidation ratio
V&A	Victoria and Albert museum site
XRD	X-ray diffraction

1. INTRODUCTION

1.1 Background of the Research

In recent years, the study of the Thermo-Hydro-Mechanical (THM) behaviour of soils has been a rapidly growing field within the geotechnical community, due to its relevance to a wide range of contemporary civil engineering applications and activities which aim to provide solutions to the challenge of meeting the increasing global demand for secure and affordable energy and tackling climate change. The field of Energy Geotechnics covers the geotechnical aspects associated with such infrastructure related to energy production, storage, transportation and waste management. One strand of the THM research has primarily focused on the use of clays in deep underground nuclear waste storage: stiff clays have been considered as potential host formations, while, as part of the multi-barrier concept, heavily compacted swelling clays, such as bentonite, have been considered for use as engineered barriers (e.g. Gens et al., 2007; Delage et al., 2010). Another strand of the THM research has investigated the use of the ground as a medium for heat storage or a heat source/sink for energy applications (e.g. Moritz, 1995; Brandl, 2006). Currently, there is a growing interest in incorporating the pipe loops for ground-source heat-pump systems into common geotechnical structures, such as piled foundations, tunnels or retaining walls (Bourne-Webb et al., 2009; Laloui and Di Donna, 2013). Substantial research has also been conducted in the oil and gas field (Addis, 1987; Dusseault et al., 1988) and in the study of the soil surrounding buried high-voltage cables (Mitchell et al., 1982). These complex geomechanical problems involve highly-coupled thermal, hydraulic, mechanical, and sometimes chemical processes and laboratory testing is essential in order to gain an understanding of their interaction.

The natural temperature of the ground is mainly affected by two different processes: a) the solar radiation and other atmospheric processes and their influence on climate and b) upward heat conduction from the interior of the Earth, known as the geothermal gradient. The first process results in daily temperature changes, affecting only the uppermost centimetres of soil,

and seasonal cycles of temperature change which can be explained by the variations in the annual mean air temperature and the thermal diffusivity of the ground. The simple harmonic function presented in Eq.[1.1] (Williams and Gold, 1976) describes the response, T_{soil}, to seasonal temperature cycles of the ground temperature at a depth z and time t, where T_{mn} is the annual mean air temperature; T_p, the annual amplitude of the monthly average air temperature; ω, the angular frequency taking the period as the duration of an annual cycle in this case; φ, the phase reflecting the delay or advance of the beginning of the sinusoid from the starting time and κ is the thermal diffusivity of the ground. In the case of London, the temperatures may be taken from the historical averages provided by the Met Office (2017), which result in T_{mn}= 11.55 °C and T_p= 6.5 °C; a phase shift to reflect the low peak is happening between January and February; and a typical saturated soil thermal diffusivity may be taken as 6E-7 m^2s^{-1}.

$$T_{soil}(z,t) = T_{mn} - T_p e^{-z\sqrt{\frac{\omega}{2\kappa}}} \cos\left(\omega t - \varphi - z\sqrt{\frac{\omega}{2\kappa}}\right) \quad [1.1]$$

The second process, associated with the geothermal heat flux, can be modelled by a gradual increase of temperature with depth, whose gradient takes an average value in the UK of 0.026 °Cm^{-1}, up to 0.035 °Cm^{-1} locally in granitic areas (Busby et al., 2009). Adding the effects of both processes, it is possible to model the near-surface temperature in London, taking into account the seasonal variations, as shown in Figure 1.1. As the depth increases, the thermal fluctuations decrease and a clear subsurface phase shift is observed. The natural temperature of the ground is relatively constant from depths of 10 m below the ground surface, approximately equal to the mean annual air temperature. Consequently, there is a temperature difference between the ground temperature and the above-ground temperatures during most of the year and this can, for example, be exploited for heating or cooling demands using ground-source heat-pumps systems. In the United Kingdom, heating and hot water for UK buildings add up to around 40% of the total energy consumption and 20% of the greenhouse gas emissions. It is essential to reduce those gas emissions to meet the targets of the Climate

Change Act and honour international agreements such as the Paris Agreement (Committee on Climate Change, 2016). Ground-source heat-pumps system have been considered a suitable renewable technology in order to achieve this and the number of installations during the last decades has increased swiftly, particularly in the London area (Mayor of London, 2004; Fry, 2009). Changes in the natural temperature field of the ground are not restricted to this type of energy applications, where heat is extracted or injected in the ground. In heavily built environments, it may come from existing infrastructure such as railway tunnels or high-voltage cables. In the particular case of London, the temperature in the soil immediately surrounding underground tunnels is between 5 °C and 11 °C higher than the expected natural temperature (Tinham, 2007). In all these cases, it is of great importance to geotechnical engineers to understand the heat transfer process and its coupled effects on the hydraulic and mechanical behaviour of the ground, in order to understand its impact in the built environment and provide efficient solutions to the big energy challenge.

1.2 Objectives

The key objectives of this research are listed as follows:

- To review the current knowledge of the thermo-hydro-mechanical behaviour of the ground, focussing on the key experimental findings and on the equipment developed which facilitated those.
- To develop new experimental capabilities at the Imperial College Geotechnics Laboratory which will enable the characterisation of the thermo-hydro-mechanical behaviour of soils, focussing on a temperature-controlled triaxial apparatus and the use of needle techniques for the determination of soil thermal properties.
- To conduct an initial testing programme using reconstituted material to characterise several aspects of the thermo-mechanical behaviour of London clay, such as the thermally-induced volume changes, including the effect of stress history, stress level and temperature history (number of cycles and amplitude), and the influence of temperature in the strength and stiffness, as well as on the compression and swelling

behaviour. This includes a benchmark reference study at room temperature with samples subjected to comparable stress histories.

- To conduct an extensive testing programme on reconstituted and intact London clay samples to measure their thermal properties using different needle techniques and to investigate the factors affecting them, including sample conditions (water content, porosity, mineralogy), measurement conditions (direction of measurement) and measurement technique (instrument and interpretative procedure)..

1.3 Structure of the thesis

This thesis consists of eight chapters. The introduction (**Chapter 1**) describes the background to the research, defines its scope, sets out the objectives and presents its structure. **Chapter 2** consists of a literature review which is structured in two blocks, looking at the experimental developments in THM testing and reviewing the main results of the experimental investigations of the thermal, thermo-hydraulic and thermo-mechanical behaviour of saturated soils. **Chapter 3** describes the development of the experimental capabilities for thermo-hydro-mechanical tests at the Imperial College Geotechnics Laboratory. **Chapter 4** describes the soil used in this thesis, London Clay, while in **Chapter 5** the testing procedures and the methods of processing the data are presented, as well as the testing programme. **Chapters 6 and 7** present and discuss the findings of the thermo-mechanical testing programme and the thermal properties testing programme, respectively. Finally, **Chapter 8** presents the conclusions of the research and proposes suggestions for further work.

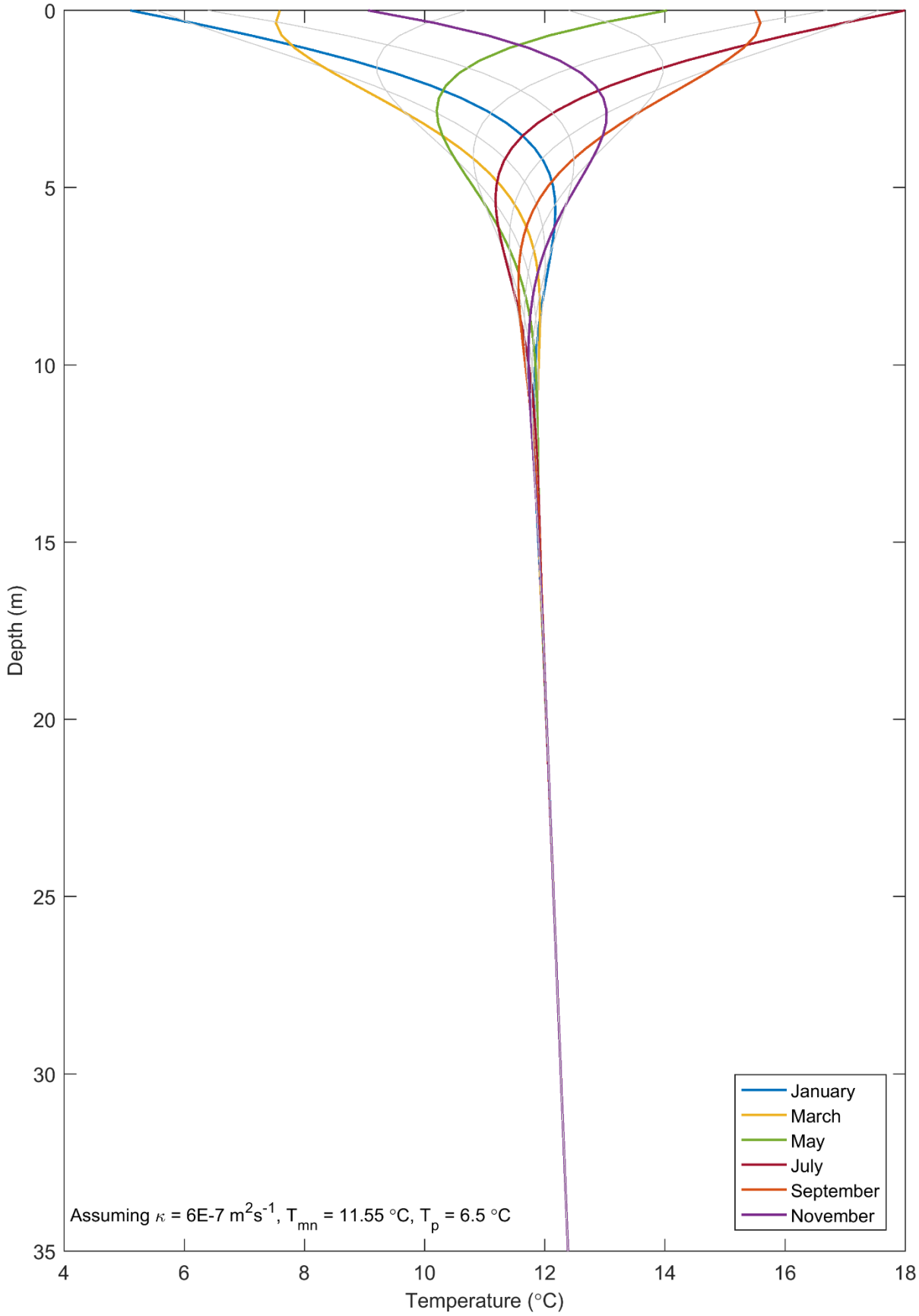

Figure 1.1 *Model of the near-surface temperature seasonal variations in London*

2. LITERATURE REVIEW

2.1 Introduction

The literature review presented in this chapter is structured in two blocks. Firstly, the main results of the experimental investigations of the thermo-hydro-mechanical behaviour of saturated soils are reviewed, focusing in particular on the thermal properties, thermo-hydraulic behaviour and aspects of the thermo-mechanical behaviour such as the thermally induced volume changes and excess pore pressures, compression properties and changes in strength and stiffness due to temperature.

Secondly, an overview of the equipment and experimental techniques for characterizing the thermo-hydro-mechanical behaviour of saturated soils is presented, with special attention to the development of temperature-controlled isotropic and triaxial apparatuses since the pioneering work of Campanella and Mitchell (1963).

2.2 Thermo-Hydro-Mechanical behaviour of saturated soils

2.2.1 Thermal behaviour

a) Heat transfer in soils

Heat transfer in geomaterials is a complex process which can involve several mechanisms. The three main mechanisms are heat conduction, convection (either free or forced) and radiation. Moreover, changes in the water phase, evaporation/condensation or freeze/thaw processes, can play a significant part in the heat transfer process.

Thermal conduction occurs in the three constituents of the soil: the solid particles (either organic or mineral), the water and the air. The conduction mechanism consists of molecular agitation without any mass motion of the constituent as whole. It slightly varies for each of the constituents. In the case of mineral solids, heat flow can be illustrated as increased vibrations in an atom causing the neighbouring ones to move as if they were linked by springs, whereas in the pore air, conduction occurs due to intermolecular collisions and a resulting increase in

their kinetic energy. The mechanism responsible for conduction in liquid water is similar to the latter, although with the additional contribution of the energy transfer by breaking and making hydrogens bonds (Farouki, 1981).

Heat convection is a form of heat transfer which occurs in fluids and involves movement of heat carrying mass through advection and/or diffusion. Radiation occurs across transparent media (air spaces for example) by heat energy propagation as electromagnetic waves. It is dependent on the temperature of the radiating body and according to Stefan-Boltzmann's law, any body above 0 K emits some energy. In the case of soils, its contribution to heat transfer can be considered negligible except for dry crushed coarse material where it may account for up to 10% of the overall heat transfer (Rees et al., 2000).

In soils, the predominant heat transfer mechanisms are shown in Figure 2.1 for different grain sizes, grain size distributions and degrees of saturation. It can be seen that for saturated clays, silts and most of the sands heat conduction is the dominant mechanism. Brandl (2006) suggests that when the grain sizes are small and also when the pore space is small relative to the soil volume considered, conduction can be assumed as the only heat transfer mechanism.

b) Thermal properties

Three properties are commonly used to describe the process of heat transfer through conduction in soils. These are the thermal conductivity, heat capacity and thermal diffusivity.

The soil thermal conductivity λ, with units of $Wm^{-1}K^{-1}$ (watts per metre-kelvin), is defined as the amount of heat passing in a unit time through a unit cross-sectional area of soil under a unit temperature gradient applied in the direction of the heat flow. It ranges between 0.3 to 4 $Wm^{-1}K^{-1}$ for most soils and up to 7 $Wm^{-1}K^{-1}$ in some rocks. The thermal conductivity of the soil is the governing parameter during steady state conditions (i.e. when temperature does not change with time). In non-steady state conditions, when temperature changes with time (i.e. soil gaining or losing heat), some of the heat flow is then used for this purpose. The amount

of it is determined by the volumetric heat capacity of the soil C, with units of $Jm^{-3}K^{-1}$ (joules per meter cube - kelvin), which is defined as the heat energy required to raise by 1 K (1 ºC) the temperature of a unit volume of soil specimen. It is the product of the density of the material ρ (in kgm^{-3}) and the specific heat capacity c (in $Jkg^{-1}K^{-1}$). The volumetric heat capacity of soil can be determined from the volume fractions x_i of each of the soil constituents (solids, liquid and air) and their corresponding heat capacities, as shown by Eq.[2.1].

$$C = c\rho = c_s\rho_s x_s + c_w\rho_w x_w + c_a\rho_a x_a \qquad [2.1]$$

At a temperature of 25 ºC, the specific heat capacities of water, c_w, and air, c_a, are 4.179 and 1.006 $KJkg^{-1}K^{-1}$ respectively while the densities ρ_w and ρ_a are 997.6 and 1.184 kgm^{-3} (IAPWS, 2007). In the case of the solids, the specific heat capacities of quartz and clay minerals are 0.8 and 0.92 $KJkg^{-1}K^{-1}$ and a weighted average of these values can be taken if the mineralogy is known. The particle density ρ_s may be obtained from the pyknometer test. As seen from Eq.[2.1], the volumetric heat capacity of soils clearly depends on the relative proportions of the different phases, described in soil mechanics by parameters such as the porosity, degree of saturation, dry density or moisture content, as well as on the mineralogy of the sample which would control the heat capacity of the solids. Assuming a fully saturated soil (with a ρ_s of 2.73 gcm^{-3}) formed by 50% of quartz and 50% of clay, the volumetric heat capacity would vary between 2.35 $MJm^{-3}K^{-1}$ at a porosity of n=0, up to 4.17 $MJm^{-3}K^{-1}$ at a porosity of n=1. For a common range of porosities found in soils, 0.3 up to 0.5, the volumetric heat capacity would range from 2.89 up to 3.26 $MJm^{-3}K^{-1}$.

The ratio of the conductivity and the volumetric heat capacity, known as the thermal diffusivity κ (with units of m^2s^{-1}, meter squared per second), is the governing parameter in the unsteady state of heat conduction. The higher this parameter, the greater is the ability of the soil for considerable and rapid changes in temperature.

$$\kappa = \frac{\lambda}{c\rho} \qquad [2.2]$$

Common values for saturated sands and silts or clays are 0.079 m^2day^{-1} and 0.056 m^2day^{-1} respectively (Gale, 2005).

c) Thermal conductivity: influencing factors and modelling

The thermal conductivity of soils is governed by intrinsic properties of the phases that form the soil (solids, liquids and gases) as well as by the variations of each phase. The conductivities of the different phases differ by up to two orders of magnitude. The thermal conductivities of the mineral solids, shown in Table 2.1 for common minerals, vary between 1.8 and 7.7 $Wm^{-1}K^{-1}$ for most minerals, although can go up to 19.20 $Wm^{-1}K^{-1}$ in the case of pyrite (Horai, 1971; Brigaud & Vasseur, 1989). Soils with higher quartz (7.7 $Wm^{-1}K^{-1}$) content have larger conductivity than very clayey soils with high contents of smectite or illite (~1.85 $Wm^{-1}K^{-1}$). A common way to express the thermal conductivity of the solid minerals, λ_s, when the proportions of the minerals present are known is the weighted geometrical mean of the individual conductivity of each mineral as shown by Eq. [2.3] (Cote and Konrad, 2005).

$$\lambda_s = \prod_{i=1}^{n} \lambda_i^{w_i} \qquad [2.3]$$

The thermal conductivity of liquid water, λ_w, varies with temperature as described by Eq.[2.4] , which was obtained using the data produced by the latest release of the equation of state for water presented by the International Association for the Properties of Water and Steam (IAPWS, 2007) and is significantly lower than the thermal conductivity of the solid phase. A commonly quoted value for λ_w is 0.607 $Wm^{-1}K^{-1}$, which corresponds to the conductivity at 25 °C.

$$\lambda_w = 1.982\times10^{-8}T^3 - 1.116\times10^{-5}T^2 + 0.002074T + 0.5623 \qquad [2.4]$$

where T is the temperature in °C. This equation is valid at atmospheric pressure and at a range of temperatures between 1 and 99 °C, although the effect of pressure in the relevant range for civil engineering applications is negligible. At 1 MPa above atmospheric pressure, the thermal conductivity of water at 25 °C is 0.608 $Wm^{-1}K^{-1}$, negligibly higher than under

atmospheric pressure. Finally, the thermal conductivity of air (λ_a) is 0.026 $Wm^{-1}K^{-1}$, approximately an order of magnitude smaller than the one of water.

The thermal conductivity of an element of soil is thus clearly influenced by the relative proportions of each phase. For the same degree of saturation, as the dry density of the soil increases, so does the thermal conductivity, given the higher proportion of highly conductive solid particles present in the mix and granular chains forming more developed heat transfer paths (Vargas and McCarthy, 2001). For the same porosity, the thermal conductivity of the soil will decrease with decreasing degree of saturation, given the very low conductivity of the air phase. Additionally, the thermal conductivity of soils is also influenced by particle size and gradation (Aduda, 1996; Gangadhara et al., 1999; Esch, 2004), packing geometry and cementation (Tarnawski et al. 2002), direction of measurement (Midttomme et al., 1998), as well as the mineralogy and temperature of the sample, given the thermal conductivity of water dependence on temperature, as previously described.

Several theoretical and empirical models have been developed in various fields of engineering and physics to estimate the thermal conductivity of multi-phase porous materials. The simplest models are the parallel (λ_1) and series (λ_2) which, in a composite medium formed by solids and fluid (only water-saturated materials are considered in this section), are schematized in Figure 2.2 and described by a weighted arithmetic average (Eq.[2.5]) and a weighted harmonic average (Eq.[2.6]) respectively.

$$\lambda_1 = \frac{\sum_{i=1}^{n} w_i \lambda_i}{\sum_{i=1}^{n} w_i} \qquad \lambda_1 = (1-n)\lambda_s + n\lambda_w \qquad [2.5]$$

$$\lambda_{2=}\frac{\sum_{i=1}^{n} w_i}{\sum_{i=1}^{n}\frac{w_i}{\lambda_i}} \qquad \lambda_{2=}\left(\frac{1-n}{\lambda_s}+\frac{n}{\lambda_w}\right)^{-1} \qquad [2.6]$$

where n is the porosity of the soil. Composite materials with such phase configurations cannot have an isotropic thermal conductivity. The average of the parallel and series configurations (λ_3, Eq.[2.7]) and the weighted geometric mean of the conductivities of the two phases (λ_4, Eq.[2.8]) have been shown to be a useful way to represent the thermal conductivity of an isotropic two-phase materials (Horai et al. 1971, Johansen, 1975).

$$\lambda_3 = \frac{\lambda_1 + \lambda_2}{2} \qquad [2.7]$$

$$\lambda_4 = \left(\prod_{i=1}^{n} \lambda_i^{w_i}\right)^{\frac{1}{\sum_{i=1}^{n} w_i}} \qquad \lambda_4 = \lambda_s^{(1-n)}\lambda_w^{n} \qquad [2.8]$$

Russell (1953), studying insulating materials, derived the effective thermal conductivity (λ_5, Eq.[2.9]) of a porous material for a distribution of uniform pores of cubical shape arranged in a simple cubic lattice, assuming parallel heat flow.

$$\lambda_5 = \lambda_s\left[\frac{n^{2/3} + \left(\lambda_s / \lambda_w\right)\left(1-n^{2/3}\right)}{n^{2/3} - n + \left(\lambda_s / \lambda_w\right)\left(1+n-n^{2/3}\right)}\right] \qquad [2.9]$$

Maxwell (1873) produced a rigorous analysis of the electrical conductivity of a two-phase medium formed by spheres of one material arranged in a cubic array in the second medium. Hashin and Shtrikman (1962) extended Maxwel's two-phase work by proposing general expressions for multiphase materials. Given the mathematical analogy of the problems, these expressions are also valid for the case of heat conduction. The thermal conductivities λ_6 (Eq.[2.10]) and λ_7 (Eq.[2.11]) represent, respectively, the maximum and minimum values that

a homogeneous, isotropic two-phase material can attain, depending on the relative geometrical distribution of the phases. The upper bound, Eq.[2.10], describes a material formed by spheres of conductivity λ_w with concentration n within a medium of conductivity λ_s; while the lower bound, Eq.[2.11], describes spheres of conductivity λ_s with concentration 1-n embedded in a medium of conductivity λ_w.

$$\lambda_6 = \lambda_s + \frac{n}{\frac{1}{\lambda_w - \lambda_s} + \frac{1-n}{3\lambda_s}} \quad [2.10]$$

$$\lambda_7 = \lambda_w + \frac{n}{\frac{1}{\lambda_w - \lambda_s} + \frac{1-n}{3\lambda_w}} \quad [2.11]$$

A big drawback of the previous two equations is that they are based on the assumption of non-interacting spheres, which restricts its use to porosities close to zero or one, rarely found in soils. Nimick and Leith (1992) highlighted and addressed this issue by proposing a new expression (λ_8, Eq.[2.12]) based on the Hashin and Shtrikman (1962) / Maxwell (1973) limits and considering solid-continuous and fluid-continuous regions in saturated granular media.

$$\lambda_8 = \lambda_7 \left[1 - \frac{3n(1-A)}{2 + A + n(1-A)} \right] \quad A = \frac{\lambda_6}{\lambda_7} \quad [2.12]$$

Finally, Gori and Corasaniti (2004) presented a theoretical model (λ_9, Eq.[2.13]) based on the assumption that the unit cell of the soil is composed of a cubic space with a cubic solid particle at the centre, surrounded by fluid.

$$\lambda_9 = \left[\frac{\beta - 1}{\lambda_w \beta} + \frac{\beta}{\lambda_w \left(\beta^2 - 1 \right) + \lambda_s} \right]^{-1} \quad \beta = \sqrt[3]{\frac{1}{1-n}} \quad [2.13]$$

In addition to the previous theoretical models which do not consider the soil fabric, several more recent models have incorporated parameters to describe the anisotropy of the soil fabric and the particle geometry and contact. A simple approach (λ_{10}, Eq.[2.14]) was proposed by

Abuel-Naga et al. (2008), which formulates a weighted average of the series and parallel models, controlled by the parameter Ω, seeking to describe the soil fabric condition.

$$\lambda_{10} = \Omega\lambda_1 + (1-\Omega)\lambda_2 \qquad [2.14]$$

As seen in Figure 2.3, this morphological parameter takes values from 0 to 1, corresponding to the cases of perfect preferred particles orientations, perpendicular and parallel to the heat flow, equivalent to the series (λ_2) and parallel (λ_1) models respectively. The intermediate 0.5 value corresponds to a more "random" particle orientation which equals the average of the series and parallel models (λ_3). Using this simple approach, Abuel-Naga et al. (2008) successfully modelled experimental data of various soils, prescribing the magnitude of the parameter Ω between 0.35 and 0.45.

Hsu et al. (1995) proposed an expression (λ_{11}, Eq.[2.15]) for the thermal conductivity of three-dimensional spatially periodic media, considering arrays of touching (with small connecting bars) in-line cubes, as seen in Figure 2.4.

$$\lambda_{11} = \lambda_w \left[1-\gamma_a^2 - 2\gamma_a\gamma_c + 2\gamma_a^2\gamma_c + \frac{\gamma_a^2\gamma_c^2}{1/\left(\frac{\lambda_s}{\lambda_w}\right)} + \frac{\gamma_a^2 - \gamma_a^2\gamma_c^2}{1-\gamma_a + \left(\gamma_a / \frac{\lambda_s}{\lambda_w}\right)} + \frac{2\left(\gamma_a\gamma_c - \gamma_a^2\gamma_c\right)}{1-\gamma_a\gamma_c + \left(\gamma_a\gamma_c / \frac{\lambda_s}{\lambda_w}\right)} \right]$$

$$n = 1-(1-3\gamma_c^2)\gamma_a^3 - 3\gamma_c^2\gamma_a^2$$

[2.15]

where the fabric parameters $\gamma_a = a/l$ and $\gamma_c = c/a$ are entangled to the porosity. The authors suggest the touching parameter γ_c to take a value of 0.13 for modelling fluid-saturated packed-spheres beds, however the applicability of this method for clays is questionable given the geometrical assumptions of the model. More recently, Yu and Cheng (2002) proposed a fractal thermal conductivity model, assuming a porous media with some particles in contact with each other forming chains and others non-touching. This model incorporates a total of seven material fabric parameters to describe the particle geometry and contact and the fractal media.

This large number of parameters and the difficulties of their estimations curbs the applicability of this model.

The aforementioned models are compared in Figure 2.5, assuming a saturated soil with a thermal conductivity of the solid minerals, λ_s, of 3 $Wm^{-1}K^{-1}$ and a thermal conductivity of water, λ_w, of 0.607 $Wm^{-1}K^{-1}$. All models satisfy the limiting conditions of $\lambda_i = \lambda_s$ and $\lambda_i = \lambda_w$ at the porosities of $n = 0$ and $n = 1$ respectively. The parallel (λ_1) and series (λ_2) models produce the upper and lower bounds of all the thermal conductivity predictions respectively. The average (λ_3) of the two series and parallel models plots for most of the porosity range, except for very dense samples (n<0.25), between the upper (λ_6) and lower (λ_7) limit bounds of Hashin and Shtrikman (1962) which represent the maximum and minimum conductivities that an isotropic material formed by non-interacting spheres can attain. These two limits plot closer to the parallel model than to the series model. The Nimick and Leith (1992) model (λ_8), which is based on the limits of Hashin and Shtrikman (1962), plots within these limits for the whole porosity range, providing a close match to the lower bound at low porosities and moving towards the upper bound at higher porosities, with an equidistance between the two limits at the intermediate porosity of 0.5. Gori and Corasaniti (2004) (λ_9) gives a very similar prediction to the average of the series and parallel models (λ_3) for porosities above 0.3, and slightly above for smaller porosities. The commonly used geometrical mean (λ_4) is within the limits of Hashin and Shtrikman (1962) for most the porosity range, except for higher porosities, where it coincides with the lower bound (λ_7). Compared to the simple average of the parallel and series model, the geometric mean gives a higher prediction for porosities below 0.35 and a smaller one for higher ones. Russell (1935)'s model (λ_5) plots above the upper limit of Hashin and Shtrikman (1962), relatively close to the parallel model, which is not surprising given the parallel heat flow assumption in the original derivation. On the other hand, Hsu et al. (1995)'s model (λ_{11}), using the parameters recommended by the authors to simulate spherical particles, plots below the lower bound of Hashin and Shtrikman (1962).

In addition to the theoretical models previously described, there are also several semi-empirical and empirical expressions to estimate the thermal conductivity of saturated porous media. A selected few are presented in this section. An early expression from Kersten (1949), who performed tests on several types of soils, links the thermal conductivity (λ_{12}, Eq.[2.16]) to the water content (w, in %) and dry density (ρ_d, in kgm^{-3}) as follows, which can be modified for saturated material to be shown as a function of porosity and specific gravity (G_s).

$$\lambda_{12} = \left[0.13\log(w) - 0.288\right]10^{0.000625\rho_d}$$
$$\lambda_{12} = \left[0.13\log\left(100 * \frac{n}{Gs(1-n)}\right) - 0.288\right]10^{0.625(Gs(1-n))} \qquad [2.16]$$

Although Kersten (1949) did not perform any tests on a saturated material, the data was extrapolated to full saturation. Johansen (1975) later suggested that this may lead to underestimations in the case of quartzitic sands and overestimations for clayey soils.

De Vries (1952) proposed an expression (λ_{13}, Eq.[2.17]) for the thermal conductivity of ellipsoidal particles in a continuous medium of water:

$$\lambda_{13} = \frac{n\lambda_w + F(1-n)\lambda_s}{n + F(1-n)} \quad F = \frac{1}{3}\sum_{a,b,c}\left[1 + \left(\frac{\lambda_s}{\lambda_w} - 1\right)g_i\right]^{-1} \qquad [2.17]$$

where the factor F is a function of the shape parameters g, which satisfy the condition that $g_a + g_b + g_c = 1$. Although the values of g were meant to be shape factors in the original derivation, Farouki (1981) noticed that they were instead used as parameters to fit experimental data and λ_{13} is therefore classed here as a semi-empirical/empirical approach. The suggested factors ($g_a = g_b = 0.125$) of De Vries (1952) correspond to needle-shape like particles, moreover particles were assumed not to be in contact which is not the case in reality.

Woodside and Messmer (1961) proposed a semi-empirical approach (λ_{14}, Eq.[2.18]) based on the well-known theoretical solution of the three-resistor model used for determining electrical conductivity and is often referred to in the literature as the modified resistor equation.

$$\lambda_{14} = (n-0.03)\lambda_w + (1-n+0.03)\left[\frac{1-n}{1-n+0.03}\lambda_s^{-1} + \frac{0.03}{1-n+0.03}\lambda_w^{-1}\right]^{-1} \quad [2.18]$$

These three semi-empirical and empirical models are compared in Figure 2.6 using the same assumptions as in the comparison of the theoretical models (Figure 2.5). Also shown in in Figure 2.6 are the predictions of the theoretical models. Only the De Vries (1952) model (λ_{13}) meets the boundary conditions of $\lambda_i = \lambda_s$ and $\lambda_i = \lambda_w$ at the porosities of $n = 0$ and $n = 1$ respectively and its predictions of thermal conductivity are bounded by the upper and lower bounds (λ_6 and λ_7) for all values of n. Furthermore, for most of the relevant porosities in soils (n<0.6), it predicts higher thermal conductivities than the geometric mean average or the average of the parallel and series models. The modified resistor model of Woodside and Messmer (1961) (λ_{14}) only satisfies the limiting condition at $n = 1$; while at $n = 0$, it predicts a smaller thermal conductivity than λ_s. For the common range of porosities in soils, the model predicts slightly lower values than the upper bound of Hashin and Shtrikman (1962). The use of the Kersten (1949) empirical approximation (λ_{12}) is restricted for water contents above 7% and for high porosities gives a smaller conductivity than the one of the fluid, which is not correct. In the mid-porosity range, the Kersten (1949) has a very different slope than all the other theoretical and semi-empirical models and its application seems questionable.

2.2.2 Thermo-mechanical behaviour

Several components of the thermo-mechanical behaviour of saturated soils are discussed independently in this section: thermally-induced volume changes and excess pore pressures, compression behaviour and changes in the strength and stiffness.

a) Thermally-induced volume changes and excess pore pressures

When testing the temperature effects on soils, two drainage conditions are usually considered: drained conditions, in which water may enter or leave the sample during the temperature changes; or undrained conditions, in which water flow in or out of the sample is prevented. It is worth noting that in the latter tests undrained conditions do not imply a zero volumetric

strain, as in conventional saturated soil mechanics. The measurement of volume changes and pore pressures developed during both types of tests presents several experimental challenges due to (a) the external and incomplete nature of the measurement if drained water is the only parameter monitored and (b) the sensitivity of the instrumentation and equipment to temperature which needs to be calibrated appropriately. The volume of drained water only accounts for a part of the total thermal volumetric strain as the different components of the soil sample, minerals and water, and their relative volumes will also be affected by temperature. As a consequence, it is necessary to use assumptions to interpret the results if a direct measurement method is not available. Campanella and Mitchell (1968) and Baldi et al. (1988) presented two different interpretative frameworks considering the water fraction in its free or adsorbed form respectively, which are later discussed in Chapter 5.

A summary of the main studies of the drained thermal behaviour of saturated clays is presented in Figure 2.7, using the same axes scale for the temperature (T) and thermal volumetric strain ($\epsilon_{v,T}$), for ease of comparison. Campanella and Mitchell (1968), pioneers in the field, showed that the first cycle of drained heating from 20 to 60 °C on a normally consolidated (NC) remoulded illite caused a significant permanent decrease in volume (contraction), which was not recovered during cooling. Subsequent temperature cycles seemed to produce additional permanent deformations, although of a much smaller magnitude. Hueckel and Baldi (1990), testing Pontida silty clay, showed again contractive behaviour upon heating of the NC sample, with a generated thermal strain only partially recovered during cooling. Increasing the overconsolidation (OC) ratio seemed to affect the thermal strain response, causing a change of sign (expansion upon heating) in heavily OC samples of this clay. Similarly, Baldi et al. (1991), testing Boom clay, showed again large and almost irreversible contraction of a NC sample during the first cycle of heating-cooling from 20 to 95 °C and back to 20 °C. However, during the same thermal cycle, the OC samples exhibited expansive thermal strain, much smaller in magnitude and largely reversible. Testing the same clay to a slightly higher temperature, Sultan et al. (2002) found that OC samples

would initially expand and then contract after reaching a certain temperature. This transition temperature seems to increase with overconsolidation ratio. The authors also showed the importance of the rate of cooling and reported further contraction upon drained cooling in all samples tested. Cekerevac and Laloui (2004) tested reconstituted kaolin samples and confirmed the findings of Sultan et al. (2002) on the transition between from dilatant to contractant behaviour while heating OC samples of kaolin in a similar temperature range of 20 to 90 °C. The magnitude of the dilation seems to increase with overconsolidation ratio and their test on a highly overconsolidated (OCR12) showed an initial rate of expansion of approximately an order of magnitude higher (~300*10^{-6} °C^{-1}) than the typical expansion of the soil minerals (~30*10^{-6} °C^{-1}). Finally, the tests of Abuel-Naga et al. (2007b) on soft Bangkok clay agree with the previous results, also showing a transition temperature during heating and largely recoverable thermal strains in heavily OC samples. Different from the previous studies is the behaviour of the NC sample of Bangkok clay which showed much larger contraction during heating to 90 °C. The magnitude of the thermal contractant strains seems to greatly depend on the type of soil, with the largest volumetric strain of about 6% generated in a sample of NC Bangkok clay during heating from 25 to 90 °C. However, the magnitudes of the dilatant thermal volumetric strains during heating of the OC samples in all presented studies are much more limited.

Demars and Charles (1982) studied the drained behaviour of several clays and silts with various stress histories during a small thermal cycle of 25 °C. The permanent reduction of void ratio for NC samples after a temperature cycle was found to be independent of the value of the confining stress and a linear relationship was observed between the permanent reduction in void ratio after a drained temperature cycle for NC samples and the plasticity index. It is worth noting that changes in void ratio and volume strains may take a different sign, as later shown in Chapter 5. In the case of overconsolidated samples, the permanent reduction of void ratio seemed to depend on soil type and degree of overconsolidation. Burghignoli et al. (2000) studied the thermal behaviour of three Italian natural clays: Todi, Fiumicino and Bologna and

showed that the void-ratio changes due to rearrangements of particles depended, in addition to the value of the temperature and the formation stress history, on the time elapsed between the end of primary consolidation of the mechanical loading and the start of the temperature loading, on the recent stress history and the rate of temperature changes. Overconsolidated samples with a recent history of reloading showed contractant behaviour while those with a recent unloading stress history dilated.

In terms of undrained heating, Campanella and Mitchell (1968) showed that during heating up to 60 °C of remoulded illite, significant excess pore pressures were generated, which were largely recoverable during cooling, showing some hysterical behaviour. Additionally, undrained heating of NC San Francisco Bay mud samples, which no prior temperature history, showed a similar response, but with a residual excess pore pressure at the end of the temperature cycle. Abuel-Naga et al. (2007b) studied the undrained thermal behaviour of soft Bangkok clay, as depicted in Figure 2.8. The thermally induced pore pressure, generated, according to the authors, duee to the difference in thermal expansion of water and mineral solids, seems to be reversible and stress level dependant for the NC samples. In the case of the OC clay samples, the thermally induced pore pressures seem to be irreversible and the cooling path shows dependence on the stress history. It is worth noting that the OCR 4 sample despite developing positive pore pressures did not show contractant behaviour in the drained heating test.

b) Compression properties and pre-consolidation pressure

Campanella and Mitchell (1968) studied the influence of temperature on the isotropic consolidation of soils. As shown in Figure 2.9 for samples of saturated remoulded illite, the compression curves obtained at different temperature plot parallel, implying that the parameter C_c or λ as a slope of the normal compression line (NCL), is independent of temperature. This finding was also confirmed later by several researchers testing other types of clay (Burghignoli et al., 2000; Graham et al., 2001; Cekerevac and Laloui, 2004; Abuel-Naga et al., 2007a). Abuel-Naga et al. (2007a) also suggested the independence on temperature of the slope of

the swelling line κ, whereas Lingnau et al. (1996) and Graham et al. (2001) report a temperature dependence on κ, which increases with increasing temperature. Several researchers, as summarised by Leroueil and Marques (1996) (Figure 2.10), have shown a reduction of the pre-consolidation pressure with increasing temperature. Leroueil and Marques (1996) suggested that the reduction of pre-consolidation pressure was approximately of 1%/°C on average for the temperature range of 5 to 40 °C.

c) Strength and Stiffness

An intriguing aspect of the thermo-mechanical behaviour of saturated clays is the influence of temperature on the strength and stiffness. This has been an area of discrepancy in the literature, with some studies pointing towards an increase in strength due to an increase in temperature, while others show a decrease or no influence of temperature on the strength of the material. Table 2.2 summarises the findings of several thermo-mechanical tests on saturated soils, considering the type of soil and the drainage conditions during the temperature changes and during shearing. Hueckel et al. (2009) pointed to the lack of emphasis on the pre-shearing thermal and mechanical history of the samples as one of the reason towards these discrepancies. This confusion only gets worse with the lack of clarity on what is described by the various researchers as “strength”, whether this is defined as the maximum value of the mobilised deviatoric stress, which is not a material parameter; or the material parameter M, defined as the stress ratio q/p' at critical state. The present work aims to bring some clarity in this topic by considering all these aspects when reviewing previous work.

The studies that point towards an increase of the undrained shear strength of the clay with temperature have in common that heating prior to shearing was performed under drained conditions. Abuel-Naga et al. (2007a) showed that soft Bangkok clay samples sheared at high temperature had a higher undrained shear strength regardless of their stress history. The increase in deviatoric stress during shearing stress was accompanied by a reduction in excess pore pressures; while at critical state no variation of M was reported. Similar findings were reported by Tanaka et al. (1997) on a reconstituted illitic shale and by Houston et al. (1985)

on normally consolidated seafloor sediments. Kuntiwattanakul et al. (1995) observed an increase in undrained shear strength with temperature only for normally consolidated kaolin samples; but no changes in the case of overconsolidated samples, as presented in Figure 2.11. On the other hand, the undrained shearing results of Chiu (1996) and Burghignoli et al. (1992 and 2000) also show that the undrained shear strength is unaffected by temperature for both normally consolidated and overconsolidated samples of Todi clay and in the case of Mitchell (1964) and Lingnau et al. (1996), lower undrained shear strengths for San Francisco by mud and sand-bentonite mixtures after drained heating are reported respectively.

There are also discrepancies in the cases where shearing is performed under drained conditions. Cekerevac and Laloui (2004), testing kaolin clay, concluded that "the strength envelope at critical state is independent of testing temperature". However, the same tests were reported in Hueckel et al. (2009) as showing a "very clear growth of M" with an increase in temperature pre-shearing. Figure 2.12 illustrates these tests, together with the authors's interpretations of critical state. An increase of the maximum deviator stress can be seen for the heated samples, particularly in the case of the normally to slightly overconsolidated samples. Abuel-Naga (2007a) performed several drained shearing tests on soft Bangkok clay at various temperatures and showed that the higher the temperature during shearing, the higher the peak deviatoric stress, although the residual deviatoric stress of the soil was independent of temperature. In such study, the slope of the critical state line in the deviatoric plane was found to be temperature independent. On the other hand, the results of drained shearing tests on Pontida clay (Hueckel and Baldi, 1990) and on a high-carbonated Spanish clay (Del Olmo et al., 1996) show a decrease of the maximum deviator stress with temperature.

Finally, there seems to be more agreement for the cases where heating was performed under undrained conditions. Moritz (1995) in the case of Linkoping clay showed a decrease in undrained shear strength with temperature, which can be associated with the decrease in effective stress in the sample due to the excess pore pressures generated during heating

under undrained conditions. The results of Murayama (1969), Sherif and Burrous (1969) and De Bruyn and Thimus (1996) on Osaka clay, kaolin and Boom clay respectively, also show a decrease in the maximum unconfined compression strength following heating under undrained conditions. On the other hand, Hueckel and Baldi (1990) performed a different type of test in which the deviatoric loading of the material began at room temperature up to a stress level far below the isothermal undrained failure load and then heated it under undrained conditions at constant stress inducing thermal failure. The value of the stress ratio at the end of the test was higher than for case of isothermal conditions for Boom clay and remained unchanged for Pontida clay. Towhata et al. (1993) showed that the unconfined compression strengths of two clays were independent of the temperature at which the clay powders were preheated before the tests.

In terms of stiffness, similar conflicting findings are found. The normally consolidated illite and smecite-rich seafloor sediments heated under drained conditions and sheared under undrained conditions, and reported in Houston et al. (1985), showed increased stiffness with increasing temperature. Similar observations were made by Kuntiwattanakul et al. (1995) on normally consolidated kaolin samples, while in overconsolidated samples only the initial stiffness at 0.1% strain level was higher in heated samples (Figure 2.11). Burghignoli et al (1992, 2000) showed that samples subjected to drained thermal cycles exhibited higher stiffness. On the other hand, Pontida clay samples tested in Hueckel and Baldi (1990), heated and sheared under drained conditions, showed reduced stiffness with higher temperature.

2.2.3 Thermo-hydraulic behaviour

The studies of the thermo-hydraulic behaviour of soil are far scarcer than those for the thermo-mechanical behaviour. The hydraulic conductivity k (commonly referred as permeability) of saturated soils changes with temperature. Several studies have been performed to measure these changes and to establish whether they solely correspond to changes in the properties (viscosity and density) of the pore fluid with temperature or whether additional factors may be responsible for these changes. Delage et al. (2000) testing Boom clay, and Morin and Silva

(1984) testing several ocean sediments at different temperatures showed that there is a unique linear relationship between the intrinsic permeability and porosity and concluded that the intrinsic permeability is independent of temperature. The intrinsic permeability K_i is defined in Eq.[2.19], where μ_w, ρ_w and γ_w are the dynamic viscosity, density and unit weight of the fluid respectively.

$$K_i = \frac{k\mu_w}{\rho_w g} = \frac{k\mu_w}{\gamma_w} \qquad [2.19]$$

By computing the previous equation at different temperatures (T and T', where $T' > T$), the ratio of the hydraulic conductivity at a high temperature to the one at a reference temperature (k'/k) can be expressed as follows:

$$\frac{k'}{k} = \frac{K_i'}{K_i}\frac{\rho_w'}{\rho_w}\frac{\mu_w}{\mu_w'} \qquad [2.20]$$

It can be seen that the changes in hydraulic conductivity with temperature are due to changes in three different factors: the viscosity factor (μ_w/μ_w'), the density factor (ρ_w'/ρ_w) and the intrinsic permeability factor (K_i'/K_i), which can be assumed to be equal to one according to Morin and Silva (1984) and Delage et al. (2000), therefore simplifying Equation [2.20]:

$$\frac{k'}{k} = \frac{\rho_w'}{\rho_w}\frac{\mu_w}{\mu_w'} \qquad [2.21]$$

The changes of density (ρ_w, in kgm^{-3}) and viscosity (μ_w, in Pa·s) under atmospheric conditions with temperature (T, in °C) may be expressed by the following equations (Eq.[2.22] and Eq.[2.23], respectively), obtained from the data produced by the latest relase of the equation of state for water (IAPWS, 2007):

$$\rho_w(T) = 999.9 + 0.0465T - 0.00734T^2 + 3.943*10^{-5}T^3 - 1.225*10^{-7}T^4 \qquad [2.22]$$

$$\mu_w(T) = 0.0009404e^{-0.05143T} + 0.0008363e^{-0.01131T} \qquad [2.23]$$

Using a reference temperature of 20 °C as a common temperature in standard laboratory conditions, the influences of the changes in viscosity and density due to temperature are presented in Figure 2.13, together with the predicted change in hydraulic conductivity as described in Eq.[2.21]. The graph clearly shows that the changes in the viscosity of the fluid are the most important contribution for the variation in the hydraulic conductivity ratio, and that the influence of the changes in density is very small for the range of temperatures considered.

In Figure 2.14, the predicted changes in hydraulic conductivity obtained by Eq.[2.21] can then be compared to the data from several soils: bentonite (Towhata et al., 1993; Cho et al., 1999; Romero et al., 2001), kaolin (Towhata et al., 1993) and soft Bangkok clay (Abuel-Naga et al., 2005). The results of the tests on soft Bangkok clay and for the lower density bentonite samples of Cho et al. (1999) show a good match with the predicted values considering the changes in viscosity and density of water only. However the increase in permeability with temperature for the high density bentonite of Cho et al. (1999), and the bentonite and kaolinite tested by Towhata et al. (1993) is considerably larger than predicted. On the other hand, Romero et al. (2001) show a very small increase of permeability with temperature on their tested bentonite. Gens (2010) suggested that additional factors, other than the viscosity and density of the fluid, may affect the saturated hydraulic conductivity and further research in the field is necessary. It is worth noting that these results come from direct and indirect (consolidation curves from oedometer data) measurements of permeability. The latter has been questioned in the literature (Burghignoli et al., 1995; Delage et al., 2000) due to their indirect nature and the product of the errors in the measurement of the coefficient of consolidation and the coefficient of volume compressibility when estimating the permeability. It can be seen that in some tests the changes in hydraulic conductivity can be explained by the changes in the properties of the fluid, while in other cases the changes are much larger, or much lower than the ones predicted by Eq.[2.21].

2.3 Overview of the development of testing equipment for the characterisation of the THM of saturated soils

This section reviews some of the major developments of laboratory testing equipment for the characterisation of the thermal properties, thermo-mechanical and thermo-hydraulic behaviour of saturated soils.

2.3.1 Measurement of thermal properties

The methods for the measurement of thermal properties in the laboratory are classified into steady state methods and transient state methods, depending on the conditions of the temperature field at the time of the measurement. Both types of method of measurement involve the application of a temperature gradient within the soil and the analysis of the data according to the relevant form of the heat conduction equation. A common challenge for both types of test, especially in the case of unsaturated soils, is the occurrence of moisture migration and convective effects as a result of the temperature gradient in the soil (Farouki, 1981).

The main steady state method is the divided bar apparatus, of which several versions have been developed during the years. Figure 2.15 shows three different relatively modern versions of the test (Kukkonen and Lindberg, 1995; Abuel-Naga et al., 2009; Barry-Macaulay et al., 2013). The operational principle is very similar in all cases, consisting of creating a temperature gradient through the sample between the two ends, measuring the heat flux and temperature loss and applying the one-dimensional form of Fourier's law of heat conduction once steady state conditions have been reached. The soil sample is usually sandwiched between heat flux sensors, which can take the form of a modern heat flux transducer as in Abuel-Naga et al. (2009), or a heat flux meter made from two aluminium or copper (very highly conductive materials) disks with an inserted thermocouple between materials of known thermal conductivity such as polycarbonate, quartz or silica glass (Kukkonen and Lindberg, 1995; Barry-Macaulay et al., 2013). The divided bar apparatus may take the form of an

oedometer, allowing for control of the vertical stress during the thermal tests (Abuel-Naga et al., 2009; Barry-Macaulay et al., 2013). Several experimental issues arise from this type of test, as significant radial heat losses may occur if insufficient insulation is placed at the sides of the sample. Another drawback is the long time required usually for reaching steady-state. Moreover, the magnitude of the temperature gradient and the length of the tests can give rise to moisture migration throughout the sample (Farouki, 1981 and Sass et al., 1984).

The mathematical analysis of heat conduction introduced by Carslaw and Jaeger (1946) put in place the foundations for the development of needle sensors, which measure the thermal properties during the transient state. Van der Held and Van Drunen (1949) for liquids, and later Hooper and Lepper (1950) and De Vries (1952) for soils, developed a method, known as the “thermal needle”, for the measurement of thermal conductivity. It consisted of a thin, long cylindrical needle, simulating a line heat source, containing a heater which produces a constant heating power and a temperature sensing element. The thermal conductivity of the surrounding media governs the observed rate of temperature rise in the needle. This method has quickly become widely accepted and used by researchers worldwide in various scientific fields. Campbell et al. (1991) proposed a dual-probe heat-pulse sensor which, by using the infinite line heat source theory of Carslaw and Jaeger (1959), enables all thermal properties (thermal conductivity, diffusivity and volumetric heat capacity) to be established. The sensor consists of two thin needles placed 6 mm apart, one containing a heating element and the other a temperature sensor which monitors the temperature rise after a short (<12 seconds) heat pulse. More recently, multi-needle heat pulse sensors have been combined with time domain reflectometry technology to allow, in addition to the thermal properties, the determination of the soil’s electrical properties and water content, density and air-filled porosity (Ren et al., 1999; Ochsner et al., 2001; Zhang et al., 2017). Transient methods have been shown to provide a rapid and accurate measurement of the thermal properties compared to more time-consuming steady-state methods (Mitchell and Kao, 1978), while the moisture migration induced by temperature gradients is minimised (Jackson and Taylor, 1986). On the

other hand, their applicability to stiff soils and rocks becomes challenging as pre-drilling may be required which can lead to significant contact resistance errors (Barry-Macaulay et al., 2013).

2.3.2 Thermo-mechanical tests

The following bibliographical overview presents some of the main temperature-controlled triaxial and isotropic cells used for the study of the thermo-mechanical behaviour of saturated soils. It is divided in three sections depending on the way in which heating occurs: circulating the confining fluid, lateral and/or external heaters and internal heaters. In addition to this type of laboratory equipment, several researchers have also adapted conventional oedometers for the control of temperature. This, however, presents several challenges such as the possible loss of one-dimensional conditions due to the distinct expansion of the metallic ring and the soil sample and the resulting uncertainty in the exact volumetric and stress state of the sample. Given that no oedometer is used in this research project, previous temperature-controlled oedometers are not discussed in this section.

a) Heating by circulating the confining fluid

Campanella and Mitchell (1963) pioneered the development of the first triaxial apparatus that permitted the control of both temperature and stresses at the University of California (Berkeley, USA). The equipment, shown in Figure 2.16, consisted of a group of four triaxial units placed individually in an air-filled heating chamber. Water was heated or cooled externally in a reservoir and then circulated to the desired triaxial cells, also acting as the confining fluid. The temperature of the soil samples was controlled over a range of 4 to 60 ºC with an accuracy of ±0.3 ºC and monitored using an iron-constantan thermocouple encased in a 1.5 mm stainless steel tube inserted about 13 mm through the base, an intrusive method of measuring temperature which may cause some disturbance to the sample. Pore pressures were monitored using an electrical pressure transducer mounted at the base and sample volume changes during temperature changes were measured from the drained water, as later detailed

in Chapter 5 (Campanella and Mitchell, 1968). Savvidou and Britto (1995) at the University of Cambridge also designed a temperature-controlled triaxial apparatus which involved circulating water, also used as confining fluid, at temperatures from ambient up to 80 ºC.

b) Heating by lateral and/or external heaters

Researchers at the ISMES (Applied Research Institute for Structural modelling) in Bergamo (Italy) developed a high-pressure, high-temperature triaxial apparatus in the 80s shown in Figure 2.17, which is presented by Baldi et al. (1987). Heating was applied more externally than in the previously described apparatuses, without the issues linked with circulating the heated confining fluid in terms of maximum pressures, constrained by the pumping capacity. A flexible rubber 1700 W heater attached to the cell and two 500 W heating elements placed within the base were used to control the temperature of the cell. These functioned independently by programmable controllers which used the feedback data from a thermocouple placed near the heaters. The apparatus was reported to be capable of performing tests at pressures up to 20 MPa and temperatures up to 200 ºC, although such extremes were not reported in subsequent published work. Another apparatus which used a similar method of external and lateral heating was the one of Lingnau (1993) at the University of Manitoba (Canada), which used two rubber band heaters on the sleeve of the cell and a continuous power base heater. A particular characteristic of this equipment was the use of silicon oil as confining fluid instead of water because of its low electrical conductivity, compressibility, viscosity and good temperature stability, which was preferred for the internal instrumentation. Its very low thermal conductivity, however, likely induced significant heat gradients. Finally, the isotropic apparatus presented in Delage et al. (2000), developed at the Ecole Nationale des Ponts et Chaussées (Paris, France), is shown in Figure 2.18. It was designed to withstand pressures up to 60 MPa and temperatures up to 100 ºC, with an accuracy of ±0.05 ºC. Heating, using coil placed in the outer wall of the cell, is controlled using a thermocouple placed within the confining water. In addition of monitoring drained water, the measurement of sample volume changes from cell fluid measurements was possible due to

the choice of a very stiff metallic system, with a reversible and repeatable response to testing cycles allowing for a reliable calibration of the system. This equipment was also capable of performing constant head permeability tests to study the thermo-hydraulic behaviour of clays. An interesting feature of this design is the thermal cut-off baths where the tubes are submerged between the cell and the instrumentation.

c) Heating by internal heaters

Demars and Charles (1982) presented the first isotropic temperature-controlled cell at the University of Delaware (USA), which is heated internally and independently from the pressure system. As depicted in Figure 2.19, the water inside the cell was heated using an interior copper circulating coil, which was able to increase the temperature of the soil samples up to 50 ºC. The Authors recommended the use of two latex membranes on the sample separated by silicon grease. Kuntiwattanakul (1991) designed a triaxial apparatus at the University of Tokyo (Japan) which consisted of two cells (outer and inner) as seen in Figure 2.20. The inner pyrex glass cell is filled with water and heated with a submerged variable power heater and circulated around the cell by a propeller driven by an external motor in order to achieve a uniform temperature quicker. The outer cell consists of an acrylic cylinder, and the chamber between the outer and inner cell walls is filled with air, which works both as an insulator and as a medium to transfer pressure to the inner cell. The apparatus is designed to withstand pressures up to 500 kPa and temperatures up to 90 ºC, with a control of ±0.1 ºC. A drawback of the design, highlighted by its authors, is air reaching the samples.

The latter mode of heating has been preferred by several researchers in the last decades. Moritz (1995) and Bergenstahl et al. (1994) at the Swedish Geotechnical Institute developed an apparatus heated by three internal heat foil sheets; while in De Bruyn and Thimus (1996)'s apparatus at the University of Leuven (Belgium) heating occurs through a submerged copper spiral through which heating fluid is circulated at temperatures up to 80 ºC in the case of water or 120 ºC if silicon oil is used. A more recent thermo-mechanical triaxial testing equipment developed at the EPFL (Switzerland), described by Cekerevac et al. (2005), presents several

similarities to the latter. It is shown in Figure 2.21 and can perform tests with a maximum cell pressure of 2 MPa and temperature of 90 ºC. Samples are also heated by circulating water inside a spiral metal tube submerged in the water-filled cell around the sample. Thermocouples placed near the sample are used for feedback signal and data recording and the system is reported to have an accuracy of ±0.25 ºC. As in Delage et al. (2000), the design incorporates a water-filled container at controlled temperature where the tubes connecting the controllers to the apparatus are placed. Finally, the equipment of Abuel-Naga et al. (2007b) uses submerged ring heaters for temperature control, with an accuracy of ±0.1 ºC.

2.3.3 Thermo-hydraulic tests

Several studies on the effects of temperature on permeability of soils simply estimated the permeability from the isotropic consolidation behaviour rather than direct measurements, as previously discussed. Other researchers have developed specific equipment for such tests (Morin and Silva, 1984; Cho et al., 1999). The previously described temperature-controlled isotropic cell of Delage et al. (2000) was also adapted for permeability measurement tests by using shorter samples and exposing the top of the sample to atmospheric pressure while increasing significantly back pressure at the bottom of the sample, generating a significant hydraulic gradient, sufficient to create a measurable flow.

2.4 Summary

This Chapter provides a brief review of the main achievements published in the literature on the investigation of the thermo-hydro-mechanical behaviour of saturated clays and an overview of some of the key laboratory equipment that enabled such discoveries.

Thermal properties

The main heat transfer mechanism in saturated clays is heat conduction, which can be described by the thermal properties of the soil (thermal conductivity, volumetric heat capacity and thermal diffusivity). These properties depend on several characteristics of the soil, such as the mineralogy, porosity (water content, density), particle contact and packing geometry

and may be measured in the laboratory using different methods, of which transient (needle) techniques can offer a quick, inexpensive and accurate solution.

Thermo-mechanical and thermo-hydraulic behaviour

Several research groups since the 60s have investigated the thermo-mechanical behaviour of saturated clays, especially the thermally-induced volume changes during drained heating and cooling, although the number of soils fully characterised remains small. In the case of London clay, its thermo-hydro-mechanical behaviour has not been previously thoroughly studied and the findings from other clay studies have to be used as a benchmark.

Most studies agree that drained heating of normally consolidated saturated clays causes a contraction of the material which is not recovered upon cooling; whereas a drained thermal cycle on highly overconsolidated clays causes a reversible expansion. In soils with intermediate overconsolidation ratios, the temperature at which the transition between dilative and contractant behaviour occurred increases with OCR. There are discrepancies however in the sign of the volumetric strains during cooling for all stress histories. Increasing temperature causes a reduction of the pre-consolidation pressure, but does not alter the slope of the normal compression lines. With regards to strength and stiffness, there is also a lack of agreement on the effects of temperature, except for the case of when heating is performed under undrained conditions, which generates an excess pore pressure and the consequent reduction of effective stress. Finally, the changes of the permeability of the clay with temperature cannot always be explained by the temperature effects on the viscosity and density of the fluid and further research on this aspect seems also necessary.

The laboratory investigation of the thermo-mechanical and thermo-hydraulic behaviour presents several challenges which need to be taken into account in the development of new experimental equipment: the adaptation of conventional soil mechanics testing equipment for the application and control of temperature and the appropriate calibration of the different measuring devices for the thermal effects.

Table 2.1 *Thermal conductivities of various minerals, water and air*

Mineral	Thermal conductivity ($Wm^{-1}K^{-1}$)	Source
Quartz	7.69	Horai (1971)
Dolomite	5.51	Horai (1971)
Calcite	3.59	Horai (1971)
Pyrite	19.20	Horai (1971)
Mica	2.32	Horai (1971)
Anhydrite	4.76	Horai (1971)
Albite	1.84	Horai (1971)
K-Feldspars	2.25	Horai (1971)
Gypsum	1.26	Horai (1971)
Smectite	1.88	Brigaud and Vasseur (1989)
Illite	1.85	Brigaud and Vasseur (1989)
Kaolinite	2.64	Brigaud and Vasseur (1989)
Chlorite	3.26	Brigaud and Vasseur (1989)
Water	0.607 (at 25 ºC)	IAPWS (2007)
Air	0.03	

Table 2.2 *Temperature effects on the shear strength of saturated clays*

Study	**Soil**	**Heating (D**rained/ **U**ndrained**)**	**Shearing (D**rained/ **U**ndrained**)**	**Strength (q_{max})**	**Strength (**ΔM (T)**)****
Mitchell (1964)	San Francisco Bay mud	D	U	Decrease	-
Murayama (1969)	Osaka clay	U	U (Unconfined)	Decrease	-
Sherif and Burrous (1969)	Kaolin	U	U (Unconfined)	Decrease	-
Houston et al. (1985)	Illite Smectite	D	U	Increase	-
Hueckel and Baldi (1990)	Pontida clay	D	D	Decrease	Unchanged
		U	U	-	Unchanged
	Boom Clay	U	U	-	Increase
Burghignoli et al. (1992 & 2000)	Todi clay	D	U	Unchanged	Unchanged
Towhata et al. (1993b)	Kaolin Bentonite	Preheated powder only	U (Unconfined)	Unchanged	-
Kuntiwattanakul et al. (1995)	Kaolin (NC)	D	U	Increase	-
	Kaolin (OC)			Unchanged	-
Lingnau et al. (1996)	Sand-Bentonite	D	U	Decrease	
Moritz (1995)	Linkoping clay	U	U	Decrease	-
De Bruyn and Thimus	Boom Caly	U	U	Decrease	-
Del Olmo et al. (1996)	High-carbonate Spanish clay	D	D	Decrease	-
Chiu (1996)	Kaolin	D	U	Unchanged	-
			D	Increase	-
Tanaka et al. (1997)	Illitic shale	D	U	Increase	Unchanged
Cekerevac and Laloui (2004)	Kaolin	D	D	Slight increase	Unchanged/ Increase*
Abuel-Naga et al. (2007)	Soft Bangkok clay	D	D/U	Increase	Unchanged

*Depending on which paper: Cekerevac and Laloui (2004) report no change in M; while re-analysis in Hueckel et al (2009) shows increase

**Several studies only present the stress-strain curves and further interpretation in terms of stress ratio at critical state is not possible to be conducted.

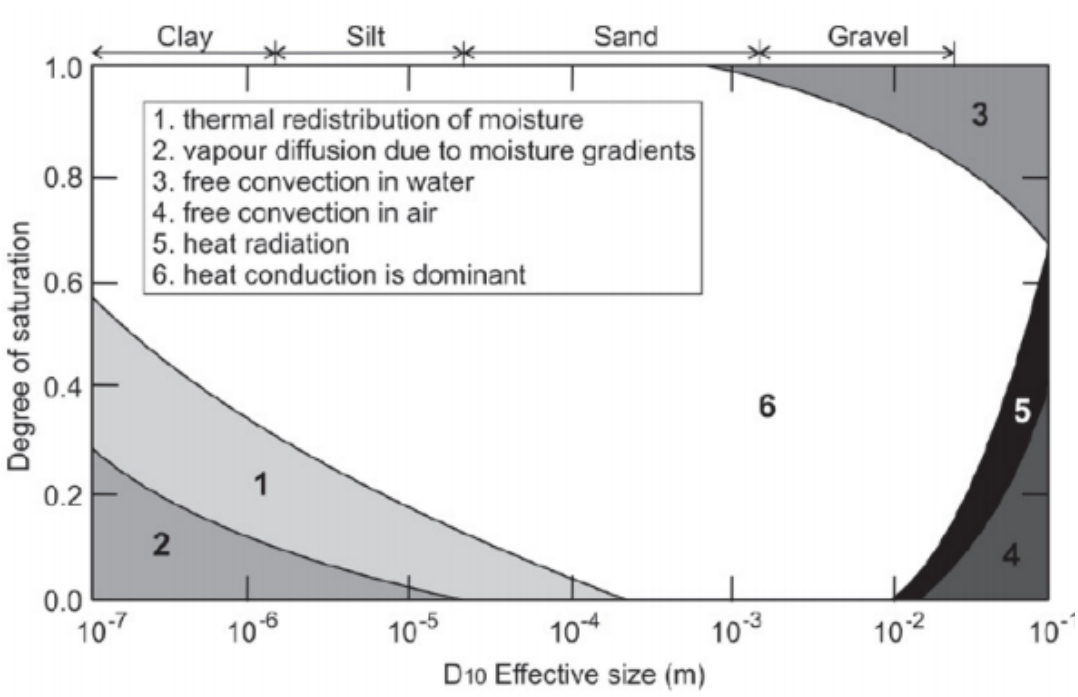

Figure 2.1 *Heat transfer mechanisms in soils (Loveridge, 2012, after Farouki, 1981)*

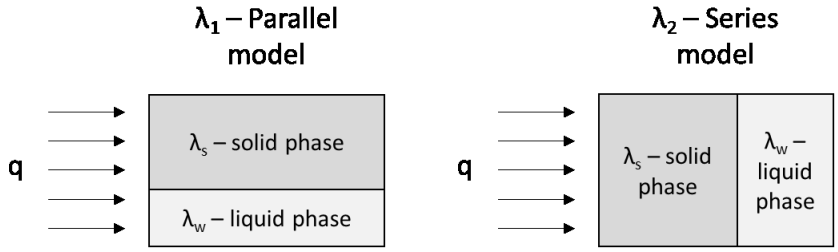

Figure 2.2 *Idealized soil elements in the parallel and series heat conduction models*

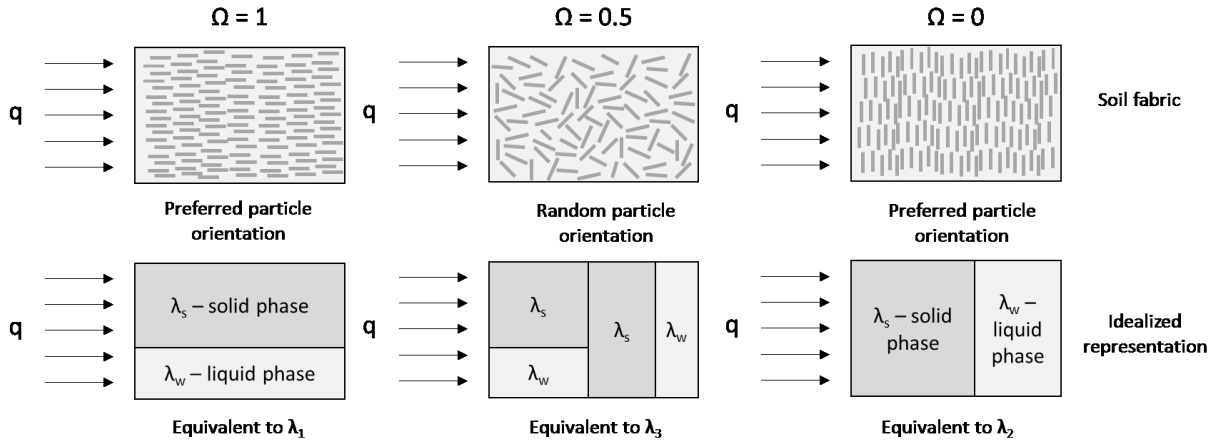

Figure 2.3 *Morphological soil parameter (after Abuel-Naga et al., 2008)*

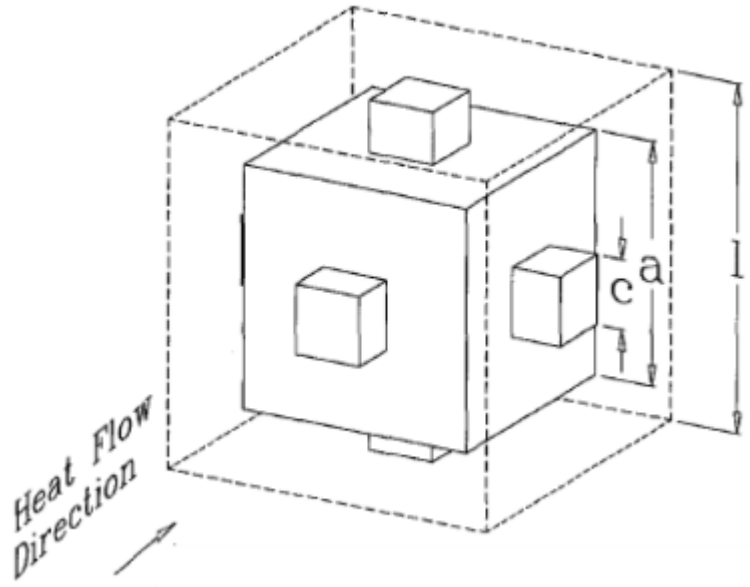

Figure 2.4 *In-line touching cube geometry (Hsu et al., 1995)*

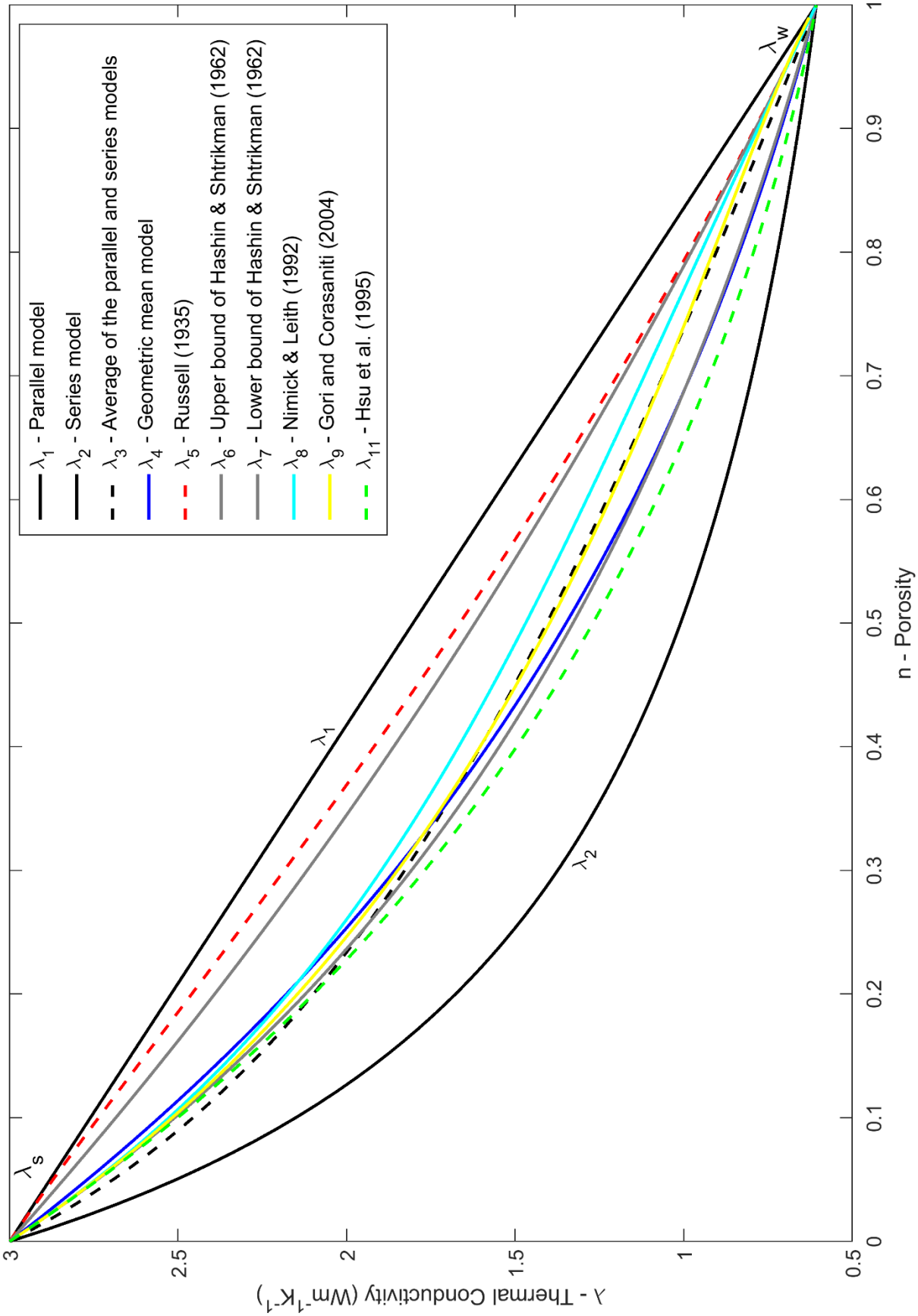

Figure 2.5 *Comparison of various theoretical thermal conductivity models (assuming λ_s=3 $Wm^{-1}K^{-1}$)*

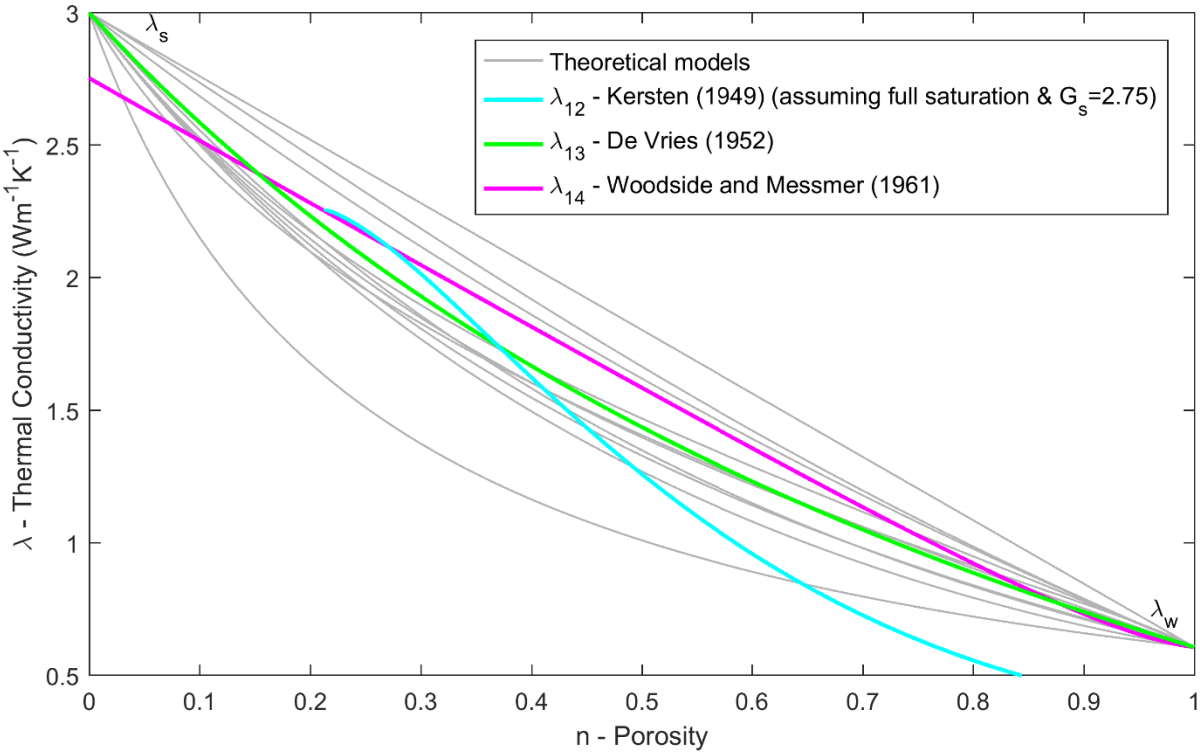

Figure 2.6 *Comparison of various semi-empirical and empirical thermal conductivity models (assuming λ_s=3 $Wm^{-1}K^{-1}$)*

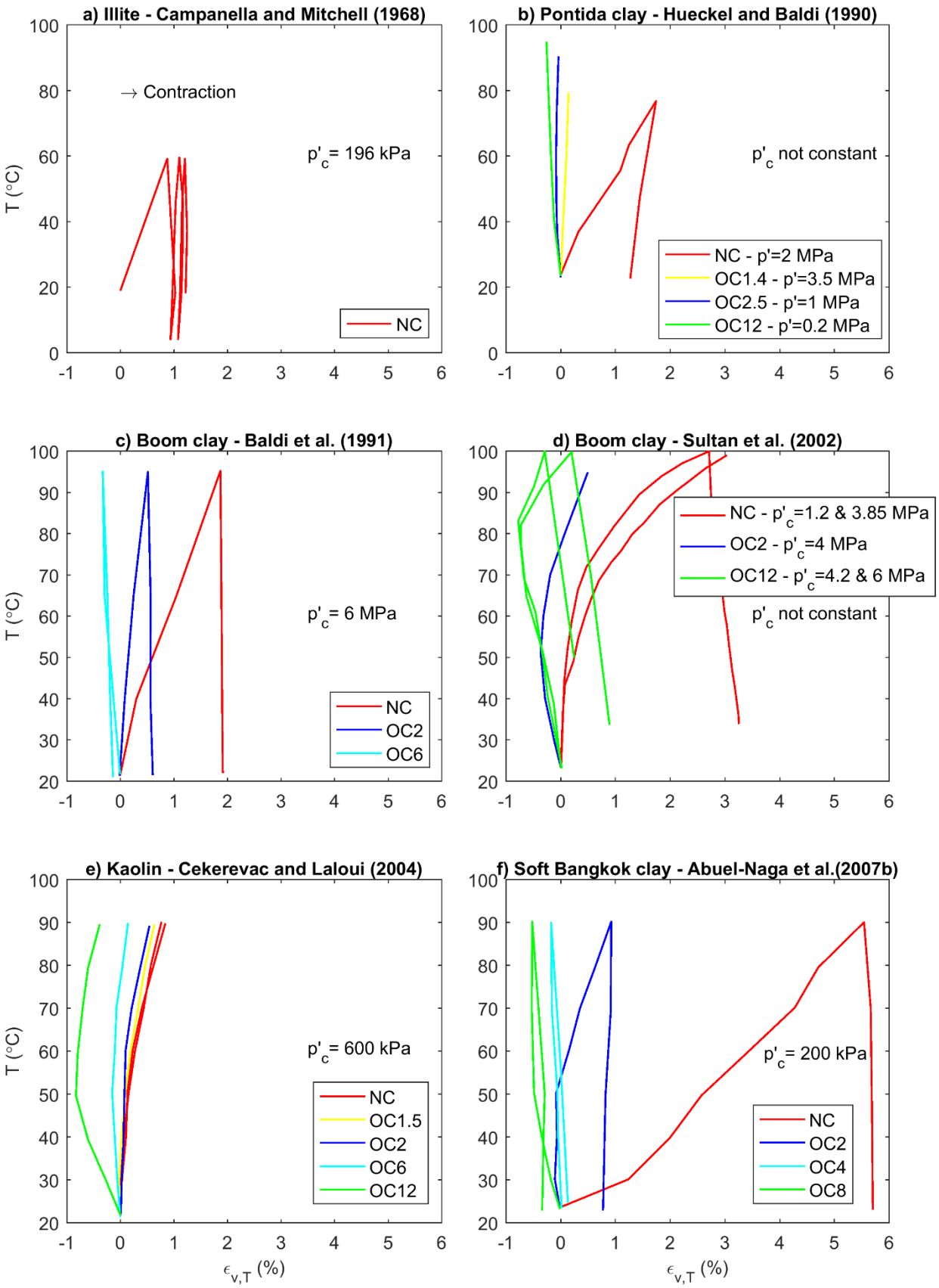

Figure 2.7 *Drained thermal behaviour of various soils*

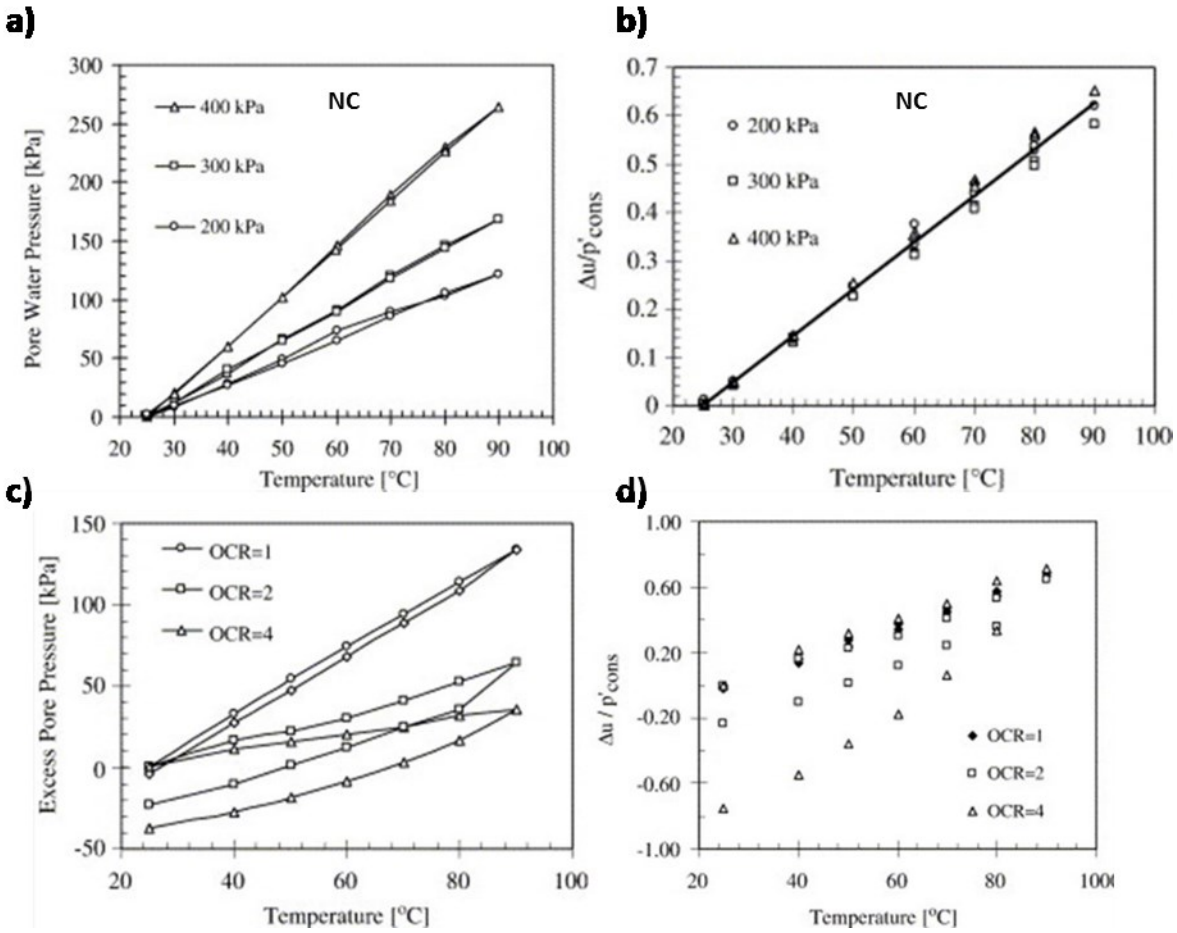

Figure 2.8 *Thermally-induced pore pressures in soft Bangkok clay samples ((a),(b) normally consolidated only; (c),(d) with different stress histories) (Abuel-Naga et al., 2007b)*

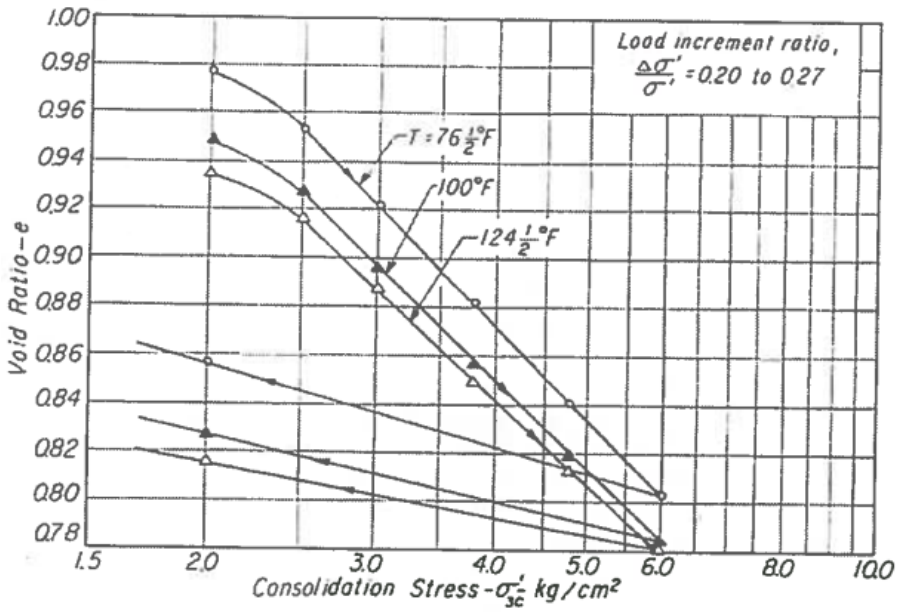

Figure 2.9 *Compression curves for saturated illite samples at different temperatures (Campanella and Mitchell, 1968)*

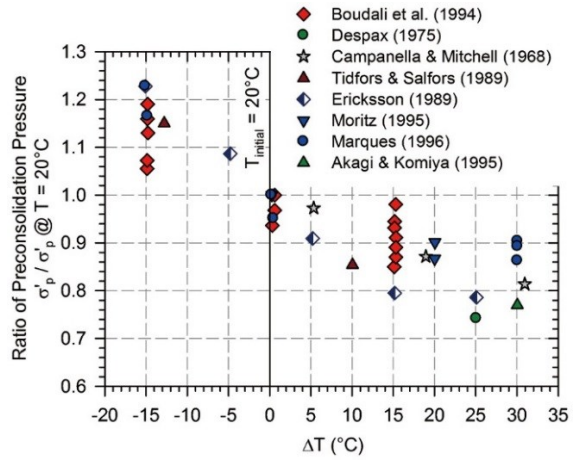

Figure 2.10 *Change in preconsolidation pressure with change in temperature (Leroueil and Marques 1996)*

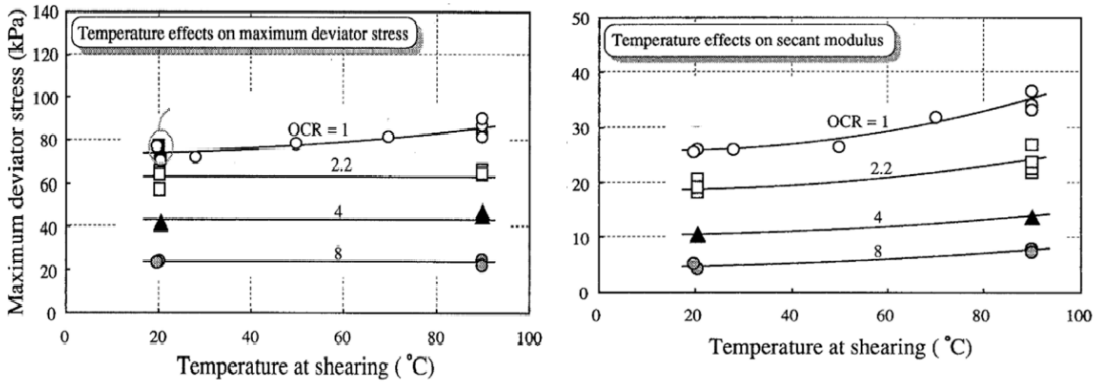

Figure 2.11 *Temperature effects on strength and stiffness from undrained shearing tests on kaolin clay after drained heating (Kuntiwattanakul et al., 1995)*[1]

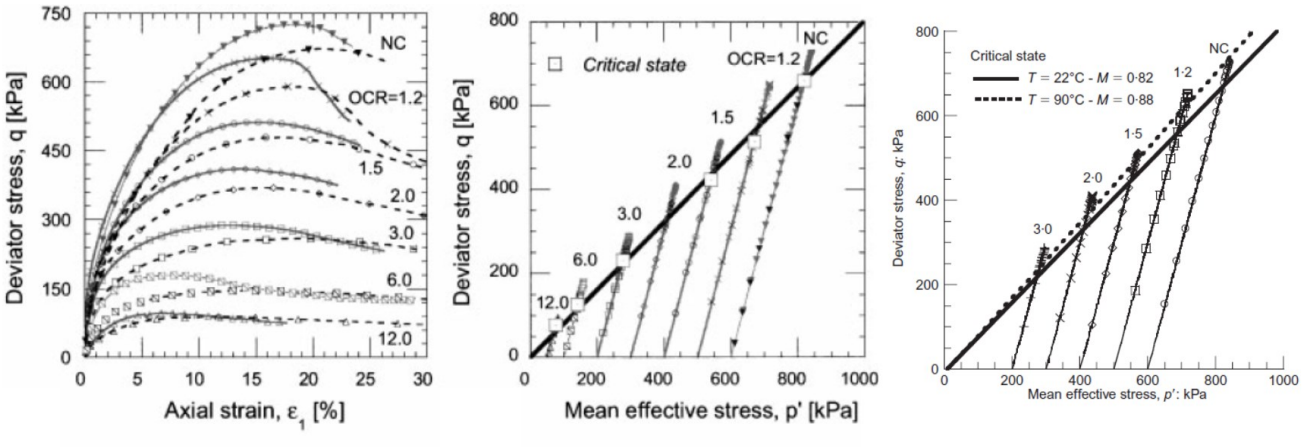

Figure 2.12 *Drained triaxial tests on kaolin (left and middle)(Cekerevac and Laloui, 2004) and interpreations of critical state (middle from Cekerevac and Laloui, 2004 and right from Hueckel et al., 2009)*[2]

[1] Vertical axys label of right figure: Secand Modulus at 0.1% strain (MPa)
[2] Legend for left figure: 22 °C – dashed lines; 90 °C – solid lines.

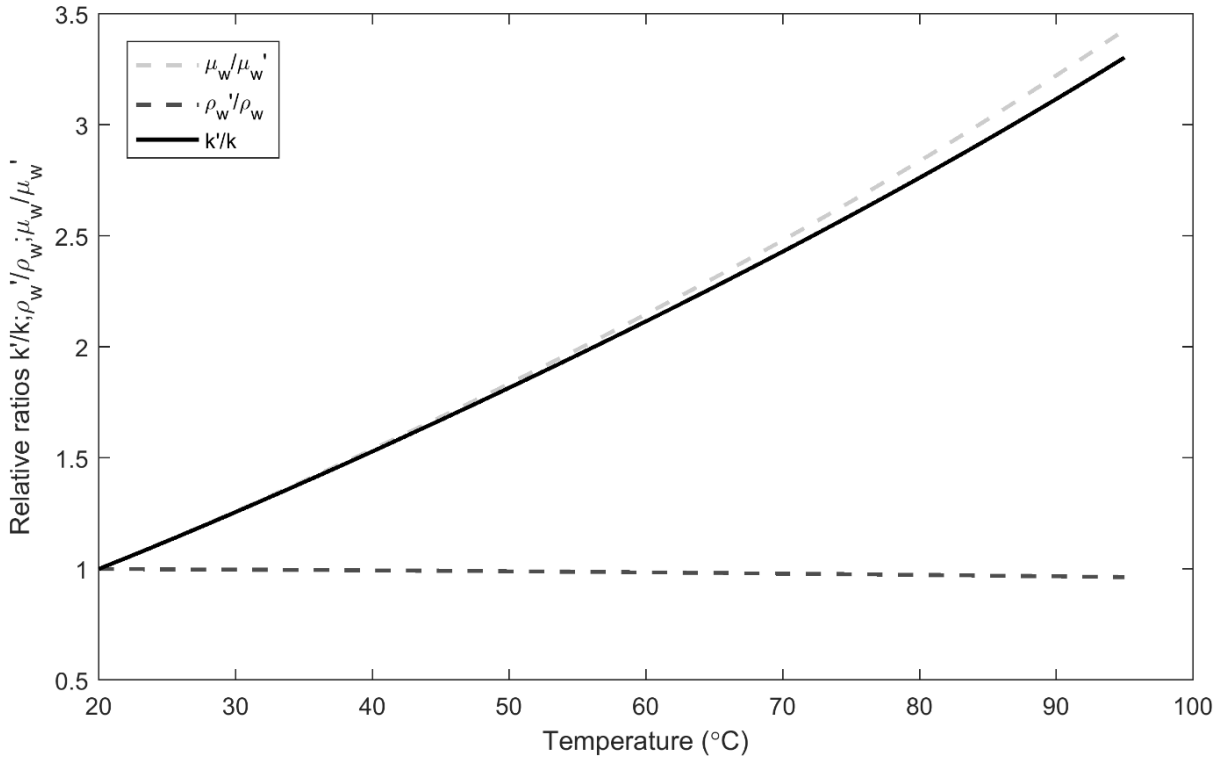

Figure 2.13 *Relative contributions of the viscosity and density of water to the permeability*

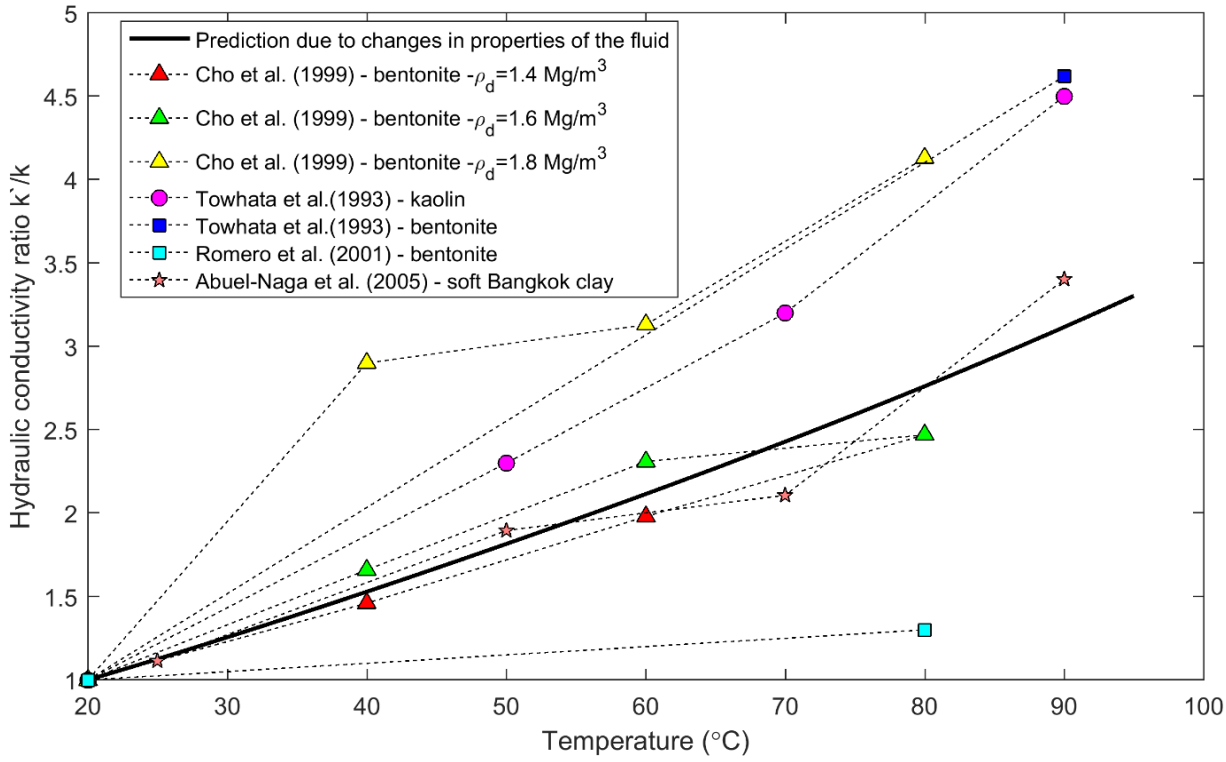

Figure 2.14 *Measured and predicted changes in hydraulic conductivity with temperature (data: Towhata et al., 1993; Cho et al., 1999; Romero et al., 2001; Abuel-Naga et al., 2005)*

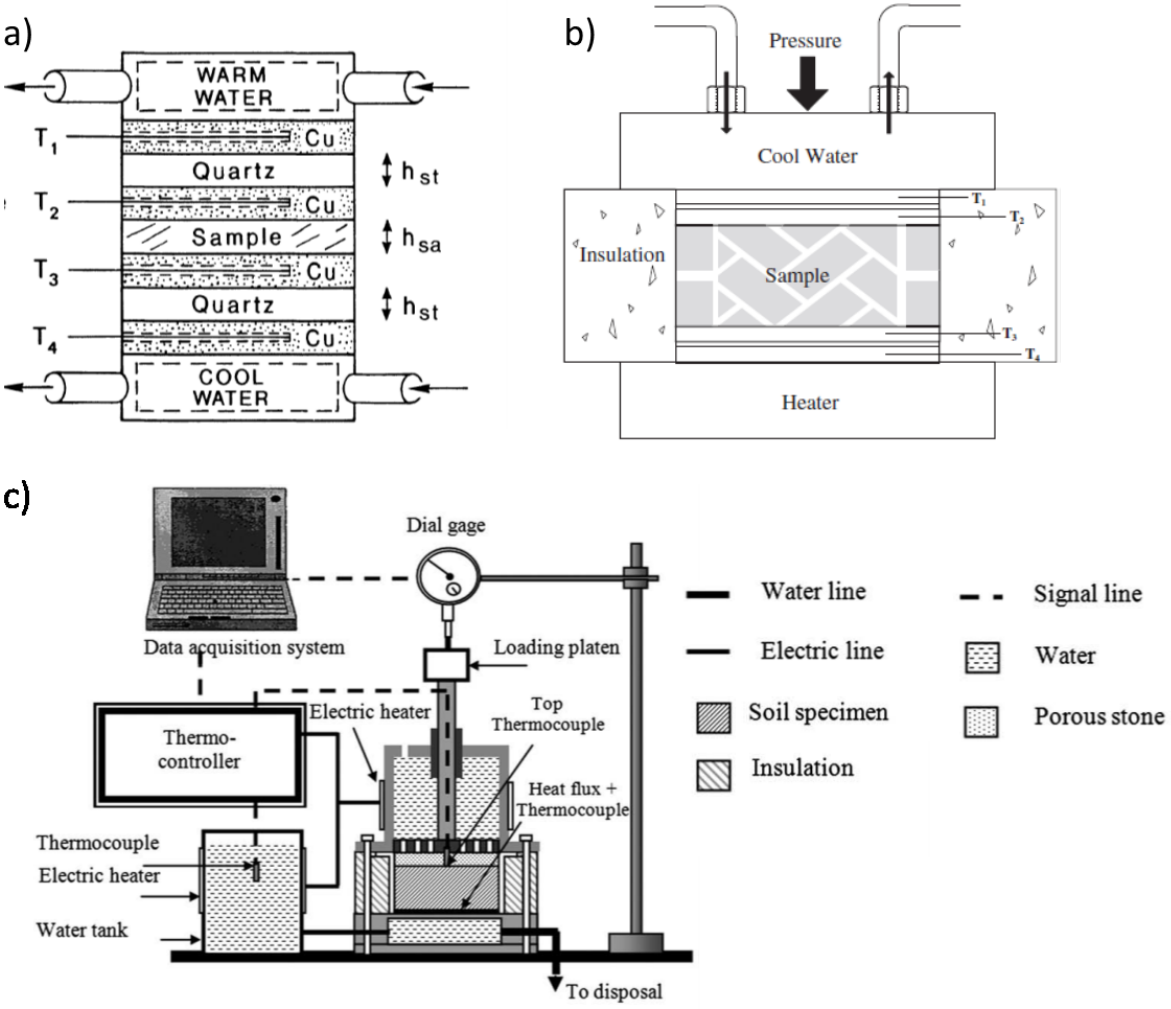

Figure 2.15 *Schematic of various divided bar apparatuses: a) Kukkonen and Lindberg, 1995; b) Barry-Macaulay et al., 2013; c) Abuel-Naga et al., 2009.*

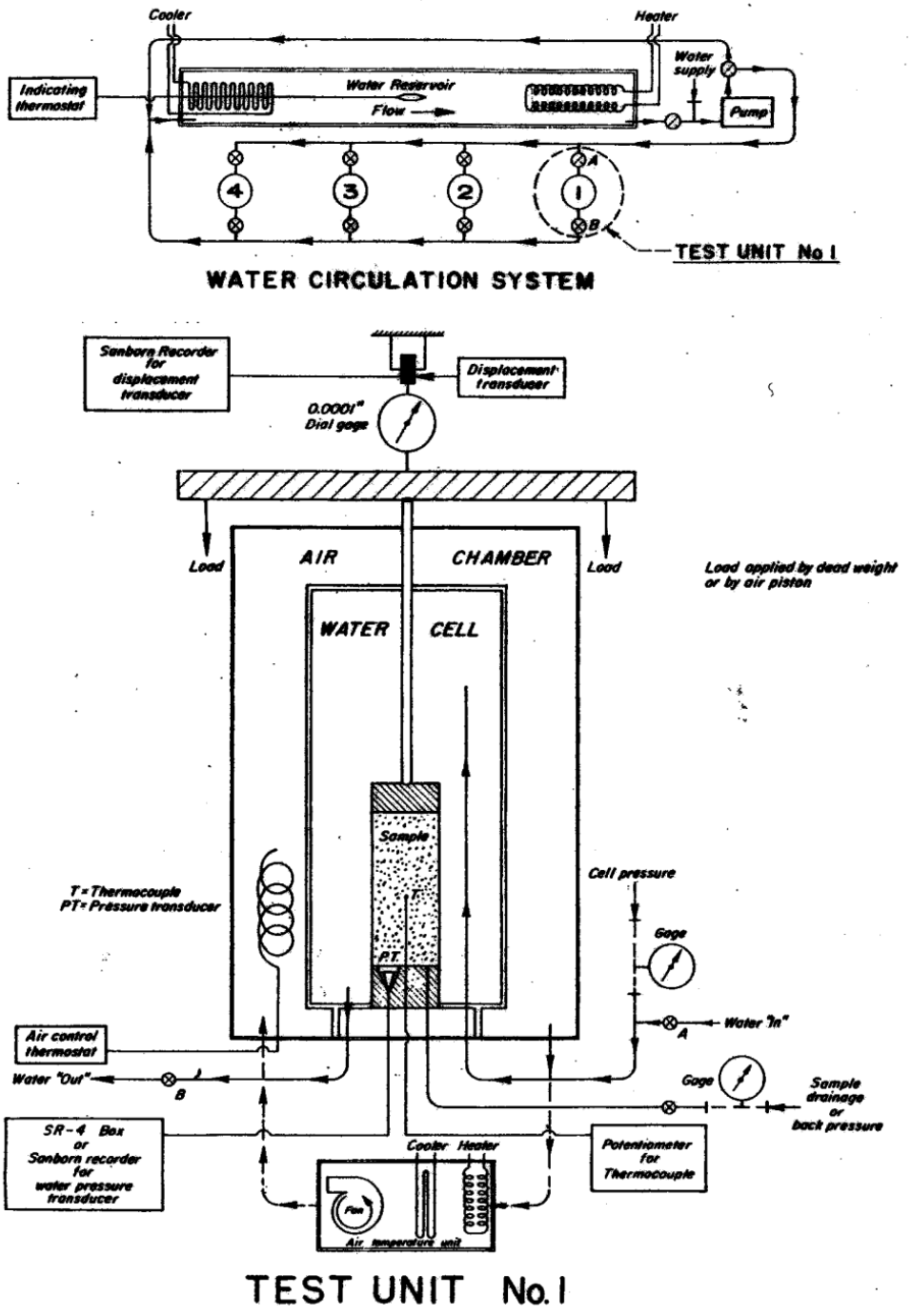

Figure 2.16 *Schematic of the temperature-controlled triaxial of Campanella and Mitchell (1963)*

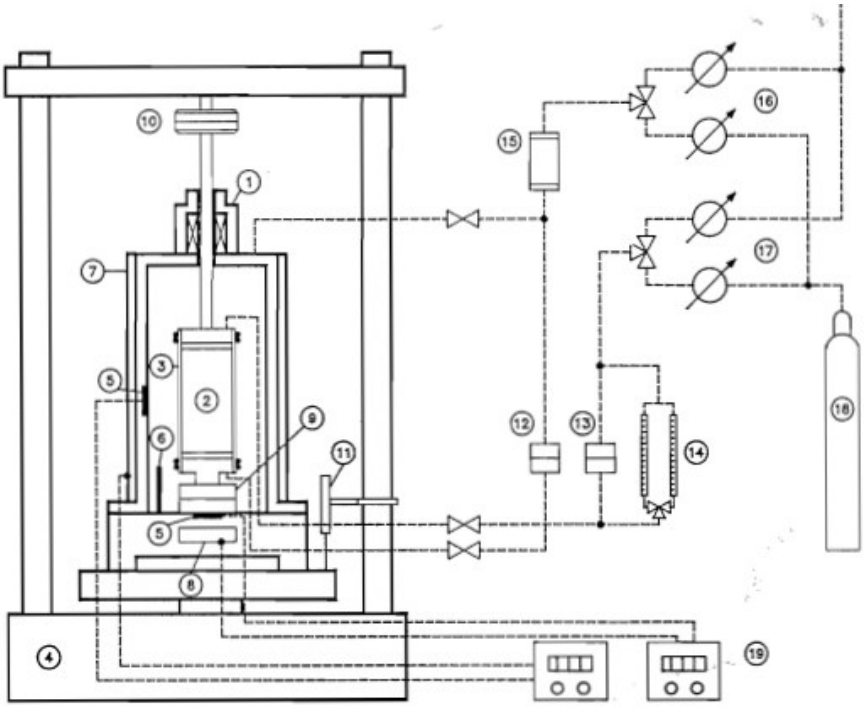

FIG. 1. Schematic of ISMES experimental setup. 1, triaxial cell; 2, specimen; 3, membrane; 4, press (load and speed controlled); 5, heater thermocouples; 6, main thermocouple; 7, lateral heater; 8, bottom heater; 9, internal load cell; 10, external load cell; 11, LVDT (axial deformation measurements); 12, differential pressure transducer (effective stress); 13, differential pressure transducer (volume change); 14, burette (volume-change measurements); 15, air–water interface; 16, cell pressure regulator; 17, back-pressure regulator; 18, nitrogen bottle, 19, data acquisition set.

Figure 2.17 *Schematic of the temperature-controlled triaxial of Baldi et al. (1987)*

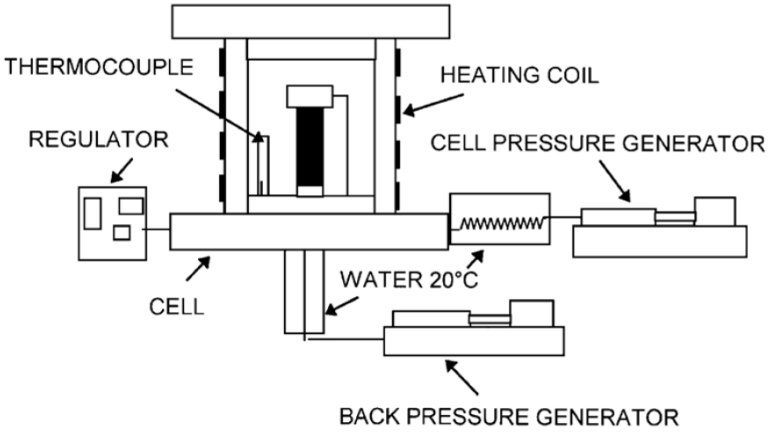

Figure 2.18 *Schematic of the temperature-controlled isotropic cell of Delage et al. (2000)*

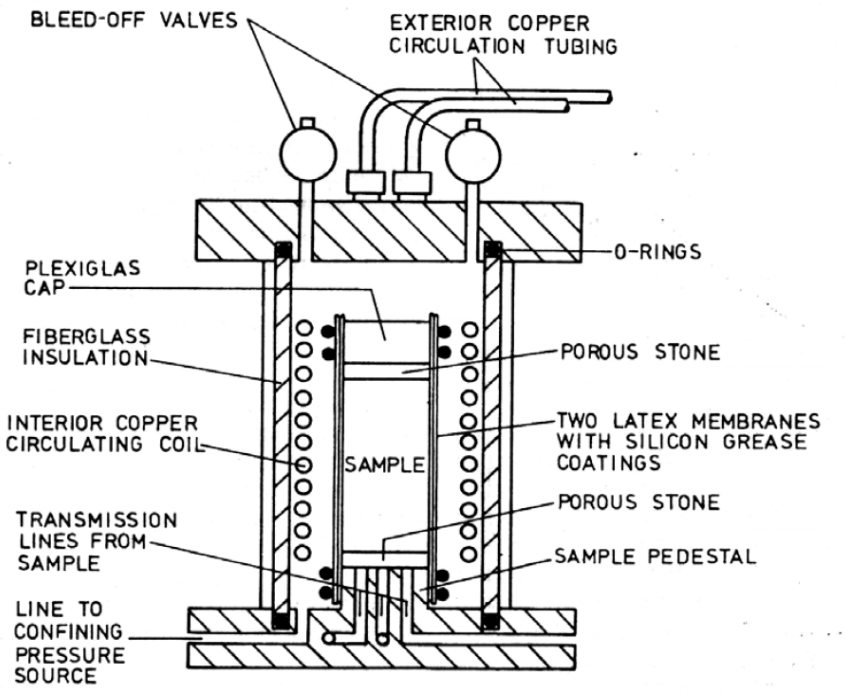

Figure 2.19 *Schematic of the temperature-controlled isotropic cell of Demars and Charles (1982)*

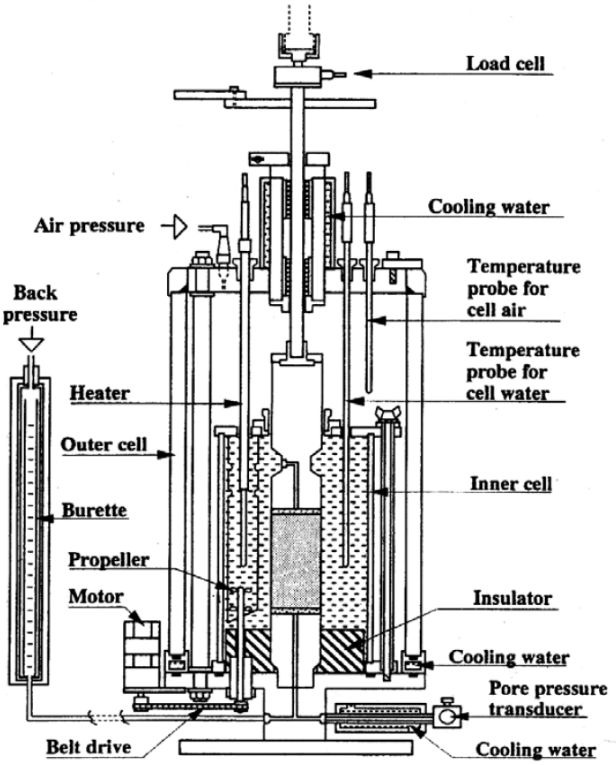

Figure 2.20 *Schematic of the temperature-controlled triaxial of Kuntiwattanakul (1991)*

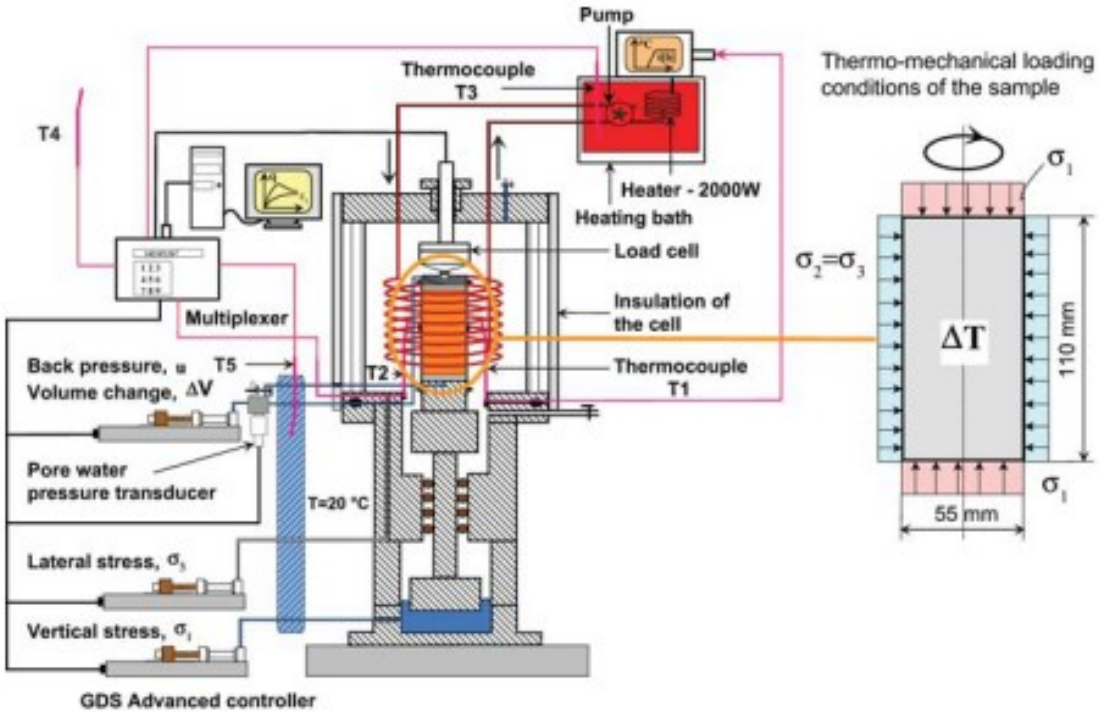

Figure 2.21 *Schematic of the temperature-controlled triaxial of Cekerevac et al. (2005)*

3. DEVELOPMENT OF NEW THM EXPERIMENTAL CAPABILITIES AT IMPERIAL COLLEGE

3.1 Introduction

This chapter presents part of the development of new experimental capabilities at the Imperial College Geotechnics Laboratory (ICGL) for the study of thermo-hydro-mechanical of geomaterials. Firstly, a conventional triaxial stress path cell used in this thesis for a reference study at normal ambient temperature conditions in the laboratory is presented. Secondly, the development of a new temperature-controlled triaxial apparatus (Martinez Calonge, 2013; Martinez Calonge et al., 2015) is presented, describing its thermal performance and calibrations performed. This was the first thermal triaxial cell developed at the ICGL laboratory in the past 20 years and therefore a number of development issues had to be resolved before and during the subsequent testing. This chapter details only some of the critical issues encountered on the way. Finally, the experimental set-up for the use of thermal needle techniques for the determination of thermal properties of soils is set out.

3.2 Standard stress-path cells

In addition to the newly developed equipment, standard 38 mm diameter sample size stress-path cells were also used in this thesis for a reference study at room temperature. The equipment is based on the conventional hydraulic stress-path triaxial apparatus, described by Bishop and Wesley (1975) and shown in Figure 3.1. The TRIAX software (Toll, 1999) was used for monitoring pressures, load and displacements and controlling stresses and strains.

The apparatus uses de-aired water as the confining fluid. The pressures are supplied by an air compressor system, supplying 800 kPa air pressure and controlled using digitally controlled stepper motors, allowing a very good control of the air pressure (±0.07 kPa). Pressures are then transferred to air-water interfaces which both incorporate 50 cm^3 Imperial College type volume gauges to monitor water flowing in and out of the cell and sample respectively. In order

to apply deviatoric stresses, a stepper-motor driven pump connected to the hydraulic system is used here for the strain-controlled shearing stages and loads are measured by a submersible load cell. All these instruments are calibrated as described in section 3.3.2.

Internal instrumentation is also used for measuring sample volume changes. In these tests, axial LVDTs, as presented by Cuccovillo and Coop (1997), shown in Figure 3.2, are used on two opposite sides of the sample. The system is attached to the sample using two glued mounts: the upper mounts hold the main body of the LVDT while the armature sits unrestrained on top of the bottom mount. Radial strains are measured using a radial belt which incorporates an LVDT. The calibration of the LVDTs (accuracy of 0.0005 mm and resolution of 0.0002 mm) was performed using appropriate mounts in an accurate micrometre.

3.3 New temperature-controlled triaxial apparatus

3.3.1 Description

The new temperature-controlled triaxial apparatus developed at the Imperial College Geotechnics Laboratory is presented schematically in Figure 3.3, with its main details pictured in Figure 3.4a. The cell is capable of testing saturated soil samples of up to 50mm diameter and 100 mm height at temperatures up to 85 °C and confining pressures up to 800 kPa.

The apparatus consists of a stainless steel cell which also uses de-aired water as the confining fluid. The application and control of cell and back pressures is identical to the one of the standard stress path cell previously described. Imperial College type volume gauges, with a sensitivity of 0.001 cm^3, are used to monitor water flowing in and out of the cell and sample respectively and are located at a distance from the cell (approximately 1 m of tubing), ensuring that there is no significant transfer of temperature to the measuring devices.

The heating system consists of six 150 W cartridge heaters evenly distributed between the top and bottom plates of the apparatus (Figure 3.4d). Each of the installed cartridge heaters is associated with its own temperature sensor to allow computer controlled temperature regulation. The heating elements are grouped into two independent units (lower cell heaters

and upper cell heaters) allowing better control of temperature and hence a more control efficient performance and heating of the cell. A seventh temperature sensor is fitted within the tip of a brass element inside the cell, to monitor the cell fluid temperature (Figure 3.4b). Additionally, the external room temperature is also constantly monitored.

Deviatoric stresses are applied to the sample using a digital computer-controlled 50 kN loading frame and are monitored using a high-resolution temperature-compensated internal load cell. The current set-up allows only tests in compression to be performed and the axial deformations during shearing are monitored using an external displacement transducer. The desired stress paths and temperature changes are controlled using the TRIAX software (Toll, 1999), with a continuous data acquisition from all instruments.

3.3.2 Standard calibrations of the components at room temperature

The pressure transducers (RS, models 461-301) used for measuring the cell and back pressures have a working range between 0 and 1MPa, with an accuracy of ±0.5 kPa and a resolution of ±0.05 kPa, and are temperature compensated, with changes in zero and shift span of less than ±0.01%/ºC. They were calibrated in regular intervals using a Budenberg dead-weight calibrator at room temperature, over the range of pressures from 70 kPa to 700 kPa, showing very similar values between themselves and with time.

The load cell (Applied Measurements Ltd, model STALC3), has a rated capacity of 3 kN, accuracy of ±1.4 N, and resolution of ±0.03 N. It was calibrated in a similar manner as the pressure transducers, with loads up to 1.54 kN. The thermal performance of the load cell is discussed separately in section 3.3.7.

A mass calibration was performed in the case of the volume gauges by flushing water from the volume gauge to a container placed on a scale. Changes in mass were converted to changes in volume, with the known density of water at room temperature, and then linked to changes in the output of the linearly variable differential transformer (LVDT), attached to the volume gauge. Finally, the external displacement transducer (model LDS-5, with an accuracy

of 0.008 mm and resolution of 0.001 mm) was calibrated by placing the transducer in a micrometre jig and recording the output at every 0.5 mm increment for the whole range of the transducer, about 30 mm, in both directions.

3.3.3 Thermal performance

Initially, key aspects of the thermal performance of the cell have been thoroughly investigated: the relationship between the temperature at the monitoring point in the cell and the temperature inside the sample, the uniformity of temperature in the sample at steady state, the thermal losses and the effect of heating rate.

Given the external nature of the heating, the first calibration test consisted of checking the uniformity of the temperature field in the sample. This was performed with three T-type thermocouple needles inserted at different heights in a soil sample (Figure 3.4e) consisting of a kaolin-based mixture, and with the heaters set at 80 °C. Table 3.1 shows the temperature measurements at steady state. The temperature gradients within the soil at steady state are insignificant, being less than 0.2 °C over the 80 mm distance between the upper and lower needle. The temperature of the soil sample can be considered as uniform. In addition, it was shown that the maximum deviation from the measured temperature in the monitoring point of the cell water and at any point of the soil sample is 0.15 °C. This confirms that the temperature sensor within the cell water is a reliable, non-intrusive method of assessing the temperature of the soil sample, which can be assumed to be equal to the cell water temperature.

In order to operate the cell, it is also essential to understand the relationship between the average temperature of the heaters (T_h) (controlled parameter) and the resulting temperature of the sample (T_s, measured at the monitoring point of the cell water). Figure 3.5 presents the difference between the temperature of the heaters and of the sample for different heater temperatures during two calibration tests performed at a fast (5 °C/h) and slow (0.5 °C/h) heating rates respectively, with full insulation applied to the apparatus as in standard testing conditions, consisting of several sheets of plastic containing air-filled pods. The cell was

heated at a constant rate in 10 °C steps, stopping for 24 hours approximately at the end of each step temperature equalisation. The fast heating rate causes significant gradients in the cell, as by the time that the heaters reach their target value, the temperature of the cell water at the monitoring position is still significantly lower (up to 10 °C at 70 °C). However, if the heating is performed at a much slower rate, the gradients are less significant. The adopted rate for testing was 0.5 °C/h to ensure that during the transient state no significant gradients are induced within the cell, nor within the sample, with the additional benefit of allowing for dissipation of excess pore pressure, if drained conditions are chosen during the heating and cooling stages.

At steady state, which is independent of the rate chosen, the difference between the temperature of the heaters and the sample increases quasi-linearly with temperature, from approximately 0.8 °C at 30°C to 4.3 °C at 70°C at a rate of approximately 0.09 °C/°C increase in the heaters. This rate of thermal losses depends on the insulation conditions of the cell and is used to calculate the control temperature of the heaters.

3.3.4 Drainage system

A key aspect of the calibration of the new equipment is the understanding of the behaviour of the drainage system with temperature, which includes water lines, pedestal and porous stone. An initial test was performed using a dummy steel rigid sample with side drains sitting on top of a saturated porous stone under a controlled cell pressure of 600 kPa and back pressure of 300 kPa, similar to standard testing conditions for normally consolidated samples applied in the subsequent thermo-mechanical testing programme. For this test, a standard latex membrane and nitrile O-rings (Figure 3.4c) were used to seal the sample, which was heated at a rate of 0.5 ºC/hr, stopping at every 10 ºC step from room temperature up to 80 ºC, as shown in Figure 3.6 together with the measured volume of drained water from the back pressure volume gauge. The sign convention used in the Figure shows water flowing out of the sample as positive (i.e. compression positive), while the water flowing towards the sample is taken as negative. Up until 50 ºC, no significant changes in volume of drained water occur.

However, during further heating and subsequent cooling, water is seen to flow from the sample to the volume gauge at a constant rate with time for constant temperature (at 80 ºC, at approximately 0.45 cm^3/day, down to 0.21 cm^3/day at 40 ºC during the cooling phase). Post-test visual examination of the membrane and O-rings showed significant degradation of the materials after exposure to high temperature, resulting in changes in colour and texture of the membrane and elongation of the O-ring. It was therefore suspected that the cell water was penetrating through the membrane and draining into the volume gauge, therefore falsely representing drainage from the dummy sample. The water intake through the membrane became more significant as its degradation presumably became more progressive at higher temperatures.

Before investigating the performance of alternative experimental set-ups since the measured drained volumes measured were unacceptable, a smaller part of the drainage system was investigated in isolation, without exposing it to the contact with the confining water. This part comprised the back-pressure volume gauge and the water lines filled with water up to the top of the pedestal which was sealed off for this purpose; and placed under pressure control at 300 kPa for a week at room temperature. The bottom plate was then heated only up to 80 ºC (the cell was not filled with water) and maintained at such temperature for an additional week. This experiment revealed a loss of water in the tested system of approximately 0.045 cm^3/day at room temperature which increased up to 0.15 cm^3/day at 80 ºC. This change in the volume of water measured by the volume gauge is of opposite sign to the changes in drained water due to seepage through the membrane and would have therefore been hidden by the much larger volume of water seeping through the membrane. This system volume loss, despite being of a very small magnitude at room temperature, did not disappear after checking valves and connections and was thought to be caused by the use of an inappropriate tubing material for long term exposures to high temperatures. After testing separately under pressure different materials of different lengths of tubing, the standard nylon tubing was replaced by steel tubing, as pictured in Figure 3.4f-g for the entire back pressure system. The daily system volume loss

was checked again for the new set-up and was reduced to the region of 0.015-0.025 cm^3/day at room temperature, which was considered to be satisfactory.

A heating and cooling test was then performed again on a dummy rigid steel sample, placed with side drains on top of a saturated porous stone, at a rate of 0.5 ºC/hr, stopping for several days at 40ºC and 60 ºC to monitor the long-term response of the system, as shown in Figure 3.7. A confining pressure of 600 kPa and a back pressure of 300 kPa were used again in this test. This time however, a different sample set-up was used, consisting of a double neoprene membrane with a thin layer of vacuum grease in between, sealed with temperature resistant Viton O-rings. The measured drained volume, amounting to under -1 cm^3 over 20 days compared to the +3.5 cm^3 before over the same time period, suggests that there is no longer any significant seepage through the membrane. Even if there is any, it is of a very small magnitude and hidden by volume changes in the other direction (from the volume gauge to the sample). The volume gauge is seen now to be constantly pushing water towards the sample in order to keep the controlled pressure at 300 kPa, at a rate equivalent to what is described here as “system loss”. It is seen to vary here from 0.025 cm^3/day at room temperature up to 0.075 cm^3/day at 60 ºC. Repeat tests under similar conditions confirmed this phenomenon, although the exact rates would vary by ±0.005 cm^3/day. Given the small magnitude of those, visual observation of the source of the problem was not feasible.

This set-up consisting of steel tubing, double neoprene membranes and Viton O-rings gave a much better system response than at any other point during the development of the equipment and was considered satisfactory. This very small daily loss in the drainage system makes the equipment unsuitable for long-term testing under undrained conditions. However, with adequate testing and analysis procedures, for example stopping every 10 ºC step in thermo-mechanical tests for several days and checking whether a clear linear volume change with time can be observed of a similar magnitude to those reported here, a correction can be applied to the raw data to take into account such system daily loss.

3.3.5 Cell volume gauge

With the final drainage system set-up, an alternative way of measuring sample volumetric changes directly from changes in volume of confining water was investigated by placing a volume gauge for monitoring the confining fluid. By performing a calibration test using a steel dummy sample of known dimensions and thermal expansion involving heating and cooling of the cell, the thermal expansion of the cell and volume changes in confining fluid could be measured and used in future tests to assess sample volume changes. Figure 3.8 shows the water flowing out of the cell (negative) and into the cell (positive) during a heating and cooling test up to 80 ºC and back to 20 ºC at a constant cell pressure of 600 kPa, for a total temperature cycle duration of 21 days. A significant amount of water, aournd 90 cm^3, leaves the cell during heating under controlled pressure due to water having a thermal expansion coefficient an order of magnitude higher than the steel, and during cooling a similar amount of water enters the cell. At the end of the test, however, there is a 3 cm^3 of excess water that has flowed into the cell. This suggests that during the cycle the same amount has been lost due to leakages mainly. This is of a similar magnitude to the thermal volume changes expected in a real test in soil, making it therefore not a suitable device in this particular apparatus to measure sample volume changes.

3.3.6 Internal instrumentation

The use of internal instrumentation for the direct measurement of sample volume changes during thermal cycles was investigated at the final stage of the development of the apparatus. Given the experimental set-up discussed previously, consisting of a double membrane separated by a thin layer of vacuum grease, attaching instrumentation to the outer membrane did not seem a reasonable option, and alternative methods had to be explored. The internal instrumentation consists, instead, of a novel ‘fixed’ system for measuring boundary radial deformations, designed by Ackerley et al. (2016) and pictured in Figure 3.9(a-b). It consists of a set of three radial LVDTs, equally spaced at 120º around the sample and at sample mid-height. Such a system, which operates independent of the sample, ensures an average radial

strain measurement which was shown to be more accurate than the usual radial belt techniques which only measure the relative change across a single diameter.

As shown in Figure 3.9(c-d), the LVDT is fixed vertically using a supporting body fixed at the bottom of the cell. The base of the LVDT armature bears on the upper part of a pivotal L-shaped component with a round-head screw locked at the other end, in contact with the sample. A change in the radius of the sample is translated into a vertical movement of the armature of the LVDT (Figure 3.9(e-f)). Issues with the determination of geometrical relationships between displacements of the armature and the rounded screw in contact with the sample are easily overcome by the direct calibration using an appropriately mounted accurate micrometer (with a resolution of 0.005 mm).

Figure 3.10 shows the measured changes in radius taken at each instrument together with the average of all three local radial strain measurements and the expected radial changes during a calibration test at temperatures between ambient and 60 °C using a steel dummy sample with known thermal expansion properties. The readings of each of the transducers are different, although with similar trends, and become unstable (e.g. unexpected changes at constant temperature) with increasing temperature. The overall radial changes measured are nearly an order of magnitude greater than the theoretical expansion of the steel dummy sample, suggesting that the readings of the instrumentation are greatly affected by temperature effects: relative expansion of each of the components and supports, and a likely uneven temperature regime in the lower part of the cell where they are fixed. Further tests showed a slightly more stable performance at constant high temperature, but with significant differences in values between each of them. Although unsuitable for the thermo-mechanical tests from a quantitative point of view, they can be of use qualitatively, to gauge an estimate of the rate of volume change in the sample.

3.3.7 Load cell thermal performance

The thermal performance of the submerged load cell was investigated by analysing the readings during heating and cooling tests, without applying any deviatoric stress (zero-load conditions). Figure 3.11 shows the changes in zero-reading of the load cell during a series of three tests. The first test begins with a constant gain in zero-load reading of approximately 0.11 N/°C until a temperature of 60 °C, after which sudden jumps in readings and no clear trends are observed. During cooling from 50 °C to ambient temperature the slope increases to approximately 0.3 N/°C, and at the end of the cycle the zero-load reading is shifted by more than 11 N. Re-calibration of the load cell using the Budenberg dead-weight calibrator showed no significant difference to the previous other than the voltage reading at zero-load. The load cell was then exposed to a second cycle up to 80 °C, which followed the same path as the first test for heating up to about 50 °C. After this, no clear trend is observed, until cooling below 50 °C again. The total shift of the zero-load reading was nearly 50% larger than for the first test. A third test showed a slightly different behaviour during the initial part of heating, however the output of the load cell started becoming very unstable until it was completely lost at 70 °C. This series of tests highlighted the unsuitability of the STALC3 load cell for exposure temperatures above 50 °C.

Unable to resolve this issue with the manufacturer, two alternative scenarios appeared as a possible solution: the use of an external load cell, appropriately insulated from the cell or using the equipment only as an isotropic cell. Given that shearing at high temperature was not one of the aims of the thermo-mechanical testing programme for this thesis, it was decided that the temperature-controlled cell would only be used for drained heating and cooling cycles and mechanical loading under isotropic conditions. Samples would then be moved and sheared in a conventional stress-path cell at the end of a thermo-mechanical test.

3.4 Needle techniques

3.4.1 Description

Two different types of sensors are used during this experimental project for the measurement of thermal properties of soils: single needles and dual probes. Both types of sensors are manufactured by East 30 Sensors (Pullman, Washington, USA). The single needle, schematized in Figure 3.12a, consists of a heating element and a thermistor embedded in a stainless steel needle of 1.27 mm diameter and 60 mm length. The heating element, Evanohm heater wire held within the needle with epoxy filler, acts on the full length of the needle and has a resistance of around 67 Ohms (the exact resistance varies slightly between the needles used during the project).

The dual-probe, shown in Figure 3.12b, consists of two parallel hypodermic stainless steel needles of 0.9 mm diameter and 30 mm length each, spaced 6 mm apart. One needle contains a heater wire along its full-length and the other needle a thermistor at its centre.

3.4.2 Calibration of the thermistors

The thermistors are a type of resistor whose resistance varies greatly with temperature, enabling their use as temperature sensors. The relationship between the temperature T (in K) and the resistance *R_THERM* (in Ohms) is described by the Steinhart-Hart equation:

$$\frac{1}{T} = A + B * \ln(R\_THERM) + C * \left[\ln\left(\left(R\_THERM\right)\right)\right]^3 \qquad [3.1]$$

where A, B and C are the Steinhart-Hart coefficients, which vary between the types and models of thermistors.

A calibration was performed for each needle used in the testing programme, by placing it in a controlled water bath at a range of temperatures from 5 ºC up to 40 ºC, together with a calibrated temperature probe. The temperature and resistance of the thermistor were recorded at different times during heating and cooling of the water bath and Eq. [3.1] was fitted to the

experimental data in order to obtain the calibration coefficients. One of the calibrations performed during the project is shown in Figure 3.13, plotted both in terms of the inverse of temperature against the logarithm of the resistance and in terms of temperature against resistance. The highly non-linear relation between these two variables becomes clear in the latter plot. A change of temperature at one temperature level does not produce the same change in resistance in the thermistor as the same temperature change from a different temperature level. It is therefore very important to calibrate it against an accurate temperature measuring device.

3.4.3 Experimental set-up

The experimental set-up for the operation of the probes, data acquisition, visualization and storage is shown in Figure 3.14. It consists of a PC, a data logger, an in-house built interface for the control and sensing of the current applied to the sensors and a small single board micro-controller (Arduino Uno). The in-house interface unit is formed of two sub-units in separate circuits: the heater unit and the temperature sensor unit, both schematized in Figure 3.15.

The temperature unit consists of a resistor, *R_DIVIDE* (10000 Ohms), which is connected in series to the thermistor in the needles, whose resistance *R_THERM* changes with temperature as described by the calibration in Eq. [3.1]. By measuring the voltages *V_DIVIDER* and *V_THERM* and knowing the value of *R_DIVIDE*, the resistance of the thermistor may be determined as follows:

$$R\_THERM = \frac{V\_THERM * R\_DIVIDE}{V\_DIVIDER - V\_THERM} \qquad [3.2]$$

By re-arranging Eq. [3.1], the temperature can now be calculated.

The heater control unit ensures that a constant known current is applied to the heater and also comprises the switch for the heater. The desired current may be achieved by adjusting the potentiometer: for single needle tests a current of around 60 mA, while for the dual-probe heat-

pulse test a current of around 300 mA is required. The design of the constant current circuit, with the operational amplifier and transistor, ensures that the current through the heater is equal to the current through a precision resistor *R_SENSE*, where the voltage drop *V_SENSE* is measured as shown in Figure 3.15. This current can be defined as:

$$CURRENT = \frac{V\_SENSE}{R\_SENSE} \quad [3.3]$$

The heating power can be determined by the known current and the resistance of the heater *R_HEATER* as:

$$POWER = CURRENT^2 * R\_HEATER \quad [3.4]$$

The switching action of the heater unit may be performed manually, as in the case of the single needle test, where the operator with the help of a stopwatch turns on and off the switch for the desired heating duration, usually 100 seconds; or semi-automatically using a programmable micro-controller for the heat-pulse tests on the dual-probe. After being activated by the operator, the micro-controller is set to wait for 10 seconds during which the operator needs to manually turn the switch to the "automatic" position and then drives a relay for the programmed heating duration (8 s for the tests reported in this thesis), which actually performs the switching action of the heaters.

The voltages *V_DIVIDER*, *V_THERM*, *V_SENSE* and *V_HEATER* are sensed by the data logger, with the latter three having an individual channel for each type of needle, as shown in Figure 3.14. This data acquisition process is run from MATLAB. The frequency of recording data during experiments can be specified by the operator in the MATLAB code, with a minimum gap of 0.45 seconds between consecutive readings, which correspond to the zero delay option in the code. The temperature, current and power are calculated after each reading and a real-time temperature-time plot is visualized during the experiments.

The scripts written in MATLAB for recording and visualizing the data during the test are presented in the Appendix. For convenience, the same variable names have been used in the equations presented in this section.

3.5 Summary

The new THM experimental capabilities developed at the Imperial College Geotechnics Laboratory during this Thesis are presented in this Chapter.

- A new temperature-controlled apparatus capable of testing saturated soils at confining pressures up to 800 kPa and temperatures ranging from ambient to 85 ºC is presented.
- The thermal performance of the cell is thoroughly investigated focusing on the effect of heating rates, the measurement of the sample temperature and its uniformity and the thermal losses of the cell. The main conclusions are that: a) given the external nature of the mode of heating, a slow heating rate is preferable in order to avoid significant thermal gradients within the cell; and b) the temperature sensor within the cell is shown to be an accurate non-intrusive method to measure the sample temperature at steady state, which is found to be uniform throughout the sample.
- Critical aspects of the behaviour of its components (drainage system, internal instrumentation, membranes, etc.) are assessed, tested and improved until a satisfactory arrangement for the purposes of the testing programme of this thesis is developed.
- Finally, the experimental set-up in order to perform thermal tests using needle techniques (single needle and dual-probe) is presented, together with the calibration of its components.

Table 3.1 *Temperatures at steady state controlling both sets of heaters at 80 °C.*

Temperature sensor	Temperature (°C)
Upper heaters	79.97
Lower heaters	79.87
Water Temperature sensor	74.03
Upper sample needle	74.04
Middle sample needle	73.96
Lower sample needle	73.88

Figure 3.1 *Conventional stress-path triaxial cell*

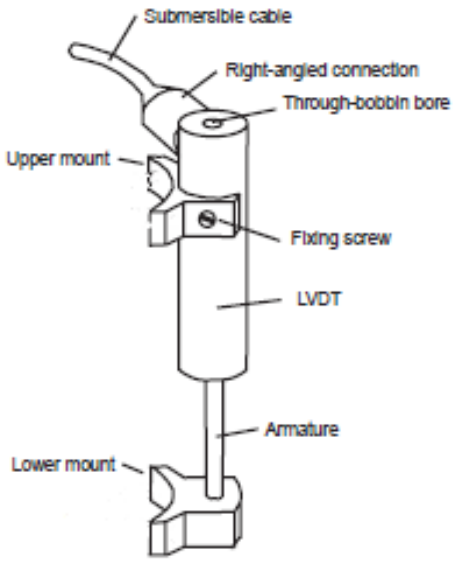

Figure 3.2 *Local axial LVDT (Cuccovillo and Coop, 1997)*

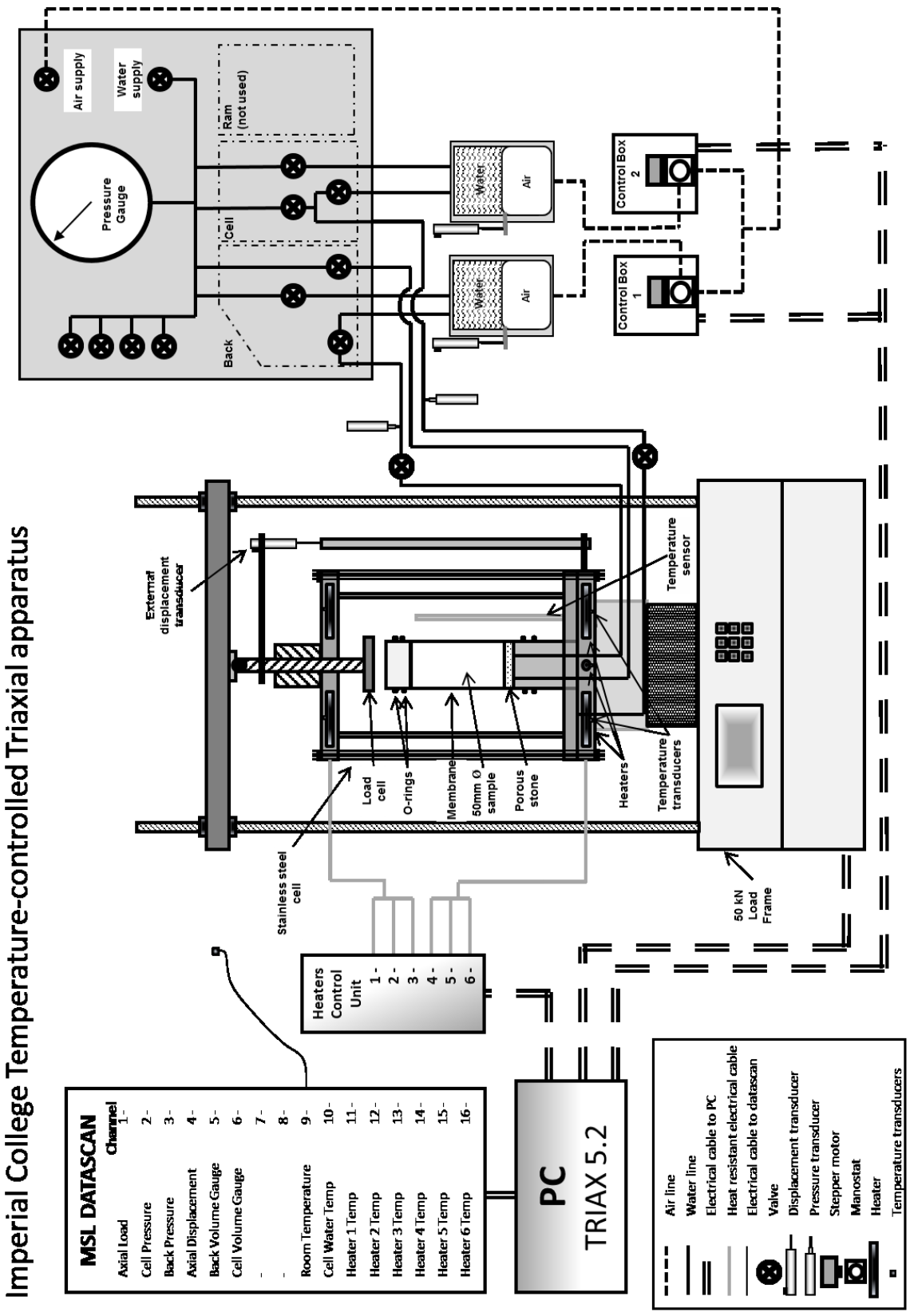

Figure 3.3 *Schematic of the new temperature-controlled triaxial apparatus*

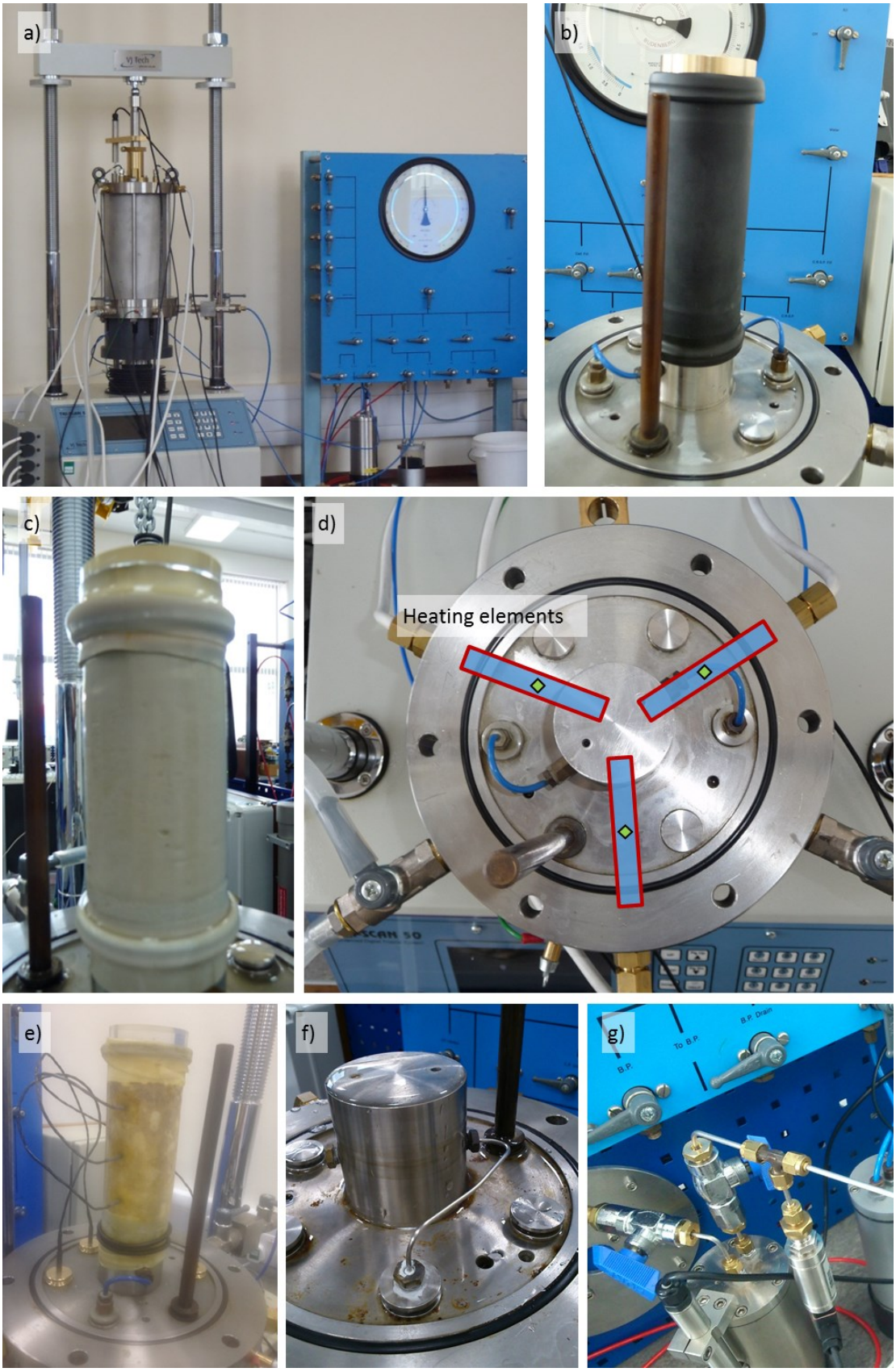

Figure 3.4 *Images of the new temperature-controlled apparatus*

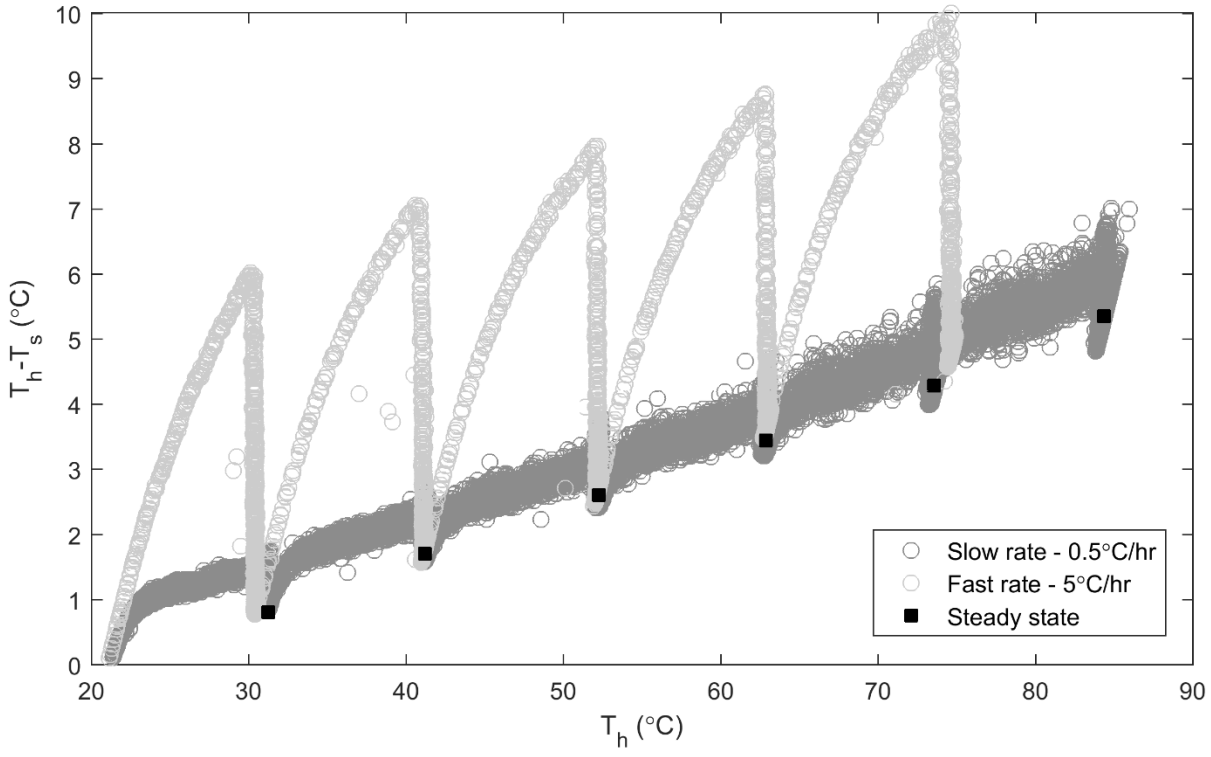

Figure 3.5 *Effect of heating rate and thermal loss of the cell*

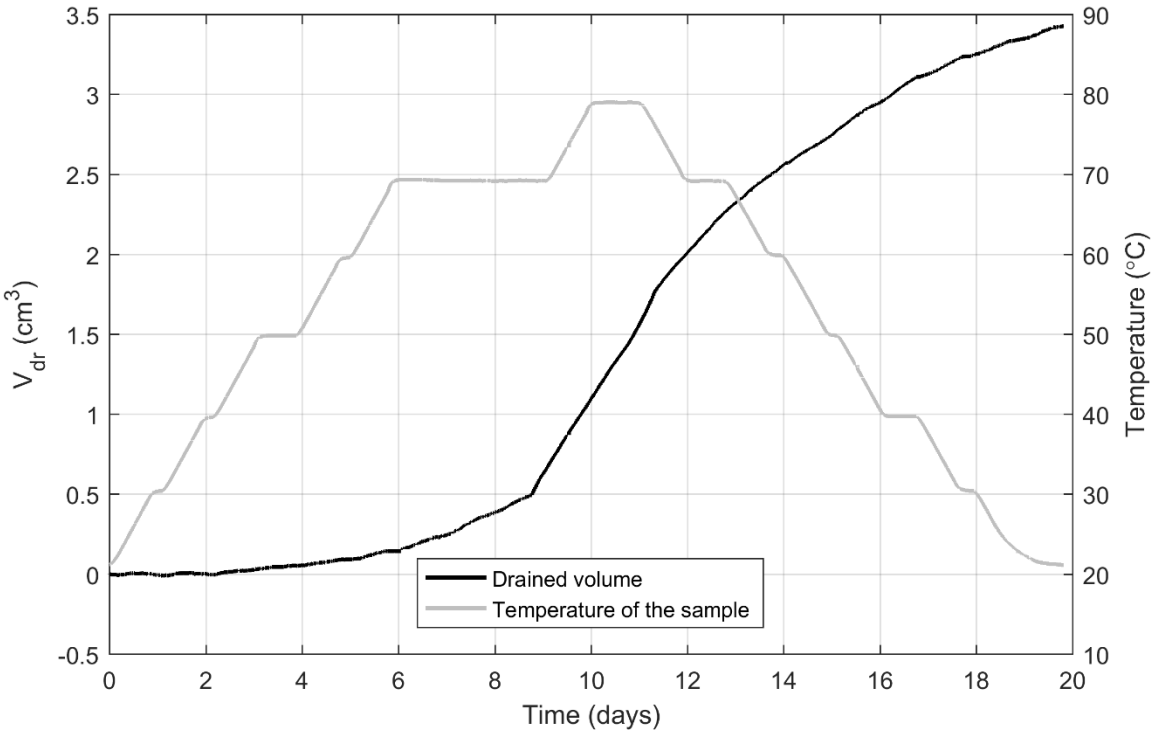

Figure 3.6 *Calibration test using a steel dummy sample, latex membranes and nitrile O-rings*

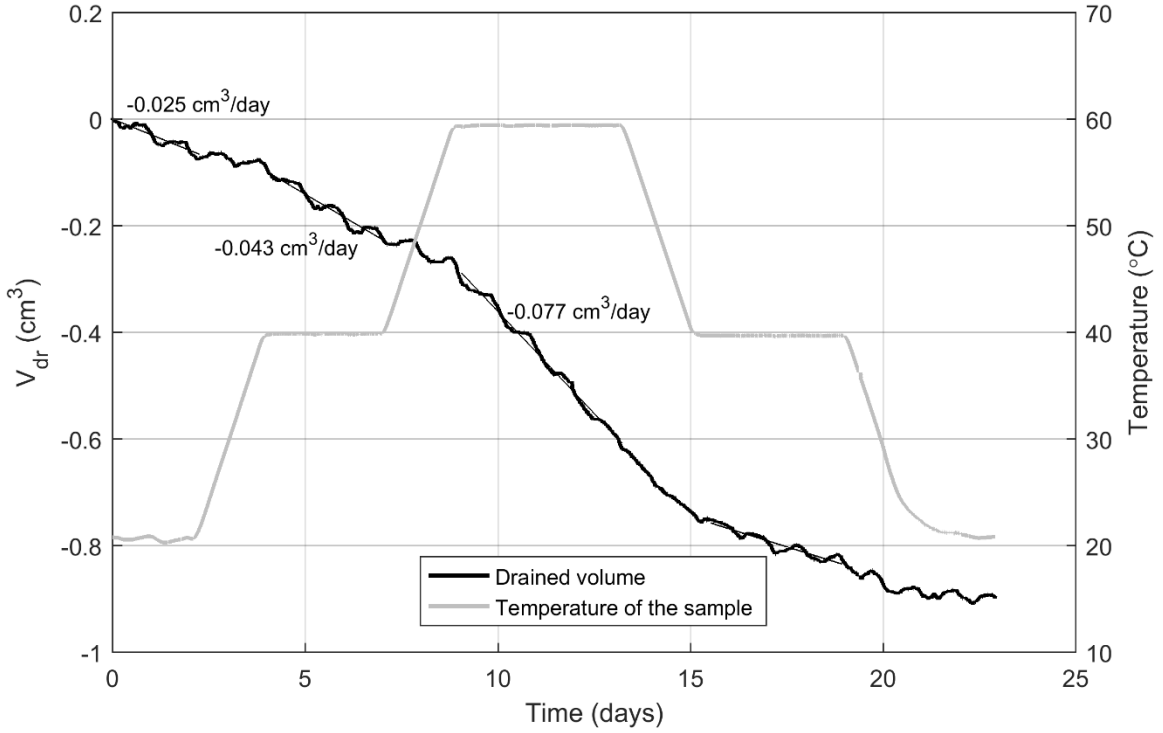

Figure 3.7 *Response of the back pressure drainage system to changes in temperature*

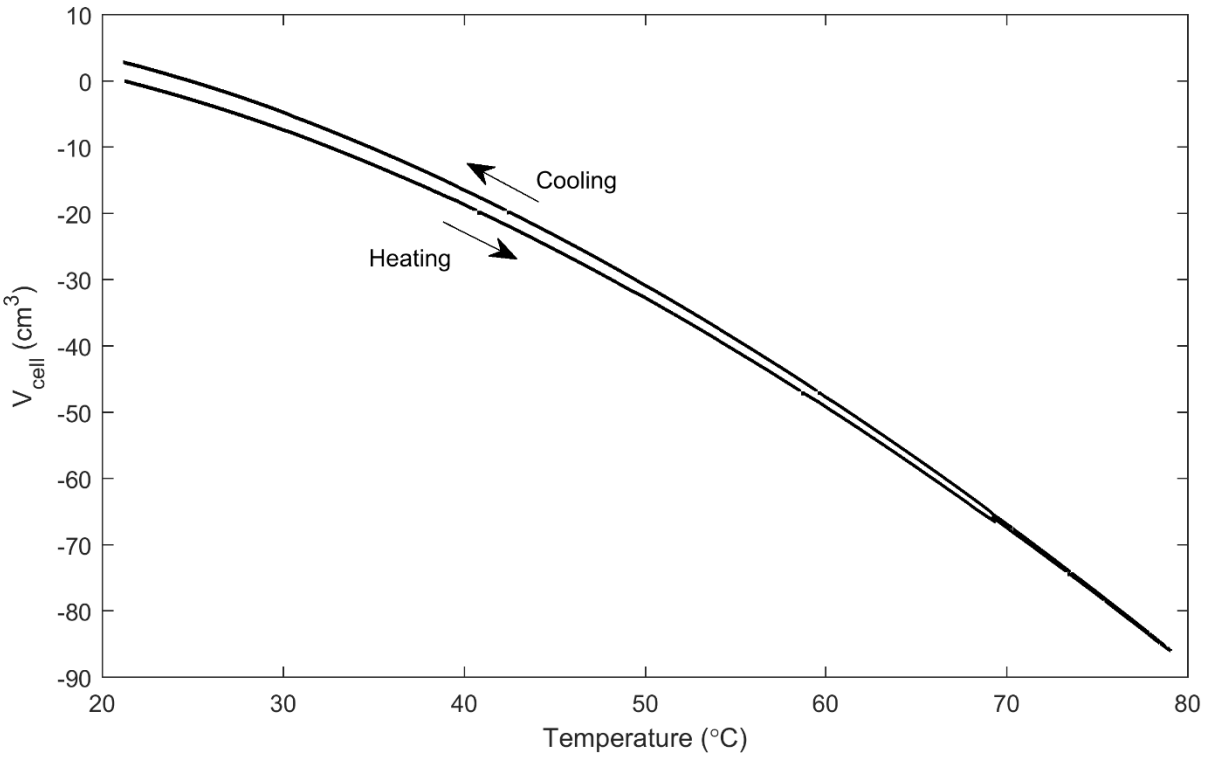

Figure 3.8 *Changes in cell volume during calibration test*

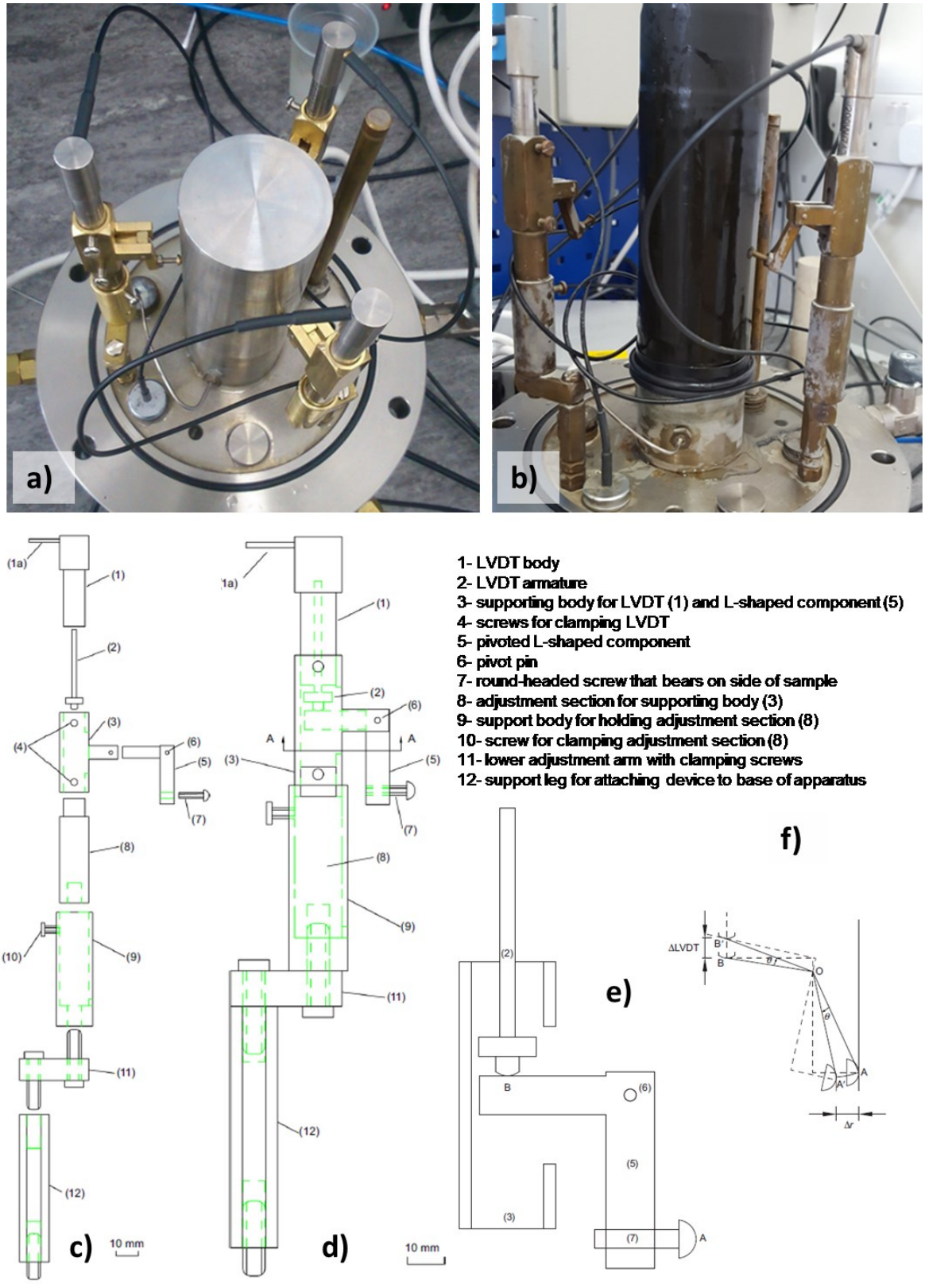

Figure 3.9 *Radial strain local instrumentation (after Ackerley et al. 2016)- (a)(b) Images, (c) schematic diagram showing various components, (d) assembled system, (e) schematic diagram of the rotating mechanism, (f) geometry of the mode of rotation*

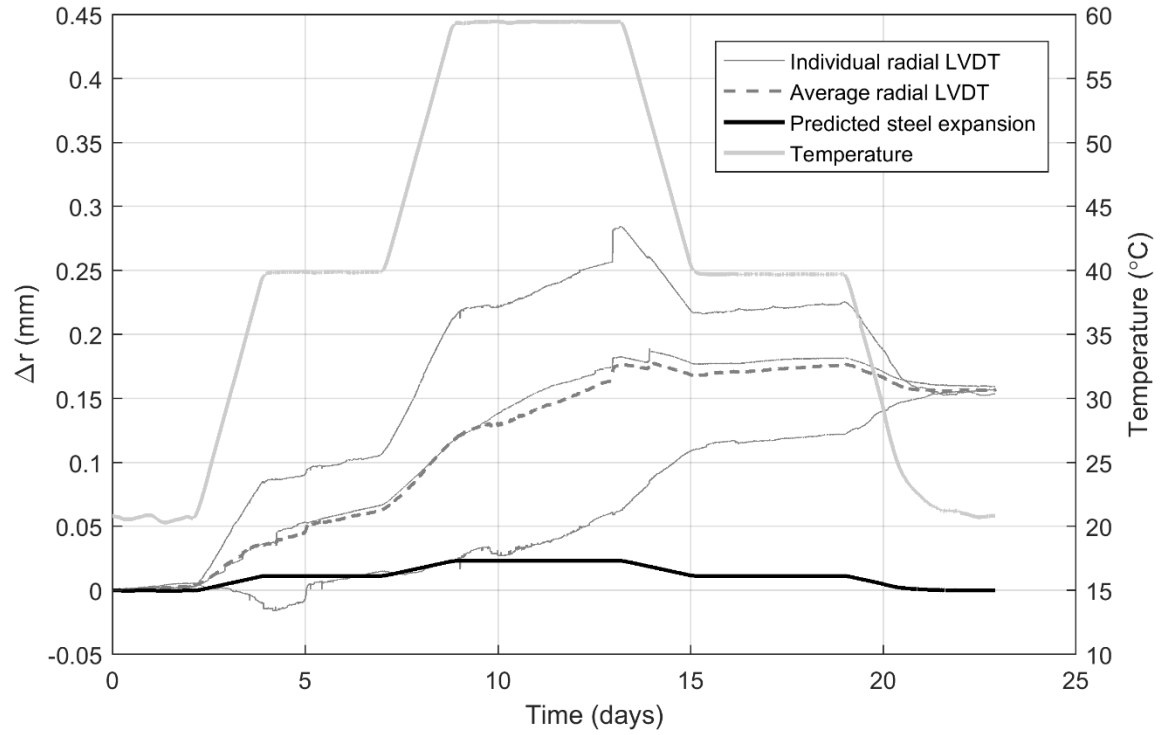

Figure 3.10 *Calibration of the internal instrumentation with a steel dummy sample*

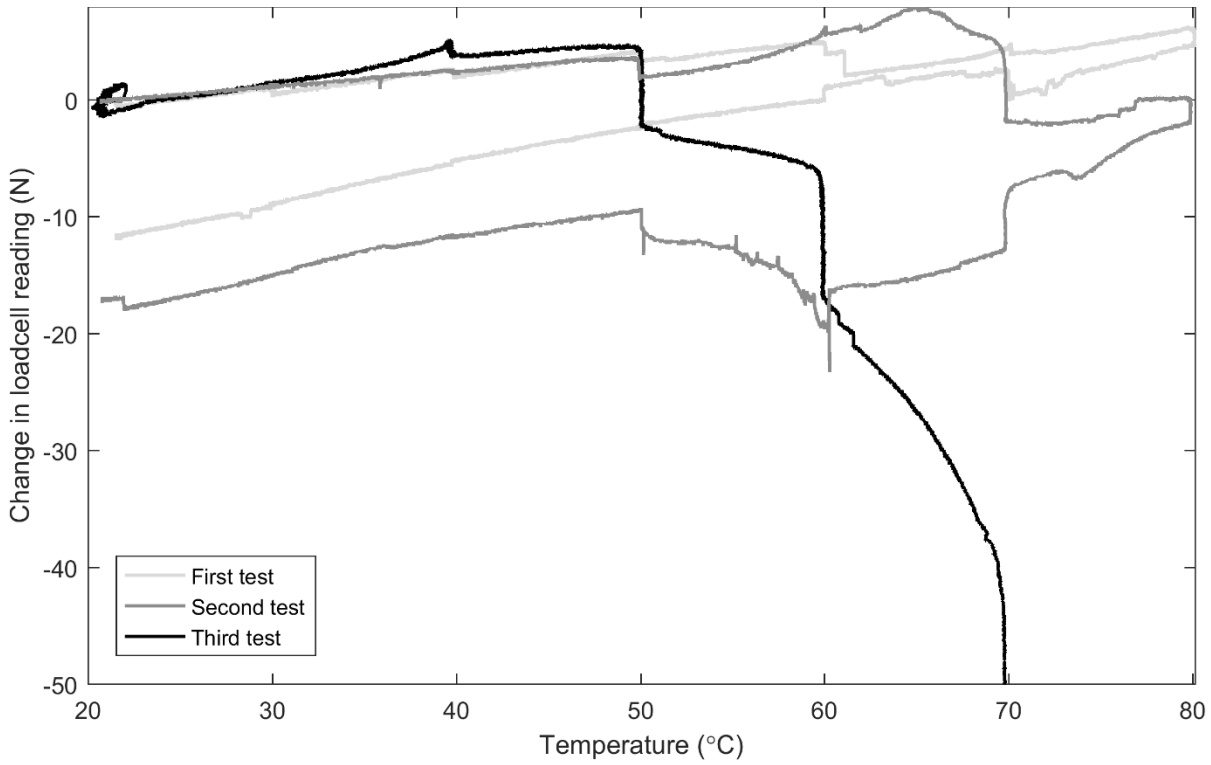

Figure 3.11 *Response of the load cell to changes in temperature*

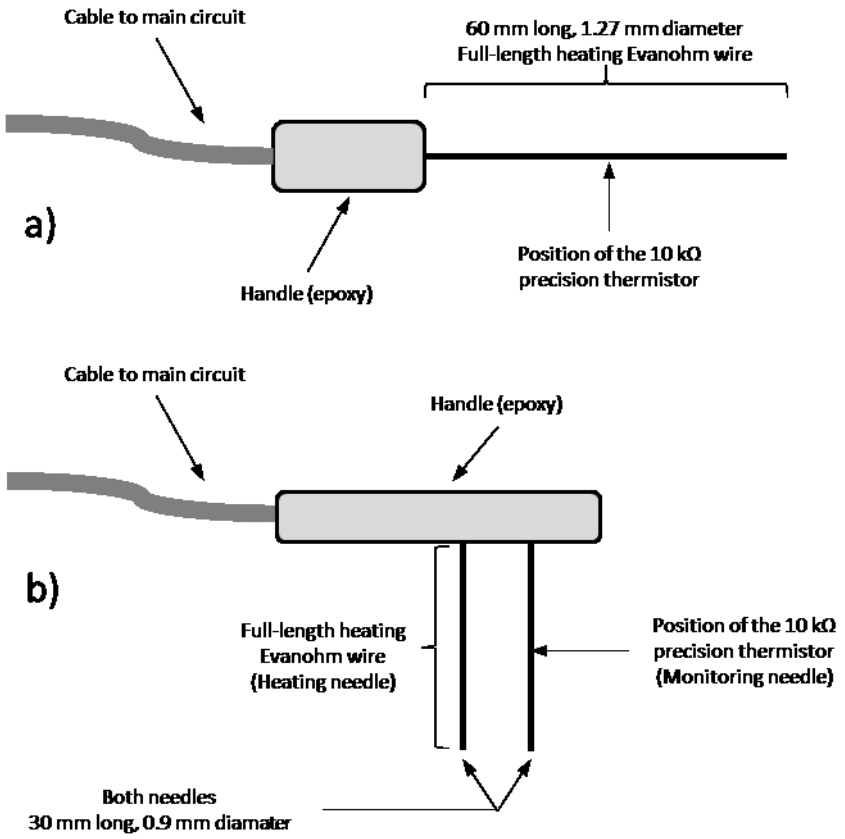

Figure 3.12 *Schematic of the needle probes (a) single needle; b) dual-probe)*

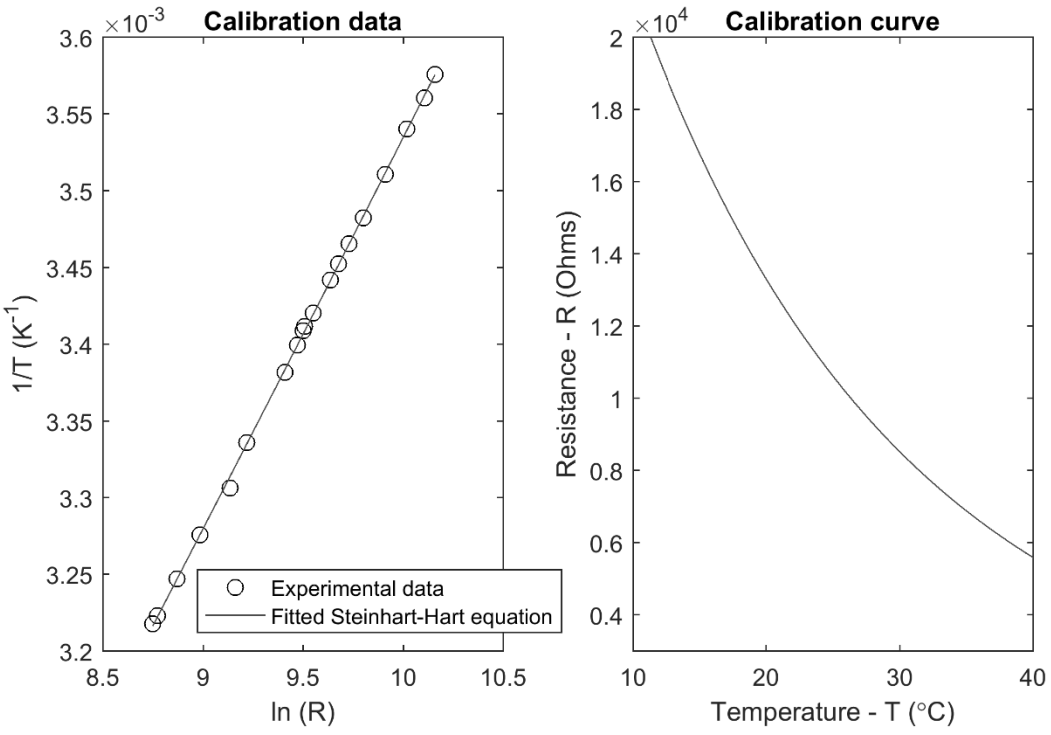

Figure 3.13 *Calibration of the thermistor*

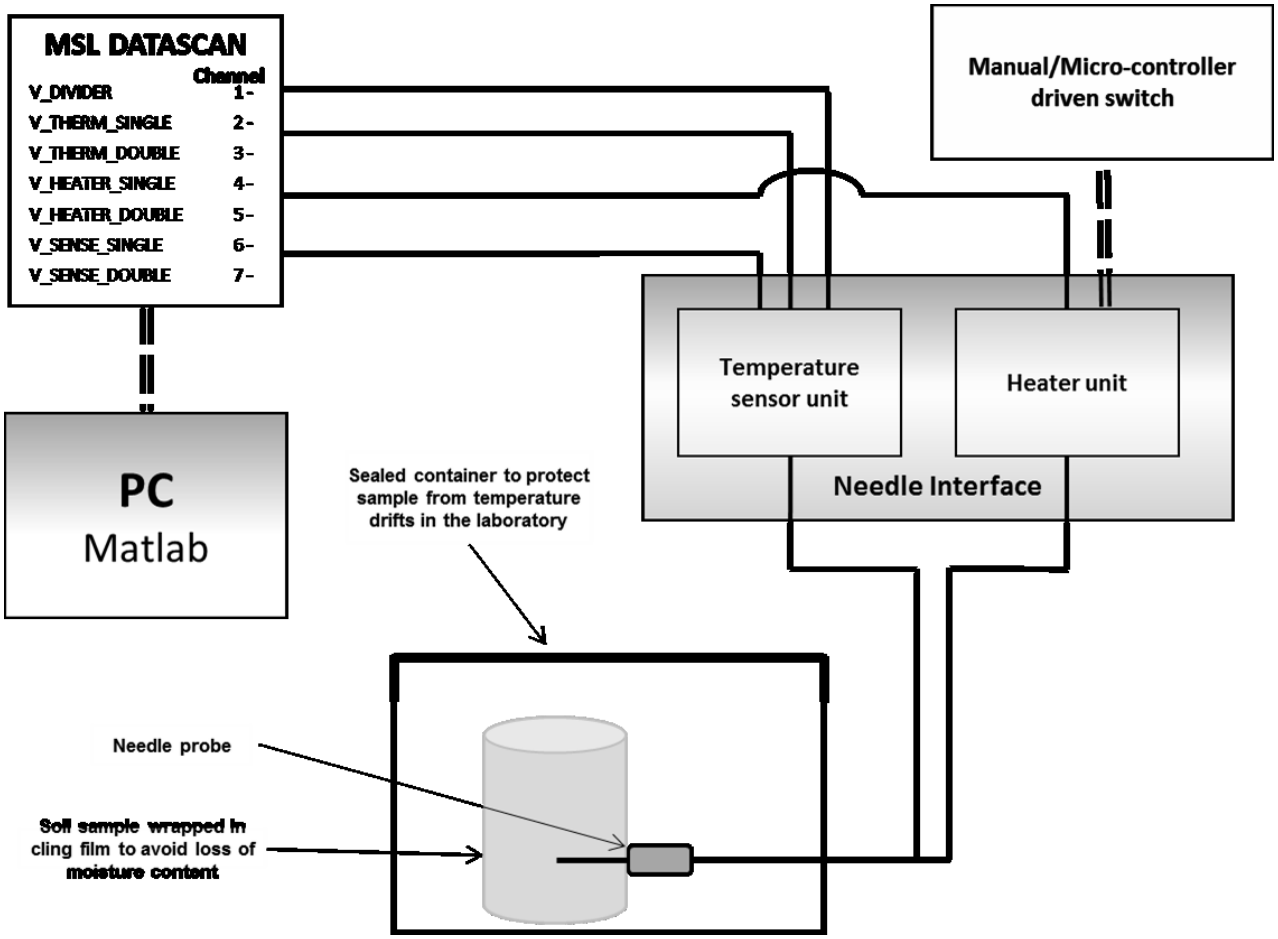

Figure 3.14 *Schematic of the experimental set-up*

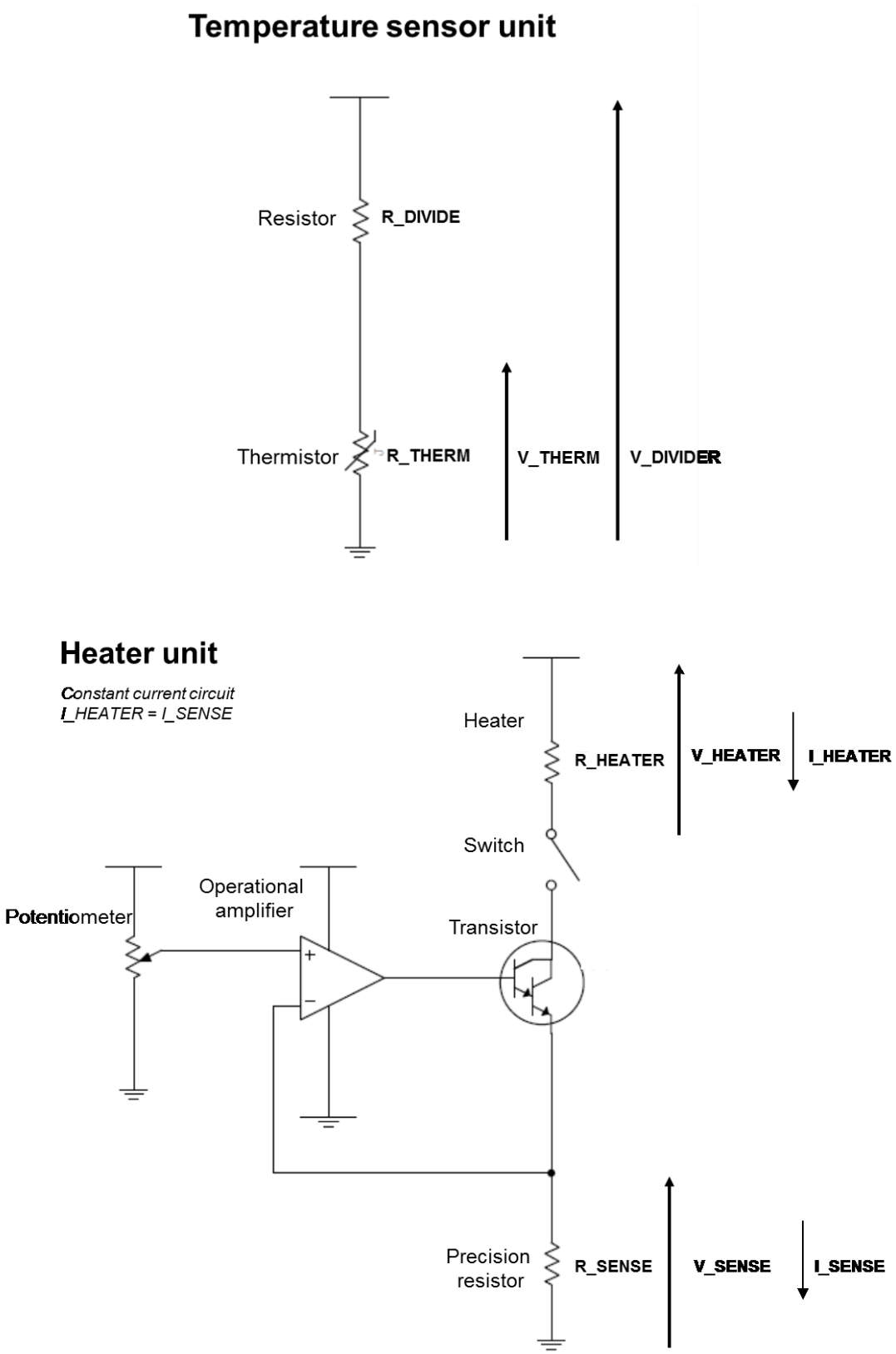

Figure 3.15 *Schematic of the temperature sensor unit and the heater unit*

4. LONDON CLAY

4.1 Introduction

This chapter describes the soil used for testing in this research project. Reconstituted London clay is used for the thermo-mechanical tests, while reconstituted and intact London clay are used for the study of thermal properties, both presented in the subsequent chapters. Firstly, the geological history of the London clay formation is presented, followed by a description of the materials sourced, including a study of the mineralogy and basic classification tests.

4.2 Geology and stratigraphy of the London Clay Formation

4.2.1 Definition

The British Geological Survey describes the London Clay Formation as “bioturbated or poorly laminated, blue-grey or grey-brown, slightly calcareous, silty to very silty clay, clayey silt and sometimes silt, with some layers of sandy clay”. Thin courses of carbonate concretions and disseminated pyrite are present in the London Clay formation, as well as a small number of thin beds of shells and fine sand partings or pockets of sand, increasing towards the base and towards the top of the formation. Glauconite is present within some of the sands and clay beds and white mica also occurs at some positions. At the base and some levels, thin beds of black rounded flint gravel are present (British Geological Survey, 2016).

4.2.2 Depositional environment

The early Eocene London Clay Formation was deposited during a widespread marine advance (56-49 Ma) from the North Sea which covered the whole of Eastern Britain from East Anglia to Dorset and southwards over the North of France, Belgium, Holland and North-west Germany. King (1981) correlated the nanoplankton, microplankton and planktonic foraminiferids to the Early Eocene successions in the London area, together with the successions in the English Channel, Belgium and Holland (Ieper Formation), northern France (Sables de Laon) and northern Germany, to present the common features of the Northern Sea

sedimentary basin. Regional geological events distinguished the different geographical areas. Two different areas of the London Clay Formation are distinguished in Southern England: the London Basin and the Hampshire-Dieppe Basin, as shown in Figure 4.1. The London Clay deposition started in an environment of raising sea levels. King (1981) linked the non-uniformities within the London Clay Formation to five transgressive-regressive sea level cycles. These changes in the depositional environment resulted in a sedimentary discontinuity at the base of each cycle. A fall in sea level gave rise to the deposition of coarser material on top of finer, while a thin glauconitic bed is indicative of a transgressive event. The soil in the Hampshire area was deposited in a shallow marine environment, near the edge of the basin and the depositional sequence is evident. On the other hand, the material in the London basin was deposited in a much deeper, and therefore, low energy environment and the depositional sequence is not as easily identified.

4.2.3 Post-depositional history

Several geological processes and events influenced the behaviour and form of the London Clay Formation. Following deposition, sporadic and isolated calcareous nodules were formed by the precipitation from calcium enriched pore water (Hight et al., 2003). The Alpine orogeny compressed the Palaeozoic basement, known as the London Platform, and its overlying sediments producing a very gentle eastward plunging syncline, known today as the London Basin. Despite some local folds, dips greater than three to one to the horizontal are rarely encountered. Some minor faults have been observed and it is presumed that such tectonics forces produced shear zones as described in Chandler et al. (1998).

The most significant post-depositional process which greatly influenced the behaviour of London clay was the erosion of significant volume of overlying sediments during the late Tertiary and Pleistocene times. Most of the overlying deposits, except for the Bagshots Beds in a few locations, and much of the London clay itself, especially in the Thames Valley, were removed. The erosion led to a mechanical overconsolidation of the clay and has been

estimated to range from 150 m in Essex (Skempton, 1961) to 300 m in the Wraysbury district (Bishop et al., 1965). Late Quaternary gravel sheets deposited then along the Thames Valley.

Weathering followed the erosional process. The clay close to the surface was desiccated, creating rough, sub-vertical discontinuities and the oxygenated groundwater changed the colour from blue to brown as the ferrous iron was converted to ferric iron. Ground freezing within the clay down to significant depths also occurred. Where the London clay outcrops to the surface, the top 9 m of clay presents a brown colour due to oxidation, with a thin transition zone to the main grey-blue clay mass. Chandler and Apted (1988) identified an apparent reduction in overconsolidation ratio and an increase in water content in the weathered material. Different conditions are found in the Thames Valley where terrace gravels cover the clay, which shows very little signs of weathering, restricted to the top 1 m of material at most (Hight et al., 2003).

Another important process that has affected the London Clay Formation is the formation of scour hollows, which are described in detail by Berry (1979) and Banks et al. (2015).

4.2.4 Stratigraphy

The thickness of the London Clay Formation varies between 50m and 150m in the London Basin and between 50m and 130m in the Hampshire Basin, decreasing westwards in both basins. The stratigraphy of the London Clay has been found to be very consistent vertically and laterally throughout the London basin and it is assumed that continuous layers of similar features persist along its thickness (King, 1981; Ellison, 2004). Using a combination of biostratigraphy, lithological variation and identifying marine flooding events, King (1981) defined five divisions in the clay (A to E). The full sequence can only be seen in some areas of the London Basin, such as in Stock and Hadleigh (South Essex), where the thickness of the London Clay formation approaches 150m. Division A is the deepest lithological unit and overlays the Harwich Formation throughout most of the basin, except in central and south London, where it sits on top of the Reading Formation or the Woolwich Formation. King (1981)

distinguished three different units A1, A2 and A3. Unit A2, with a thickness of approximately 12 m, sits above a basal pebble bed and comprises poorly graded clayey silt to silty clay with numerous partings and lenses of silts and fine sands with no calcareous fauna present throughout. A3 has a thickness of 15 m and can be subdivided in subunits representing the base and top parts. It comprises a homogeneous silty clay at the base (A3i), with increasing clayey silts with fine sand partings at the top (A3ii). Division B has a total thickness of approximately 25 m and is subdivided into two units. The base of unit B is defined by a change to homogenous silty clays, occasionally with some pebbles at the interface with division A. A thin sandy clayey silty unit approximately 8 m above the base, overlain by a glauconite-rich horizon marks the base of the B2 unit, with some more silts and very fine sand appearing towards its top. Division C, with a thickness of 20m is subdivided in three units. Units C1 and C2, both formed of silty clays, can be separated by sharp changes in the abundance and diversity of the macro fauna. The top unit C3 consists of sandy clayey silts, micaceous and lignitic which transitionally pass down into unit C2. Divisions D and E, both between 20 and 25 m thickness are not encountered in central London. The sediments in division D are noticeably siltier than the units B and C; D1 is formed of micaceous clayey silts and silty clays while the top unit D2 consists of sandy clayey silts. More clayey soils appear again in unit E1, consisting of silty clays, passing up to very silty clays and clayey silts, while E2 is made of sandy silts. The top unit of London clay (E3) according to King's (1981) classification is also known as the Claygate member and is formed of laminated and interbedded clays and silty sands.

The London clay formation should not be exclusively treated as a clay but as an assemblage of sediments of a similar age, in this case, a layered formation consisting of mainly silty clays with varying amounts of silts and sands at some levels (De Freitas and Mannion, 2007), therefore making stratigraphical information very important to geotechnical engineers. Standing and Burland (2006) presented a correlation between moisture content variation and lithological units in their investigation at St. James's Park. Gasparre (2005) tested several

intact and reconstituted samples from different lithological units and concluded that the soil had the same mechanical behaviour and engineering parameters within a stratum regardless of depth, but differences in strength and stiffness were observed for samples from distinct units, highlighting the differences in nature and structure of the clay in each division.

The British Geological Survey (Ellison, 2004) proposed an alternative “informal classification” after the study of an extensive body of data and information from several stratigraphical boreholes and recent excavations. King’s (1981) classification remains nevertheless widely used and is the reference for the lithostratigraphical information given in this present study.

4.3 Material sourced

The London clay used in this project was sourced in two central London locations. The bulk of London clay was recovered from the piling works at the Victoria and Albert Museum (Spiral Project) on Exhibition Road, just outside Imperial College. This material was from a depth of between 11 and 12 m. Micropaleontological biostratigraphical investigations performed by Bailey (2016) on two different samples of the recovered material revealed that it belongs to unit C1.

Additionally seven unused sealed intact samples from an earlier Crossrail project at Imperial College, reported in Wan and Standing (2014), were also used for the measurement of the thermal properties. These samples were recovered from a borehole in Hyde Park, from various depths: samples CS16, CS18, CS22, CS30, CS36 and CS44 of unit B2, from depths of 8.95 m, 12.35 m, 17.8 m, 23.85 m, 26.75 m and 32.35 m respectively and sample CS60 of unit A3II from a depth of 40.6 m.

Figure 4.2 shows the location of the two sites, less than two kilometres apart, and their respective ground profiles are depicted in Figure 4.3. Both sites present a very typical central London profile, with a thick layer of the London Clay Formation (56.9 m at Hyde Park and 59.25m at the V&A). In both locations, the London clay layer is overlain by 4-6 m of terrace gravels, slightly thicker at the V&A location, and 0.5m of made-ground. At Hyde Park, the

London clay sits on top of a sand channel (1.65m thick) of the Harwich Formation, which is underlain by laminated beds (4.05 m thick) and the Lower Mottled beds from the Lambeth group. At the V&A site, the London clay sits directly on top of the Lower Mottled Beds. The borehole record from the V&A site does not allow for the characterisation of the C1, B2 and B1 units, but the limits of the A3 and A2 units can be estimated from the soil descriptions. For the Hyde Park location, the different units of the London Clay Formation are clearly delimited.

4.4 Mineralogy of the sample

As part of the characterization of the material, a short study on the mineralogical composition of the clay from the V&A site was carried out at the Natural History Museum laboratory under the supervision of Dr. Jens Najorka. This was performed for the interpretation of the thermo-mechanical and thermal properties tests, as well as the modelling of the latter based on the individual conductivities of the minerals presented earlier in Table 2.1.

4.4.1 XRD Technique

X-ray diffraction is a powerful, versatile and non-destructive technique to provide detailed information on several material properties such as structure, phase composition, texture on powder samples, solid or even liquid samples. In the case of soils X-ray powder diffraction is very useful for the identification of the minerals present. The theoretical principles of the XRD technique as well as common experimental procedures are vastly described in the literature (Bish and Post, 1989; Moore and Reynolds, 1997; Harris and White, 2008), and its main characteristics are briefly summarised in this section.

X-rays, a type of electromagnetic waves of high energy and very short wavelength, are produced by the rapid deceleration of fast-moving electrons when they strike on matter (Klug and Alexander, 1974). For XRD analyses the generation of X-rays is achieved using a sealed X-ray tube, as seen in Figure 4.4, where electrons emitted by a hot filament (cathode) are accelerated by high voltage difference towards the anode material (usually copper (Cu), molybdenum (Mo), cobalt (Co) or chromium (Cr)). Their kinetic energy is then converted to

heat and a small portion (usually less than 1%) is converted to X-rays which are emitted from the tube through thin beryllium windows. As shown in Figure 4.5, X-rays produced by the tube pass through optical components such as slits to control the divergence of the beam and reduce its scatter, and other modules such as filters or monochromators, to reduce and eliminate the effects of unwanted radiation. They then irradiate the sample and are diffracted by its phases, before passing through secondary optical components and entering a silicon-based position-sensitive detector, which counts the incoming photons. By changing the diffraction angle (2θ, described as the angle at which the diffracted beam deviates from the incident beam as seen in the Figure 4.6) through movement of the sample or tube and the detector, intensities can be counted for a range of diffraction angles to create a diffractogram.

X-ray diffraction takes place when X-rays are scattered by atoms arranged in orderly planes in crystals. The atoms act as scattering centres, re-emitting X-rays at the same wavelength λ in all directions; this phenomenon is known as coherent scattering (Moore and Reynolds, 1997). The orderly structure of the atoms in crystals results in the scattered rays being either in phase in a specific direction dictated by symmetry and atomic spacing or out of phases in the other directions. When the X-rays are in phase, they constructively interfere and emerge as intense diffracted beams from the crystal (Figure 4.6), as described by Bragg's equation ([4.1]), while rays out of phase destructively interfere. Bragg's condition states that for constructive interference to happen the difference between the path lengths of the two waves need to be equal to an integer multiple of the wavelength:

$$n\lambda = 2d\sin\theta \qquad [4.1]$$

, where n is an integer, d is the distance between equivalent atomic planes, λ is the wavelength and 2θ is the angle that the diffracted beam deviates from the incident beam. When such condition is met, an XRD peak is observed in the diffractogram. By fixing the wavelength and measuring the angle at which a peak occurs, when testing a pure mineral, Equation [4.1] can be solved for the d-spacing, therefore gaining important structural detail of such mineral. This is very important for the identification of minerals when testing a soil sample which is formed

of several different minerals. In such case, the peaks observed in the diffractogram are compared to comprehensive databases of minerals such as the Mineral Powder Diffraction Files, published by the International Centre for Diffraction Data.

The system used in this project consists of the PANalytical X-Pert PRO diffractometer equipped with a Philips PW3373/10 X-ray generator and an X'Celerator detector. Data was acquired by exposing samples to Cu-Kα_1 X-ray radiation, which has a characteristic wavelength of 1.54056 Å, generated from a copper (Cu) anode operated at 45kV and 40 mA. The 2θ angular regions between 2° and 90° were recorded with a scan step size of 0.0167° and a nominal time per step of 200 s, except in the measurements on the coarser samples where a nominal time per step of 100 s was taken.

4.4.2 XRD Analysis of the London clay samples

Two different small portions of the V&A sample in powder form (referred to in this section as Batch 1 and Batch 2) were tested. Initially, a simple scan was performed in the untreated, randomly-oriented, air-dried powder of both batches. This is presented in Figure 4.7, which shows very little difference in the XRD patterns of the two samples, which gave confidence in the uniformity of the soil recovered from the V&A site for this project. It is worth noting that in the following figures showing the XRD results, the data series have been shifted in the vertical axis (by multiples of 1000 for Figure 4.7 and Figure 4.8 and 1500 in Figure 4.9 and Figure 4.10) to allow comparison. This is a common procedure to visualise the diffractogram data.

A portion of each batch was then mixed with distilled water in a bottle and placed in an ultrasonic bath for 40 minutes to bring the powder into suspension. The bottle was then placed in the centrifuge at 1000 rpm for 4 minutes in order to leave only the 2 μm clay fraction. The remaining suspension was decanted into another bottle, leaving the coarser sediments in the bottle which was then refilled with water and re-centrifuged. The process was re-iterated five times for both batches, until the bottle containing the coarse sediments had only a very clear fluid on top, indicating that most of the clay had been removed. The bottles containing the clay

suspension were then placed in the centrifuge for 20 minutes at 4000 rpm in other to remove practically all fines from the suspension.

Both the resulting coarse and fine fractions were oven-dried at 60 °C. The coarse material was mounted between Kaplon foil layers, a very low absorbing material before scanning. On the other hand, in order to create an oriented mount for the fines, a glass slide was covered by a thin layer of suspended fine material and left to air dry overnight on a hot plate at a modest temperature (40-50 °C) before scanning (test referred to as “Oriented–AD”). The clay slide was then saturated with ethylene glycol in a desiccator at 60 °C for at least 24 hours before re-scanning (test referred to as “Oriented–GLY”). Two more scans followed on the clay slide after exposures to 400 °C and 550 °C for at least 4 hours respectively (tests referred to as “Oriented–GLY400” and “Oriented–GLY550” respectively). The measured diffraction patterns for Batch 1 coarse and fine material are shown in Figure 4.8 and Figure 4.9, while the patterns for Batch 2 coarse and fine fractions are shown in Figure 4.8 and Figure 4.10 respectively. Both batches present very similar patterns, indicating the uniformity of the material sourced.

The analysis of the diffractograms involve a qualitative and a quantitative component: identifying the minerals present in the sample and establishing their proportions. The identification is performed by carefully observing the peaks and their intensities and comparing them to known values in the literature and databases (Moore and Reynolds, 1997). Smectite can be easily identified by looking at the “Oriented-AD” and “Oriented-GLY” patterns for both batches of material (Figure 4.9 and Figure 4.10). The treatment with ethylene glycol shifts the peak at 6º in the air-dried condition to a stronger reflection at 5.2º. The broad reflection with a high shoulder at low-angle is indicative of interstratified illite. The heated samples (“Oriented-GLY”) provide further confirmation of the presence of smectite, as after exposure to 400 ºC it collapses to an illite like pattern, as seen by the increase of the illite 001 reflection at around 8.9º. Illite can also be easily identified as its profile is unaffected by neither glycol solvation nor heating up to 550 ºC. Clear characteristic peaks are observed at around 8.9º and around 17.8º for all four tested conditions. Kaolinite and chlorite, despite having very different structures,

usually present more difficulties in identification as their series of diffraction peaks very nearly superimpose (C 002-K 001 and C 004-K 002). Iron-rich chlorites have very weak odd-order reflections making the distinction between the two minerals very challenging. This is however not the case for these samples, as the C 001 peak at 6.2º is clear, except for the air-dried condition where it is hidden by the broader and more important smectite peak, as well as the C 003 at 18.8º, visible also in the air-dried condition. The presence of kaolinite is confirmed by the peaks at around 12.4º and 24.9º with a smaller chlorite peak in their shoulders at higher angles (12.5º and 25.1º respectively). Heating to 550 ºC ("Oriented-GLY550") makes the kaolinite amorphous to X-rays and its pattern disappears while the hydroxide sheet of the chlorite dehydroxilates, causing changes in the diffraction pattern. The chlorite 001 reflection increases significantly and is shifted to about 6.4º, while the other reflections are very weakened, as clearly seen in the diffractograms of both samples.

The scan of the coarser material (Figure 4.8) is used for the identification of non-clay minerals in detail. Quartz is the most recurrent mineral seen in the scan of both samples' coarser fractions, with its clear characteristic peaks at 26.7º, 20.8º, 50.2º, 36.6º, 39.5º and 60º (listed by intensity). Traces of quartz can also be found in the scans of the fine fractions for both materials. Both potassium-rich feldspars, K-Feldspars (microcline), and plagioclase feldspars (albite) are present in both batches of material with the most intense peaks at 27.5º and 28º respectively. Dolomite, a type of carbonate, can also be identified with a small peak at 31º. No clear traces of other minerals such as pyrite or gypsum, often found in London clay (Kemp and Wagner, 2006), can be identified.

The quantification of minerals from XRD patterns presents several challenges and although the precision, understood here as repeatability, can be very good (replicate analysis with the standard deviation of less than 5% of the amounts present), the accuracy, meaning the difference between the obtained and true results, is not as promising. Moore and Reynolds (1979) describe a quantitative analysis as "good", with errors up to ±10% of the amounts

present for the major constituents, with concentrations greater than 20%, and up to ±20% for the remaining constituents.

Two different techniques were used in this study for the quantification of the minerals present in the tested samples: the Rietveld structural refinement method (Rietveld, 1969) and the Moore and Reynolds (1997, Chapter 9) peak intensities approach. In the Rietveld´s method, a structural model is initially built to calculate a diffraction pattern. It then uses a least squares method to refine the idealised structural model, by adjusting some user-determined parameters, in order to minimise the differences between the calculated and the observed pattern. In order to use this method, a good starting structural model is required, with accurate information on the types of crystalline structure, atomic coordinates, lattice parameters, sample geometry, experimental conditions, etc. In Moore and Reynolds method, by decomposing specific peaks, calculating the areas of the individual peaks, which give a measure of their relative peak intensities, and by using known values of mineral reference identities (Moore and Reynolds, 1997, p. 319), the relative proportions of minerals present in the sample can be estimated.

An advantage of the Rietveld's method is that it is applicable to the whole range of the angular diffraction pattern, extracting the maximum of information. However, its use becomes more complicated and much less reliable in samples with a preferred orientation, as the reflections shown are very distinct from those predicted from a random distribution. On the other hand, Moore and Reynolds method provides decent results when clear clay peaks are seen in oriented mounts, however, non-platy, non-clayey minerals cannot be included in the same quantification due to their different morphologies, resulting in completely different preferred orientations. Moreover, the analysis is restricted to the region of the chosen peaks for the calculation and ignores the rest of the diffraction pattern.

Rietveld's refinement was performed using the Profex 3.5.0. software for the randomly oriented bulk samples shown in Figure 4.7, while the peak decompositions (smectite 005, illite 003, chlorite 003 and kaolinite 002) and area calculations for Moore and Reynolds method

were performed using the HighScorePlus software for the glycolated non-heated mounts of both batches ("Oriented-GLY in Figure 4.9 and Figure 4.10). The results are shown in Table 4.1 for the bulk analysis and Table 4.2 for the clay minerals only, where the back-calculated proportions from Rietveld's refinement are also included.

The results show that the main component of the London clay sourced at the V&A Spiral Project site is smectite (28-32%), followed by illite (~26%) and quartz (21-24%). There is also chlorite (~7.5%), kaolinite (~5%), K-feldspars (~5%), dolomite (2-3%) and albite (<1.5%). Grouping the minerals together, phylosillicates/clays account for 67-70 % of the sample, quartz for 21-24 %, feldspars for 6% and carbonates for 2-3%. The differences between the two batches tested are very small, giving again an indication of the uniformity of the soil sourced at the V&A site for this project. The Rietveld error indices (weighted profile R-factor R_{wp}, expected R-factor R_{exp} and goodness of fit parameter χ^2) for both batches are R_{wp}=6.63%, R_{exp}=6.38%, χ^2=1.039 and R_{wp}=7.85%, R_{exp}=6.34%, χ^2=1.238 respectively. These error indices indicate that the structural model is very good, especially for Batch 1. For an ideal model, R_{wp} and R_{exp} would be equal and small and χ^2 would be one (Toby, 2006). However, for a diverse multi-crystal sample as the one tested, single-digit error factors and χ^2 close to one are indicative of a good quantitative analysis. Given the nature of the sample and of the experiment, the refinement can be considered very good (Najorka, 2016).

Considering the clay fraction only, the results show that smectite is the main constituent (41.6-51.3 %) followed by the illite (29.8-39.4%), smaller proportions of kaolinite (6.3-14.1%) and chlorite (4.8-11.1%). There appear to be significant differences between the results obtained by the Moore and Reynolds method and the proportions calculated form the bulk analysis, especially for the minor constituents. Although expected given the different nature of the method, the fact that significant traces of illite and chlorite are present in the "coarse" sample, as shown in Figure 4.8, may explain part of the discrepancy. If they had been in the fine mount instead, it would have resulted in higher proportions of both chlorite and illite, bringing them

closer to the results back calculated from the bulk analysis and reduced the proportions of smectite and kaolinite, which are higher than observed in the bulk analysis.

The results from mineralogical studies by Kemp and Wagner (2006) and Huggett and Knox (2006) for samples from the London basin are also shown in Table 4.1 and Table 4.2 for comparison purposes. The results of the bulk analysis agree well with the findings of Kemp and Wagner (2006), with the V&A sample being slightly more clayey and with less quartz than the samples examined by Kemp and Wagner (2006). There is more discrepancy in the results of the clay only fraction, especially for the proportions of kaolinite and chlorite. Both studies present higher values of such minerals, with kaolinite being more significant in both, however Huggett and Knox (2006) also reports an increase in chlorite and reduction in kaolinite for samples from Hampstead Heath closer to the surface, which may explain the higher chlorite content of the sample tested in this study. It is also worth noting that significant differences exist between the proportions reported by Kemp and Wagner (2006) and Huggett and Knox (2006), with the tested values being closer to the latter, and that more stratigraphical information of the sample tested would help in understanding the differences.

4.5 Classification tests

Basic classification on samples of London clay were undertaken to assess the particle density of solids, plasticity of the material and particle size distribution.

4.5.1 Specific gravity

The specific gravity of the solids, G_s, was measured in accordance to the procedure specified by the small pyknometer method in the BS 1377-2:1990 for oven-dried materials. Samples from both locations (V&A Museum and Hyde Park) were mechanically grinded and oven-dried before testing in the standard 50 mL pyknometers. Five pyknometers were used to measure the particle density of the solids for each of the samples.

The results are summarised in Table 4.3. The average specific gravity for the V&A sample is 2.774 while the values for the Hyde Park borehole vary between 2.764 and 2.782, with an

average value of 2.774. It is worth noting that the standard deviation calculated between the results of each individual pyknometer was always less than 0.01 for each sample tested, indicative of consistent measurements. This very constant value of specific gravity of solids between the different sites and depths tested may be indicative of a similar composition of all the samples tested in this project, and that the mineralogical composition described in section 4.4 may be assumed for the samples from the Hyde Park borehole, since no mineralogical study was performed on them. Gasparre (2005) reports similar values, generally around 2.75-2.77 for comparable depths.

4.5.2 Atterberg limits

The plastic and liquid limits of the clay were measured by the thread rolling technique and the cone penetrometer method, respectively, as specified by the British Standard BS1377:1990 and are presented in Table 4.3, together with the calculated plasticity indexes and the remaining classification tests performed. In addition, the natural water content of the intact samples recovered from the Hyde Park site is also reported in Table 4.3.

The water contents at plastic and liquid limit of the V&A samples are 29% and 74% respectively with a corresponding plasticity index of 45%. The water content at plastic limit and liquid limit for the Hyde Park samples vary between 26 and 29% (average value of 27.7%) and between 66% and 74% (average value of 70.4%) respectively, with plasticity indexes ranging between 40 and 45% (average value of 42.7%).

These values agree well with other tests performed on the same London clay units by Bishop et al. (1965) (plastic limit ~30% and liquid limit 69-71%), Skempton et al. (1969) (plastic limit ~29% and liquid limit 62-76%) and Gasparre (2005) (plastic limit 23-32% and liquid limit 63-75%).

The natural water contents of the Hyde Park samples range between 24 and 31% with most of the values between 24-27%, slightly drier than the plastic limit, except for sample CS22

(17.8m depth) that has a water content of 31%. There is no clear relationship between water content and depth.

4.5.3 Sedimentation

A sedimentation technique, the hydrometer test, was used to establish the fine size part of the particle size distribution of all the samples. For each test, 30 g of dry powder were added to a flask containing 100 mL of a standard sodium hexametaphosphate dispersing solution, which was mechanically shaken overnight to bring the soil into suspension. Wet sieving followed to remove the sand particles (>63 μm) to quantify to proportion of course particles in the sample, before performing the sedimentation test using the hydrometer procedure described in the BS1377:1990.

Figure 4.11 presents the particle size distributions for all samples tested, together with the envelope of particle size distributions for London clay presented by King (1991). The V&A sample and the seven Hyde Park samples present very similar particle size distributions

The clay content, measured from the sedimentation tests, is presented in Table 4.3 with the rest of the classification tests. More than half of the particles of all samples are clay-sized, concretely 61 % in the V&A sample and varying between 54 and 62% in the Hyde Park samples. The top samples of the B2 unit at Hyde Park (CS16 and CS18) are coarser than the rest of the unit, as well as the deepest sample, from the A3II unit (CS60) which is siltier than B2 samples, and also presents a remarkably lower liquid limit.

During the wet sieving prior to sedimentation, the proportion of sand retained in the 63 μm sieve was less than 5% of the total sample mass for all samples, and less than 1% for the bottom samples of the B2 unit (CS30, CS36 and CS44).

4.6 Summary

A brief history of the depositional and post-depositional history of the London clay formation, together with details on its stratigraphy, is presented in this chapter. The London clay material

used in this thesis is recovered from two central London locations with very typical ground profiles: a big bulk of clay from piling works at the V&A Spiral project site corresponding to the C1 unit and seven intact samples from different depths corresponding to the units B2 and A3II from a Hyde Park borehole. Basic classifications tests (specific gravity, Atterberg limits and particle size distribution) performed on all samples show very similar and consistent results in all samples.

A full qualitative and quantitative characterisation of the mineralogical composition of the soil from the V&A site is performed using XRD techniques, revealing that phyllolsilicates/clays are the main component (67-70%), mainly smectite and illite and small proportions of chlorite and kaolinite, followed by quartz (21-24%), feldspars (~6%) and carbonates (<3%).

Table 4.1 *Mineral quantification of the bulk sample*

Mineral	V&A Batch 1	V&A Batch 2	Kemp and Wagner (2006)	
			Mean	Range
Smectite	32.3 %	28%	-	-
Illite	26.1 %	26.5 %	-	-
Kaolinite	4.4 %	5.2%	-	-
Chlorite	7.3 %	7.5 %	-	-
Quartz	21.5 %	23.6 %	-	-
Albite	1.3 %	0.5 %	-	-
K-Feldspar	4.7 %	5.6 %	-	-
Dolomite	2.5 %	3 %	-	-
Phyllosilicates/Clay	70.1 %	67.2 %	66.8 %	41.8 – 81.3 %
Quartz	21.5 %	23.6 %	26.8 %	16.2 – 49.2 %
Feldspars	6 %	6.1 %	3 %	0 – 9.1 %
Carbonates	2.5 %	3 %	1.5 %	0 – 7.8 %

Table 4.2 *Mineral quantification of the clay fraction only*

Mineral	V&A Batch 1		V&A Batch 2		Kemp and Wagner (2006)		Huggett and Knox (2006)
	Moore and Reynolds (1997) method	Back-calculated from bulk analysis	Moore and Reynolds (1997) method	Back-calculated from bulk analysis	Mean	Range	Mean
Smectite	51.3 %	46.1%	44.2 %	41.6 %	38 %	15 – 65 %	45 %
Illite	29.8 %	37.2%	34.1 %	39.4 %	25.6 %	16 – 36 %	37.5 %
Kaolinite	14.1 %	6.3 %	13.8 %	7.8 %	24.5 %	9 – 34 %	11.5 %
Chlorite	5.5 %	10.4%	7.9 %	11.1 %	12.5 %	9 – 19 %	6 %

Table 4.3 *Summary of the classification tests*

Sample		Depth (m)	w_{nat} (%)	w_p (%)	w_l (%)	PI (%)	G_s	Clay (%)
V&A		11-12	-	29	74	45	2.774	61
Hyde Park	CS16	8.95	26.3	28	71	43	2.773	56
	CS18	12.35	25.4	27	67	40	2.779	55
	CS22	17.8	30.7	29	74	45	2.771	59
	CS30	23.85	24.3	29	72	43	2.772	57
	CS36	26.75	26.7	28	73	45	2.782	62
	CS44	32.35	24.7	27	70	43	2.776	59
	CS60	40.6	23.9	26	66	40	2.764	54

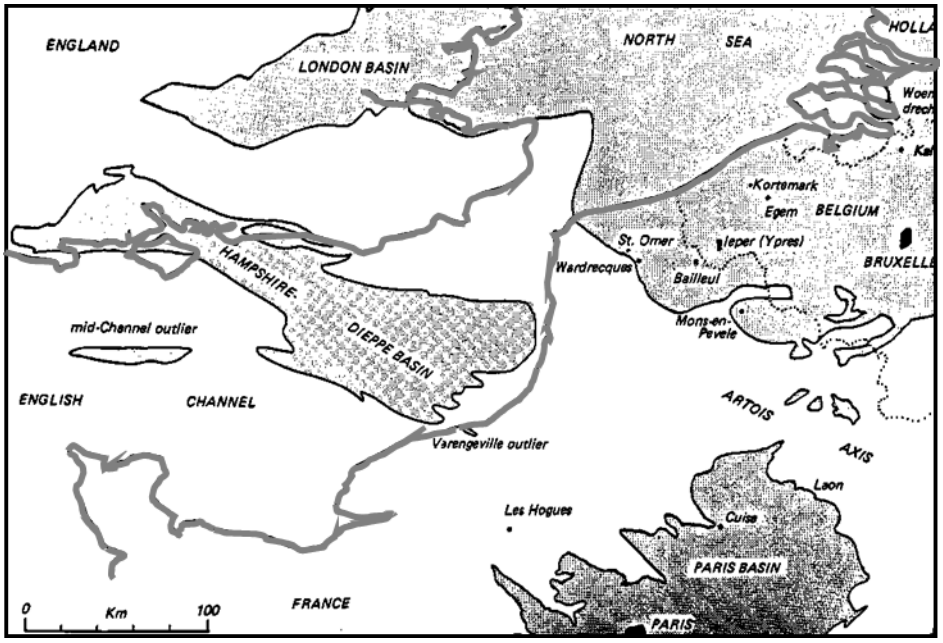

Figure 4.1 *Early Eocene deposits (shaded) in the southern edge of the North Sea Basin (after King, 1981)*

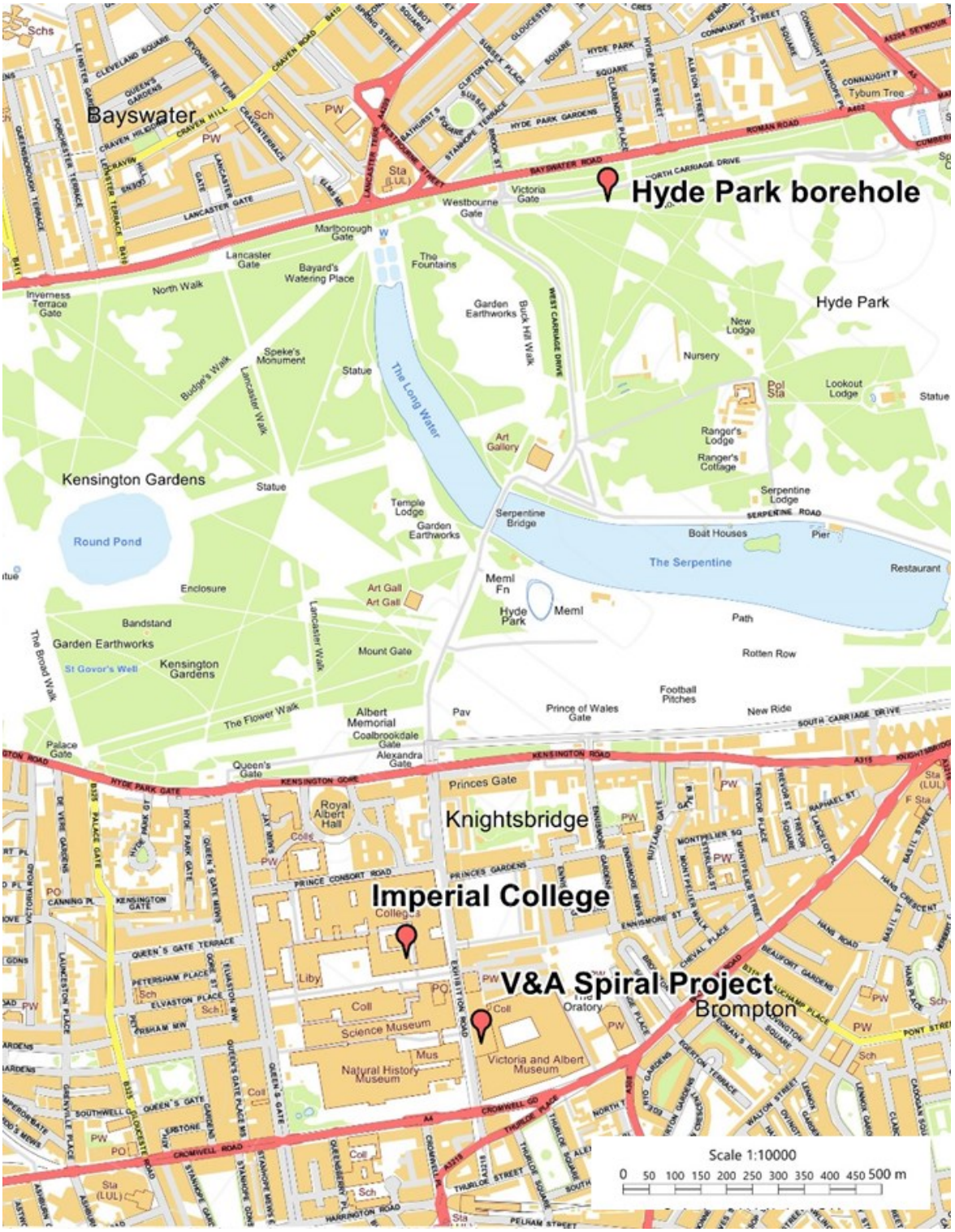

Figure 4.2 *Location of the material sourced*

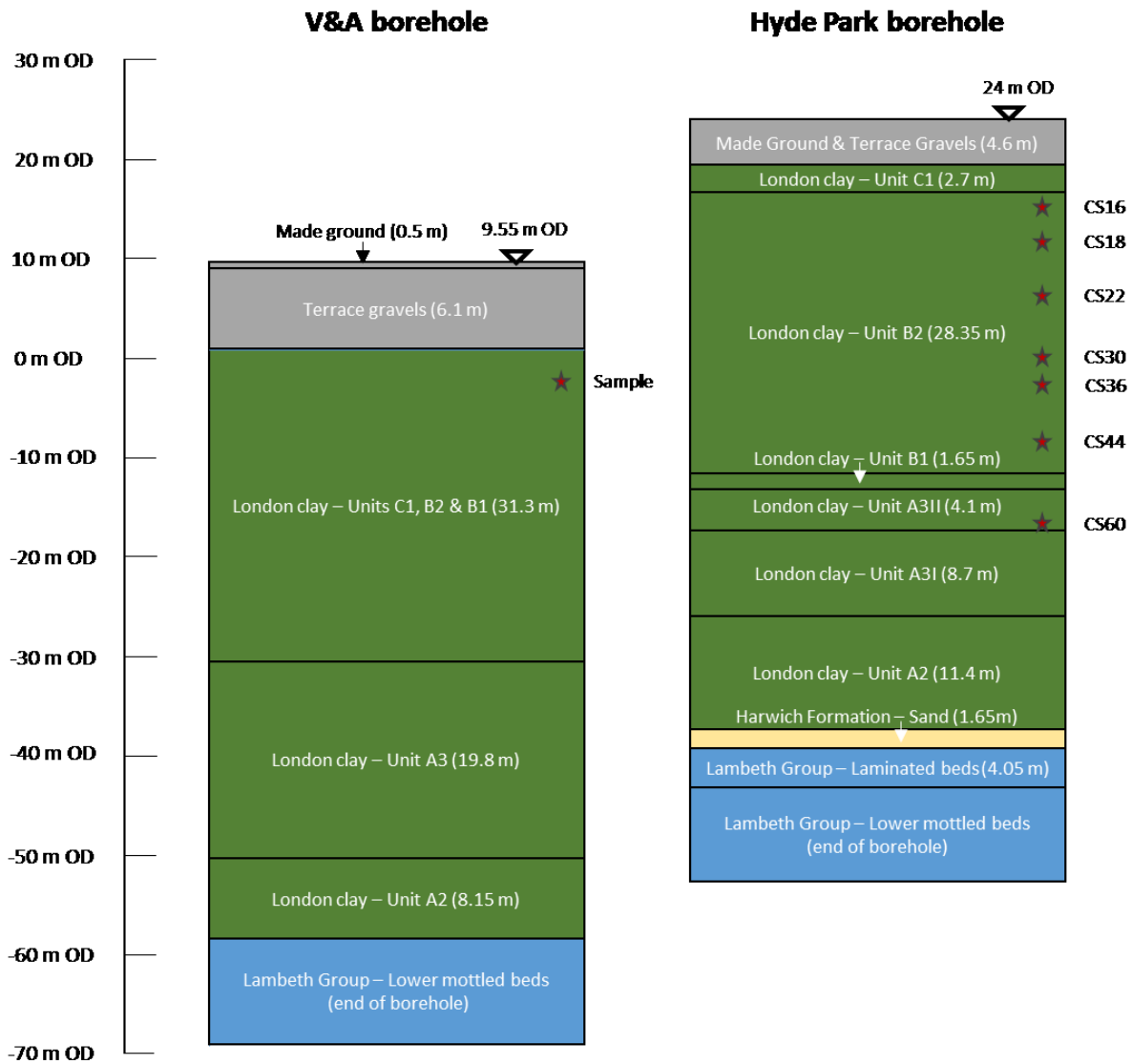

Figure 4.3 *Ground profile at the V&A site and Hyde Park*

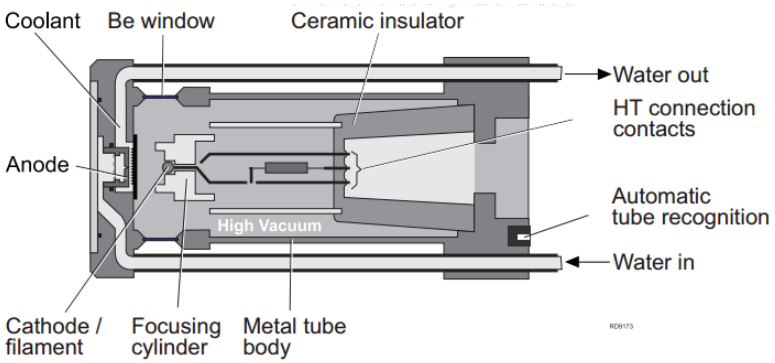

Figure 4.4 *Schematic of a sealed X-ray tube (Ermrich and Opper, 2013)*

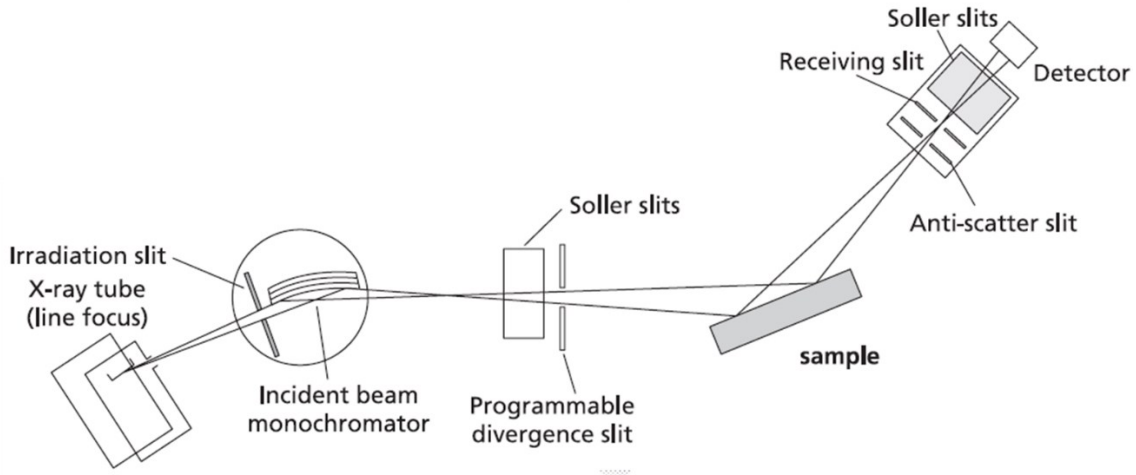

Figure 4.5 *Typical XRD set-up (after Ermrich and Opper, 2013)*

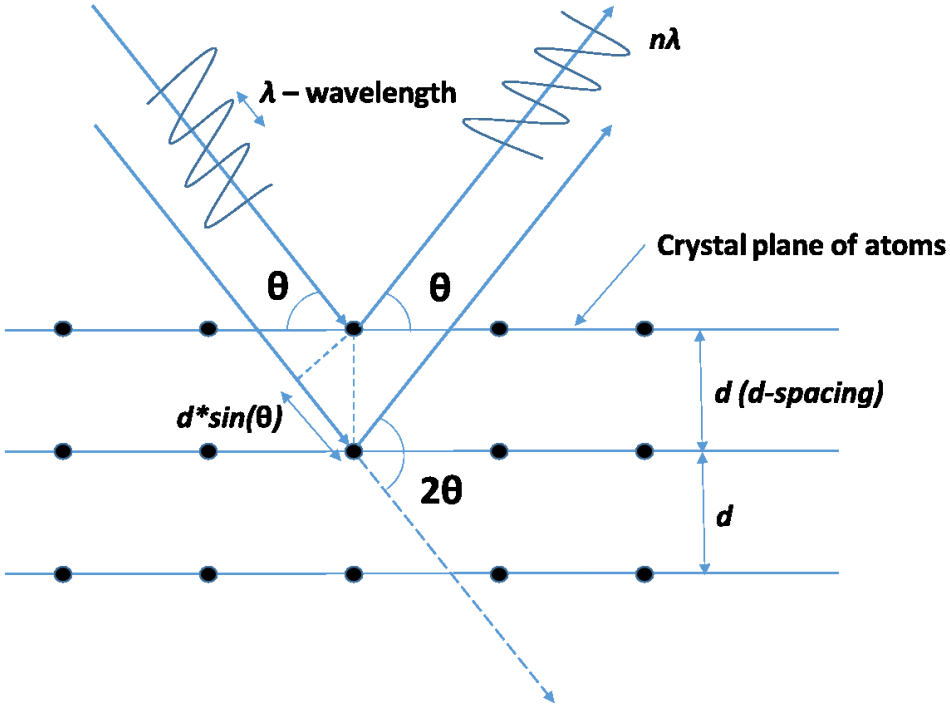

Figure 4.6 *Bragg's law of diffraction*

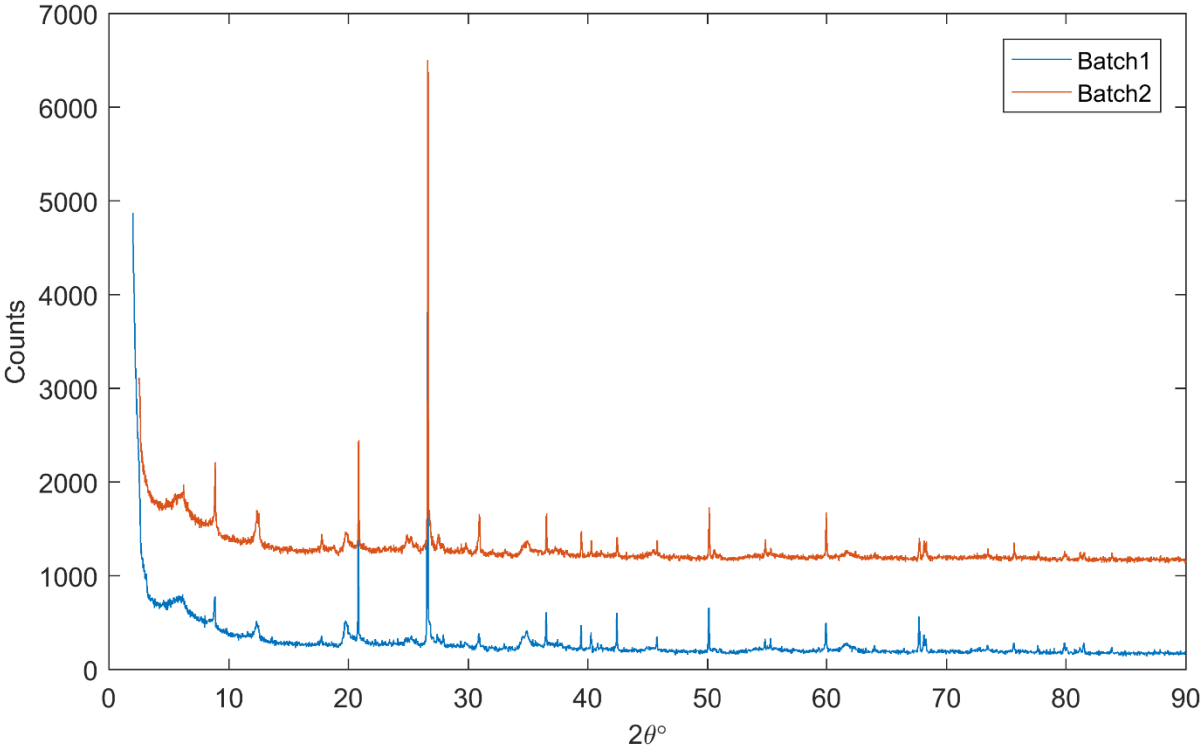

Figure 4.7 *Diffractogram of randomly oriented samples*

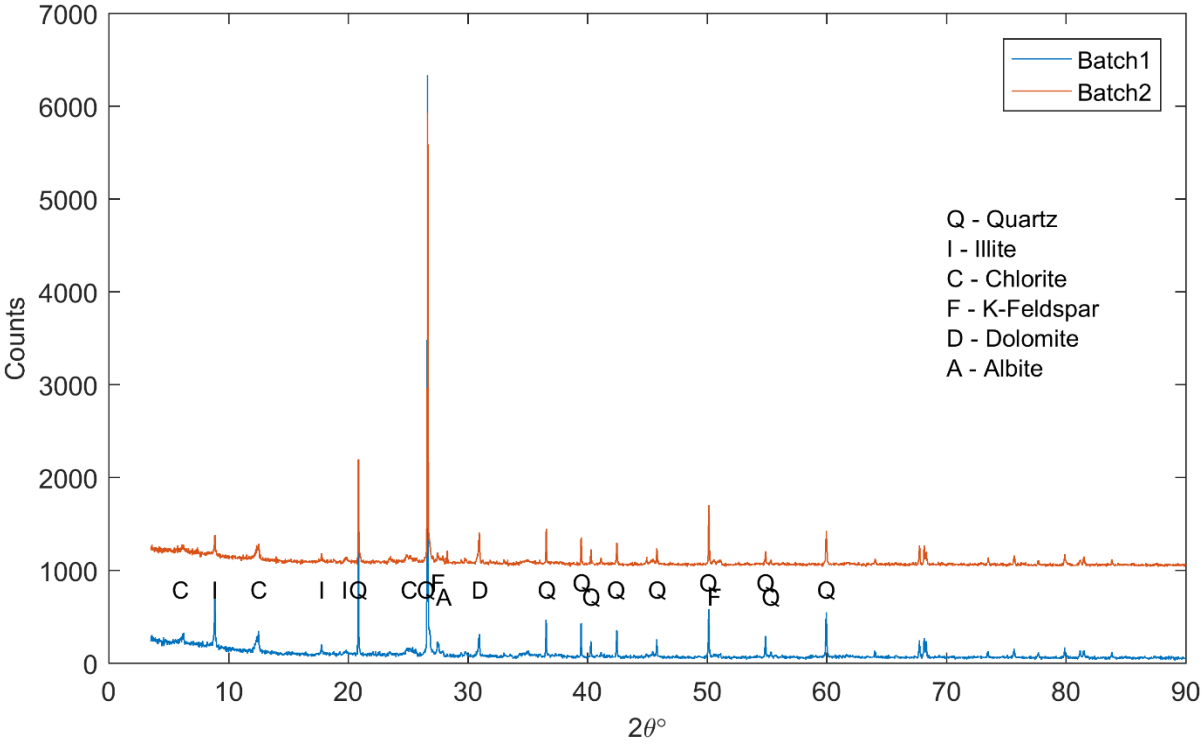

Figure 4.8 *Diffractogram of the coarse fraction of both samples*

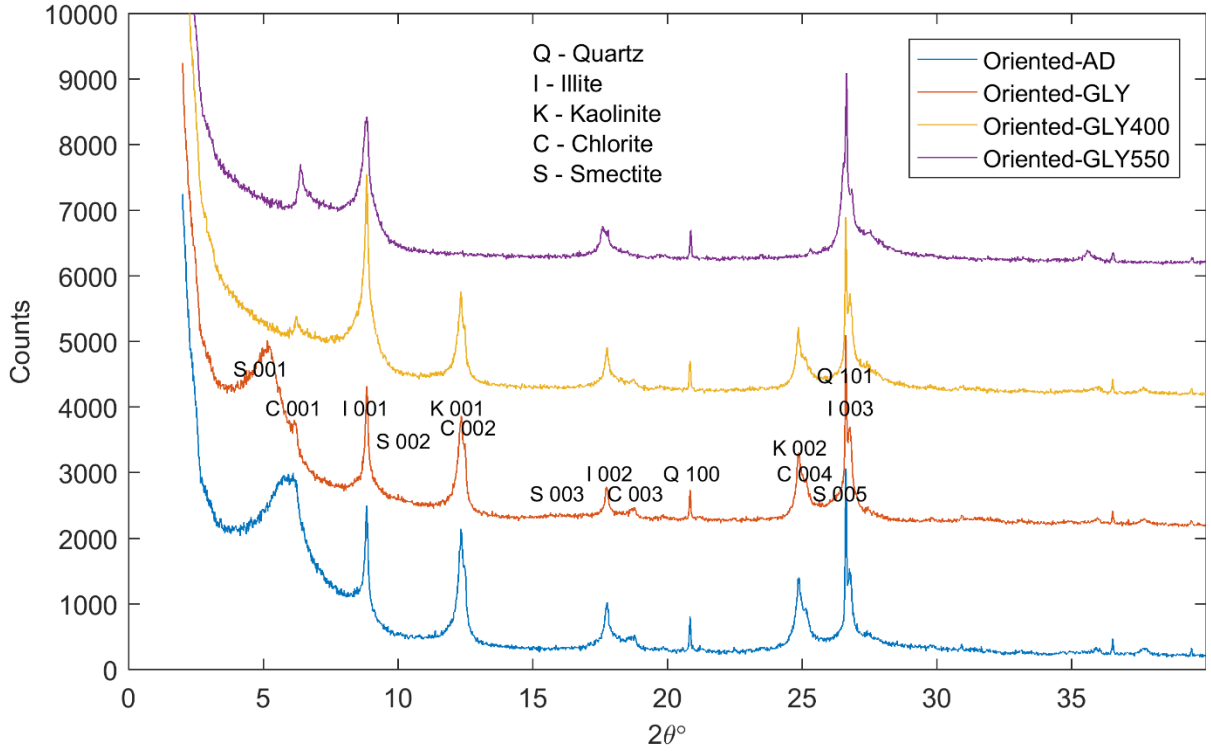

Figure 4.9 *Diffractogram of the fine fraction of Batch 1*

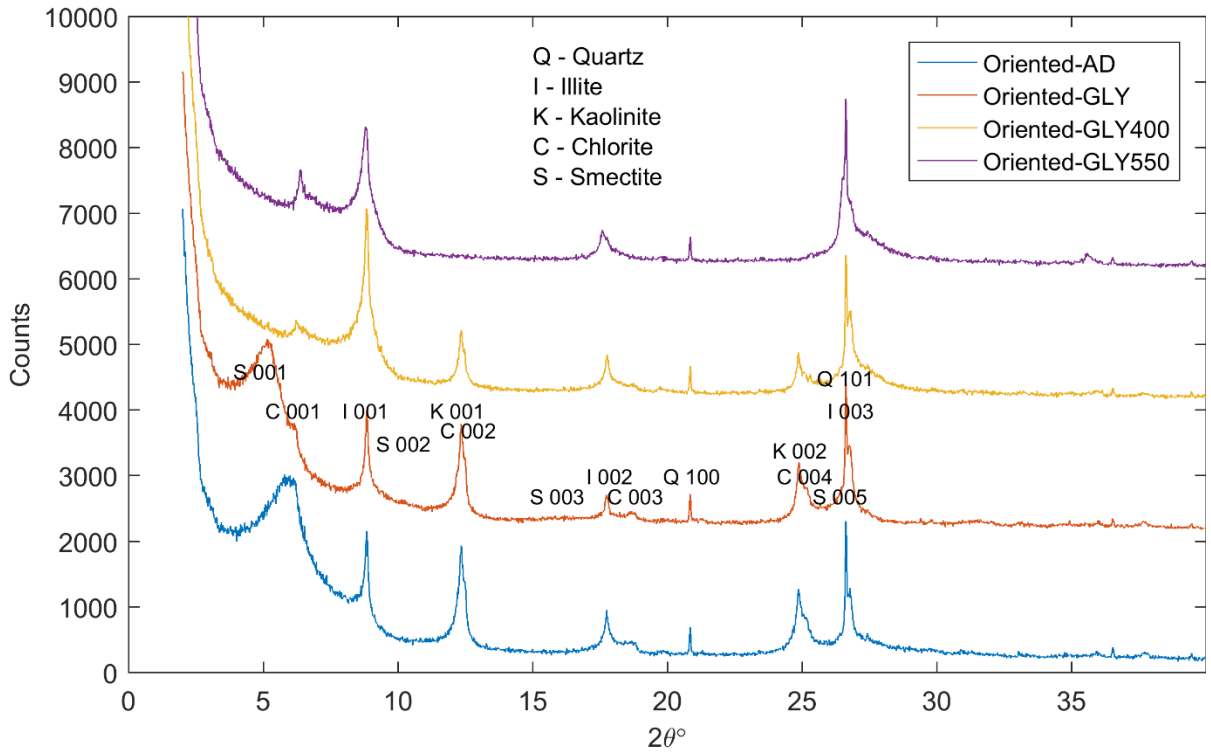

Figure 4.10 *Diffractogram of the fine fraction of Batch 2*

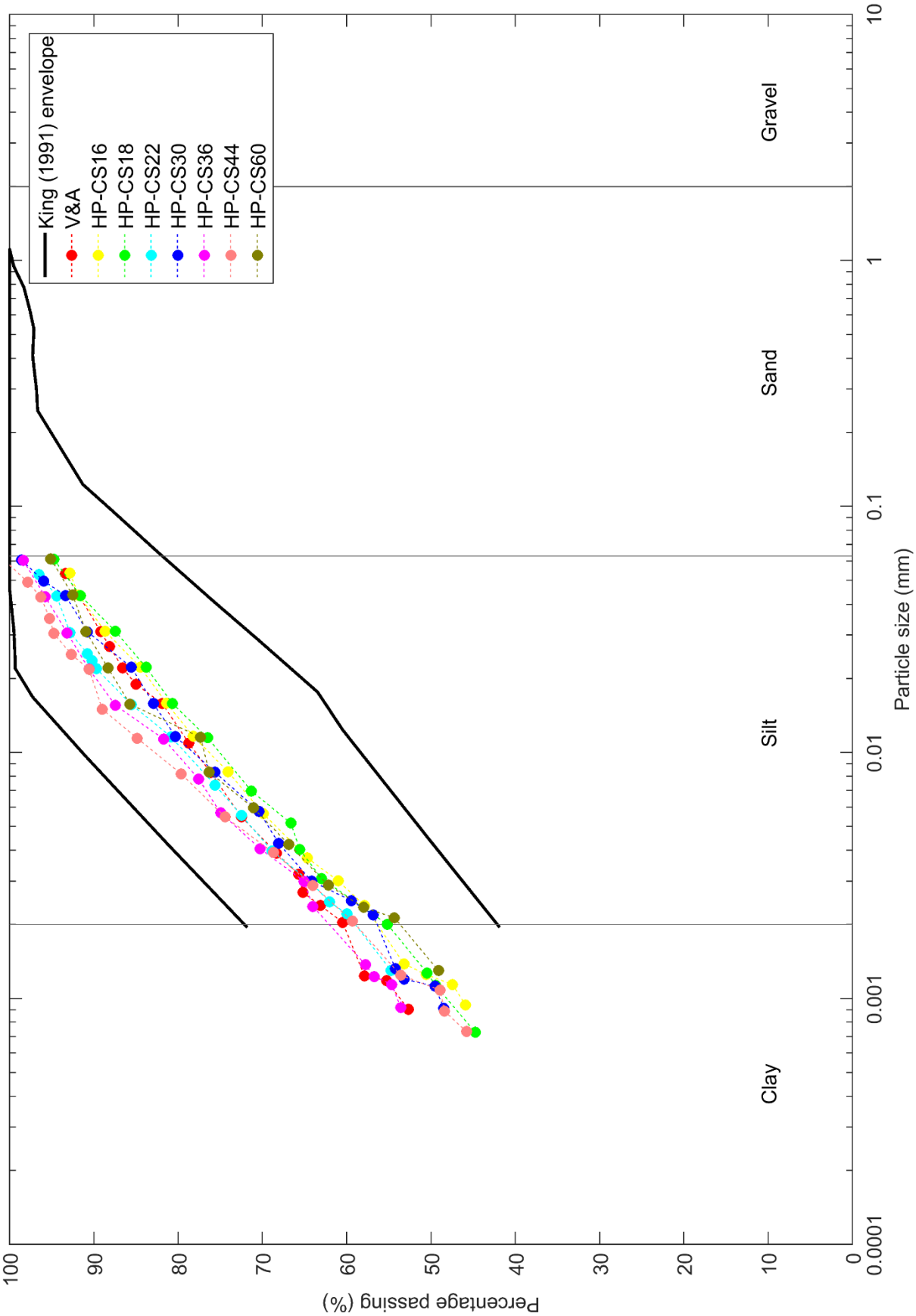

Figure 4.11 *Particle size distributions*

5. EXPERIMENTAL METHODS

5.1 Introduction

This chapter presents the testing objectives, procedures and programmes, as well as the data analysis and interpretation procedures followed in the thermo-mechanical and thermal properties tests performed on London clay samples. The measurement of thermal strains, one of the key challenges in thermo-mechanical tests, and the measurement of thermal properties are discussed in detail in separate sub-sections.

5.2 Measurement of thermal strains

The volumetric strains during standard drained triaxial tests on saturated samples are usually measured by monitoring the drained water in or out of the sample or from local instrumentation. In tests where the temperature of the sample is changing, the former method is not valid, as the sample constituents (solids and water) may expand or contract additionally. For the latter method, as discussed in Chapter 3, it may be difficult to successfully calibrate the local instrumentation for temperature changes during the test. Consequently, in the absence of direct measurements of thermal volume changes, two different approaches (Campanella and Mitchell, 1968 and Baldi et al., 1988) have been presented in the literature in order to estimate thermal volumetric strains in isotropic and triaxial cells from the measured parameters.

5.2.1 Campanella and Mitchell (1968) free water approach

The approach presented in Campanella and Mitchell (1968) computes the thermal volumetric strain, $\varepsilon_{v,T}$, during drained heating or cooling tests by correcting the measured volume of drained water, V_{dr}, in (negative) or out (positive) of the sample by the expansion of the water and solid phases in the sample due to a temperature change, ΔT, as shown in Eq.[5.1]. Parameters α_s and α_w are the thermal expansion coefficients of the solids and water respectively; V_s and V_w are the volumes of the solids and water in the sample and V_0 is the

original total sample volume. Following the soil mechanics sign convention, strains which result in a reduction in volume (contraction) are considered as positive.

$$\varepsilon_{v,T} = \frac{V_{dr} - \left(\alpha_s V_s + \alpha_w V_w\right)\Delta T}{V_0} \quad [5.1]$$

Following this framework, the change in void ratio (Δe) caused by a change in temperature during a drained test is described by Eq.[5.2], where e_0 is the initial void ratio prior to the change in temperature.

$$\Delta e = e_0 \left[\frac{\left(\alpha_w - \alpha_s\right)\Delta T - \frac{\Delta V_{dr}}{V_w}}{1 + \alpha_s \Delta T} \right] \quad [5.2]$$

This implies that the sample can maintain a constant void ratio (i.e. $\Delta e = 0$) during heating if the whole sample volume expands by $\alpha_s \Delta T$. Another implication is that the volumetric strains can no longer be calculated from the commonly used expression (ε_v^*) relating the change in void ratio to the initial void ratio (Eq. [5.3]), but is instead related to thermal volumetric strains as shown in Eq.[5.4].

$$\varepsilon_v^* = \frac{-\Delta e}{1 + e_0} \quad [5.3]$$

$$\varepsilon_{v,T} = \varepsilon_v^* \left(1 - \alpha_s \Delta T\right) - \alpha_s \Delta T \quad [5.4]$$

5.2.2 Baldi et al. (1988) adsorbed water approach

Baldi et al. (1988) presented an alternative interpretation of the thermal volumetric strains as shown in Eq. [5.5], where Δv_a is the volume of expanded adsorbed water per unit surface of clay mineral and per ºC, S_s is the specific surface of the clay mineral, ρ_d is the dry density of the soil and n is the porosity.

$$\varepsilon_{v,T} = \frac{V_{dr}}{V_0} - \left[\Delta v_a S_s \rho_d - \alpha_s (1 - n)\right]\Delta T \quad [5.5]$$

5.2.3 Comparison of both frameworks

The differences between both interpretative frameworks lie in their basic assumptions. The Campanella and Mitchell approach (1968) assumes that all the water in the clay sample is in its free form and both phases behave independently. According to Baldi et al. (1988), this may be acceptable for clays with a low adsorption potential and at relatively low effective stresses. Conversely, they argued that this was not the case for low-porosity clays with high adsorption potential, where the water is mainly in the form of adsorbed water and its thermal expansion is greatly altered by electrochemical and electrical interactions in the microstructure. Using double layer theory, the volume of expanded adsorbed water is estimated assuming that the water molecules are under a pressure which decreases exponentially with distance from the clay particles, which are treated as uniform, long and parallelly arranged with a constant thickness (a key parameter in this procedure). The inputs of the Baldi et al. (1988) method, thickness of particle and specific area of the mineral, suffer from natural variability and are difficult to measure.

Delage et al. (2000) compared both thermal strain estimations with “direct” measurements obtained from monitoring the change in confining fluid (cell water) during drained thermal cycles. It was shown that the difference between the two approaches is not significant compared to the experimental scatter. For the Campanella and Mitchell (1968) free water approach, two scenarios were compared, one using a constant thermal expansion coefficient, and the second varying the expansion coefficient with temperature and pressure. The predictions given by the pressure- and temperature-dependent free water model were found to lie between the curves of the constant α_w free water model and the adsorbed water model. Given the natural variability of clays, the scatter in the results and the complicated determination of microstructural parameters of the Baldi et al. (1988) adsorbed water model, the simpler Campanella and Mitchell (1968) free water approach, accounting for the pressure and temperature dependence of α_w, was considered satisfactory (Delage et al., 2000).

For the experimental investigation reported in this thesis and in the absence of reliable "direct" measurements of volume changes during drained heating/cooling cycles as discussed in Chapter 3, the simpler free water approach of Campanella and Mitchell (1968) is used in the interpretation of the experimental results.

5.2.4 Coefficient of thermal expansion of water

A key parameter for the interpretation of the data is the coefficient of thermal volumetric expansion of water, α_w, which is a function of both pressure and temperature. For a given pressure p, it is defined as follows (Eq. [5.6]), where ρ_w is the density of water.

$$\alpha_w = -\frac{1}{\rho_w}\left(\frac{\partial \rho_w}{\partial T}\right)_p \qquad [5.6]$$

Baldi et al. (1988), as well as presenting the alternative absorbed water interpretative framework described earlier, also presented an expression (Eq. [5.7]) for the thermal expansion of free water as a function of pressure and temperature, by interpolating experimental data from Juza (1966). The pressure is expressed in its relative value with respect to atmospheric pressure (i.e. 0 MPa is equal to 0.101325 MPa in absolute terms).

$$\alpha_w(T,p) = \beta_0 + (\beta_1 + \beta_2 T)\ln(m*(p+p_0)) + (\beta_3 + \beta_4 T)*(\ln(m*(p+p_0)))^2 \qquad [5.7]$$

where p and T are in MPa and ºC respectively, p_0 is the atmospheric pressure (0.101325 MPa) and the coefficients are:

β_0 = 4.505*10^{-4} (ºC^{-1})

β_1 = 9.156*10^{-5} (ºC^{-1})

β_2 = -1.200*10^{-6} (ºC^{-2})

β_3 = 6.381*10^{-6} (ºC^{-1})

β_4 = -5.766*10^{-8} (ºC^{-2})

m = 0.15 (kbar^{-1})

Inspection of Eq.[5.7] implies that all additive components must have the unit of °C^{-1}, in order for α_w to have the correct unit of °C^{-1}. Further implication of this is that the expression under the logarithm, $(m \cdot (p + p_0))$, must be dimensionless, and hence the coefficient must have the units of MPa^{-1} for pressures expressed in MPa. Consequently, the definition in Baldi et al. (1988) of the coefficient m as being equal to 0.15 kbar^{-1} is inconsistent with Eq.[5.7]. Some researchers have attempted to rectify this by using consistent units in Eq.[5.7]; Cekerevac et al. (2005) used MPa for both m (=15 MPa^{-1}) and p, while Uchaipichat (2006) arbitrarily changed the value of m to 1 MPa^{-1}

Eq. [5.7] is assessed here by using three possible scenarios for units: (i) parameters are considered as presented in Baldi et al. (1988) (i.e. m=0.15 kbar^{-1} and p in MPa); (ii) consistent units in MPa are adopted (i.e. m=15 MPa^{-1} and p in MPa, as in Cekerevac et al. (2005)); and (iii) the case using only kbar is considered (i.e. m=0.15 kbar^{-1} and p in kbar). The resulting variations of α_w with temperature are shown in Figure 5.1 for three different pressure levels. The value of α_w is seen to be very dependent on the choice of units for both m and p, in particular for combinations (i) and (ii).

Unable to find further guidance in the literature on the use of Eq. [5.7] and without having access to the data of Juza (1966), this fundamental parameter for water is revisited here using the formulations published by the International Association for the Properties of Water and Steam (IAPWS), formerly known as the International Association for the Properties of Steam (IAPS). This body coordinates international research in this field and is responsible for the international standards of several thermophysical properties. In 1995, the IAPWS adopted the equation of state of water derived by Pruss and Wagner (1995) at the Ruhr-Universitat-Bochum as the new international scientific standard, under the name of “The IAPWS Formulation 1995 for the Thermodynamic Properties of Ordinary Water Substance for General and Scientific Use’’. In 1997, IAPWS approved a close approximation of the IAPWS-95 as the new formulation for general industrial and scientific use, referred to as the IAPWS-IF97 (IAPWS, 2007).

The IAPWS Industrial Formulation 1997 consists of a set of equations for five different regions of temperature and pressure which cover the following range of validity: 273.15 K < T ≤ 1073.15 K for p ≤ 100 MPa and 1073.15 K < T ≤ 2273.15 K for p ≤ 50 MPa, where the pressure is expressed in absolute value (i.e. atmospheric pressure is 0.101325 MPa). Region 1 is of interest for soil mechanics as it covers the following range of temperature and pressure: 273.15 K ≤ T ≤ 623.15 K and $p_s(T) \leq p \leq$ 100 MPa, where p_s is the saturation pressure. The basic equation that covers this region is a fundamental equation for the specific Gibbs free energy g , which is given in its dimensionless form, $\gamma = g/(R_c T)$, as shown in Eq. [5.8].

$$\frac{g(p,T)}{R_c T} = \gamma(\pi,\tau) = \sum_{i=1}^{34} n_i (7.1-\pi)^{I_i} (\tau - 1.222)^{J_i} \qquad [5.8]$$

where $\pi = p/p^*$ and $\tau = T/T^*$ with p^* = 16.53 MPa and T^* = 1386 K; R_c is the specific gas constant of ordinary water R_c = 0.461526 kJ kg^{-1} K^{-1} and the coefficients and exponents n_i, I_i, J_i are shown in Table 5.1

All the thermodynamic properties (specific volume, specific internal energy, specific entropy, enthalpy, etc.) can be obtained using the appropriate relations of the dimensionless Gibbs energy and its derivatives. The specific volume v, defined in Eq.[5.9], can be derived using the relation shown in Eq.[5.10].

$$v = \left(\frac{\partial g}{\partial p}\right)_T \qquad [5.9]$$

$$v(\pi,\tau)\frac{p}{RT} = \pi\gamma_\pi \qquad [5.10]$$

where the derivative γ_π is given in [5.11].

$$\gamma_\pi = \sum_{i=1}^{34} -n_i I_i (7.1-\pi)^{I_i - 1} (\tau - 1.222)^{J_i} \qquad [5.11]$$

Taking the density ρ as the inverse of the specific volume, $\rho\ (p,T)$ data can be calculated for the region of interest, and then applying the definition of the thermal expansion coefficient α_w

shown in Eq.[5.6], α_w can be calculated for all the points of interest. In this case, the coefficients of thermal expansion of water were calculated in 2250000 points equally subdividing the temperature range from 1 to 99 °C and pressures from 0 to 10 MPa (relative to atmospheric pressure). A basic polynomial was then fitted to all the calculated values in order to obtain Eq. [5.12], shown in Figure 5.2, with the goodness of fit parameters as follows: r-squared R^2 = 1.000; and the sum of squares due to error: SSE = 5.2155e-09.

$$\alpha_w(T,p) = \alpha_0 + \alpha_1 T + \alpha_2 p + \alpha_3 T^2 + \alpha_4 Tp + \alpha_5 T^3 + \alpha_6 T^2 p \qquad [5.12]$$

where the coefficients are:

α_0 = -4.392*10^{-5} (ºC^{-1})

α_1 = 1.444*10^{-5} (ºC^{-2})

α_2 = 3.043*10^{-6} (ºC^{-1}MPa^{-1})

α_3 = -1.113*10^{-7} (ºC^{-3})

α_4 = -8.279*10^{-8} (ºC^{-2}MPa^{-1})

α_5 = 4.714*10^{-10} (ºC^{-4})

α_6 = 3.867*10^{-10} (ºC^{-3}MPa^{-1})

Note that for convenience, pressure (in MPa) in Eq.[5.12] is expressed in its relative value with respect to atmospheric pressure (i.e. 0 MPa is equal to 0.101325 MPa in absolute terms) and temperature is expressed in °C.

The variations of the thermal expansion coefficient with temperature and pressure given by the new expression (Eq.[5.12]) are also plotted in Figure 5.1 at discrete pressure levels, showing a significantly different relationship compared to the three interpretations of Eq.[5.7]. Most notably, the new expression suggests that α_w is reasonably nonlinear with temperature, contrary to the quasi-linear relationships implied by all three interpretations of Eq.[5.7]. The interpretation of Eq.[5.7] which shows variation trends closest to that of Eq.[5.12] is the one that assumes units of kbar for m and p (i.e. case (iii)). Further comparison of the new

expression with the latter interpretation of Eq.[5.7], as shown in Figure 5.3, suggests that the influence of pressure on the thermal expansion coefficient implied by Eq.[5.12] is negligible in the range considered (Figure 5.3a), compared to that implied by Eq.[5.7] (Figure 5.3b). The pressure-dependency is even more pronounced with the remaining two interpretations of Eq. [5.7] (i.e. cases (i) and (ii)). For further interpretation of results obtained during this Thesis, Eq.[5.12] is adopted for the calculation of α_w.

5.2.5 Coefficient of thermal expansion of solids

The coefficient of thermal expansion of the mineral solids is considered in both interpretative frameworks. Coefficients for common minerals are summarised in Table 5.2. Two types of coefficients are presented depending on the mineral type: the volumetric thermal expansion coefficient, $\alpha_{s,v}$, (α_s), and the linear expansion coefficient in the direction of the measurement $\alpha_{s,l}$. The thermal expansion of clay minerals is highly anisotropic and it is necessary to distinguish the expansion coefficient in both the perpendicular, α_{s,l^1}, and parallel, α_{s,l^2}, direction to the layers of the mineral structure. It is worth noting that most of these measurements have been performed at atmospheric pressure and at a very wide range of temperatures, often up to 600 ºC. Only the values applicable to the relevant temperature range for THM testing (up to 99 ºC) are presented. Based on the mineralogy of the soil, a thermal expansion coefficient of the solids, α_s, may be estimated from a weighted average of the coefficients of the different minerals present in the soil. For the tested London clay, given the results of the chemical micro-analysis described in Chapter 4 and the values in Table 5.2 , a value for the coefficient of thermal expansion of the solids α_s of 29.9*10^{-6} °C^{-1} is taken.

5.2.6 Measurement of drained water

The volume of water flowing in and out of the sample is the only actual measurement during testing considered in both interpretative frameworks. This measurement may be affected by factors such as the long-term behaviour of the drainage system since temperature tests last a considerable period of time, or the expansion of the system, (drainage lines, pedestal and

porous stone) due to temperature. In addition, the measurement of the drained water may also be affected by seepage through the membrane due to the degradation of the membrane and O-rings after prolonged exposure to high temperatures. These factors can be accounted for by a thorough examination and calibration of the behaviour of the system, as discussed in Chapter 3.

5.3 Thermo-mechanical tests

5.3.1 Testing schedule

A testing schedule, summarised in Table 5.3 and Table 5.4, was designed with the aim of characterising several aspects of the thermo-mechanical behaviour of reconstituted, saturated London clay. These tests were performed in the standard triaxial stress path cell and in the newly-developed isotropic thermal cell. The nomenclature used for the tests reported in this thesis is as follows. The first part of the name gives information of the stress history of the sample (nc – for normally consolidated samples and oc(i) for overconsolidated samples to an OCR of i), the subsequent presence of the “h” character indicates the exposure to a drained temperature heating and cooling cycle, followed by t(i), where the i is a number to distinguish between the tests performed with the same stress history. For example, both #oc6ht1 and #oc6ht2 have the same stress history but are exposed to different temperature histories, which are summarised in Table 5.4. The duration of the thermo-mechanical tests is also described in Table 5.4, significantly longer than standard tests. Additional tests not reported here were performed but failed due to external laboratory issues before any meaningful results could be obtained. In the case of #oc4ht1, there was a loss of power, affecting the control of temperature and pressures during the initial drained heating phase; however the data until that point is reported in this thesis.

The specific objectives of the thermo-mechanical tests performed are the investigation of:

- Thermally induced volume changes during heating and cooling of saturated London clay samples and the influence of the stress level, stress history, number and amplitude of the temperature cycle on these.
- The influence of the temperature cycles, of different number and amplitude, on the strength and stiffness of London clay samples at different stress levels and with different stress histories.
- The comparison of the results interpreted with the updated Campanella and Mitchell approach (section 5.2) and expressions found in the literature for the estimation of thermal strains.

In order to address the aforementioned objectives, three types of tests were planned:

- The first group of tests consists of a basic reference study of the strength and stiffness of the material. They are performed at room temperature, in a standard triaxial stress-path cell on samples 38 mm in diameter and 76 mm high, and comprise all the tests summarised in Table 5.3. These tests involve isotropic consolidation to a mean effective stress levels p'_c, and in some cases isotropic swelling, always from p'_c =300 kPa, prior to undrained shearing.
- The second group of tests are performed in the temperature-controlled apparatus initially, following the temperature-stress path shown in Figure 5.4a on samples 50 mm in diameter and 100 mm high. It comprises the following tests: #ncht2, #ncht1, #oc4ht1, #oc6ht1, #oc6ht2 and #oc6ht3, which are detailed in Table 5.4. Samples are isotropically consolidated to different stress levels (O→A), and some of them swelled to different overconsolidation ratios, but always from p'_c =300 kPa (A→B), before applying heating and cooling cycles of various forms (A→C→A or B→D→B). As explained in Chapter 3, due to the load cell instability under temperature, shearing of the samples is not attempted in the temperature-controlled cell. Instead, at the end of the temperature cycles, samples are removed, trimmed to smaller size (D=38 MM, H= 76 mm), brought back to their final stress state (A or B) and sheared under undrained

conditions in a standard stress-path triaxial apparatus at ambient temperature. This group of tests provides information on the influence of several aspects on the thermally induced volume changes and the strength and stiffness of the material. The influence of stress level is assessed by the tests on the two normally consolidated samples, #ncht2 and #ncht1, consolidated to p_c' = 300 kPa and p_c' = 150 kPa respectively. The influence of stress history is assessed by comparing the normally consolidated samples to those overconsolidated to an OCR of 4 (#ocr4ht1) and of 6 (#ocr6ht1, #ocr6ht2 and #ocr6ht3). A number of temperature histories are considered for each set of samples with a similar stress history. For normally consolidated samples, #ncht2 undergoes a relatively long series of heating and cooling cycles with a change of amplitude at the final cycle (20-60-20-60-20-70-20 ºC), while #ncht1 is exposed to much simpler cycle (20-60-20 ºC). Similarly, for the overconsolidated samples with an OCR of 6, #oc6ht2 undergoes a single cycle (20-60-20 ºC) while #oc6ht1 experiences also a single cycle but of smaller amplitude (20-40-20 ºC). Finally, sample #oc6ht3 is exposed to five small cycles (20-40-20 ºC x5).

- The third group of tests comprises tests #oc4ht2 and #oc4ht3 and are also performed initially in the temperature-controlled apparatus, but following the more complex temperature-stress path depicted in Figure 5.4b. Samples are isotropically consolidated up to p_c' =300 kPa (O→A), and swelled to an OCR of 4, p'=75 kPa (A→B), heated under drained conditions (B→C) up to 40 ºC for #oc4ht2 and up to 60 ºC for #oc4ht3, reloaded at such temperature past the maximum previous stress up to p'=350 kPa (C→D), followed by a further drained temperature cycle (D→E→F). Sample #oc4ht2 is heated to up 60 ºC and cooled down to room temperature, while sample #oc4ht3 is cooled directly from 60 ºC. As with the previous group, at the end of the cooling phase, samples are removed from the cell, trimmed, brought back to the final stress state (F) and sheared under undrained conditions in a standard stress-path triaxial apparatus. This type of test aims to detect the changes in the pre-consolidation

pressure and the evolution of the consolidation parameters with temperature during the reloading phase performed at different temperature in the two samples. Additionally, it also provides information on thermally induced volume changes for OCR 4 samples during the initial drained heating phase (B→C) and for normally consolidated (after the reloading) samples during the final thermal phase (D→E→F). Furthermore, information on the effects of these complex temperature histories on the strength and stiffness of the material is examined.

5.3.2 Sample preparation

The London clay from the V&A site was used for thermo-mechanical tests. The preparation of reconstituted samples started by breaking the natural samples into small pieces, before leaving them to air-dry for several days and removing any unusual material (in colour or size). The clay was then grinded mechanically before making a slurry at approximately 1.25 times the water content at liquid limit, as recommended by Burland (1990). The slurry was then consolidated in a large consolidometer up to a vertical stress of 200 kPa over a period of three weeks. The resulting cakes were subsequently covered by several layers of cling film and wax to maintain the moisture content. Samples were then trimmed to the desired size depending on the test performed: samples used for the temperature-controlled cell were 50 mm in diameter and 100 mm in height (all those in Table 5.4), while samples tested in the standard triaxial stress-path cells were 38 mm in diameter and 76 mm in height (Table 5.3). Radial trimming was performed using a metal string saw and a trimming frame and the correct sample length was adjusted using a two-piece metal hollow mould.

Before each test the water lines in the system were left overnight to fully saturate under a pressure of 700 kPa, also as a check for leaks. The trimmed samples were then placed on top of a saturated porous stone, previously left under vacuum for 4 hours, and filter paper drains were installed at the side of the sample and between the bottom of the sample and the porous stone.

A top cap (with a half-ball for the shearing tests) without drainage was placed on top of the samples, which were then sealed by a membrane and O-rings. For tests in the temperature-controlled apparatus, the set-up consisted of a double neoprene membrane, with a thin layer of grease in between and Viton O-rings, as well as of a steel top cap, while for the tests in the conventional triaxial apparatus, a plastic top cap, thin latex membrane and standard nitrile O-rings were used.

5.3.3 Testing stages

After the installation of the sample, the saturation stage began by applying a cell pressure under undrained conditions similar to the maximum the sample has experienced in the past. For the reconstituted samples in this programme, a pressure of 200 kPa was applied and the increase in pore pressure was monitored, until it became stable. Head (1998) defines the difference between the cell pressure and the pore pressure at that point as the “initial effective stress”. The saturation of the sample began by opening the sample to back pressure and increasing both cell and back pressures simultaneously at a rate of 50 kPa/hr keeping the difference between the two constant until the back pressure reached 300 kPa, holding such pressures afterwards. Samples were left to saturate for at least 48 hr when a B-test was performed. If the B-value was above 0.97, the saturation was considered satisfactory and the test proceeded to the next stage. Otherwise, the samples were left to saturate for a longer period until such condition was met.

For the consolidation and swelling phases, step loading in increments or decrements of approximately 75 kPa was preferred instead of the commonly-used rate loading, given the nature and drainage conditions of the sample: relatively large samples with low permeability with single drainage only, and the lack of mid-height pore pressure measurements. To ensure uniform stress states, samples were allowed to creep down to a rate of 0.01%/day in terms of total volume monitored by the volume gauge before subsequent loading steps or testing stages.

The heating and cooling stages were performed by controlling the temperature of the heaters at the bottom and top parts of the cell with the TRIAX software. A nominal rate of 0.5 ºC/hr was chosen for the heaters, the actual rate on the sample was always smaller (approximately 0.3 ºC/hr). Heating/cooling stages were stopped at each 10 ºC increment or decrement until volume changes in the sample stabilised.

Subsequent to the end of the last cooling cycle, the samples were quickly unloaded under undrained conditions and removed from the cell. The membranes were inspected before removal and the sample was weighted and measured. It was then trimmed down to a standard 38 mm diameter sample for the upcoming shearing in a standard triaxial cell, with the trimmings used for moisture content measurement. Upon placement in the standard stress-path cell, samples were “re-saturated” and “re-consolidated” under the conditions described earlier to their last stress state in the thermal cell, before shearing. Undrained shearing was performed at a nominal axial strain rate of 5%/day.

For the reference study at room temperature, the same procedures detailed above were used for the saturation, consolidation/swelling and shearing stages.

5.3.4 Analysis of the data

Prior to set-up, the dimensions and mass of the sample were measured and the water content was estimated from the trimmings. In the samples tested in the temperature-controlled apparatus, the dimensions and mass were also measured upon removal, with the trimmings to estimate the moisture content at the end of the heating/cooling cycles, when reducing the sample prior to installation in the standard triaxial stress path apparatus. Post shearing, the geometry of the sample was measured, as well as the dry mass.

Volumetric strains, ε_v, during the consolidation/swelling stages were calculated from the volumes of water flowing in and out of the sample, V_{dr} , measured by the volume gauge as follows:

$$\varepsilon_v = \frac{V_{dr} - c \cdot t}{V_0} \quad [5.13]$$

where V_0 is the sample volume at the end of the previous stage, c is the daily drift of the volume gauge/system loss and t is the duration of the stage. The daily loss of the system is discussed in section 3.3 for the new temperature-controlled apparatus (~0.015 cm^3/day at room temperature) and can be ignored for tests in the standard stress-path cells.

In the standard stress-path cells, volumetric strains may also be calculated (Eq.[5.14]) from the internal local instrumentation which measures the axial and radial strain, ε_a and ε_r:

$$\varepsilon_v = \varepsilon_a + 2\varepsilon_r + \varepsilon_r^2 \left(\varepsilon_a - \frac{2\varepsilon_a}{\varepsilon_r} - 1 \right) \approx \varepsilon_a + 2\varepsilon_r \quad [5.14]$$

The thermally induced volumetric strains during the drained heating and cooling phases are estimated using Eq.[5.1] with the newly proposed expression for α_w (Eq.[5.12]), as discussed earlier in this chapter.

During shearing, the estimation of the **current cross-sectional area,** A_c, of the sample is essential for the calculation of the deviatoric stress. A common procedure is to assume that the sample deforms as a right cylinder (La Rochelle et al., 1988). The current area may be calculated as given by Eq.[5.15], where ε_v is the change in volume during shearing and A_0 is the cross-sectional area of the sample prior to shearing.

$$A_c = A_0 \frac{1 - \varepsilon_v}{1 - \varepsilon_a} \quad [5.15]$$

It is worth noting that this expression may also be used for the calculation of the cross-sectional area during any other stage of the test (consolidation/swelling/drained thermal cycles), inserting the relevant volumetric strain.

In undrained shearing tests (as all reported in this thesis), the expression can be simplified further to:

$$A_c = A_0 \frac{1}{1-\varepsilon_a} \quad [5.16]$$

The aforementioned area correction is appropriate for bulging failure (illustrated in Figure 5.5a), despite not meeting the geometrical condition of its assumption.

In the case of the formation of a shear plane, the calculation of the cross-sectional area becomes more difficult and relies on the measurement of its geometry after the test, which may have been significantly altered during the removal of the sample. Figure 5.5b shows an idealized pure single shear plane failure and an approach of calculating the cross-sectional area. This idealised failure may be closely encountered in very stiff clays and shales, but rarely in softer material. In many cases, there is a mixture of both modes of failure, making the estimation of the cross-sectional area very challenging. On the one hand, there is a contribution from the movement along the slip plane causing a reduction in area; while on the other hand, the contribution from localised bulging causes an increase in the area. In such cases, La Rochelle et al. (1988) recommend calculating the corrected cross-sectional area from the contact area on the shear plane at the end of the test A_{ce}, given by the surface of the ellipse depicted in Figure 5.6, where d_a and d_b are its major and minor axes respectively, measured at the end of the test (Eq.[5.17]).

$$A_{ce} = \frac{\pi}{4} d_a d_b \quad [5.17]$$

La Rochelle et al. (1988) suggest using the right cylinder approximation in Eq.[5.16] until the peak in the stress-strain curve, when the shear plane is usually initiated despite not being fully visible until larger strains, and then apply the reduction or increase in area as measured at the end of the test ([5.17]) proportionally for the remaining strain region:

$$A_c = A_{peak} + \left(A_{ce} - A_{peak}\right)\left(\frac{\varepsilon_a - \varepsilon_{peak}}{\varepsilon_e - \varepsilon_{peak}}\right) \quad [5.18]$$

where A_{peak} and ε_{peak} are the cross-sectional area and axial strain at peak strength and A_{ce} and ε_e are the cross-sectional area and axial strain at the end of the test.

Another important correction in the analysis of the shearing data is the **membrane correction** due to its restraining effect which adds a small contribution to the compressive resistance and is dependent on the elastic properties of the membrane as well as on its initial diameter. Figure 5.7 shows the method for the measurement of the elasticity modulus, as proposed by Henkel and Gilbert (1952) and Bishop and Henkel (1962), where the extension of a strip of membrane suspended between two rods is measured for different loads. For the latex membranes used for the sheared samples, with an average thickness of 0.35 mm, the load-strain data used for the calculation of their elastic properties is shown in Figure 5.8. The extension modulus, calculated as the secant at 10 % strain, is 0.36 N/mm.

Head (1998) recommends initial unstretched diameters of the membrane of between 75 and 90% of the diameter of the sample, with a membrane thickness not exceeding 1% of the specimen diameter in order to minimise the initial confining pressure, p_{0m}, that the membrane applies to the sample, given by:

$$p_{om} = 2M_i \frac{d_0 - d_{im}}{d_0 d_{im}} \qquad [5.19]$$

where M_i is the initial tangent modulus at 1% strain, d_0 is the diameter of the sample at the end of consolidation and d_{im} the initial unstretched diameter of the membrane.

After detailed examination of previous corrections proposed by Henkel and Gilbert (1952) and Duncan and Seed (1967), La Rochelle et al. (1988) proposed the following correction, σ_{3m}, to be added to the minor principal stress:

$$\sigma_{3m} = p_{0m} + 0.75 \frac{M_s \sqrt{\varepsilon_a}}{d_0} \qquad [5.20]$$

where M_s is the secant modulus at 10% strain and ε_a is the axial strain of the specimen.

In the tests showing a shear plane failure, a different correction is applied, as the membrane correction is now governed by the amount of movement occurring in the shear plane.

$$(\sigma_1 - \sigma_3)_m = \frac{1.5\pi d_0 \sqrt{M_s f d_0 \delta}}{A_c} \quad [5.21]$$

where f is the unit friction between the membrane and the sample (Eq.[5.22]), calculated as a product of the minor effective stress and the tangent of the angle of shear resistance of the soil ϕ'(La Rochelle, 1967) and a strain δ is described by Eq.[5.23]

$$f = \sigma_3' \tan\phi' \quad [5.22]$$

$$\delta = \delta_e \frac{\varepsilon_a - \varepsilon_{peak}}{\varepsilon_e - \varepsilon_{peak}} \quad [5.23]$$

where δ_e is the strain due to the movement along the shear plane as measured after the test and calculated as follows:

$$\delta_e = \frac{\Delta h_p}{h_0} = \frac{\Delta d \tan\alpha}{h_0} \quad [5.24]$$

with the displacements Δh_p, Δd and angle α sketched in Figure 5.5b.

Head (1998) suggests an additional correction to be applied to the deviatoric strain to allow for the restraint imposed by the vertical side drains. The magnitude of the filter paper correction increases quickly with strain up to 2% strain, remaining constant for larger strains, and is inversely proportional to the diameter of the sample. For the 38mm samples, the maximum **side drain correction** to be deducted from the measured deviatoric stress is of 10 kPa (BS 1377-8:1990). It is applied linearly from zero with increasing strain up to 2% strain, remaining at 10 kPa thereafter.

5.4 Measurement of thermal properties

5.4.1 Theoretical background

The needle techniques for the measurement of thermal properties are based on the analytical solution of Carslaw and Jaeger (1959) for radial conduction from an infinite line heat source, in an infinite homogenous medium at a uniform initial temperature. For a heating period of duration t_0, the temperature rise at any radius from the line heat source is given by Equations [5.25] and [5.26] (for any time $t \leq t_0$ and $t > t_0$ respectively),

$$\Delta T(r,t) = -\frac{Q}{4\pi\lambda} Ei\left(\frac{-r^2}{4\kappa t}\right) \qquad [5.25]$$

$$\Delta T(r,t) = -\frac{Q}{4\pi\lambda}\left[-Ei\left(\frac{-r^2}{4\kappa t}\right) + Ei\left(\frac{-r^2}{4\kappa(t-t_0)}\right)\right] \qquad [5.26]$$

where λ is the thermal conductivity (W/(mK)) (and may be substituted by $\kappa \cdot (c\rho)$), κ is the thermal diffusivity (m^2/s), the product $(c\rho)$ is the volumetric heat capacity ($J/(m^3K)$), and Ei is the exponential integral, a special function on the complex plane, defined as one particular definite integral of the ratio of an exponential function and its argument (Eq.[5.27])

$$Ei(x) = -\int_{-x}^{\infty} \frac{e^{-u}}{u} du$$
$$Ei\left(\frac{-r^2}{4\kappa t}\right) = -\int_{\frac{r^2}{4\kappa t}}^{\infty} \frac{e^{-u}}{u} du \qquad [5.27]$$

The heat input Q (W/m) is computed using Eq.[5.28], taking into account the resistance R (Ω) and length L (m) of the heating element and the current I (A) flowing through it.

$$Q = \frac{I^2 R}{L} \qquad [5.28]$$

Equations [5.25] and [5.26] cannot be solved explicitly for both the conductivity and diffusivity, so a non-linear least-squares inversion method or, if adequate, a simplified analysis must be

used. Moreover, the needles are neither infinitely thin nor long as the idealised line heat source, but have instead finite dimensions (diameter and length), as well as heat capacity and contact resistance between the soil and themselves. Consequently, the conductivity and diffusivity terms in such equations may not correspond to the actual diffusivity and conductivity of the soil and calibration tests in materials with known properties are essential (ASTM, 2014). These issues are discussed in the subsequent sections for the different types of needles used.

5.4.2 Single needle test

The thermal conductivity of soils can be measured using a needle probe with a large length to diameter ratio to simulate the conditions of an infinitely long and thin heating source. A known current and voltage are applied to a heating element of known resistance and the temperature rise with time is recorded, as well as the temperature decay after termination of heating. The thermal conductivity is then determined from an analysis of the heating and cooling temperature time data series, based on the analytical line heat source solution (ASTM, 2014).

For large values of time, the exponential integral described in Eq.[5.27] may be approximated by the series expansion (Abramowitz and Stegun, 1972) shown in Eq.[5.29],

$$\begin{aligned} Ei(x) &= \gamma + \ln|x| + \sum_{n=1}^{\infty} \frac{x^n}{nn!} \\ Ei\left(\frac{-r^2}{4\kappa t}\right) &= \ln\left(\frac{r^2}{4\kappa t}\right) - \frac{r^2}{4\kappa t} + \frac{r^4}{64\kappa^2 t^2} - \frac{r^6}{1152\kappa^3 t^3} + \ldots + \gamma \end{aligned} \qquad [5.29]$$

where γ is the Euler-Mascheroni's constant (=0.577216…).

By neglecting all terms of the order of $1/t$ and higher in Eq.[5.29], separating the logarithm and substituting into Eq.[5.25], Eq. [5.30] is obtained.

$$\Delta T(r,t) \cong \frac{Q}{4\pi\lambda}\left[\ln t + \ln\left(\frac{4\kappa}{r^2}\right) - \gamma\right] \qquad [5.30]$$

It follows from Eq.[5.30], that for all cases, the curve of temperature rise against the logarithm of time reaches a linear asymptote. The temperature in the needle is then approximated by Eq.[5.31], and Eq.[5.32] for the cooling part.

$$\Delta T(t) \cong \frac{Q}{4\pi\lambda} \ln t \qquad [5.31]$$

$$\Delta T(t) \cong \frac{Q}{4\pi\lambda} \ln\left(\frac{t}{t - t_0}\right) \qquad [5.32]$$

Once the linear region is identified from the temperature-log time plots described by the previous two equations and its slope S is calculated, the thermal conductivity can be determined for both the heating and cooling parts of the test, by applying the following expression (Eq.[5.33]):

$$\lambda = \frac{Q}{4\pi S} \qquad [5.33]$$

A typical test, considering just the initial heating part, is schematised in Figure 5.9, showing Wechsler (1966) identification of three different regions in the temperature-time data series. Region A corresponds to the initial part of the test and is dominated by initial lag effects. Region B represents the linear temperature-log time region which should be used for the calculation of the thermal conductivity, while Region C corresponds to the portion of data which is dominated by edge and end effects. The magnitude of the initial lag effects is controlled by the probe geometry, the thermal properties of the needle and the surrounding medium, and the contact resistance (Farouki, 1981). Similar initial lag effects are observed in the initial part of the cooling data, while its final part, at times greater than the equivalent heating duration, may be significantly affected by the changes in temperature in the laboratory.

Another important aspect to discuss is the sample size effect, since the medium is not infinite as the theoretical solution assumes. The sample should be of at least the same length as the length of the needle, although larger samples are recommended (ASTM, 2014), at least 20% longer than the probe. Heat will flow radially away from the probe but, depending on the

conditions at the boundary, it may be reflected or absorbed, therefore influencing the rate at which temperature rises in the probe (Wechsler, 1966). The radius of the finite soil sample, R_S, should be large enough so that the heat that reaches its boundary is insignificant compared to the heat input. Wechsler (1966) states that the following criteria (Eq.[5.34]) needs to be met:

$$\exp\left(-\frac{R_s^{\,2}}{4\kappa t_0}\right) < 0.02 \qquad [5.34]$$

The minimum required radius of the soil sample does not depend on the geometry of the probe, but on the thermal diffusivity of the soil and the duration of the heating part of the test. The effects of a long heating time and a small radius manifest themselves in the form of a change in slope of the temperature – log time curve (Mitchell and Kao, 1978). For a typical diffusivity of saturated clays and silts of 0.056 m^2/day (Gale, 2005) and a sample radius of 35 mm, which corresponds to the smallest sample tested in this thesis, Figure 5.10 shows that a heating of 100 s is appropriate, as it maximises the heating period without exceeding the limit presented by Eq.[5.34]. This is taken as the standard heating time for the tests in this thesis.

Another important potential source of error, specific to unsaturated materials, is moisture migration, as redistribution of water during the measurement caused by the thermal gradients in the material. To prevent issues related to surface evaporation and drying during the tests, the sample is wrapped in cling film for the duration of the testing.

Before its use in the testing programme on London clay samples, the thermal needle probe apparatus needed to be calibrated by comparing the experimental measurement of the thermal conductivity of standard materials to their known values. A calibration factor, C_f, can then be obtained as shown in Eq.[5.35], which is the ratio of the conductivity measured in the experiment to the real known value.

$$C_f = \frac{\lambda_{measured}}{\lambda_{real}} \qquad [5.35]$$

All subsequent measurements are then multiplied by the calibration factor, C_f, which is unique for each single needle used. Hanson et al. (2004) showed that the calibration factor is a function of thermal conductivity when large diameter needles (>2.54 mm) are used, and that in such cases it would be necessary to determine C_f at various thermal conductivities, covering the range of measurement. This is however not necessary in this case as the needle diameter is small (1.27 mm). Instead, two standard calibration materials were chosen: glycerine (glycerol) and water-agar mixture, and the results of the calibration tests are summarised in Table 5.5.

In order to prevent convection, water can be stabilised by adding agar powder (5 g/L) when boiling to form a water-agar jelly with the same thermal properties as those of pure water (λ=0.607 W/(mK) at 25 °C). A total of seven calibration tests were performed on water-agar jellies, showing an average thermal conductivity of 0.674 W/(mK), taking into account the conductivities obtained during heating and cooling for all tests. The ratio between the measured and known (real) values of thermal conductivity is 1.11, defined as the calibration factor. An example of the calibration tests performed on the water-agar jelly is shown in Figure 5.11. The temperature of the needle is constantly monitored for 15 min (Figure 5.11a), at the start of which a constant power of 6.7 W/m is applied for 100 s (Figure 5.11b). The resulting temperature rise and decay in the needle is plotted against time in a logarithmic scale and the linear regions are identified for both the heating and cooling data in order to calculate the conductivity (Figure 5.11c).

An additional material, anhydrous glycerine (λ =0.286 W/(mK) at 25 °C) was used to verify the calibration factor obtained using the water-agar mix. Since glycerine is a fluid, and therefore subjected to free convection, arising from density gradients created by the thermal gradients in the fluid the temperature rise in the needle needed to be limited to values less than 2 °C, by reducing the current and heating duration, to avoid significant convection effects (ASTM, 2014). The average thermal conductivity of the seven tests performed, λ =0.319 W/(mK), gives a calibration factor of 1.115, nearly identical to the one obtained with water-agar. This result

therefore confirms the magnitude of the calibration factor, which was then applied to all single needle measurements in this thesis.

5.4.3 Dual-probe heat-pulse test

The thermal conductivity, heat capacity and thermal diffusivity can all be determined by a dual-probe heat-pulse test. As for the single needle, the geometry of the heating probe aims to simulate a line source. However, the temperature rise is now monitored in a second needle at a distance r, instead of in the heating needle itself, as in the case of the single needle test.

The interpretation of the test data is also based on the analytical solution for radial heat conduction from an infinite line heat source in an infinite homogeneous medium at a uniform initial temperature presented in Eq.[5.26]. By taking the derivative of Eq.[5.26] with respect to time, setting the result equal to zero, which describes the time instant, t_m, where the temperature rise at a known radial distance r from the heat source (in this case, the probe spacing) is a maximum, T_m, and performing some re-arrangement, an expression for the diffusivity κ can be obtained:

$$\kappa = \frac{r^2}{4}\left[\frac{\frac{1}{t_m - t_0} - \frac{1}{t_m}}{\ln\left(\frac{t_m}{t_m - t_0}\right)}\right] \qquad [5.36]$$

where t_0 is the duration of the initial heat pulse.

Once the diffusivity has been determined, it can be re-inserted in [5.26], for the time of the temperature maximum in order to obtain the heat capacity $c\rho$:

$$c\rho = \frac{Q}{4\pi\kappa T_m}\left[Ei\left(\frac{-r^2}{4\kappa\left(t_m - t_0\right)}\right) - Ei\left(\frac{-r^2}{4\kappa t_m}\right)\right] \qquad [5.37]$$

And finally, the thermal conductivity λ is given by the product of the two other properties

$$\lambda = \kappa * (c\rho) \qquad [5.38]$$

This method of extracting the thermal properties from the temperature maximum has been referred to in the literature as the "single-point method" (Bristow et al., 1995) and is illustrated using as an example a test performed during this research project in Figure 5.12. A constant power Q (112.5 W/m) is applied for a heating duration t_0 (8 s) in the heating needle (Figure 5.12a) and the temperature rise is measured in the monitoring needle at a distance r (6 mm) from the heat source, in order to identify the time t_m and magnitude T_m of the temperature peak (Figure 5.12b).

a) Measurement error evaluation in the single-point method

Given the inter-dependency of the expressions used for estimating the properties, a measurement error analysis is important to understand how an error in the estimation of the diffusivity (Eq.[5.36]) and later in the heat capacity (Eq.[5.37]) is brought forward to the determination of the thermal conductivity. There are five different sources of experimental error: the inter-probe spacing r, the duration of the heat-pulse t_0, the time t_m and magnitude T_m of the temperature peak, and the heating power Q. The relative errors in the estimation of the three thermal properties are analysed in detail in Figure 5.13 from the relative errors in each of the possible measurement errors using computer-generated temperature time series from Eq. [5.26], assuming r=6 mm, t_0=8 seconds, Q=112.5 W/m (testing conditions of the probe used in this thesis as described in section 3.4), and a soil thermal diffusivity of κ=0.056 m^2/day and conductivity of λ=1.67 W/(mK) (usual values for a saturated clay).

The estimated thermal diffusivity κ (Figure 5.13a) is seen to be independent of measurement errors of the heat input Q and maximum temperature T_m, however, greatly influenced by the error in the inter-probe spacing r and to a lesser extent by the time measurements t_m and t_0, which result in errors of opposite sign. A positive 5% relative error in the spacing, which is just +0.3 mm in absolute terms for the needle used in this thesis, would lead to approximately a 10% overestimation of the thermal diffusivity. The estimated volumetric heat capacity $c\rho$ (Figure 5.13b) is again greatly affected by the error in the inter-probe spacing, although in the opposite direction as in the case of the diffusivity. A similar effect, but of a smaller magnitude,

is caused by an error in the measurement of the maximum temperature, while the opposite effect is caused by errors in the heat-pulse time and heating power. On the other hand, the measurement of the heat capacity is practically independent of errors in the time measurement of the temperature peak.

The opposite effect of the relative error in the probe spacing in the diffusivity and heat capacity makes the estimation of the thermal conductivity independent of it, as shown in Figure 5.13b. Positive relative errors in the measurements of the heating time and the heat input would lead to an overestimation of the thermal conductivity, while positive errors in the measurements of the time and magnitude of the temperature would lead to an underestimation by similar magnitude.

Given that the parameter with the most likely error in the experiments is the probe spacing, as the needles may bend when inserted in the soil; the thermal conductivity seems to be the thermal property measured with the most confidence. The remaining four errors are all below 1% in relative magnitude. The heat input may be affected by errors in the values of the resistors in the system (heater and precision resistor in the constant current circuit) and in the voltage readings of the data logger. The error in the measurement of the temperature may come from the calibration of the thermistor, the voltage reading in the data logger and the accuracy of the divider resistor. The time measurements may be offset by a maximum of 0.2 s (absolute error), which is half of the data acquisition frequency of the system, while the duration of the heat pulse is controlled by the micro-processor and has an error of less than 0.1 s in absolute terms.

b) Comparison with other methods and calibration

A downfall of the single-point method is that a clear, “true” temperature peak (Figure 5.12b) may not always be observed, leading to errors in the calculation of all properties, in the cases of a stationary peak or noise in the measurement around peak. Bristow et al. (1995) presented a different approach in which a greater part of the time series was considered, instead of the peak only. It involves a nonlinear regression analysis, fitting Eq.[5.26] to the experimental data

optimizing for the parameters κ and $c\rho$. Given the nature of Eq.[5.26], Bristow et al. (1995) recommend the use of the Levenberg-Marquart fitting algorithm for this least squares curve fitting problem.

The average results obtained by the two different methods (single-point and nonlinear ffit) were compared during an initial set of seven tests on water-agar, prepared to the same specifications as for the single needle calibration tests, and are shown in Table 5.6. Three analyses were performed: a) using the single-point method, b) nonlinear fit of 300 s of experiment to include most of the temperature decay and c) nonlinear fit of the area around peak only, including the data set points which obey $\Delta T(t) \geq 0.75T_m$. On average, the results obtained using the single-point method and the nonlinear fit around peak only are very similar and more accurate than the nonlinear fit which include 300 seconds of experimental data. The errors relative to each of the known thermal properties of water (IAPWS-97), given in the last column in Table 5.6, are small in magnitude overall and have the same sign for the three different types of analyses. The diffusivity is overestimated by 5.56% in the case of the nonlinear fit around peak, 5.90% in the case of the single-point method and 7.76% in the case of the broader nonlinear fit. The heat capacity is underestimated by 2.24% in the case of the broad nonlinear fit, 2.26% in the case of the nonlinear fit around peak and 2.57% for the single-point method. Finally, the thermal conductivity is overestimated by 3.13% in both the single-point method and the nonlinear fit around peak and by 5.44% for the broader nonlinear fit. For all cases, the nonlinear fit around peak gives more satisfactory results, however the difference in the error compared to the single-point method is not bigger than 0.5%, despite the greater computational effort required. Figure 5.14 shows the temperature rise after the heat-pulse in one of the calibration tests, together with temperature-time curves generated using Eq.[5.26] with the measured thermal properties from each of the three analyses. The nonlinear fit around peak gives a very good approximation for the experimental data in such area, while the single-point method seems the worse approximation to the data, just capturing well the temperature maximum. The broader nonlinear fit is more controlled by data long after the peak, which is

the part used for the thermal properties and may be affected by temperature drifts in the laboratory. This also explains why the error in Table 5.6 is greater for this method of analysis. Both the nonlinear fit of the data points which obey $\Delta T(t) \geq 0.75T_m$ and the simpler single-point method are adopted for the analysis of the data in this Thesis.

Given the small magnitude of the errors observed during this test, the dependency between the different variables when obtaining the thermal properties, their individual different contribution to the global measurement error, and the very likely different error in the real probe spacing between samples when testing stiffer materials, it is not considered adequate here to apply a straight-forward single calibration factor as for the single needle test and unfactored properties will be reported in this thesis for dual-probe heat-pulse tests.

c) Further discussion of the underlying assumption of the method

Apart from the measurement error, it is also necessary to consider the model error as the dimensions of the heating probe (30 mm length, 0.9 mm diameter), significantly shorter than the one for the single needle test, may not be described as an “infinite line”. Kluitenberg et al. (1995) presented an analytical solution for radial conduction after a short heat-pulse away from a finite cylinder of radius a and half-length b, incorporating more rigorously aspects of the dual-probe as illustrated in Figure 5.15. The temperature rise ΔT at a radial distance r from the z-axis and at a time t in the plane $z = 0$, for a heater coincident with the z axis between $z = b$ and $z = -b$ is given by:

$$\Delta T(r,t) = \frac{Q}{4\pi\lambda} \int_{\frac{r^2}{4\kappa t}}^{\frac{r^2}{4\kappa(t-t_0)}} u^{-1} \exp(-u) \exp\left[-\left(\frac{a}{r}\right)^2 u\right] I_0\left(\frac{2au}{r}\right) erf\left(\frac{b}{r}\sqrt{u}\right) du \qquad [5.39]$$

, where $I_0(x)$ represents a modified Bessel function of order zero and $\mathrm{erf}(x)$ represents the error function.

When the limit of a/r approaches zero, the exponential term containing it and the modified Bessel function both tend to unity, and the model describes a finite line heat source. Similarly,

when the limit of b/r approaches infinity, the error function approaches unity and the model describes an infinitely long cylindrical heat source. When both a/r approaches zero and b/r tends to infinity, the model of Eq.[5.39] simplifies to the infinite line heat source of Eq.[5.26].

The relative error of the infinite line heat source model compared to the finite cylindrical heat source model is analysed in Figure 5.16, which considers different finite geometries in terms of the dimensionless ratios a/r and b/r. Temperature-time series were generated using Eq.[5.39] (finite cylindrical heat source) for the thermal properties of a typical saturated clay and standard testing conditions previously described for different dual-probe geometries. The thermal properties were then extracted by locating the temperature maximum and using the infinite line heat source single-point method, and were then compared to the "known" values used to create the data series.

The infinite line heat source model causes an overestimation of both the thermal diffusivity and conductivity (Figure 5.16a,c), increasing significantly for probe geometries of short length, less than four times the inter-probe spacing ($b/r < 2$). Increasing the b/r above 2.5 and reducing the a/r below 0.1 do not produce much improvement in the model errors, relatively small for such range of probe geometries. The infinite line model causes a negligible model error of less than 0.1% in the estimation of the heat capacity for probes of dimensions $a/r < 0.2$ and $b/r < 2.5$ (Figure 5.16b). While the probe design should take into account the model error caused by the deviation from the infinite line assumption, there are also practical restrictions on the other end of the design. Thin and long probes, in addition to manufacturing issues, would present serious difficulties when testing most materials, including soil samples, in order to avoid bending of the probes, resulting in the critical error in the assumed r spacing between the two probes. As explained earlier, this parameter alone can lead to very large errors in the estimation of the thermal properties (Figure 5.13), much greater than the model errors of slightly thicker, shorter and stockier probes. For the dimensions of the current probe $a/r = 0.45/6 = 0.075$ and $b/r = 15/6 = 2.5$, the relative model errors in the estimation of the

thermal diffusivity, heat capacity and thermal conductivity are +1.04%, +0.05% and +1.09% respectively.

It is worth noting that not even the finite cylindrical heat source model is a perfect model for the dual-probe heat-pulse tests, as it only physically approximates the heating probe, which consists of several strands of heating wires accommodated within the stainless steel needle with epoxy filler, as a cylinder producing a constant heat source assuming infinite conductivity and zero heat capacity of its physical constituents. None of the models consider the contact resistance between soil and the needle and both assume an exact temperature measurement in the sensing probe.

Figure 5.17 shows the temperature-time series generated for the current probe's geometry and testing conditions, assuming the thermal properties of typical saturated clay. Very little difference can be seen between the predictions of the two models during the initial part of the simulated test. Both models predict a very similar temperature rise, peak, and initial decay; however they diverge for the late part of the temperature decay, with the cylindrical finite heat source model predicting a faster drop. The differences at longer times in the temperature-time series do not manifest themselves in the estimation of the thermal properties since they are calculated with the data around the peak. Given the complexity of this alternative model, the small differences obtained and the common assumptions of both models, the use of the infinite line heat source model is considered satisfactory and adequate for this thesis.

5.5 Thermal properties tests

5.5.1 Sample preparation and testing schedule

For the investigation of the thermal properties of London clay, two different types of samples are considered: reconstituted samples (V&A site) and intact samples (Hyde Park borehole). The slurry of remoulded material from the V&A Museum site was consolidated to various vertical stresses to produce saturated samples of different porosities, while the samples from the Hyde Park were tested in their intact form. Table 5.7 summarises the testing schedule

together with the initial conditions of soil samples. In total, six reconstituted samples with porosities from 0.435 to 0.619 and water contents from 0.278 to 0.586, and seven intact samples with porosities from 0.398 to 0.422 and water contents from 0.239 and 0.307 were tested.

The testing schedule aims to a) measure the thermal properties of London clay using different needle techniques and compare the results, b) compare the results of intact and reconstituted material, together with the predictions of thermal conductivity models and c) investigate the factors affecting the thermal properties of the soil. For the latter, a wide range of densities, water contents and porosities, as well as the direction of measurement, are considered.

5.5.2 Testing procedure

Before testing, reconstituted and intact samples were slightly trimmed to a cylindrical shape radially and longitudinally to remove the slightly drier outer surface. Some sections of the curved sides were trimmed further to create a flat surface in order to ensure a good contact between the soil and the full-length of the needle when inserted, as shown in Figure 5.18a. The samples were then wrapped in cling film to prevent loss of moisture during the test, which was performed inside a closed container to minimise the effect of the daily temperature fluctuations in the laboratory. As shown in Figure 5.18b, both needles, coated with a thin layer of highly conductive thermal grease to ensure good contact between the sample and the probe, were inserted and the temperature was monitored for several hours until temperature equilibration of the sample in the testing environment was achieved. This process lasted usually for 2 to 3 hours. In stiff samples, pre-drilling with a dummy needle of a slightly smaller diameter was necessary before inserting the probes.

Each test started by running the relevant data recording script written in MATLAB, presented in section 3.4. In the case of the single needle test, the heater switch was manually operated and the heating time was monitored using a stopwatch. A constant current of a magnitude between 65-70 mA was set for heating, producing a heat source of approximately 5-6 W/m

and the chosen duration of heating for all tests was 100 seconds. In the case of the dual-probe heat-pulse test, a current of approximately 300 mA was set, producing a heat source of approximately 115 W/m. After data recording started, the micro-controller was energised, which was initially programmed to pause for 10 seconds, while the switch was manually turned to the “automatic control” position. After this, the micro-controller would drive a relay to perform the switching action of the heater for the programmed exact 8 seconds of heat-pulse duration. In both cases, data was continuously recorded for 20 minutes at a frequency of approximately 2.22 readings per second, which corresponded to the zero delay option between readings in the script. This 20 minute period allowed the temperature in the sample to equalize again, after which the latest probe used was inserted in a new location bringing it back in equilibrium with the sample, while the other probe was being used. This sequence was systematically repeated until all target locations in the sample were tested.

Several locations in each sample were chosen for testing, inserting the needles perpendicularly to the surface of the specimen. As shown in Figure 5.19, in order to study any anisotropy in the thermal properties, two heat source directions were considered: a) vertical line heat source, which creates a heat flow parallel to the horizontal plane and b) horizontal line heat source, which creates a heat flow parallel to the vertical plane perpendicular to the needle. For case b), the monitoring needle in the case of the dual-probe heat-pulse test was oriented at 0, 45 and 90 º from the heat source relative to the horizontal plane.

In total a minimum of five tests for each type of needle were aimed to be performed as a vertical line heat source in each sample, plus an additional minimum of five for the single needle as a horizontal heat source and of three for the dual-probe as a horizontal heat source for each of the three orientations presented in Figure 5.19b.

Once all tests were performed, the water content of the sample was measured by sampling sections at various places of the specimen. The remaining parts of the sample were kept in order to perform the classification tests described in section 4.5. Figure 5.18c shows a section through the sample at the end of testing, clearly showing the holes created by the probe and

the issues with the interprobe spacing (non-parallel, bent probes) which are discussed in detail in Chapter 7.

5.5.3 Analysis of the data

The individual datasets, which include arrays of time, current, temperature and power data, were then post-processed using separate MATLAB routines for single needle tests and dual-probe heat-pulse tests. The first part of the data post-processing is common for both types of tests and involves identifying the period of heating in order to establish starting time of the experiment. Once a sudden jump in the power data array is seen, the time between such data reading and the precedent is taken as the zero time. The same process applies for the determination of the end of heating, which manifest itself in the form of a sudden drop in the recorded power in the following data entry. Since the gap between readings is always of 0.45 s, the maximum absolute error in the determination of the time measurement is less than 0.225 s.

For the single needle test, the initial one third of the heating and cooling phases of the temperature-log time data are deleted since they are affected by initial lag errors, as previously discussed (corresponding to Region A in Figure 5.9). Moreover, the later stages of cooling, at times greater than the duration of heating are also removed. Using the remaining data for both heating and cooling phases, the linear parts of the temperature-logtime plots were identified and their respective slopes calculated in order to estimate the thermal conductivities using Eq.[5.33]. The gradients were determined by a linear regression analysis using datapoints evenly spaced in logarithmic time, in order to remove any bias that the analysis would have had from having points very close together at the end of the line due to the logarithmic scale. The thermal conductivities were then corrected by dividing them by the calibration factor obtained during the calibration tests on water-agar and glycerol.

For the dual-probe heat-pulse needle, the time and magnitude of the temperature maximum are identified in the recorded data and used for the calculation of the thermal properties using

Equations [5.36], [5.37] and [5.38]. In the case where multiple identical values of temperature maximum are present in the data, the time at maximum is taken as an average of all the data points where the temperature is a maximum. Additionally, the thermal properties are also calculated for each experiment by fitting the portion of the data that obeys $\Delta T(t) \geq 0.75T_m$ to the linear heat source analytical solution and solving for the thermal diffusivity and heat capacity, which are the parameters optimised in the fitting procedure. The Levenberg-Marquardt algorithm is chosen for this least squares curve fitting problem, giving as the starting guess in the fitting routine the values of diffusivity and heat capacity obtained using the single-point method, which are close to the expected solution.

5.6 Summary

This chapter presents the testing methodology and programmes for the investigation of the thermo-mechanical behaviour and thermal properties of London clay:

- Initially, the measurement of thermal strains is discussed and the use of the Campanella and Mitchell framework is considered for this thesis. Discrepancies in the published literature on the values used for the thermal expansion of water arising from the Baldi et al. (1888) expression are highlighted and a new expression for the thermal expansion coefficient of water as a function of temperature and pressure is presented based on the latest IAPWS formulation.
- A testing programme on reconstituted London clay is presented together with the testing and data analysis procedures. The programme aims to study the thermally induced volume changes during heating and cooling cycles and the influence of the temperature on the mechanical behaviour of the clay.
- The measurement of thermal properties using needle techniques is thoroughly investigated, discussing the overlaying theory, calibration and potential sources of errors.

- A testing programme to investigate the thermal properties of reconstituted and intact London clay samples is presented, together with the testing and data analysis procedures. It aims to compare the thermal properties, obtained using different needle techniques, of intact and reconstituted material, together with the predictions of thermal conductivity models and to investigate the factors, such as density, water content, porosity or the direction of measurement, affecting the thermal properties of the soil.

Table 5.1 *Coefficients and exponents for the calculation of Eq. [5.8] (IAPWS, 2007)*

i	I_i	J_i	n_i	i	I_i	J_i	n_i
1	0	-2	1.4632971213167E-01	18	2	3	-4.4141845330846E-06
2	0	-1	-8.4548187169114E-01	19	2	17	-7.2694996297594E-16
3	0	0	-3.7563603672040E+00	20	3	-4	-3.1679644845054E-05
4	0	1	3.3855169168385E+00	21	3	0	-2.8270797985312E-06
5	0	2	-9.5791963387872E-01	22	3	6	-8.5205128120103E-10
6	0	3	1.5772038513228E-01	23	4	-5	-2.2425281908000E-06
7	0	4	-1.6616417199501E-02	24	4	-2	-6.5171222895601E-07
8	0	5	8.1214629983568E-04	25	4	10	-1.4341729937924E-13
9	1	-9	2.8319080123804E-04	26	5	-8	-4.0516996860117E-07
10	1	-7	-6.0706301565874E-04	27	8	-11	-1.2734301741641E-09
11	1	-1	-1.8990068218419E-02	28	8	-6	-1.7424871230634E-10
12	1	0	-3.2529748770505E-02	29	21	-29	-6.8762131295531E-19
13	1	1	-2.1841717175414E-02	30	23	-31	1.4478307828521E-20
14	1	3	-5.2838357969930E-05	31	29	-38	2.6335781662795E-23
15	2	-3	-4.7184321073267E-04	32	30	-39	-1.1947622640071E-23
16	2	0	-3.0001780793026E-04	33	31	-40	1.8228094581404E-24
17	2	1	4.7661393906987E-05	34	32	-41	-9.3537087292458E-26

Table 5.2 *Coefficients of thermal expansion for different minerals (*10^{-6} ºC^{-1})*

Mineral	$\alpha_{s,v}$	$\alpha_{s,l1}$	$\alpha_{s,l2}$	Sources
Muscovite	24.8	17.8	3.5	McKinstry (1965)
Kaolinite	29	18.6	5.2	McKinstry (1965)
Serpentine	24	10.2	6.9	McKinstry (1965)
Chlorite	31.2	9	11.1	McKinstry (1965)
Smectite	39	--	--	Laloui and Di Donna (2013)
Illite	25	--	--	Laloui and Di Donna (2013)
Quartz	27.1	--	--	Fei (2013)
Albite	24.5	--	--	Fei (2013)
K-Feldspar	15.7	--	--	Fei (2013)
Pyrite	26.3	--	--	Fei (2013)
Calcite	69.5	--	--	Fei (2013)
Aragonite	62.1	--	--	Fei (2013)
Dolomite	23.3	--	--	Fei (2013)

Table 5.3 *Testing programme for the reference study at room temperature*

Sample	Isotropic consolidation/swelling		Undrained shearing
	p'_c (kPa)	OCR	
#nct1	150	1	
#nct2	300	1	
#nct3	300	1	
#nct4	350	1	
#oc2t1	300	2	
#oc6t1	300	6	
#oc6t2	300	6	

Table 5.4 *Testing programme for the thermo-mechanical tests*

	→→→→→Testing stages→→→→→						
Sample	**Isotropic consolidation/ swelling**		**Main Temperature history**	**Further loading up to**	**Further temperature changes**	**Undrained shearing**	**Duration**
	p'_c (kPa)	OCR	(ºC)	p' (kPa)	(ºC)		(days)
#ncht1	150	1	20-60-20	-	-	YES	60
#ncht2	300	1	20-60-20-60-20-70-20	-	-	YES	126
#oc4ht1	300	4	20-40	-	-	NO	55
#oc4ht2	300	4	20-40	350	40-60-20	YES	252
#oc4ht3	300	4	20-60	350	60-20	YES	277
#oc6ht1	300	6	20-40-20	--	-	YES	81
#oc6ht2	300	6	20-60-20	-	-	YES	105
#oc6ht3	300	6	20-40-20 x5	-	-	YES	176

Table 5.5 *Calibrations tests for the single needle test*

Material	λ_{ave} (W/(mK)) – (SD)	λ_{real} (W/(mK))	Calibration Factor – C_f
Water-agar @ 25 °C	0.674 (0.018)	0.607	1.110
Anhydrous glycerine @ 25 °C	0.319 (0.009)	0.286	1.115

Table 5.6 *Calibration tests for the dual-probe heat-pulse test on water-agar*

Thermal property *(error %)*	Single-point method	Nonlinear fit (all data)	Nonlinear fit (>0.75T_{max} only)	Real values @ 25 °C
Diffusivity κ – (m^2/s)	1.543E-07 *(+5.90%)*	1.570E-07 *(+7.76%)*	1.538E-07 *(+5.56%)*	1.457E-7
Heat capacity (cρ) – (kJ/(kg*m^3))	4062.7 *(-2.57%)*	4075.51 *(-2.26%)*	4067.9 *(-2.24%)*	4169.7
Conductivity λ – (W/(m*K))	0.626 *(+3.13%)*	0.640 *(+5.44%)*	0.626 *(+3.13%)*	0.607

Table 5.7 *Initial conditions of the samples tested for the study of the thermal properties*

Sample	n (porosity)	w (Water content)	ρ (Density) (Mg/m^3)
Reconstituted samples			
#V&At1	0.619	0.586	1.676
#V&At2	0.574	0.486	1.755
#V&At3	0.546	0.433	1.806
#V&At4	0.516	0.384	1.859
#V&At5	0.473	0.324	1.934
#V&At6	0.435	0.278	2.002
Intact samples (Hyde Park)			
#CS16	0.422	0.263	2.025
#CS18	0.414	0.254	2.043
#CS22	0.460	0.307	1.957
#CS30	0.402	0.243	2.059
#CS36	0.426	0.267	2.022
#CS44	0.407	0.247	2.054
#CS60	0.398	0.239	2.062

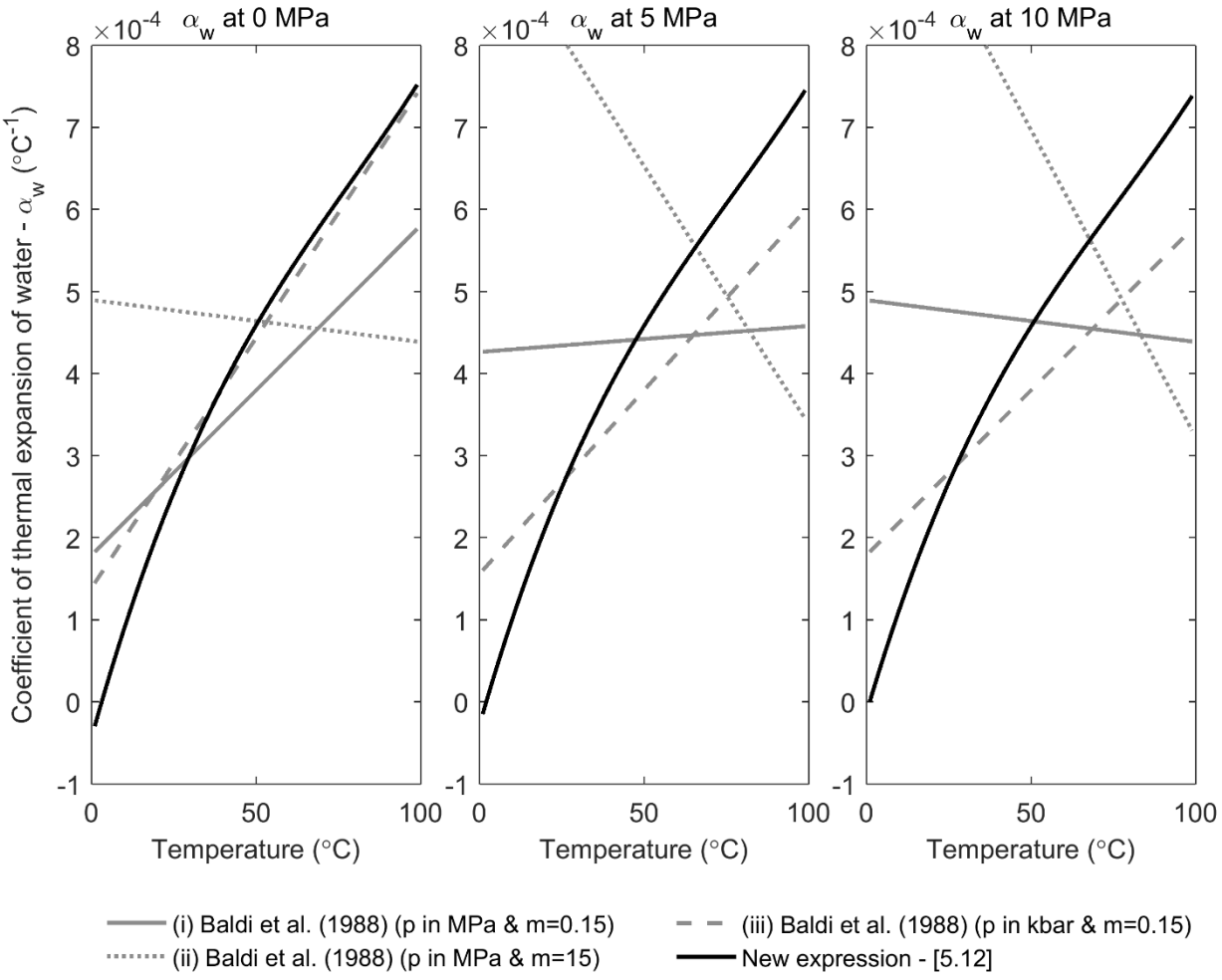

Figure 5.1 *Coefficient of thermal expansion of water at 0, 5 and 10 MPa according to the three scenarios for Baldi et al.(1988) and the new expression [5.12]*

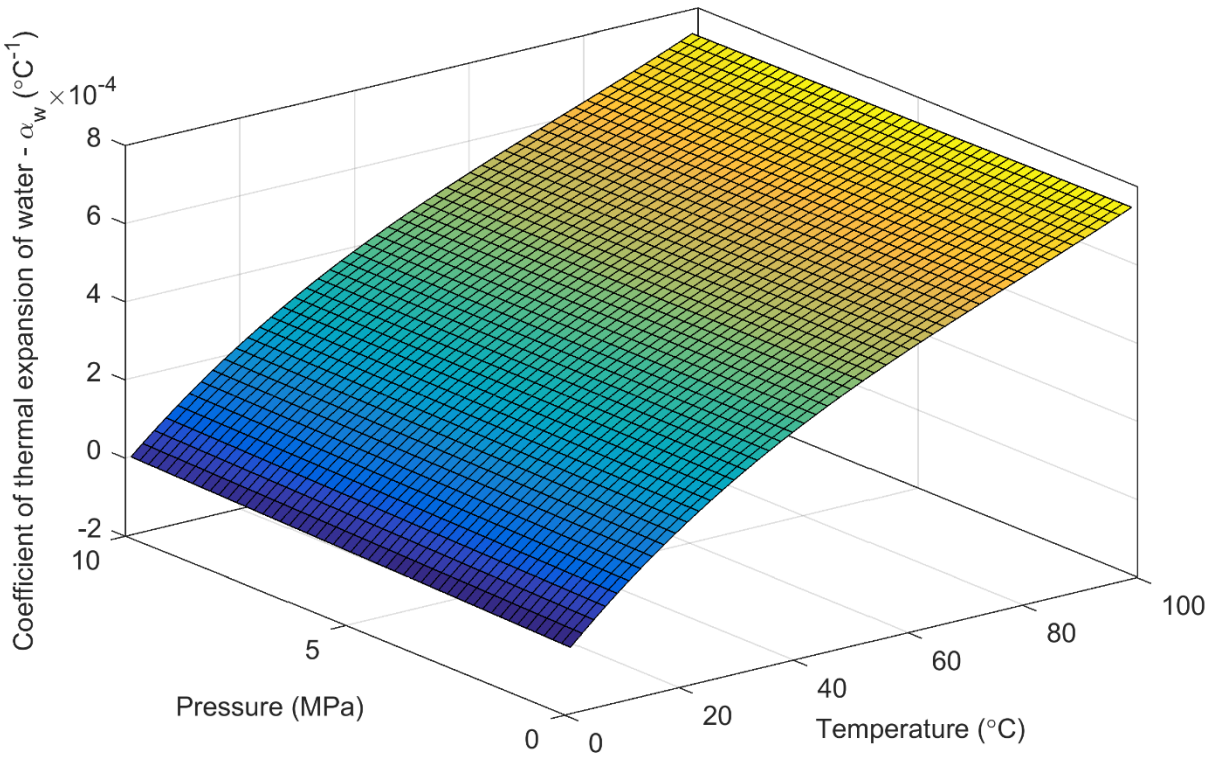

Figure 5.2 *Coefficient of thermal expansion as a function of temperature and pressure calculated using [5.12]*

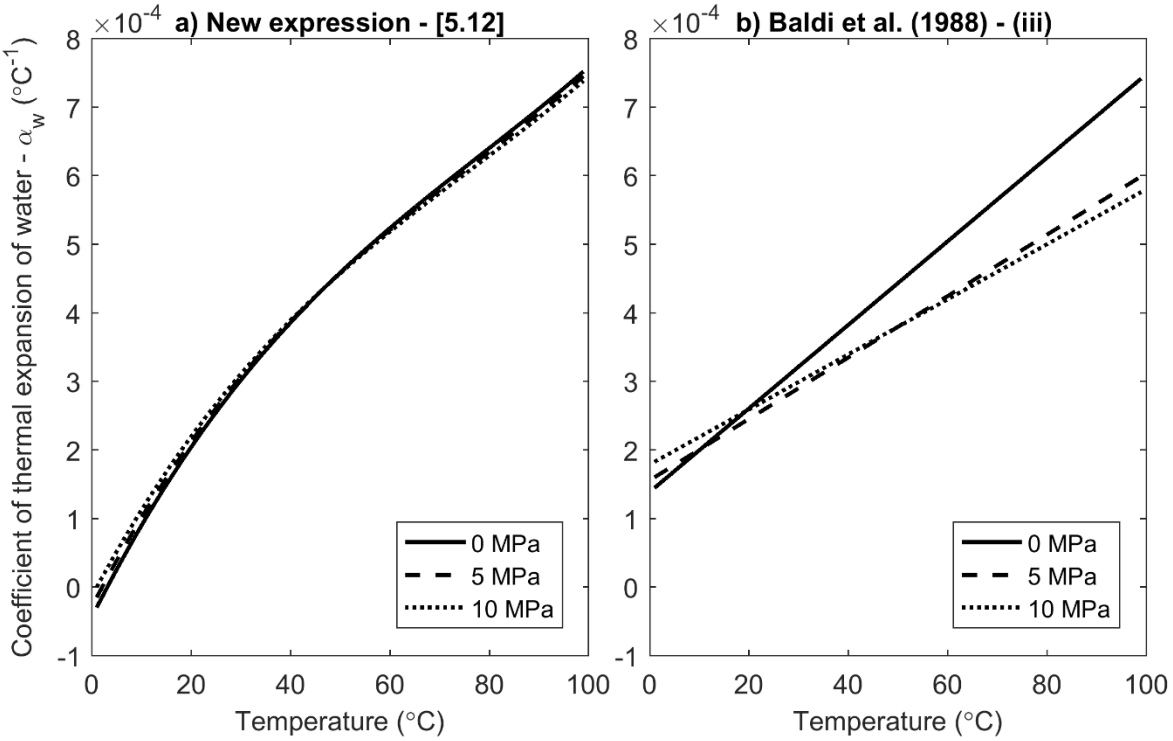

Figure 5.3 *Coefficient of thermal expansion of water at different pressure levels according to the new expression [5.12] and Baldi et al. (1988)*

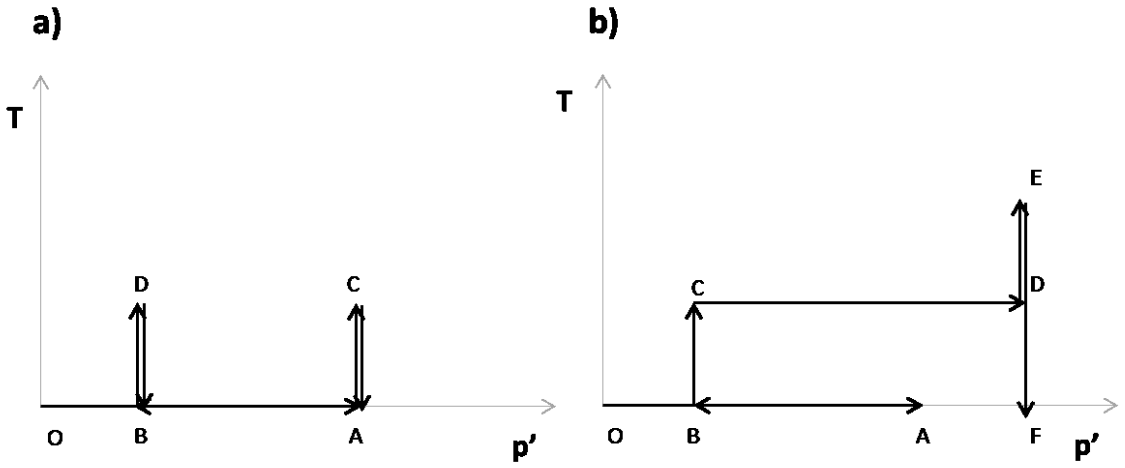

Figure 5.4 *Thermo-mechanical testing paths*

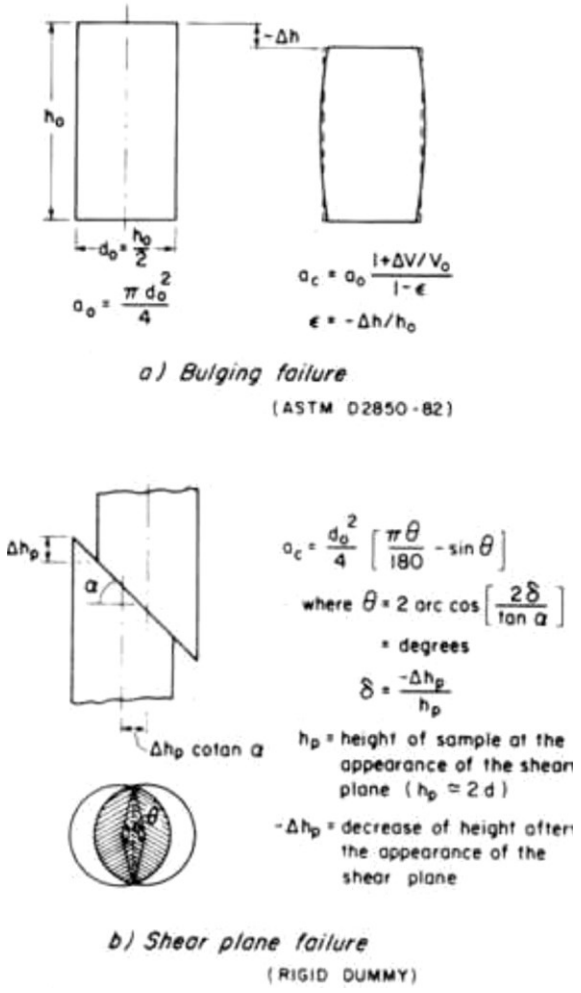

Figure 5.5 *Bulging and shear plane failures (La Rochelle et al., 1988)*

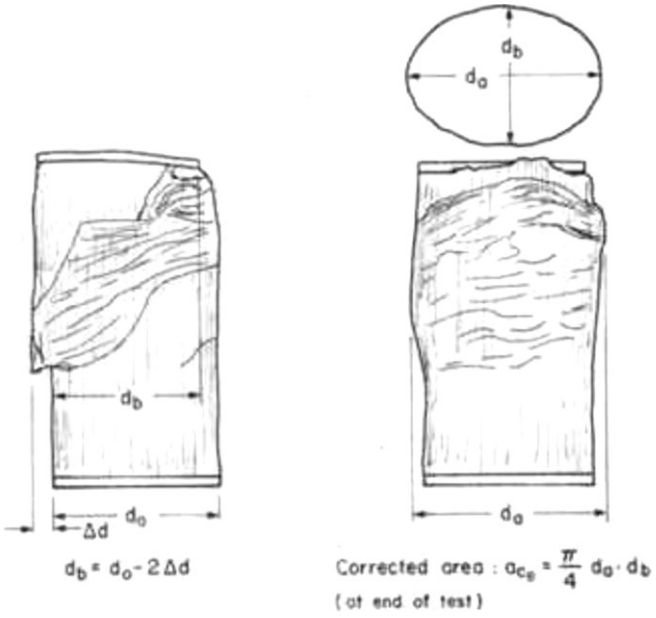

Figure 5.6 *Area correction at the end of test for combined bulging and shear plane failure (La Rochelle et al., 1988)*

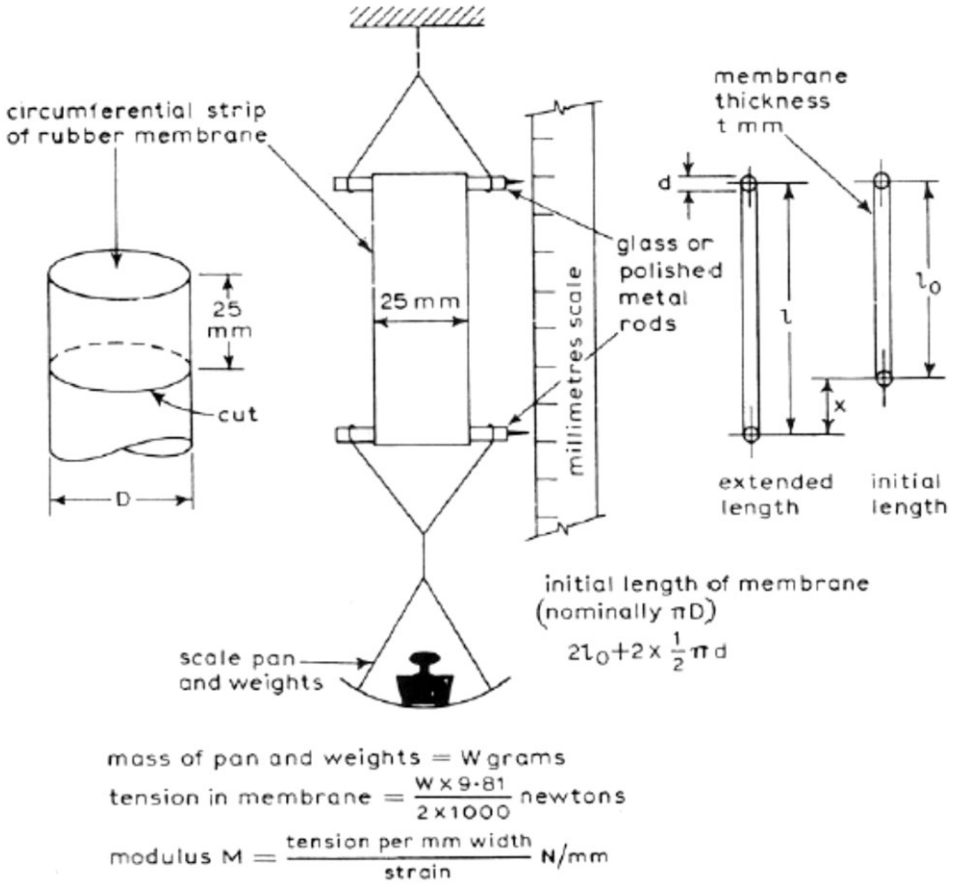

Figure 5.7 *Measurement of the elastic properties of the membrane (Head, 1992)*

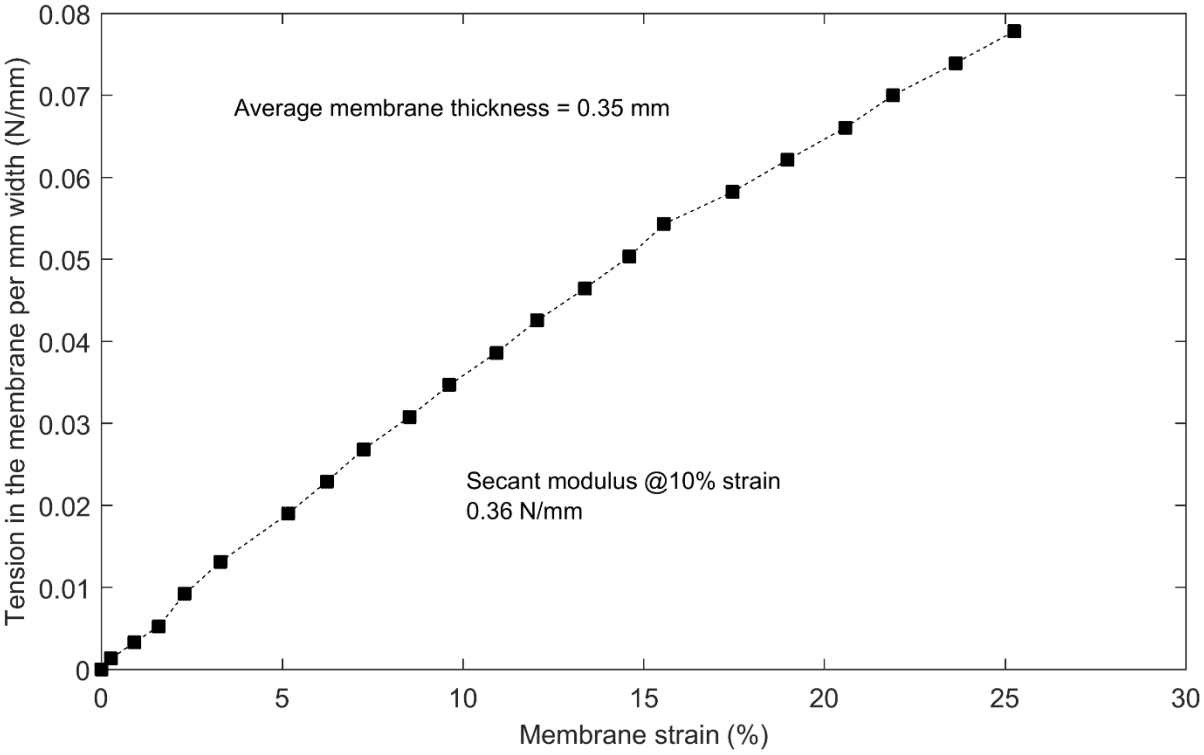

Figure 5.8 *Load-strain curve of a latex membrane*

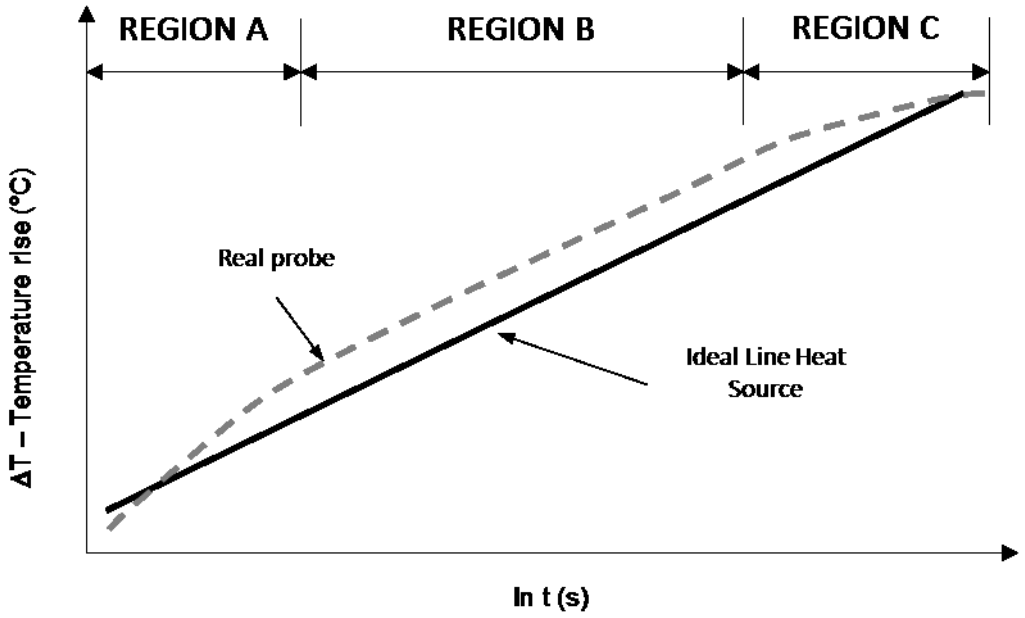

Figure 5.9 *Typical temperature log time profile for a probe (after Wechsler, 1966)*

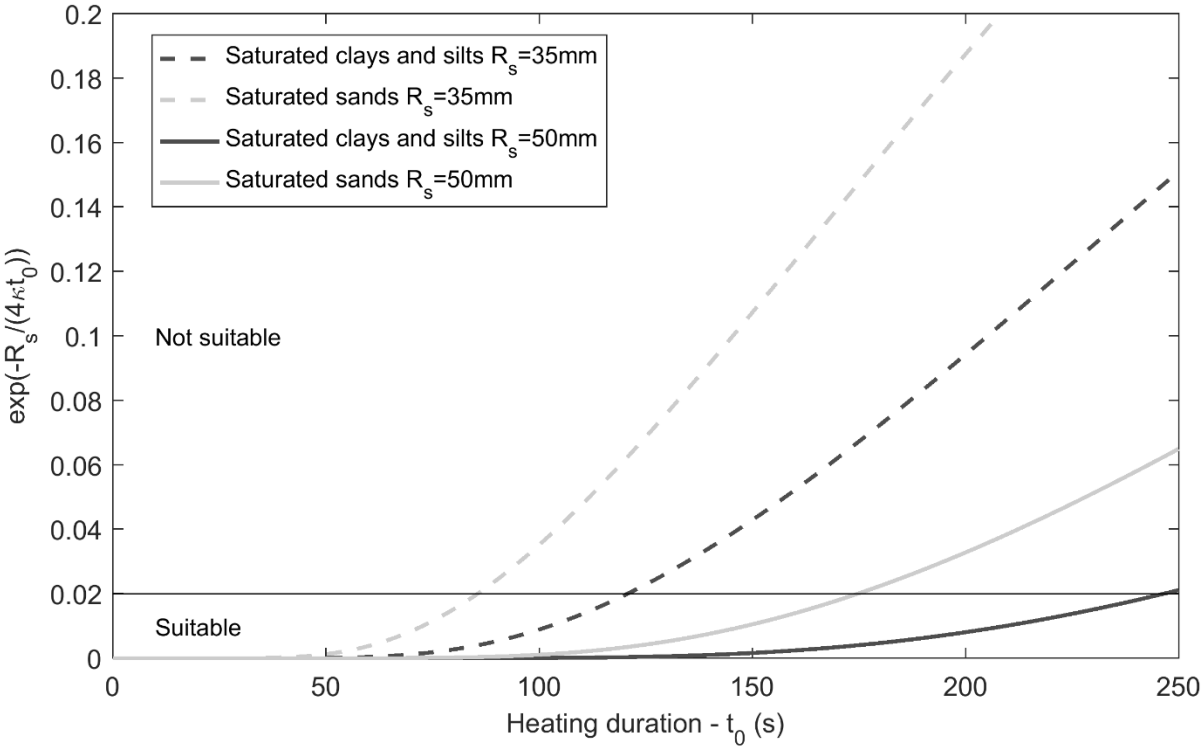

Figure 5.10 *Heating durations for different soil types and sample sizes.*

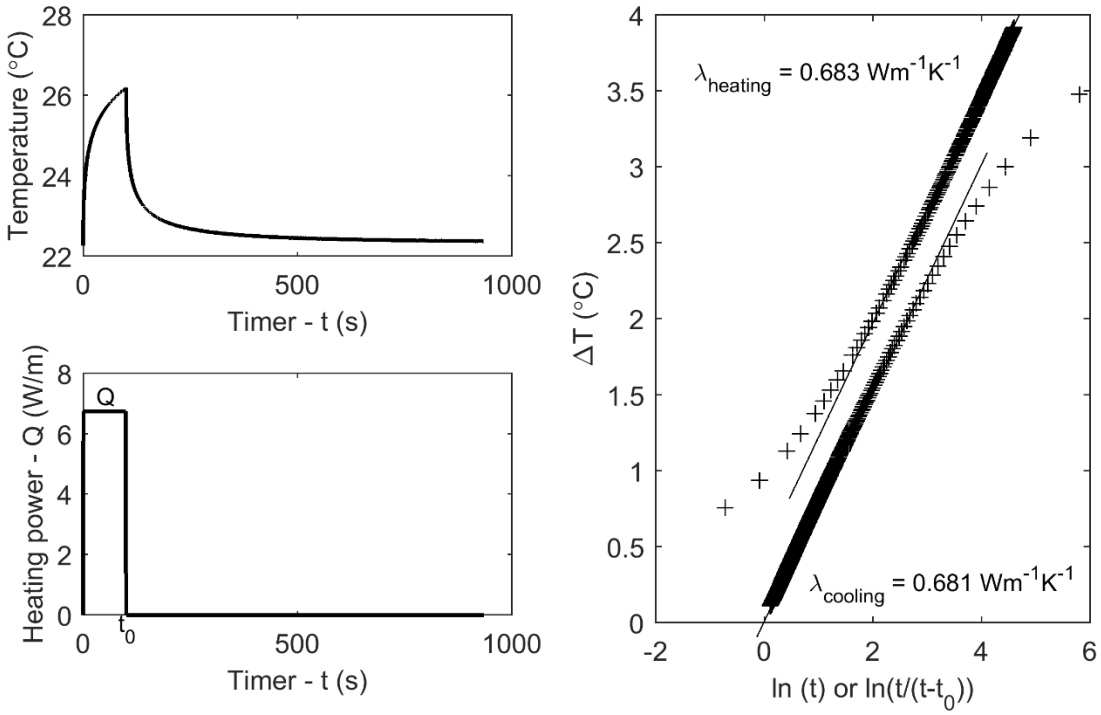

Figure 5.11 *Single needle calibration test on water-agar*

a) Power in heating needle

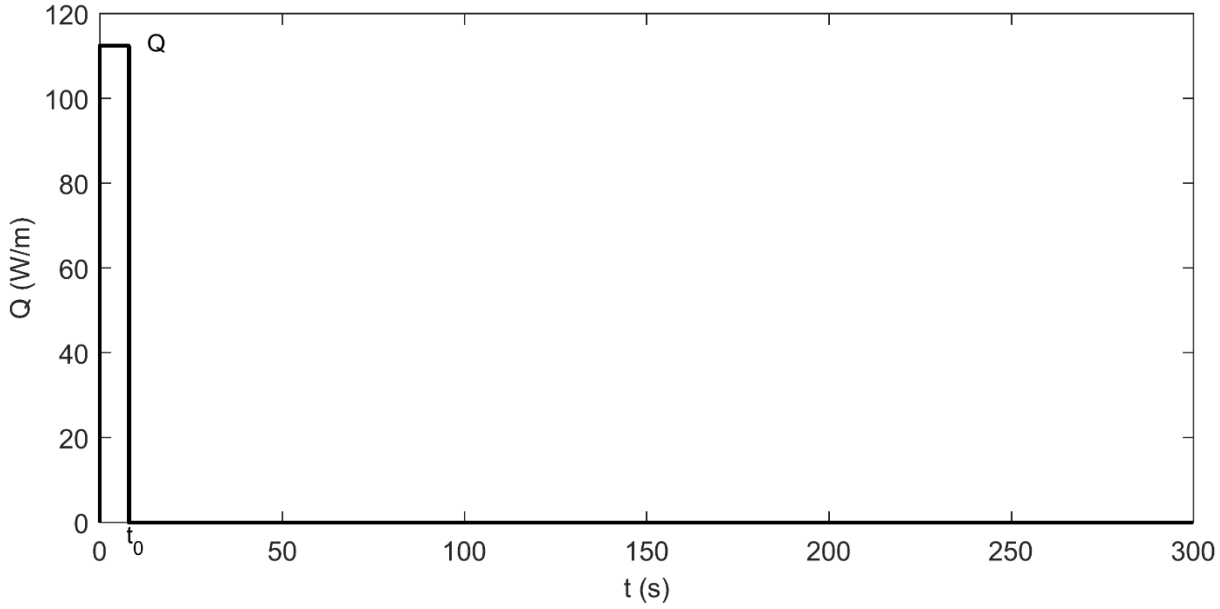

b) Temperature rise in monitoring needle

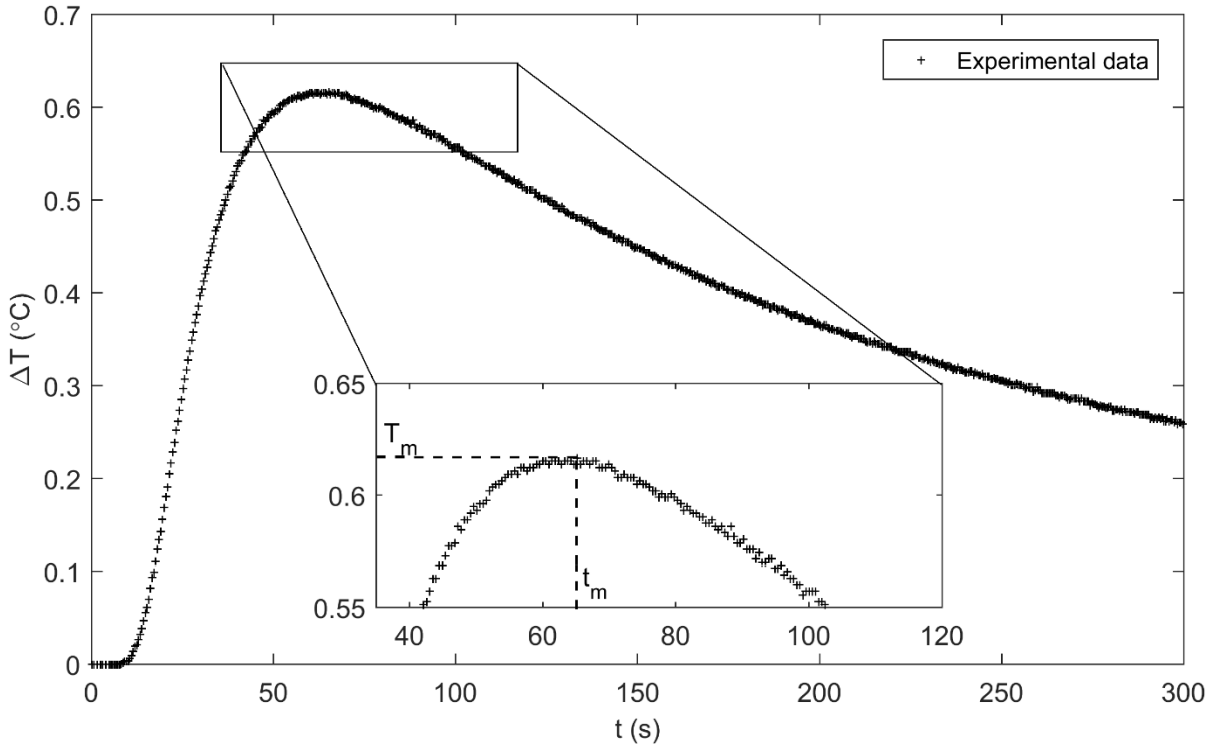

Figure 5.12 *Example of a dual-probe heat-pulse test*

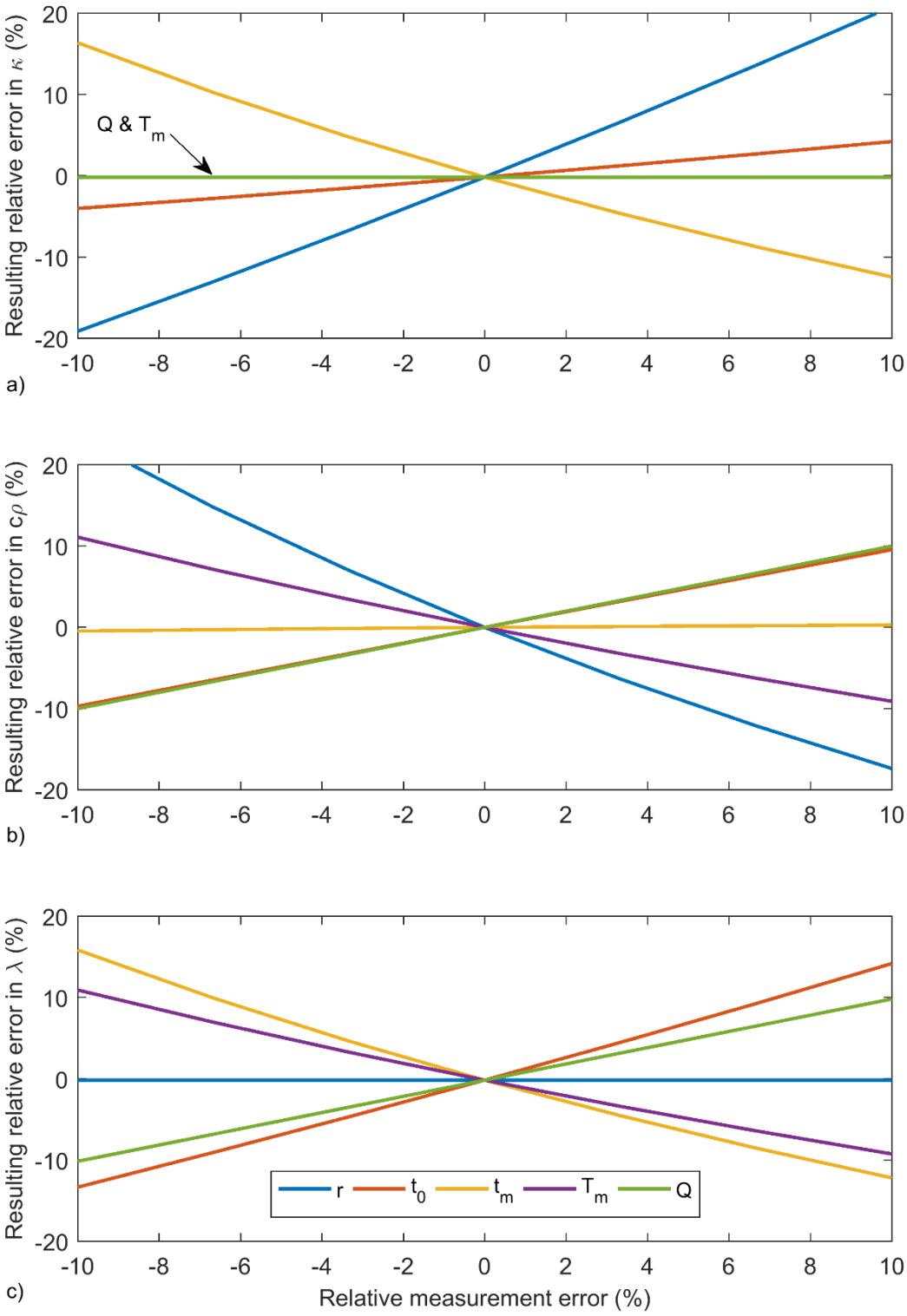

Figure 5.13 *Relative errors in the thermal properties estimated from a dual-probe heat-pulse test*

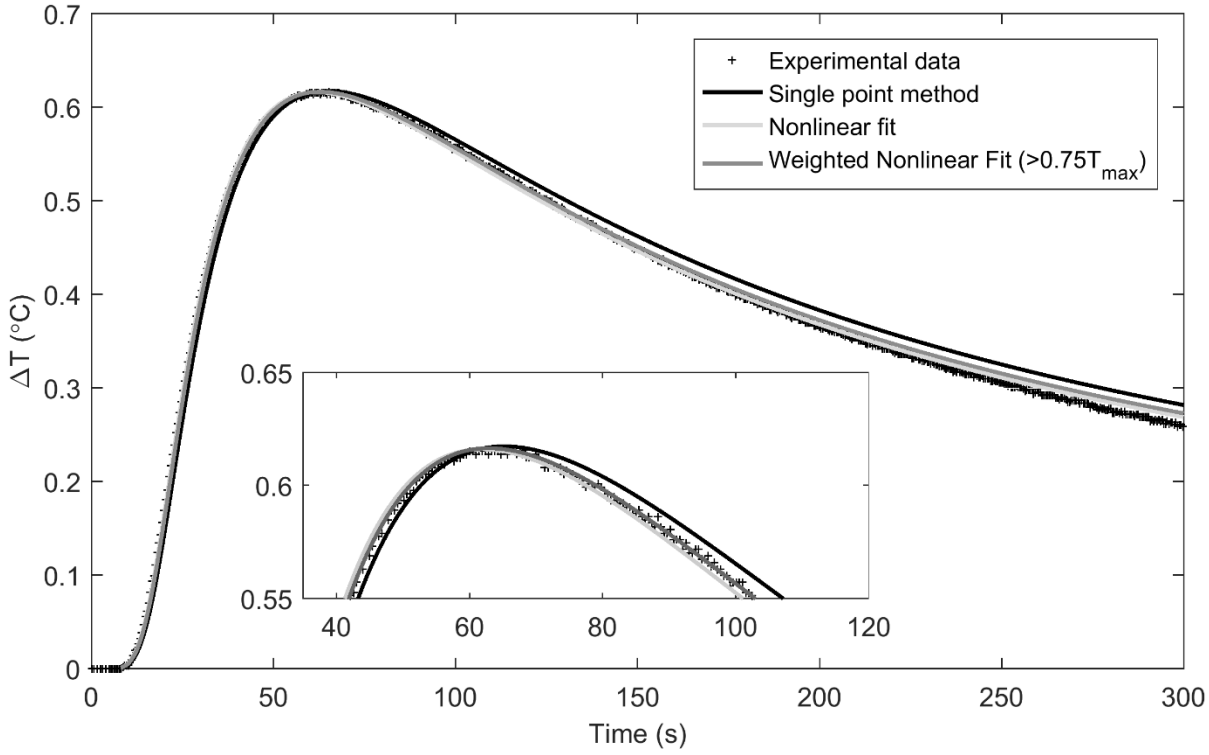

Figure 5.14 *Comparison of the different methods on a calibration test on water-agar*

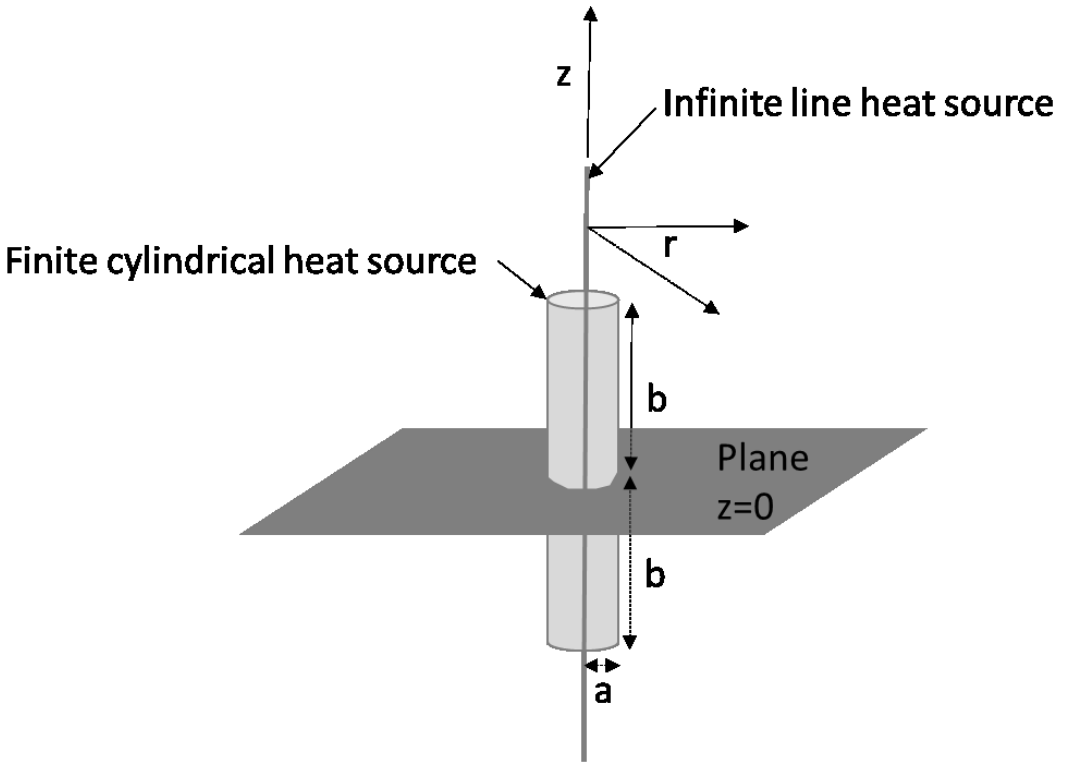

Figure 5.15 *Geometry of the finite cylindrical heat source model*

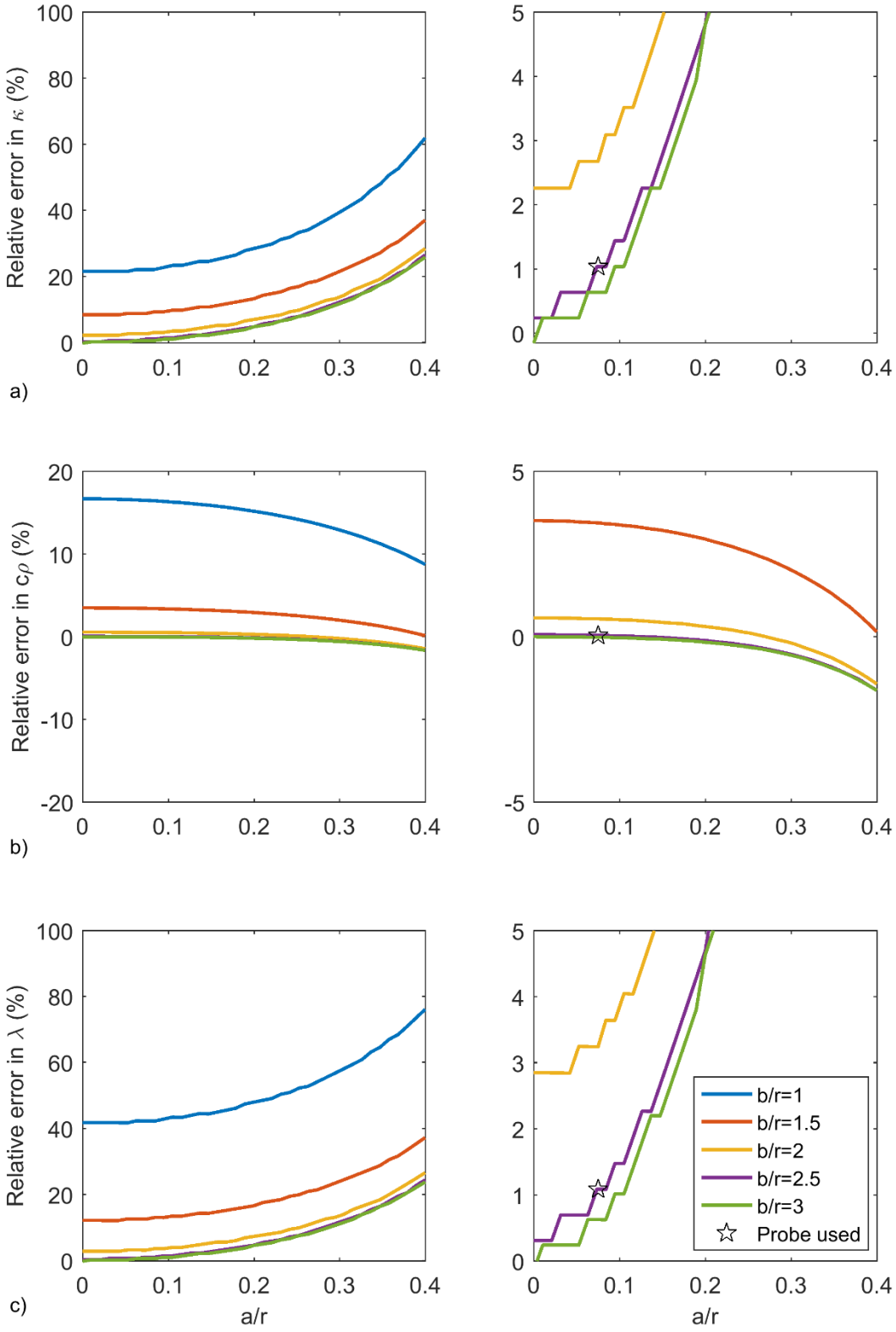

Figure 5.16 *Relative errors in the thermal properties estimated assuming an infinite line heat source model compared to those using a finite cylindrical heat source of half-length b and radius a*

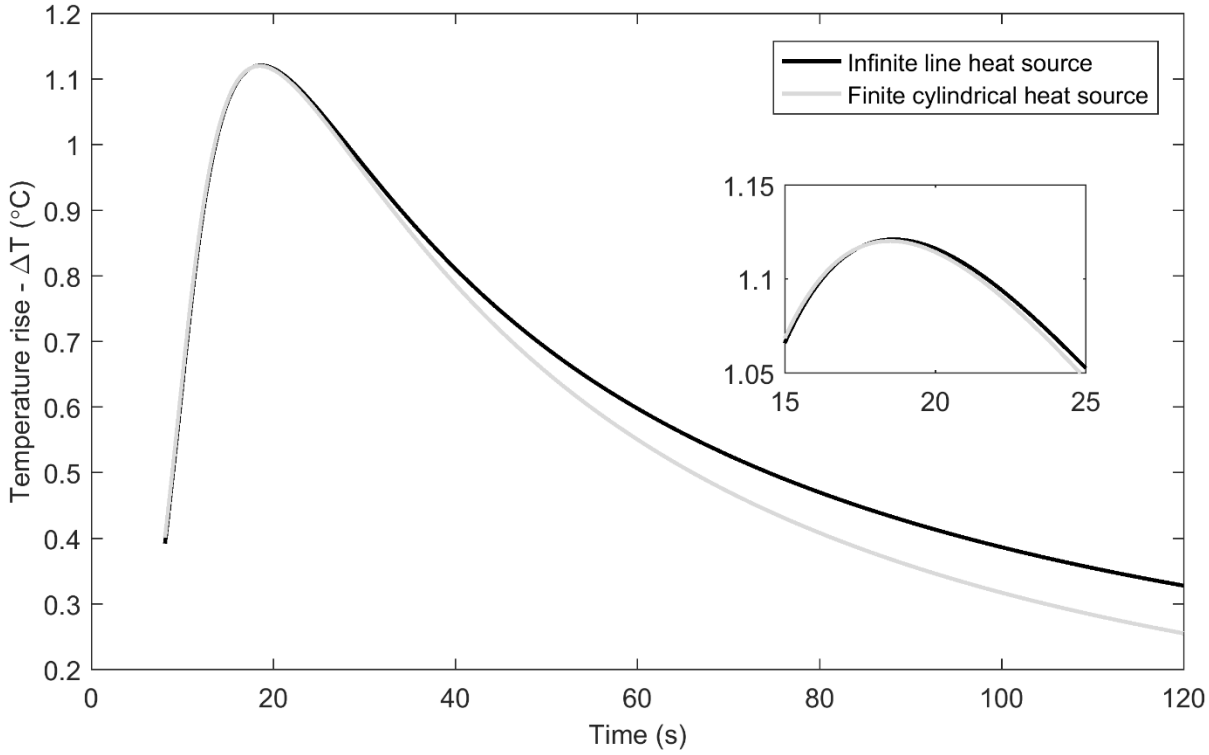

Figure 5.17 *Temperature rise in the monitoring needle (r=6 mm) during a heat-pulse test modelled with an infinite line heat source and finite cylindrical heat source*

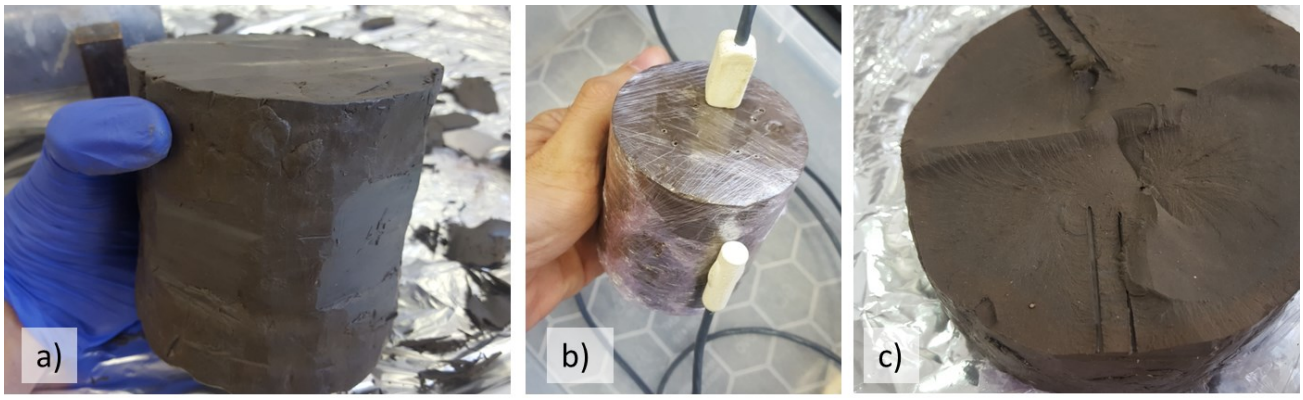

Figure 5.18 *Photographies of the thermal properties tests*

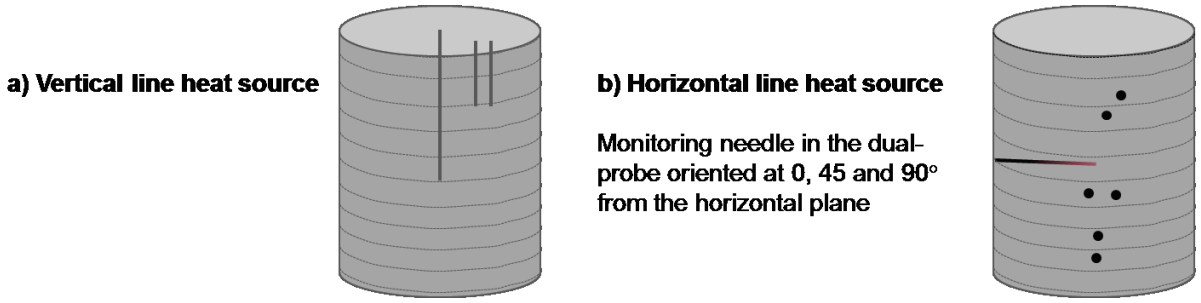

Figure 5.19 *Heating directions considered in the tests of the thermal properties*

6. THERMO-MECHANICAL TESTS

6.1 Introduction

This chapter presents and discusses the results of the thermo-mechanical tests performed on reconstituted London clay, in particular the thermally induced volume changes during drained heating and cooling cycles, changes in the compression properties and pre-consolidated pressure, and finally the temperature effects on the strength and stiffness of the material.

Table 6.1 presents the sample condition in terms of void ratio prior to the first heating phase and to the undrained shearing stage for all samples.

6.2 Thermally induced volume changes

6.2.1 Individual results

Drained heating and cooling cycles, with different number of cycles and temperature amplitude, were applied to a total of eight reconstituted samples at different stress levels and histories, as previously summarised in Table 5.4. The estimated thermal volumetric strains, calculated using Eq.[5.1] with the newly proposed expression for α_w (Eq.[5.12]), are presented firstly in this section, separately for each stress history considered.

Figure 6.1 presents the results of the interpreted thermal volumetric strains from the normally consolidated samples #ncht1 and #ncht2. Sample #ncht1 was normally consolidated to a mean effective stress of p'_c =150 kPa and applied a single temperature cycle of 20-60-20 °C. It contracted by 0.44% during heating, with an accumulated contraction of 0.25% at the end of cooling. Sample #ncht2 was consolidated isotropically to a mean effective stress p'_c =300 kPa before applying the temperature cycle of 20-60-20-60-20-70-20 °C. During the initial heating, the total volume reduced by 0.43% and when the sample was cooled down to room temperature the accumulated volume strain reduced to 0.26%. The results of the first cycle show that it followed a very similar path to sample #ncht1 despite the different confining stress. The following cycle up to 60 °C followed a heating path similar to the previous cooling stage,

reaching practically the same deformation at 60 °C. At the end of the cycle, after cooling to 20 °C, the previous 0.26% accumulated strain remained. The final heating up to 70 °C followed a similar path as in the previous cycle until reaching the previous maximum temperature of 60 °C, after which the slope changed to that similar to the first 20 to 60 °C heating part. A maximum cumulative volumetric contraction of 0.54% was attained at 70 °C and the subsequent cooling followed a path parallel to previous cooling paths and the second 20-60-20 °C cycle, leaving a permanent contraction in the sample of 0.32%.

The thermal volumetric strains for the three samples with an overconsolidation ratio of 6, with the same initial p' of 50 kPa, are shown in Figure 6.2. Three different temperature histories are considered: samples #oc6ht1 and #oc6ht2 were exposed to single temperature cycles from room temperature up to 40 °C, and to 60 °C respectively, while sample #oc6ht3 was subjected to five cycles from ambient temperature up to 40 °C. Sample #oc6ht2 was affected by a loss of pressure and temperature control during the initial heating stage up to 30 °C, due to a power-related incident in the laboratory, and the data points at 30 and 40 °C should be treated with caution, as the sample had to be brought back to the previous stress state. All three samples contract during heating and expand during cooling in what seems to be a very reversible process. If the initial heating affected by the external laboratory issues is ignored, the gradient of the thermal strains with respect to temperature is similar between the three samples tested. The five temperature cycles applied to the sample #oc6ht3 do not seem to produce significant accumulated stains. At the end of each cycle the accumulated strain is always within ±0.02% of the zero starting value.

Figure 6.3 presents the results of the thermal volumetric strains for the three samples with an overconsolidation ratio of 4 (p'=75 kPa, p'_c =300 kPa). Sample #oc4ht1 was exposed to drained heating to 40 °C, producing a contractive strain of 0.11%, after which a power failure in the laboratory caused the interruption of the test. Sample #oc4ht2 followed the same initial heating path to 40 °C as #oc4ht1, producing a nearly identical contraction, which was followed by reloading to 350 kPa, passing its maximum previous mean effective stress (p'_c =300 kPa).

The sample was then further heated drained up to 60 °C and cooled down to room temperature. The thermal strains shown in Figure 6.3 are re-zeroed at the start of this further thermal cycle of 40-60-20 °C. Heating from 40 up to 60 °C produced a volumetric contraction of 0.46%, and the accumulated strain after cooling down to room temperature was 0.30%. Sample #oc4ht3 was also exposed to a similar complex thermo-mechanical history, with initial heating at an OCR of 4 up to 60 °C producing a volumetric contraction of 0.17%. This was followed by loading the sample to 350 kPa, also passing its previous maximum stress (p_c' =300 kPa), at constant temperature of 60 °C, after which the cooling to room temperature resulted in volumetric expansion of approximately 0.18%. This magnitude is, in absolute terms, nearly identical to the volumetric contraction during heating to 60 °C, in its previous overconsolidated state.

6.2.2 Combined results

The results of thermal strains from the previous three figures are combined in Figure 6.4, showing the overall results which can be discussed in terms of (a) influence of stress history, (b) influence of stress level, (c) number of cycles. This comparison identifies two different constant and temperature-independent gradients, defined in Eq.[6.1] by the change in volume with respect to temperature: the first one, $\alpha = \alpha_e$, marks approximately a reversible process which occurs during the heating and cooling of the two different types of overconsolidated samples and during cooling of the normally consolidated samples, as well as during further heating up to the maximum past temperature, as shown in blue in Figure 6.5; the second one, $\alpha = \alpha_p$, seen in normally consolidated samples, is greater in magnitude and includes irrecoverable deformations, shown in red in Figure 6.5.

$$\alpha = \frac{d\varepsilon_{v,T}}{dT} \qquad [6.1]$$

The magnitudes of these two gradients, in units of °C^{-1}, are presented for each test independently in Table 6.2. In the case of the tests #oc4ht2 and #oc4ht3, separate values are calculated for the thermal history following reloading of the samples to a new normally

consolidated state. The value of α_e, which describes the reversible thermal contraction, ranges from 3.00E-05 up to 5.72E-05 °C^{-1} with an average value of 4.65E-05 °C^{-1} and a standard deviation of 7.33E-06 °C^{-1}. The magnitude of this coefficient can be considered as reasonably uniform and constant for all tests considered and there are no clear signs of its dependency on aspects such as stress level, stress history or number of cycles. In fact, the average value calculated from the cooling part of four samples at a normally consolidated state (#ncht1 and #ncht2, at different stress levels, and #oc4ht2 and #oc4ht3 after the reloading stage) is identical to the average value from the heating and cooling paths calculated for the samples with an overconsolidation ratio of four and six.

The average value of α_p, which includes the permanent, irrecoverable thermal contraction in the normally consolidated samples #ncht2 and #ncht1 is 1.09E-04 °C^{-1} (standard deviation of 6.2E-06 °C^{-1}), showing very little difference between the two samples. These two normally consolidated samples were tested at different stress levels, 150 and 300 kPa, and the similar values of both α_p and α_e in both tests indicate that the permanent thermally-induced volume changes seem to be independent of stress level, at least at small stresses. However, sample #oc4ht2, reloaded past its maximum previous mean effective stress at high temperature, presents a value of α_p during the applied further thermal loading more than two times higher (2.28E-04 °C^{-1}). This may indicate that the temperature at which the sample is mechanically loaded could control the magnitude of the thermal strains thereafter. Further tests would be necessary to explore this behaviour.

In summary, all samples contract upon heating and expand during cooling, regardless of the stress history for the three cases considered (normally consolidated and overconsolidation ratios of four and six). Part of the contraction is not recoverable in the normally consolidated samples and this irrecoverable contraction seems to be independent of the samples' intial stress levels at the same initial temperature. The recovered component during cooling in normally consolidated samples as well as the thermally-induced volume changes during heating in subsequent cycles are of a very similar magnitude and direction as the thermal

strains in overconsolidated samples. The application of multiple temperature cycles with the same minimum and maximum temperature in both normally consolidated and overconsolidated samples does not seem to produce additional strains in the soil.

A direct interpretation of the results can be performed in terms of void ratio, calculated in accordance with the framework of Campanella and Mitchell described in Chapter 5, as shown in Figure 6.6. Drained heating produces a reduction in the void ratio of all the samples tested, while cooling induces an increase in the void ratio. The change in void ratio with temperature is very linear and two different rates, α_e^* and α_p^*, defined by Eq.[6.2], can be identified, in a similar way as thermal volume changes described before. It is important to note that during thermal tests the rate of change in volume and in void ratio are not equal, as ealier shown in Eq.[5.4], and the coefficients describing the change in void ratio with temperature are presented in Table 6.3.

$$\alpha^* = \frac{de}{dT} \qquad [6.2]$$

The thermally induced changes in void ratio are relatevily small in all cases. For example, for sample #ncht1, where the greatest reduction of void ratio takes place during the the thermal history of 20-60-20-60-20-70 °C, the accumulated change in void ratio takes a value of only -0.014. The coefficient α_e^*, which describes the reversible changes in void ratio, ranges from 1.28E-04 up to 1.82E-04 °C^{-1} in all tests, with an average reduction of 1.59E-04 per 1 °C increase in the soil temperature (with a standard deviation of 1.55E-05 °C^{-1}). This reasonably uniform value in all the tests performed indicates thus the independence from stress level, stress history and number of cycles. In the case of the coefficient α_p^*, the same observations as for α_p apply: a similar value in both initially normally consolidated samples and a much higher value in the sample brought to a new normally consolidated state a higher temperature.

6.2.3 Comparison with published work

The results of these tests present some departure, but also some similitude with previous published results of the thermo-mechanical behaviour of saturated clays reviewed in Chapter 2. As in the existing studies on other clays, drained heating of normally consolidated samples resulted in a volumetric contraction. The magnitude of this contraction, of about 0.43%, after heating both normally consolidated samples of reconstituted London clay up to 60 °C, is very similar to the test reported by Sultan et al. (2002) (around 0.45%, Figure 2.7d) in a very comparable material (natural Boom clay, which is also a marine clay of similar plasticity, PI=37-50%, although of a more recent geological age). It is however the behaviour of the overconsolidated samples tested in the current study and the behaviour during cooling in the normally consolidated samples that present the biggest discrepancies with the published work. Only a test performed on reconstituted Pontida clay (Hueckel and Baldi, 1990; Figure 2.7b) shows a clear expansion during cooling, while in the present work a very similar expansion during cooling is seen for all samples irrespective of their stress or temperature history. On the other hand, Sultan et al. (2002) reported a consistent contraction during cooling for samples with different stress histories (Figure 2.7d). Moreover there are also signs of further contraction during cooling in the normally consolidated drained heating and cooling tests of soft Bangkok clay (Abuel-Naga et al. (2007b); Figure 2.7f) and remoulded illite (Campanella and Mitchell, 1968; Figure 2.7a).

Perhaps the largest difference between the results presented here and those published is the contraction of intermediate to highly overconsolidated samples during drained heating even at modest temperatures (below 60 °C) compared to the expansion reported in literature. The previous studies show that overconsolidated samples of similar stress histories tend to initially expand at modest temperatures and then start contracting at higher temperature, around 80 °C in the case of Boom clay (Sultan et al., 2002) or 50 °C in the case of kaolin (Cekerevac and Laloui, 2004; Figure 2.7e); while other cases show even expansion for the whole temperature increase up to 90 °C, such as the intact soft Bangkok clay (Abuel-Naga et al.,

2007b) or other tests performed on intact Boom clay (Baldi et al., 1991; Figure 2.7c). Another very distinct aspect of the results of this thesis is the very linear behaviour with temperature for all samples, irrespective of the stress history, which was not observed in previous studies.

6.2.4 Validation of the methodology

Given such results, and in order to examine the validity of the interpretation methodology for thermaly induced strains adopted in the current study, additional tests involving drained heating/cooling cycles in the same experimental set-up, but on a different porous material unaffected by processes involved with clayey soils, were performed. A standard laboratory silica sand, known as the 16/30 sand sourced at Leighton Buzzard, Bedfordshire, UK was chosen for these additional tests. The particle size distribution of the sand is presented in Figure 6.7 showing that this is a poorly-graded coarse sand, with no fines passing the 0.4 mm sieve and no particles retained by the 1.18 mm sieve. A sample, with an initial void ratio of e_0 = 0.621 (relative density of 55%, G_s=2.67), of 50 mm in diameter and 110 mm high, was prepared and loaded up to a mean effective stress of 300 kPa where it was heated up to 60 ºC and cooled down to room temperature under drained conditions, in the same manner as the reconstituted London clay samples. The sample was then unloaded to a mean effective stress of 50 kPa, and the same heating and cooling cycle was applied. Figure 6.8 presents the thermal volumetric strains during the temperature cycles at those two different stress levels, together with the predicted strains assuming no change in void ratio. This assumption results in the sample expanding according to the coefficient of thermal expansion of the solid particles (quartz in this case, α_s= 27.1*10^{-6} ºC^{-1}), as discussed in the previous chapter. The same results are superimposed to the results of the reconstituted London clay samples in Figure 6.9 in terms of thermal volumetric strains, and in Figure 6.10 in terms of thermally-induced void ratio changes.

The results of the two cycles on the 16/30 sand show a practically identical development of thermal volumetric strains. In both tests, the sand sample expands at the rate predicted by the thermal expansion coefficient of the quartzitic particles and there is no change in void ratio

during the test. This test agrees very well with the theoretical assertion of Khalili et al. (2010) that in homogenous porous media the thermal expansion of the porous skeleton as a whole is identical to the one of the soil grains. These results, although of a limited scope, provide some justification of the methodology adopted for the interpretation of the thermo-mechanical tests presented in this thesis and highlight the very different response to heating of porous coarse free-draining material and low permeability clays.

6.2.5 Discussion of the nature of the thermal strain measurement and influence of α_w

An important aspect in the assessment of the results of this type of thermo-mechanical tests, in which direct measurement of the thermally induced strains is not possible, is to discuss the nature of such measurements. An example of such assessment is illustrated in Figure 6.11 for the test #ncht1. In this study, as in other published characterizations of the thermo-hydro-mechanical behaviour of soils, the thermal volumetric strains are estimated using the Campanella and Mitchell (1968), presented in section 5.2.1. The only measured parameter is the drained water coming in and out of the sample in the backpressure system, which is then corrected for the expansion of the solids and water in the sample to produce the thermal volumetric strains. For the test illustrated in Figure 6.11, the accumulated strain measured by the drained water flowing out of the sample (V_{dr}/V_0), during heating form 20 to 60 °C, is of 1.26%. The accumulated correction for the thermal expansion of the solids and water in the sample ($(\alpha_s V_s \Delta T + \alpha_w V_w \Delta T)/V_0$), shown by the grey solid line, is -0.82%, resulting in an accumulated contraction ($\varepsilon_{v,T}$) of 0.44%. This shows that the "unmeasured" correction is nearly twice as large as the resulting "measurement" of thermal volumetric strains. The relative magnitudes of the measured and corrected terms highlight the indirect nature of the measurement. In the absence of a more reliable "direct" measuring technique, it is of great importance to minimise the error in the measured drained water, as discussed in Chapter 3, by avoiding seepage through the membrane at high temperature and understanding the behaviour of the drainage system through calibration tests. It is also important to use the

appropriate parameters in the correction term, in particular the coefficient of thermal expansion of water, as this is an order of magnitude higher than the coefficient of thermal expansion of the solids and therefore governs the magnitude of the correction term.

Chapter 5 highlighted the fact that the coefficient of thermal expansion of water, α_w, has not always been taken into account properly in the published literature. The effects of using different values of α_w in the estimation of the thermal volumetric strains are presented in Figure 6.12 for all tests conducted in the current study, but for three different cases in terms of α_w: (a) using the new expression derived in section 5.2.4 (Eq.[5.12]); (b) using the expression of Baldi et al. (1988) with pressure in units of MPa and with the parameter m= 15 MPa^{-1}, as in the characterization of kaolin presented by Cekerevac and Laloui (2004) and Cekerevac et al. (2005) (case (ii) in Figure 5.1); and (c) using the expression of Baldi et al. (1988) with pressure in kbar and with the parameter m = 0.15 kbar^{-1} (case (iii) in Figure 5.1). The differences between the estimated thermal volumetric strains in cases (a) and (b) are very large in terms of the implications of the interpreted thermo-mechanical behaviour of the material, whereas case (c) presents a much better agreement with the case (a). The interpretation (b) would suggest that the overconsolidated samples initially expand during heating until a temperature of about 50 ºC, contracting subsequently with further heating. It would also imply that the normally consolidated samples contract during heating, but also during cooling, with this being the case also for overconsolidated samples. All of these features are common aspects reported in the published literature. However, for the tests performed in this thesis, they are a result of the selection of a different (and likely wrong) coefficient of thermal expansion of water. The interpretation (c) gives slightly larger strains, but the trend in the overall behaviour is identical to the one reported in this thesis. The latter is explained by the close agreement at small pressures and modest temperatures (between 20 and 60 °C) between the α_w values obtained using the new expression and the one used for case (c), as shown in Figure 5.1.

The analysis of previous published experimental data using the new expression for α_w is possible if the initial sample conditions prior to the temperature cycle are known and there is

certainty in the value of α_w used by the authors, or the original measurements of drained water are known. Using the sample information and testing conditions provided in Cekerevac and Laloui (2004) for kaolin clay, it was possible to reanalyse in Figure 6.13 two tests on samples with different stress histories. One is a normally consolidated sample with initial porosity n=0.388 (Figure 6.13a), and the other is an overconsolidated sample with OCR=6 and n=0.417 (Figure 6.13b). The thermal volumetric strains presented in the original paper (black solid line with circles in Figure 6.13) can be corrected by adding the difference between the correcting term for the thermal expansion of the solids and water ($(\alpha_s V_s \Delta T + \alpha_w V_w \Delta T)/V_0$) estimated to have been used by authors in the original paper and the one calculated in this study. The latter correction term (red dashed lines in Figure 6.13) assumes α_s=31E-6 °C^{-1} for kaolin and uses the new expression for α_w. The former correction term (black dashed lines in Figure 6.13) assumes the same value for α_s and the value for α_w that corresponds to case (b) in Figure 6.12, as used by Cekerevac and Laloui (2004) and Cekerevac et al. (2005).

The recalculated thermal volumetric strains (red solid lines with circles) indicate quite a different soil behaviour compared to the original interpretation. In the case of the normally consolidated sample, the new estimation of the thermal strains shows a contraction with increasing temperature at a very linear rate, as reported in this thesis, contrary to the temperature-dependent contraction suggested by the original interpretation. For the overconsolidated sample, the new estimation shows a slight contraction, and again mostly linear, with increasing temperature, contrary to the initial expansion followed by contraction at higher temperature shown by the original interpretation. The new estimation based on the expression for α_w presented in Eq.[5.12] agrees very well with the contractant behaviour observed during drained heating in the six overconsolidated samples presented in this thesis.

The presented analysis highlights the difficulty of the “indirect” nature of the measurement of thermal strains and the importance of the parameter α_w. It also suggests that the initially-thought “surprising” behaviour of the overconsolidated reconstituted London clay may not be

that unusual, as shown by the re-examination of previous published results where a different, and likely wrong, value of α_w was used.

6.2.6 Further discussion

A key assumption of the interpretative framework adopted in the current study is that the water in the sample is in its free (bulk) form. This assumption is certainly valid for sands and coarse materials and the appropriateness of the method was clearly demonstrated with the tests on the 16/30 Leighton Buzzard sand, with the results agreeing with the theoretical predictions of volumetric behaviour. However, the nature of water in clays is much more complex. Water in clays may be present in different forms: (i) free or bulk water, able to flow due to hydraulic gradients; (ii) bound water or adsorbed water, held to the surface of the clay particles by electrochemical fields at inter or intra-cluster level; and (iii) structural water or hydroxyl, which forms part of the structural lattice of the clay mineral and cannot leave the solid at temperatures below 350 °C (Hueckel, 1992). The first two cases are of relevance in this discussion, particularly the adsorbed water, whose physical properties and structure are different to those of free water. In order to obtain electroneutrality, given the presence of a net negative charge on the surface of a clay mineral, a diffuse double layer is created. The thickness of this adsorbed water layer is positively related to the water content of the clay (Dolinar and Macuh, 2016) and the adsorbed water content depends on the specific surface area of the mineral and the thickness of the layer. Pusch and Carlsson (1985) showed that for soils mainly formed of minerals with a very high specific surface area such as smectite, most of the pore water is not in its free form even for high moisture contents. Baldi et al. (1988) presented a different interpretatitve framework (Section 5.2.2) considering all the water as adsorbed water. Qualitatevely assessing its use for the estimation of the thermal volumetric strains in Baldi et al. (1988) and Delage et al. (2000), it can be concluded that it predicts in all cases a more contractive strain than the free water approach of Campanella and Mitchell (1968). This suggests that the use of Baldi et al. (1988) adsorbed water approach should yield an even more pronounced contraction upon heating compared to the approach used in this thesis,

further suggesting that observations in this thesis of the “unsual “ contractive thermal strains in overconsolidated samples are not an artefact of the applied interpretative method.

Contraction upon heating, an unusual feature in most materials, has often been attributed to physio-chemical effects in the clay-water interaction and there is no clear and conclusive explanation of the processes as yet. Lambe (1960) tried to explain the decrease in volume in clayey soils upon heating using theoretical expressions for the double layer, under the assumption of the temperature-independence of the dielectric constant. It was suggested that a depression of the electric double layer and re-arrangement of particles would be caused by an increase in temperature. Yong et al. (1962) reported, however, an expansion of the double layer with increasing temperature and Kenney (1966) artificially expanded the thickness of the layer by leaching and this resulted in an overall decrease in volume of the soil specimen. Plum and Esrig (1969) combined the previous findings to hypothesize that expansion of the double layer could lead to overall contraction of the material, as a result of a drop in the shearing resistance at the particle contacts due to higher interparticle repulsion. Morin and Silva (1984), using the theoretical expression of the double layer thickness presented by Van Olphen (1977), suggested that the double layer thickness increases with increasing temperature. Mitchell (1993), using the same analytical expression, considered that the double layer thickness would remain relatively constant, as the temperature increase would be balanced by a decrease in dielectric constant. Microscopic experiments by Pusch and Guven (1990) concluded that heating up to 150 °C causes a rearrangement and heat-induced dehydration and contraction of the stacks of smectite flakes, leading to larger voids, which was followed by rehydration and expansion during cooling to room temperature. Only further heating up to 200 °C led to stronger microstructural changes and permanent contractions. Derjaguin et al. (1986) suggested that at temperatures higher than 70 °C the structural peculiarities of water disappear and the thermal expansion in the pores and bulk phase coincide. Recent experiments by Shao et al. (2012) on different types of clay have revealed that the adsorbed water content decreases linearly with increasing temperature and this effect was more

profound in clays with a higher content of smectite. This conversion of adsorbed water to free water, while imposing constant effective stress conditions, may be responsible for the thermally-induced reorganization of the particles and the resulting contractive strains. However, it is important to note that the effects at molecular-level discussed above seem to be reversible processes with temperature and that would affect the soil regardless of the stress history and should therefore not just be used in isolation to justify the contraction in normally consolidated clays, but need to be also considered in overconsolidated material, which may well have a higher proportion of adsorbed water. The results of this thesis show for all stress histories a generation of thermal strains in the same direction and these are reversible processes, except when the soil is at its mechanical yield limit, where part of the contraction is not recovered.

An aspect of the thermo-mechanical behaviour that deserves further attention is the possible rate dependence effects which may contribute to explain some of the differences seen with published experiments. The heating and cooling rates used in this thesis are very slow: a nominal rate of 0.5 °C/hr was applied to the heaters but the real rate in the soil was slightly smaller, between 0.3-0.4 °C/hr. This information is unfortunately not available in all published studies. Cekerevac and Laloui (2004) and Graham et al. (2001) used heating rates of 3.33 °C/hr and 6 °C/hr, while Sultan et al. (2002) showed that the use of different cooling rates (0.75, 0.6 and 0.4 °C/hr) influenced the gradient of the curve in the temperature vs strain plot and that cooling rates smaller than 0.4 °C/hr were necessary in order to avoid rate effects. Cui et al. (2009) showed that if fast rates are used the separation between thermal consolidation and creep processes is complicated, and further tests with pore pressure measurements are recommended. Thermal-volume changes under constant temperature in tests of low permeability material, using fast temperature change rates, may be the result of the dissipation of excess pore pressures generated during the temperature change and not of secondary compression.

On a different note, another aspect to discuss in the applicability of these results to intact material, focussing on London clay and the energy geostructures applications, is that the current study has been limited to isotropic conditions and the different components of the thermal strain in the various directions are not individually measured. It is well known that the thermal expansion of the clay minerals is not an isotropic property and future apparatus design should aim to measure all strain components.

6.3 Compression properties and pre-consolidation pressure

The compression data of the reconstituted London clay used in this project is presented in Figure 6.14, using all isotropic compression and swelling paths from tests performed at room temperature. Although showing slightly different initial void ratios, the samples from the two different cakes of reconstituted material display the same behaviour in compression. From Figure 6.14, showing the specific volume, v, versus the mean effective stress, p', on a logarithmic scale, the material parameters corresponding to the slope, λ, of the normal compression line (NCL), slope of the swelling lines, κ, and the specific volume, N, of the NCL at p'=1 kPa may be determined. The magnitude λ = 0.182 is slightly higher than the value of 0.168 obatined by Gasparre (2005), from reconstituted samples from several lithological units (A to C). The value of κ is 0.064, being the same as the value reported in the study of Gasparre (2005).

Figures 6.15 and 6.16 present the evolution of the specific volume during the complex thermo-mechanical path applied to samples #oc4ht2 and #oc4ht3, respectively. After the initial isotropic compression to p'=300 kPa, sample #oc4ht2 was swelled isotropically to p'=75 kPa and an OCR value of 4 at room temperature (path A-B). It was then heated to 40 °C under drained conditions (path B-C) and reloaded isotropically at 40 °C in steps to p'=350 kPa (path C-D). A similar stress-temperature path was applied to sample #oc4ht3, but with temperature raised to 60 °C. Both samples indicate that the initial slope of the recompression path C-D at constant but elevated temperature, may be approximated with the gradient κ of the swelling

line estimated at the ambient temperature. This may suggest that the magnitude of the parameter κ is independent of temperature, at least in the temperature range considered.

The latter part of the reloading paths C-D was unfortunately stopped too early to provide a more definitive answer on the exact yield stresses and post-yield behaviour at two distinct temperature values. The tangent from the last two data points on the recompression C-D path at 40 °C in Figure 6.15 indicates that the post-yield compression at 40 °C may be of the same slope as the NCL at ambient temperature, in which case the parameter λ would also be temperature-independent. However, this is not so clear from Figure 6.16.

Furthermore, the intersection of the two tangents from the initial and latter parths of the C-D curve in Figure 6.15 indicates that the yield stress at higher temperature is smaller than that at ambient temperature, which is consistent with the established framework of the shrinking yield surface at elevated temperatures (previously shown in Figure 2.10). Similar construction is attempted at Figure 6.16, but with a higher uncertainty due to the lack of data in the reconsolidation path.

6.4 Strength and Stiffness

The results of undrained shearing to failure, applied to the samples after isotropic stress and temperature changes described in the previous sections, are presented and discussed in this section, together with the results from reference tests with the same consolidation histories but performed solely at ambient temperature.

6.4.1 NC samples

The stress-strain curves in terms of the deviatoric stress, q, and axial strain, ε_a, for all normally consolidated samples are shown in Figure 6.17a. The respective excess pore pressures, Δu, during undrained shearing are shown in Figure 6.17b.

The four reference samples consolidated to different p_c' at ambient temperature, show the expected effect of the mean effective stress in terms of the mobilised maximum deviatoric

stress. This is much smaller after shearing at p_c' =150 kPa, compared to shearing at p_c' =300 or 350 kPa (Figure 6.17a). The latter tests show a marginal difference in q_{max} (~10%). A similar patern is seen in terms of excess pore pressures in Figure 6.17b.

Sample #ncht1, subjected to a single drained temperature cycle (20-60-20 °C) after isotropic consolidation to p_c' =150 kPa, can be compared to sample #nct1 which is consolidated to the same stress level. Their initial behaviour in shearing up to 2% axial strain is almost identical, exhibiting slight differences thereafter in the maximum mobilised deviatoric stress and the generation of excess pore pressures. It is the sample with temperature history, #ncht1, that mobilises a slightly higher peak stress (q_{max}≈108 kPa) compared to the one of the reference study (q_{max}≈100 kPa).

Sample #ncht2, exposed to several drained temperature cycles (20-60-20-60-20-70-20 °C) after isotropic consolidation to 300 kPa, presents no significant differences to its reference counterparts #nct2 and #nct3 which were subjected only to isotropic consolidation to 300 kPa prior to shearing. In fact, the shearing behaviour of sample #ncht2 is practically identical to the behaviour of #nct2.

Also included in Figure 6.17 are the two samples initially overconsolidated to OCR=4 from p_c'=300 kPa, heated to a higher temperature and recompressed to p'=350 kPa at that temperature, before further thermal loading under drained conditions to ambient temperature and subsequent undrained shearing. These are the samples #oc4ht2 and #oc4ht3, which exhibit a very similar behaviour in shearing despite the difference in their previous thermo-mechanical paths: the former recompressed at a temperature of 40 °C before a drained cycle of 40-60-20 °C, and the latter recompressed at a temperature of 60 °C before cooling to 20 °C. The mobilised maximum deviatoric stress in both tests is 210 kPa, which is significantly higher than in the reference test #nct4 (q_{max}≈175 kPa), which was normally consolidated to p'=350 kPa at ambient temperature (Figure 6.17a). The higher q_{max} in the samples with thermal history occurs despite the very comparable initial void ratios prior to shearing (Table 6.1) to sample #nct4.

In most samples, it is interesting to note the unexpected drop in deviatoric stress after about 10% of shearing. This was observed to happen on the onset of localised shear failure planes, which makes the calculation of the cross-sectional area particularly challenging. Despite the application of the standard correction for shear planes discussed in the previous chapter, the test data at large strains should be treated with caution. This correction is based on a simplified geometry of the failure plane measured at the end of the test and thus may include errors caused by deformation of the sample during unloading and removal from the cell. Moreover, the geometry of the failed samples is very complex, involving bulging as well as non-unique shear planes.

The stiffness curves, in terms of undrained tangent stiffness, E_{tan}^{u}, and its normalised value by the current mean effective stress, E_{tan}^{u}/p', against axial strain, ε_a, for all the normally consolidated samples described above, are plotted in Figure 6.18(a) and (b) respectively. As for the q-ε_a plots, samples #ncht1 and ncht2 do not present significant differences to their reference counterpart tests #nct1 and #nct2/#nct3. On the other hand, samples #oc4ht2 and #oc4ht3 expose significant differences in stiffness both in absolute and normalised values in the whole range of relevant strains levels to the reference sample #nct4. At the 0.01% strain level, the tangent stiffness of samples #oc4ht2 (~142 MPa) and #oc4ht3 (~135 MPa) is significantly greater than sample #nct4 (~105 MPa). At 0.1% strain, the tangent stiffness of samples #oc4ht2 (~46 MPa) and #oc6ht3 (~41 MPa) remains noticeably greater than sample #nct4 (~32 MPa). The small differences between samples #oc4ht2 and #oc4ht3, with a stiffer response in #oc4ht2, may be explained by the different void ratios between the samples (Table 6.1), with #oc4ht2 being in a slightly denser state. Nevertheless, the densities of these two samples with complex thermo-mechanical paths can not explain the significantly higher stiffness during shearing compared to the reference test #nct4, of a very comparable porosity.

6.4.2 OC samples

The stress-strain curves q-ε_a and Δu-ε_a are shown in Figure 6.19(a) and (b), respectively for the three overconsolidated samples exposed to temperature and those of the reference study at room temperature.

As shown in Figure 6.19a, the two reference samples mobilise a similar maximum deviatoric stress q_{max} of around 94 kPa, which is around 15% higher on average than the three samples with different magnitude and number of temperature cycles. In the case of sample #oc6ht1, only exposed to a single cycle up to 40 °C, q_{max} takes a value of 78 kPa, while sample #oc6ht3, exposed to five of those cycles, mobilises a maximum deviatoric stress of 84 kPa and sample #oc6ht2, exposed to a single thermal cycle up to 60 °C, mobilises a slightly lower maximum deviatoric stress (q_{max}=82 kPa).

The reference ambient temperature samples #oc6t1 and #oc6t2 develop initially positive excess pore pressures up to maximum values of Δu_{max} between 16 and 20 kPa, but present at the end of shearing an identical negative excess pore pressure of approximately -10 kPa. On the contrary, the three samples exposed to thermal loading display a positive excess pore pressure at the end of shearing, with the maximum excess pore pressure happening at slightly larger axial strains compared to the reference samples (Figure 6.19b). Samples #oc6ht1 and #oc6ht3 both exposed to 40 °C have near identical excess pore pressure mobilisation in the later stages of shearing (Δu =3 kPa), but present some differences in the earlier stages, with the sample with a higher number of cycles developing a higher Δu_{max}. Sample #oc6ht2, exposed to the highest temperature, 60 °C, is the one that ends up with a higher excess pore pressure at the end of shearing (Δu =7 kPa), as well as the highest Δu_{max}.

Figure 6.20 shows the stiffness curves, E_{tan}^{u}-ε_a and E_{tan}^{u}/p'- ε_a for the overconsolidated samples described. The two samples without temperature history present a higher stiffness at small strain levels than the samples with temperature history, both in terms of absolute and normalised values. At larger strains above 0.07%, the undrained tangent stiffness of all

samples seem to converge and the differences between them are minimal. The thermally-induced differences in the shearing and stiffness behaviour of the overconsolidated samples cannot be explained by thermally-induced volume changes reported in Figure 6.2, as those suggest an elastic, reversible process.

6.4.3 Combined critical state discussion

The results of all samples are plotted in Figure 6.21 in terms of the stress ratio q/p' during undrained shearing. All samples seem to start converging to a stable q/p' ratio at around 10-12% axial strain, before the effect of the localised failure (shear planes) becomes very apparent for the normally consolidated samples, resulting in a significant drop in strength. In this strain range, as well as subsequently, it is impossible to distinguish a particular effect of temperature on the ultimate (critical state) value of q/p', suggesting that it would be independent of temperature. The average value of 0.86 of the stress ratio is derived from Figure 6.21, which is very similar to the critical state parameter M (0.85) obtained by Gasparre (2005) during an extensive testing programme at ambient temperature of reconstituted and intact London clay samples from different lithological units.

The values of the stress ratio at peak strength of the overconsolidated samples (1.29-1.43) exposed to temperature are significantly greater than those of the reference samples (1.2-1.24). The results suggest an increase with increasing temperature and increasing number of cycles as shown by samples #oc6ht1 (1.29) and #oc6ht2 (1.43), both exposed to a single cycle up to 40 and 60 °C, and sample #oc6ht3 (1.42) exposed to five cycles up to 40 °C. The higher stress ratio achieved in these three samples, despite the lower maximum deviatoric stress q_{max} than the samples with no temperature history, is explained by the more significant effect of the higher generation of positive excess pore pressure during shearing in the samples with temperature history. This is highlighted in the normalised plot of the excess pore pressure presented in Figure 6.22. The combined analysis of both figures reveals some interesting patterns: while the higher peak stress ratio suggests a more “overconsolidated” behaviour in

the samples exposed to temperature, the shift towards more positive excess pore pressure is less indicative of overconsolidated clay behaviour.

There is less uniformity in the shearing behaviour in the case of the normally consolidated samples. On the one hand, no significant changes are observed in the case of samples heated from a normally consolidated state at ambient temperature, #ncht1 and #ncht2, compared to to the two reference samples tested at the same stress level, both in case of the stress ratio evolution and generation of excess pore pressures during shearing. On the other hand, the samples with the more complex thermo-mechanical history, #oc4ht2 and #oc4ht3, present a significant differences compared to #nct4, as earlier discussed. Both samples with thermal history present a similar behaviour in these normalised plots (Figure 6.21 and Figure 6.22), showing higher stress ratios at small strains (converging later at approximately 10% strain) and lower excess pore pressure generation during all stages of shearing.

Finally, the effective stress paths for all the samples in the q/p' plane are presented in Figure 6.23, and Figure 6.24 considers just the data to 11% strain. The test #oc2t1, conducted at OCR=2 and at ambient temperature, is also added to these figures to add information for material behaviour at p'=150 kPa. The stress paths of all normally consolidated samples bare to the left from the initial isotropic stress condition as the deviatoric stress increases, reaching in all cases a well-defined peak before an abrupt turn and a significant, usually unexpected in normally consolidated samples, drop in deviatoric stress, which is attributed to the shear planes developed in all samples. Visible evidence of the generation of the shear planes, at angles between 50 to 60 °, appears at strains larger than 10-12% in the case of the normally consolidated samples. Based on the evolution of the stress ratio during shearing presented in Figure 6.21 and the stress paths presented in Figure 6.23, the value for the stress ratio at critical state, M, is estimated at 0.86. The nearly stable changes in excess pore pressure at the moment of appearance of the shear plane in the normally consolidated samples allow for this interpretation of critical state. Burland et al. (1996) and a later discussion by Georgiannou and Burland (2001) noted that critical state conditions were reached in highly plastic

reconstituted Pietrafitta clay samples prior to the development of the shear planes at 15% axial strain, dropping to post-rupture strength conditions thereafter.

The effective stress paths of heated samples #ncht2 and #ncht1 are very similar to the ones of the reference study. On the other hand, clear differences in the shape of the stress paths are seen in the case of the samples #oc4ht2 and #oc4ht3 compared to their reference ambient sample #nct4, which has a more pronounced traverse to the left due to the higher generation of positive excess pore pressures as seen in Figure 6.17. In the case of the overconsolidated samples, the stress paths of the samples exposed to temperature show a shorter trajectory to the right, which also occurs at higher deviatoric stresses than in the ambient reference samples. This is explained by the negative, dilatant excess pore pressures which are only seen in the samples of the reference ambient study as shown in Figure 6.19. The stress paths are also shown normalised by the equivalent effective stress, p'_e, in Figure 6.25. The normalising stress is determined for each test in relation to the NCL established at ambient temperature. Although the number of tests is not sufficient to appropriately characterise the state boundary surface, there seems to be an indication that exposure to temperature may lead to steeper surfaces in both the overconsolidated (as shown by all tests) and normally consolidated sides (for the tests which involved mechanical reloading at higher temperature). Further experimental work is required to address this aspect and allow further coherent constitutive interpretation.

Finally, the shearing data is plotted in the volumetric plane, v -$\ln(p')$, in Figure 6.26, for both the reference samples and those of the thermo-mechanical study, together with the normal compression line at ambient temperature derived in Figure 6.14. In the view of the failure mode of all samples, and the corresponding difficulty in establishing the stress state at large strains, there is some degree of uncertainty in the final points of each test after undrained shearing (Δv=0). Nonetheless, a unique “critical state” line (CSL), parallel to the NCL at 20 °C, may be drawn for both types of sample as attempted in Figure 6.26. This would suggest that the critical state line is independent of temperature, although further experimental work is required for a

clearer understanding of the influence of temperature on the strength of the reconstituted London clay.

6.5 Summary

This chapter presents the results of the thermo-mechanical tests performed on reconstituted London clay samples, with the main findings and points of discussion listed as follows:

- All samples contract upon heating and expand during cooling, regardless of the stress history for the three cases considered (normally consolidated and overconsolidation ratios of four and six).
- Part of the contraction is not recoverable in the normally consolidated samples and its magnitude seems to be independent of the stress level, for the samples brought to the normally consolidated state at the same temperature.
- The reversible component during cooling in normally consolidated samples as well as the thermally-induced volume changes during heating in subsequent cycles are of a very similar magnitude as the thermal strains in overconsolidated samples.
- The application of multiple temperature cycles in both normally consolidated and overconsolidated samples does not seem to produce additional strains in the soil.
- These results present similitudes as well as discrepancies with published past results on different clays, which are discussed in terms of the nature of the measurement, interpretative framework and experimental conditions, as well as the proposed physical mechanisms. The importance of the use of correct value of thermal expansion coefficient of water in the interpretation of the thermal strains when direct measurements of the thermal strains are not possible is highlighted.
- Although there is no sufficient data to establish conclusive trends, the slopes of the swelling and compression lines seem to be temperature independent.
- For the samples normally consolidated at ambient temperature, exposure to higher temperatures does not cause significant changes in terms of strength and stiffness.

On the other hand, the samples brought to a normal consolidation state at higher temperatures present a higher stiffness and higher initial strength, and lower excess pore pressure during shearing, than comparable samples without thermal history.

- In the case of the overconsolidated samples, exposure to temperature leads to lower maximum deviatoric stress values, higher initial stress ratios, higher positive excess pore pressures and lower stiffness. These effects become more pronounced with higher maximum temperature and increased number of cycles.
- The stress ratio of all samples, with and without temperature history, seems to converge at larger strains before the development of localised shear planes in the normally consolidated samples, suggesting that critical state conditions would be temperature-independent.

Table 6.1 *Initial void ratios*

Test	e_0 prior to any mechanical loading	e_0 prior to thermal loading	e_0 prior to undrained shearing
#nct1	1.152	-	1.105
#nct2	1.209	-	0.992
#nct3	1.207	-	0.975
#nct4	1.178	-	0.941
#oc2t1	1.219	-	1.030
#oc6t1	1.207	-	1.083
#oc6t2	1.155	-	1.085
#ncht1	1.130	1.082	1.094
#ncht2	1.204	0.996	0.999
#oc4ht1	1.158	1.050	-
#oc4ht2	1.137	1.060	0.926
#oc4ht3	1.136	1.077	0.955
#oc6ht1	1.220	1.110	1.125
#oc6ht2	1.185	1.105	1.125
#oc6ht3	1.153	1.103	1.120

Table 6.2 *Rate of development of thermal volumetric strains with temperature (in* $°C^{-1}$*)*

Test	α_e	α_p
#ncht1	4.73E-05	1.15E-04
#ncht2	4.72E-05	1.03E-04
#oc4ht1	5.72E-05	
#oc4ht2	5.59E-05	
#oc4ht3	4.23E-05	
#oc6ht1	5.06E-05	
#oc6ht2	4.27E-05	
#oc6ht3	3.00E-05	
#oc4ht2 after reloading at high T	4.34E-05	2.28E-04
#oc4ht3 after reloading at high T	4.84E-05	

Table 6.3 *Rate of change in void ratio with temperature (in °C^{-1})*

Test	α^*_e	α^*_p
#ncht1	1.62E-04	3.04E-04
#ncht2	1.56E-04	2.77E-04
#oc4ht1	1.82E-04	
#oc4ht2	1.79E-04	
#oc4ht3	1.52E-04	
#oc6ht1	1.72E-04	
#oc6ht2	1.56E-04	
#oc6ht3	1.28E-04	
#oc4ht2 after reloading at high T	1.43E-04	4.98E-04
#oc4ht3 after reloading at high T	1.55E-04	

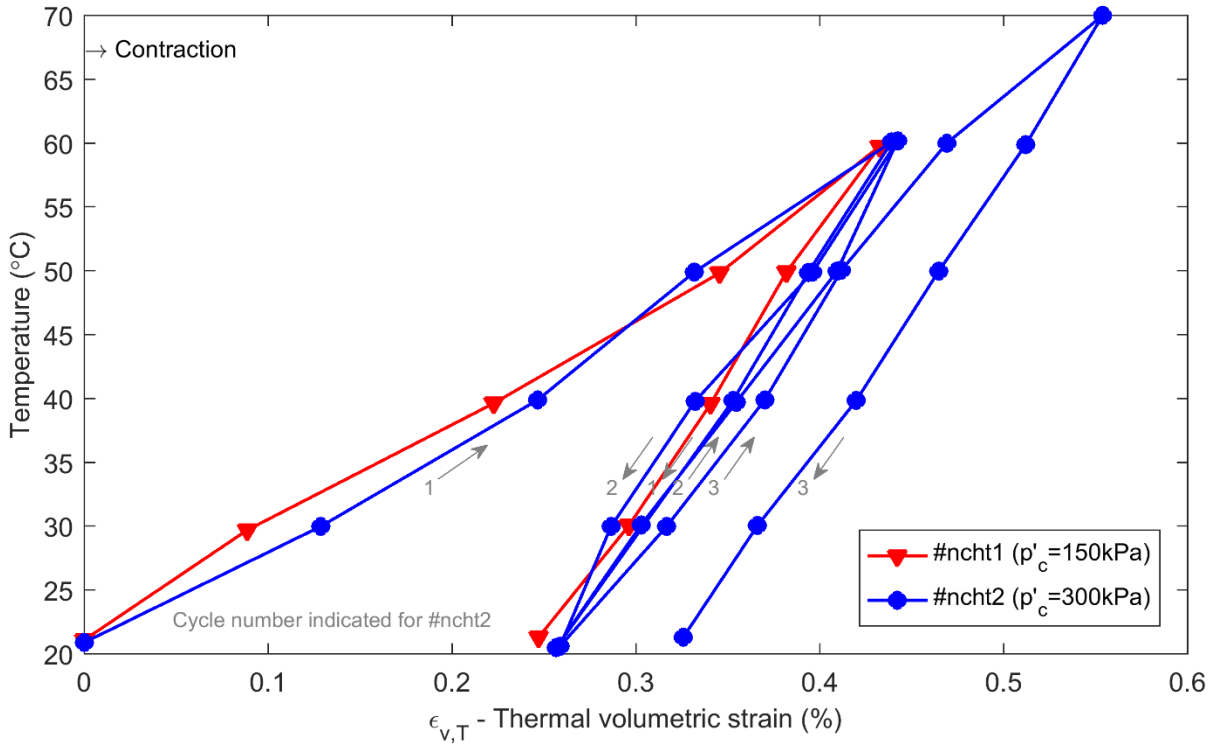

Figure 6.1 *Thermal volumetric strains for the normally consolidated samples*

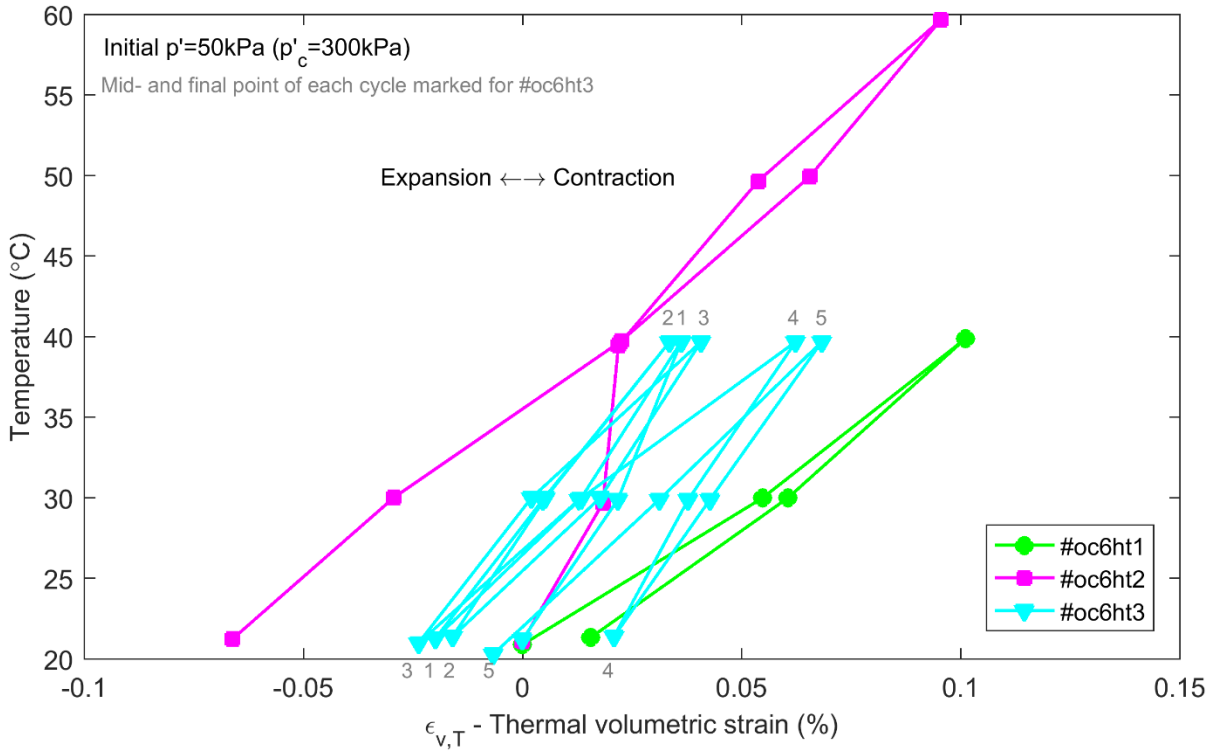

Figure 6.2 *Thermal volumetric strains for the OCR6 samples*

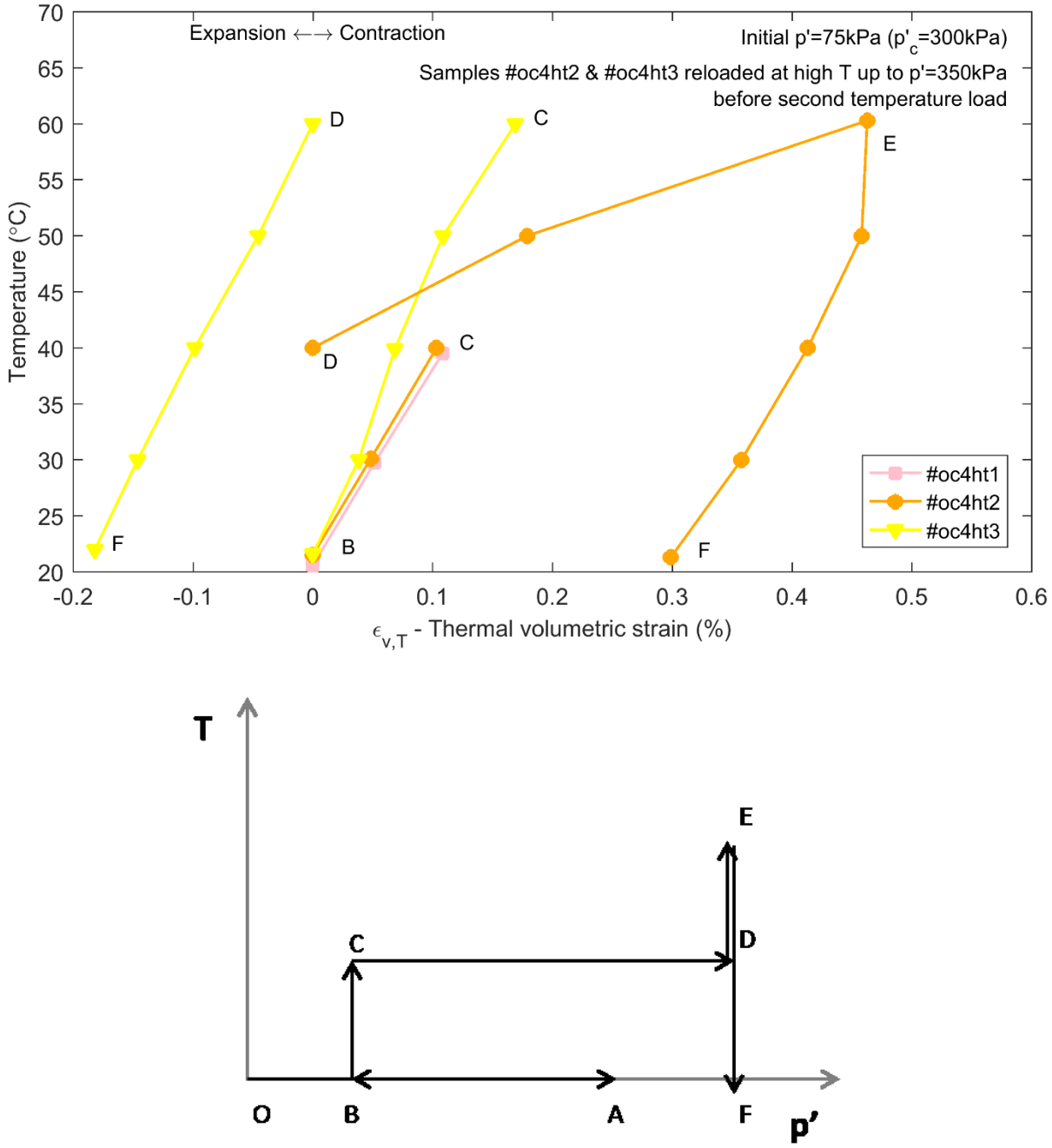

Figure 6.3 *Thermal volumetric strains for the OCR4 samples (also reloaded at high T)*

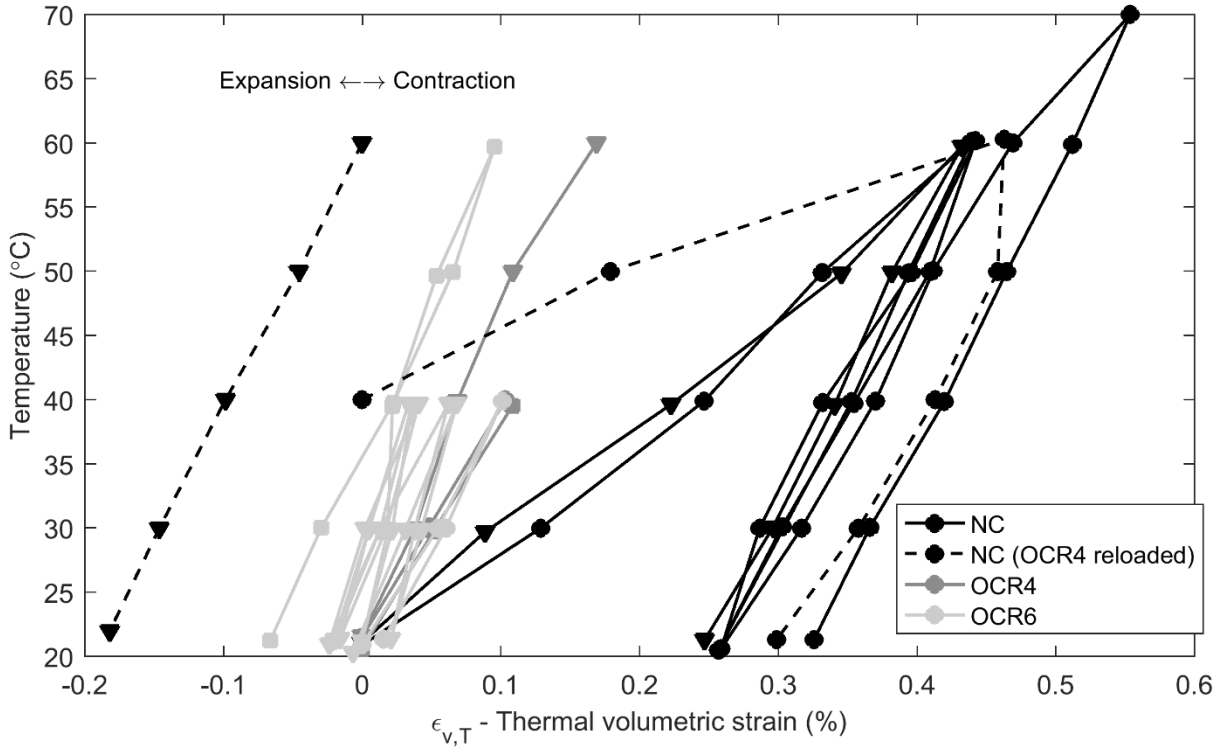

Figure 6.4 *Thermal volumetric strains for all samples*

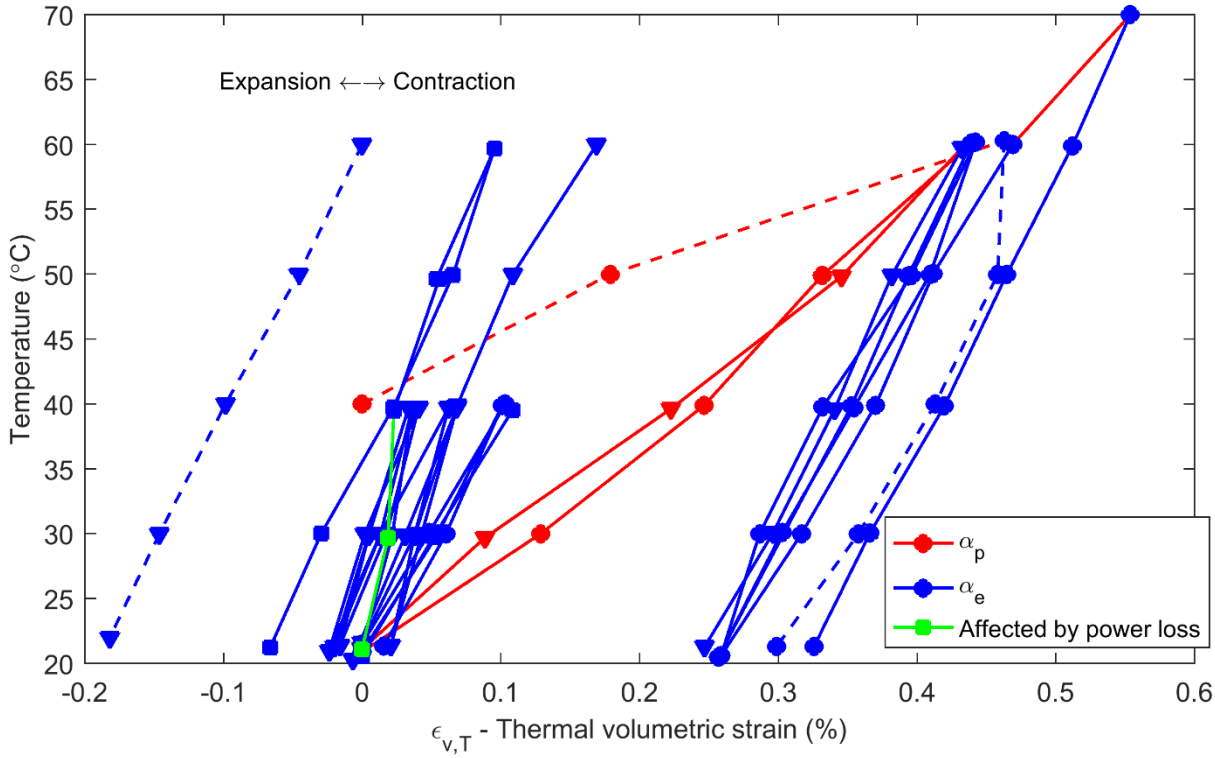

Figure 6.5 *Different gradients of volume changes with temperature*

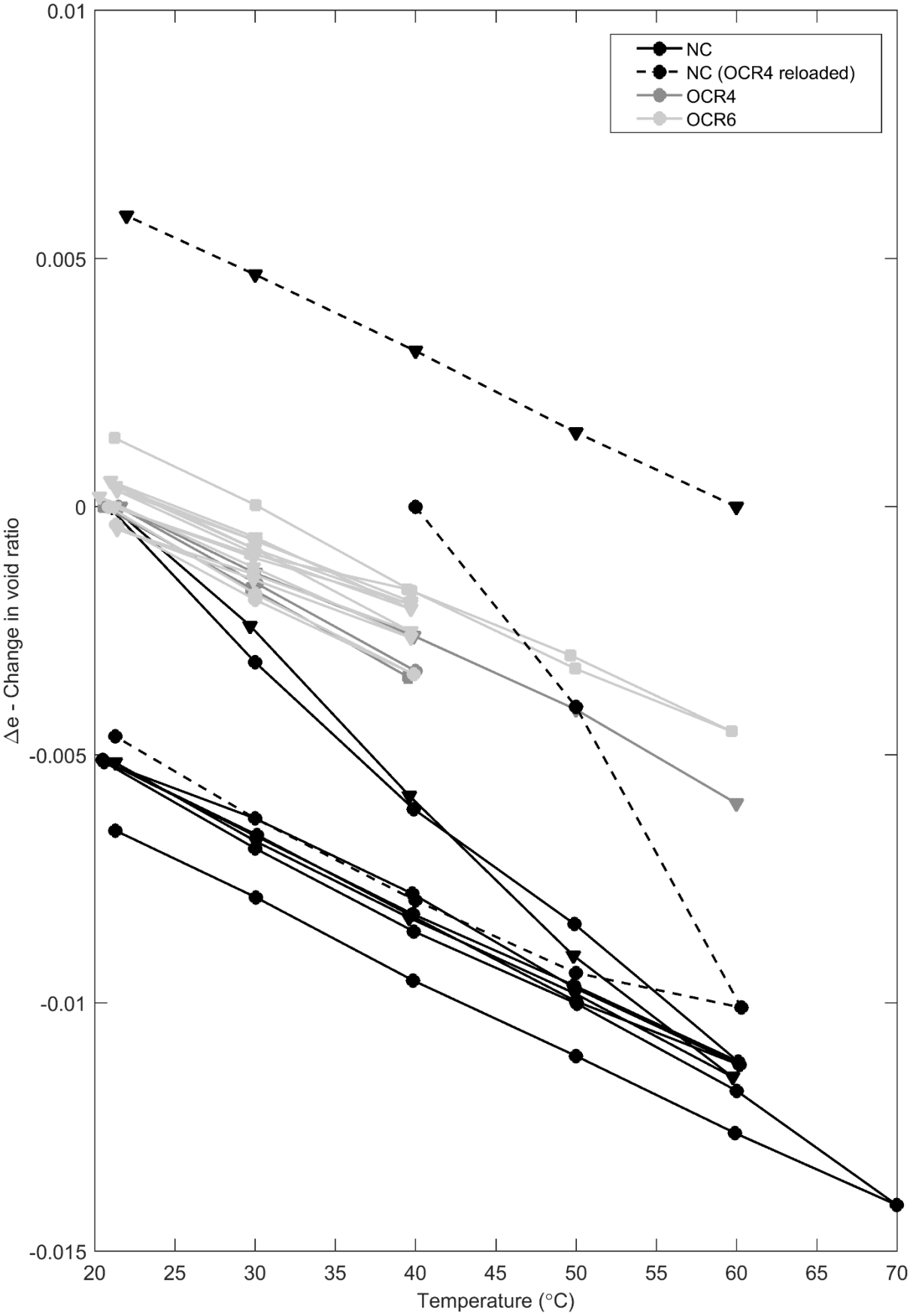

Figure 6.6 *Changes in void ratio during drained temperature changes for all samples*

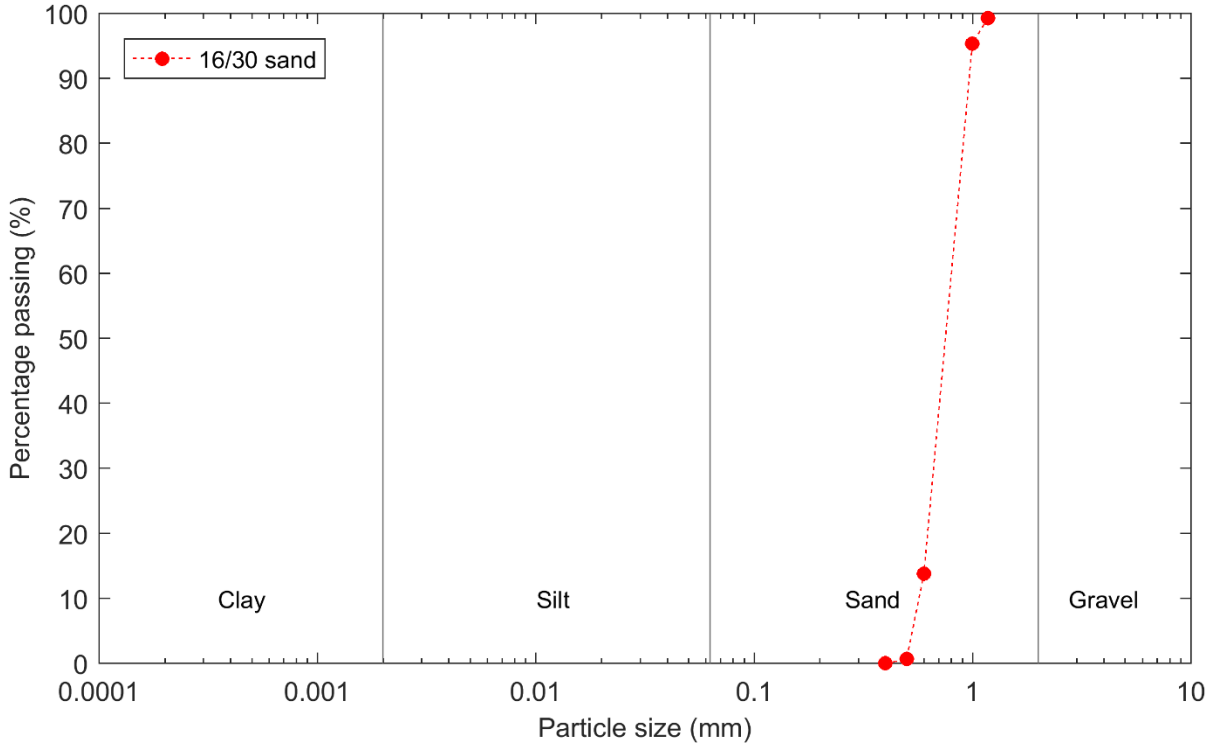

Figure 6.7 *Particle size distribution of the 16/30 sand*

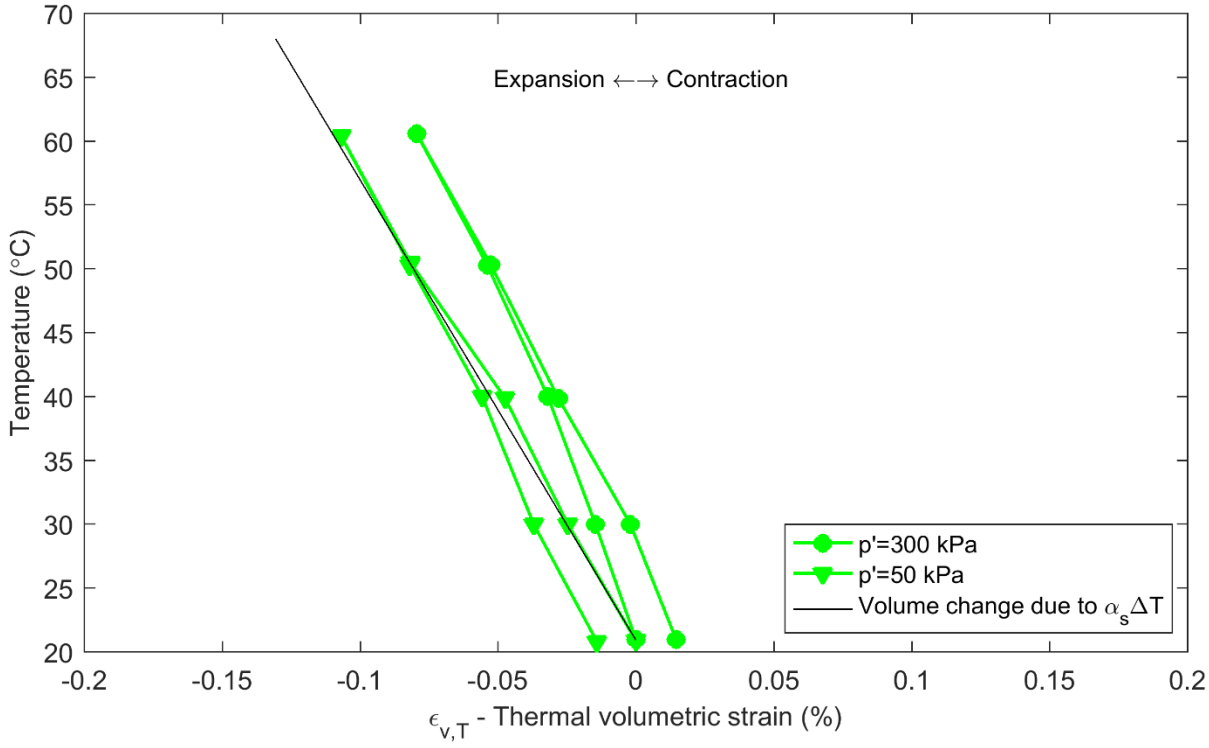

Figure 6.8 *Thermal volumetric strains of the 16/30 sand sample*

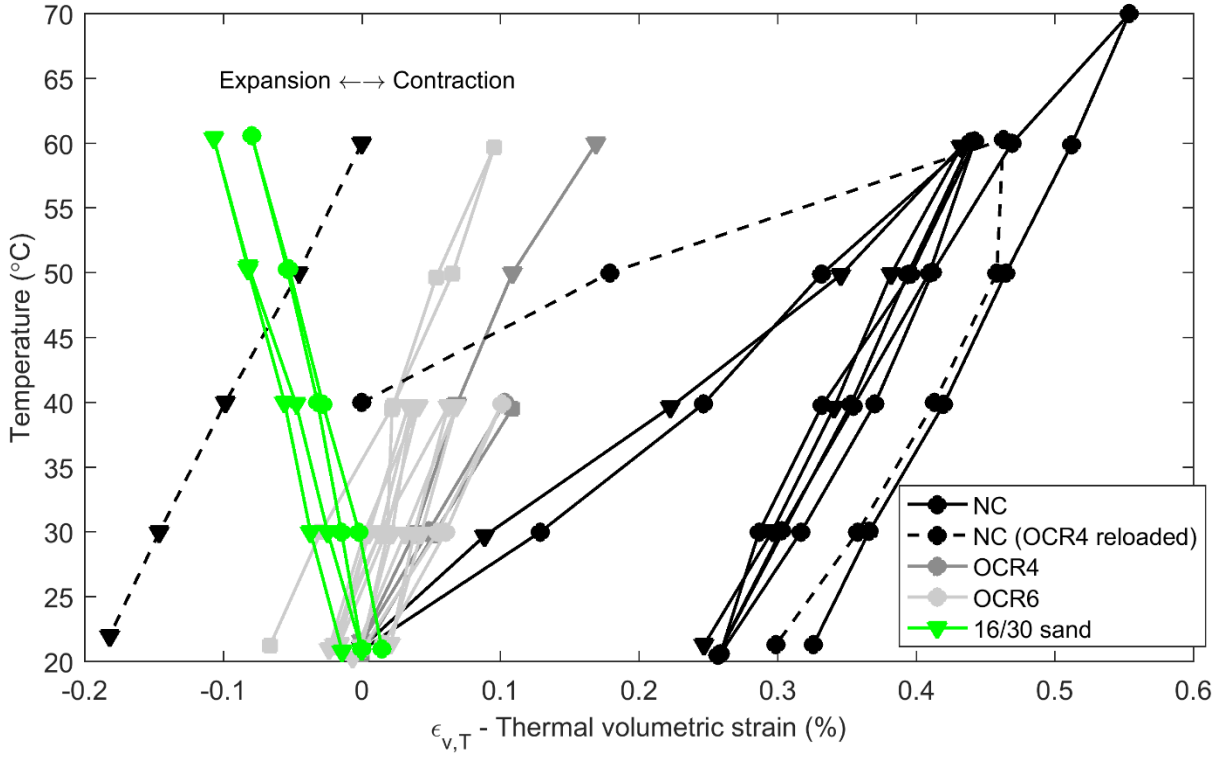

Figure 6.9 *Thermal volumetric strain results of the 16/30 sand and London clay together*

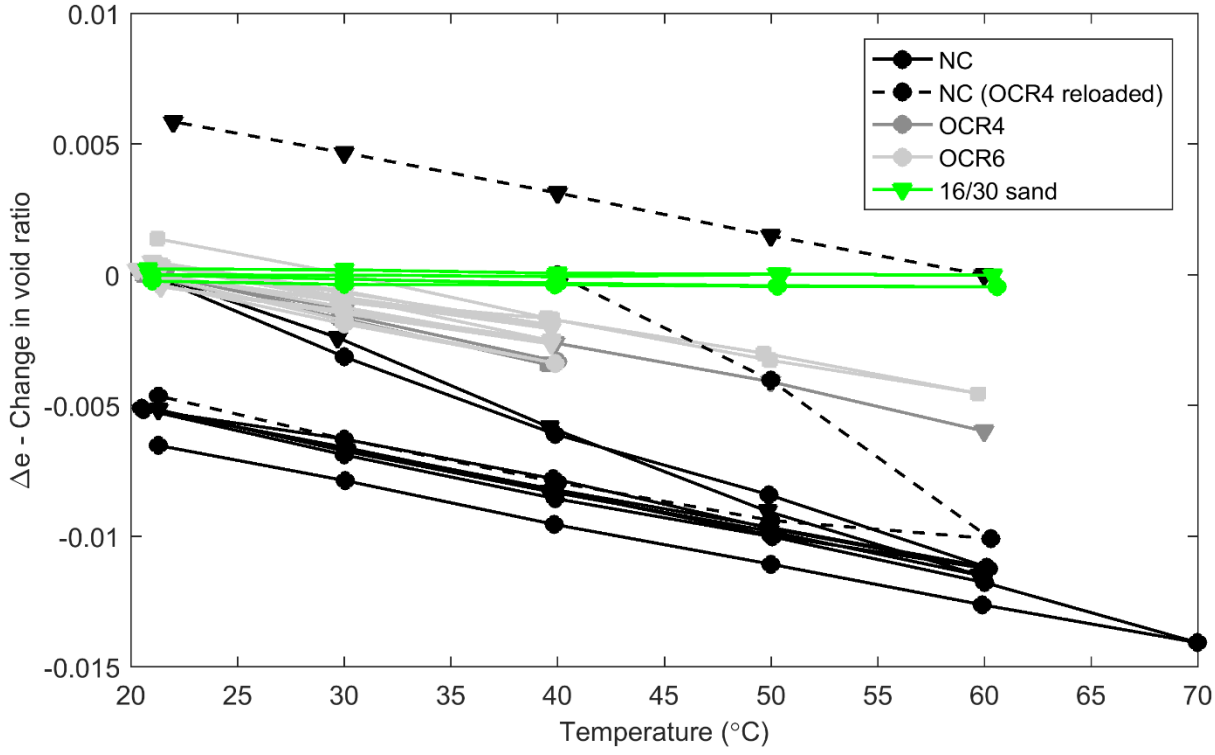

Figure 6.10 *Thermally-induced changes in void ratio results of the 16/30 sand and London clay together*

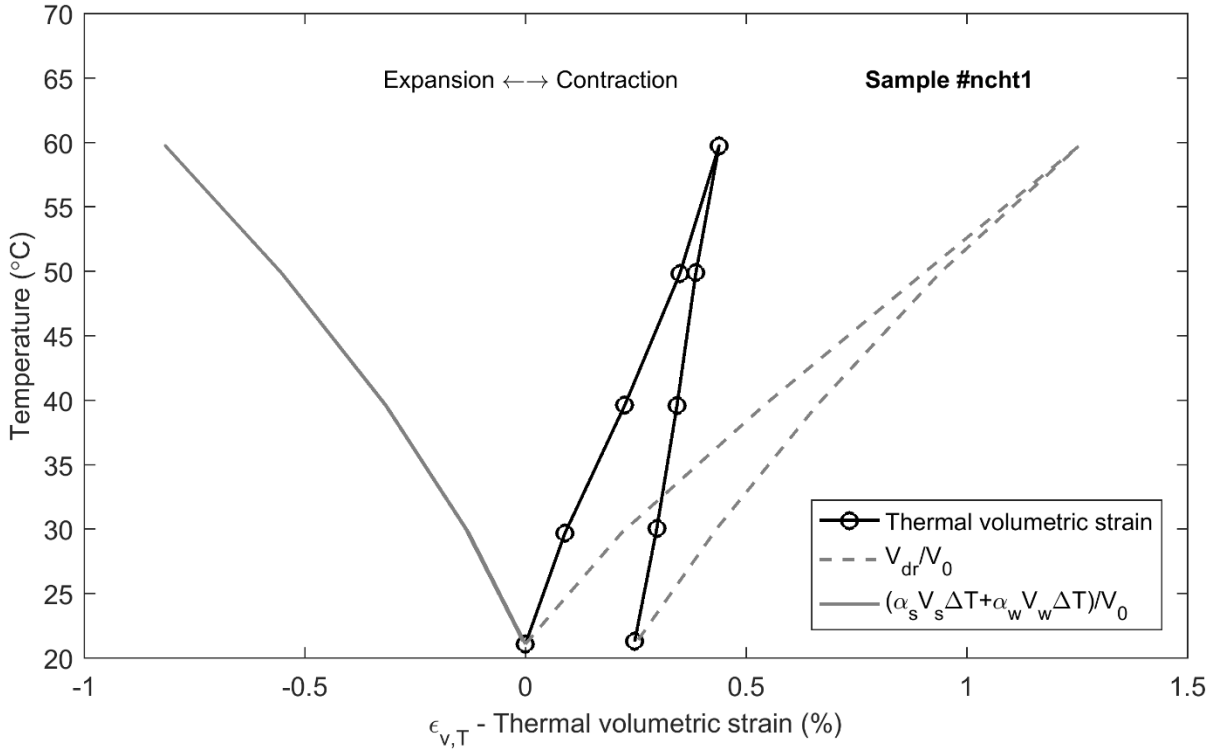

Figure 6.11 *Estimation of the volumetric thermal strain from the Campanella and Mitchell framework in test #ncht1*

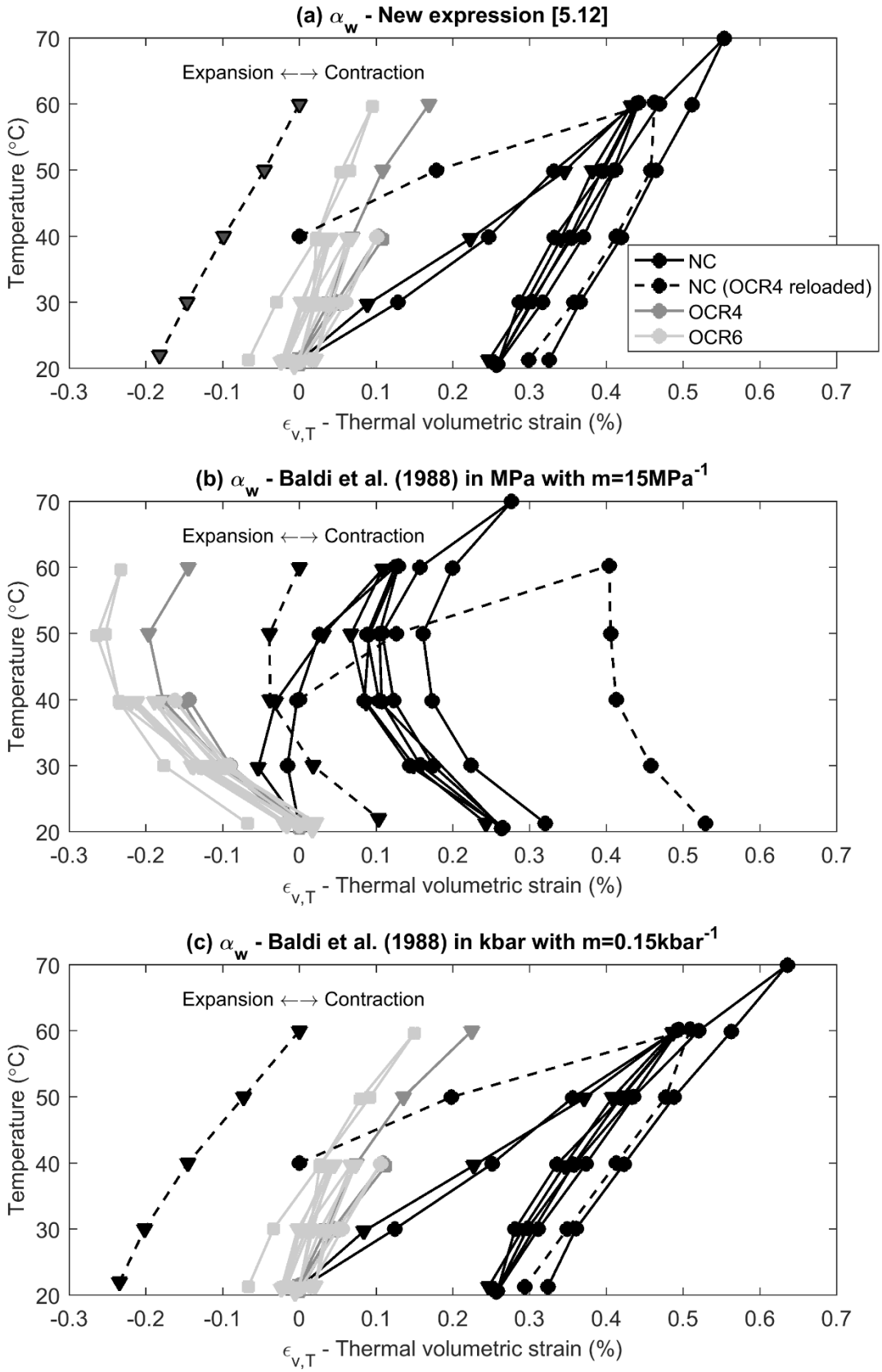

Figure 6.12 *Influence of the choice of the coefficient of thermal expansion of water*

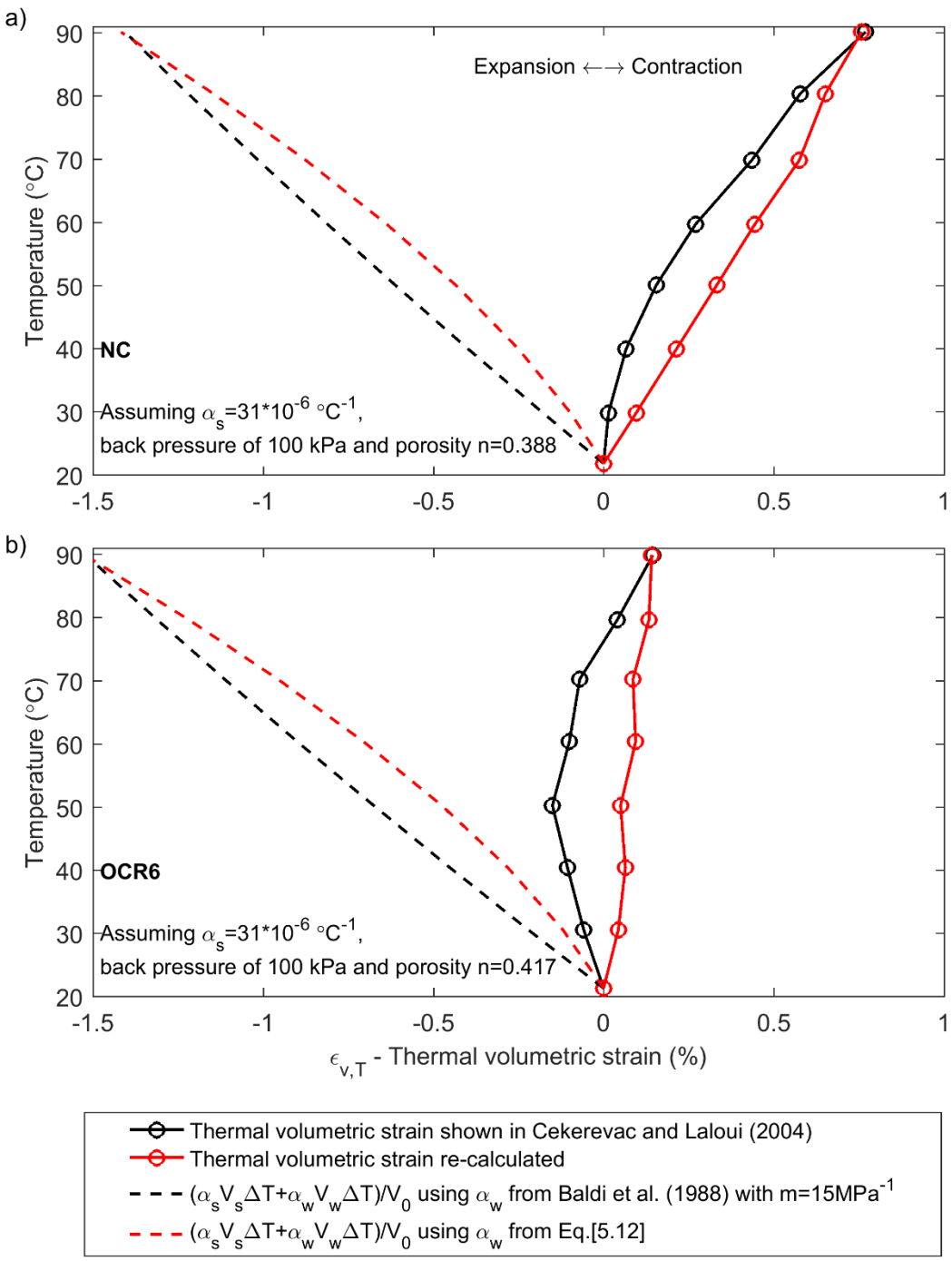

Figure 6.13 *Reanalysis of the thermal strains reported in Cekerevac and Laloui (2004)*

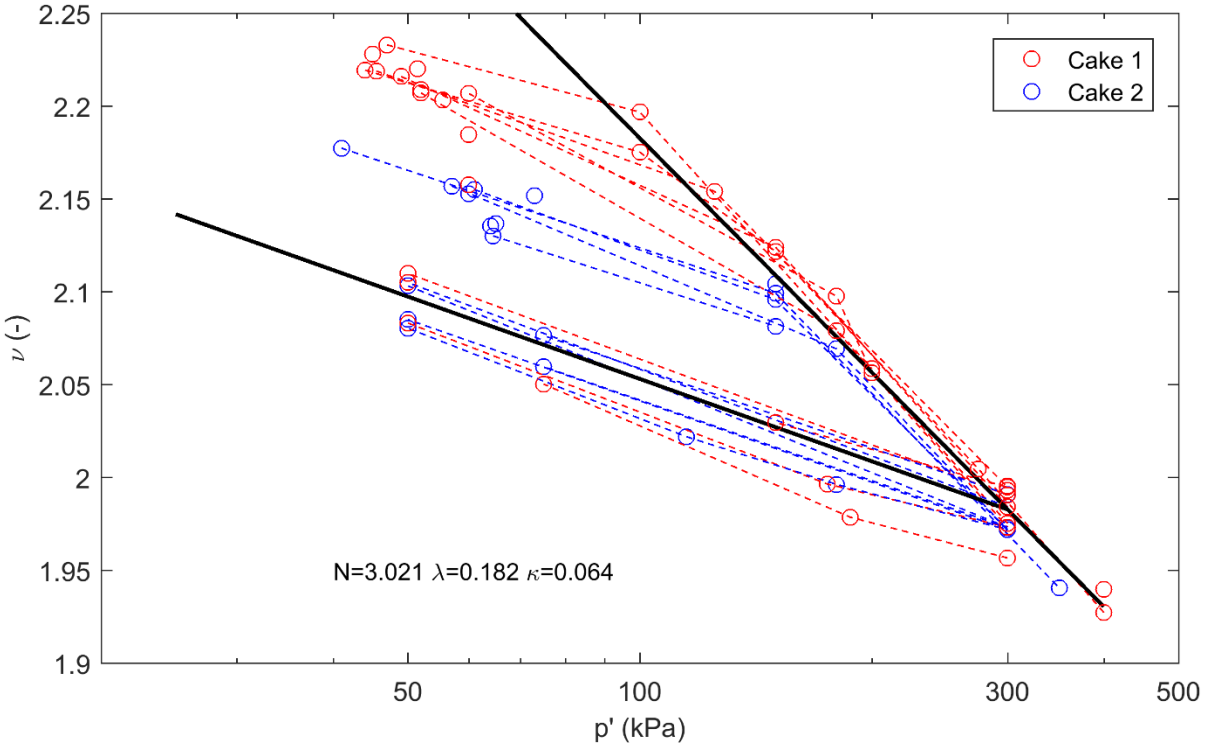

Figure 6.14 *Compression data at room temperature*

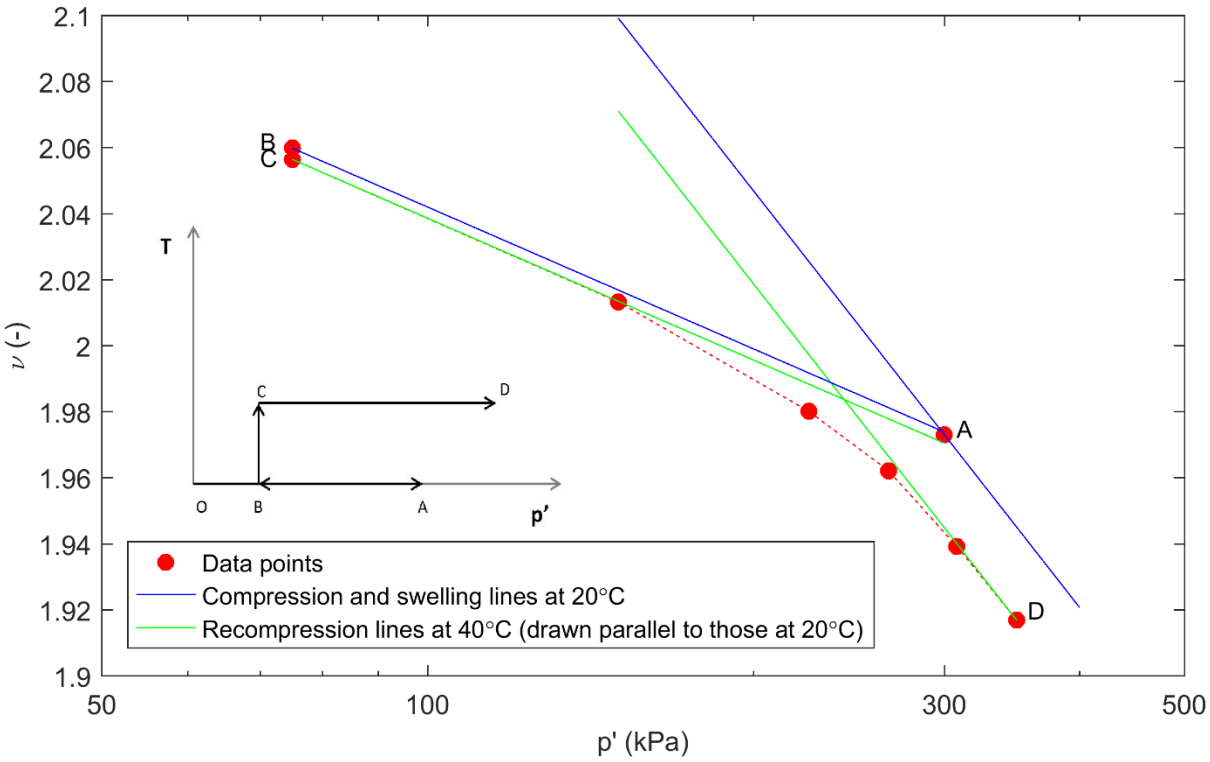

Figure 6.15 *Reloading at 40 °C of sample #oc4ht2*

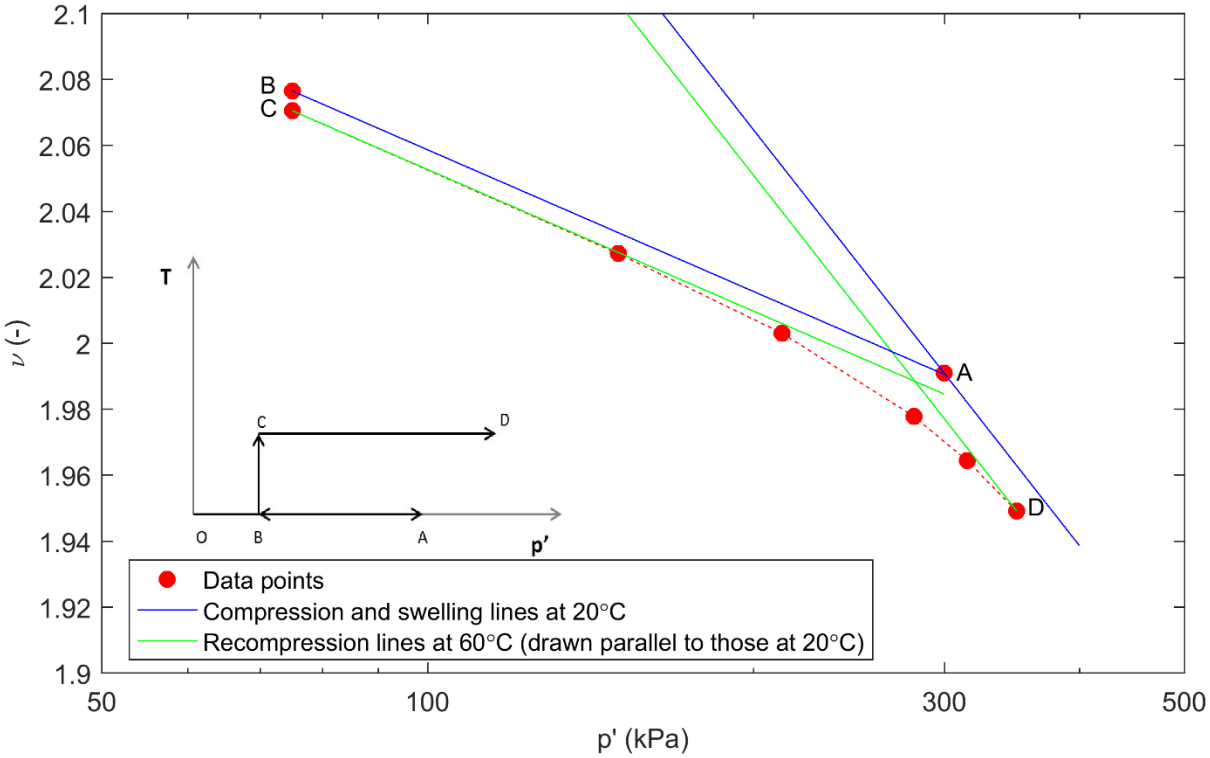

Figure 6.16 *Reloading at 60 °C of sample #oc4ht3*

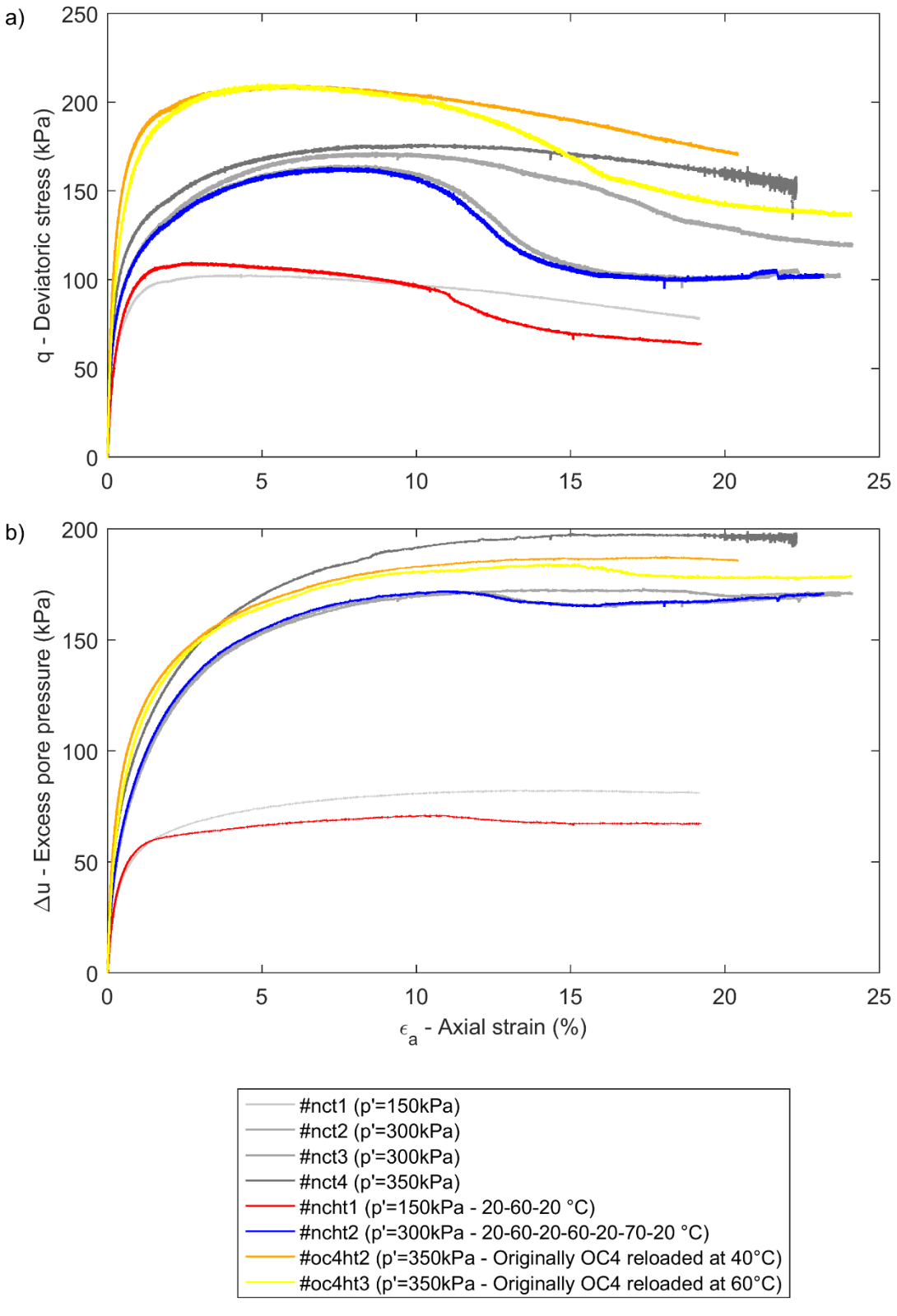

Figure 6.17 *Shearing data of the normally consolidated samples*

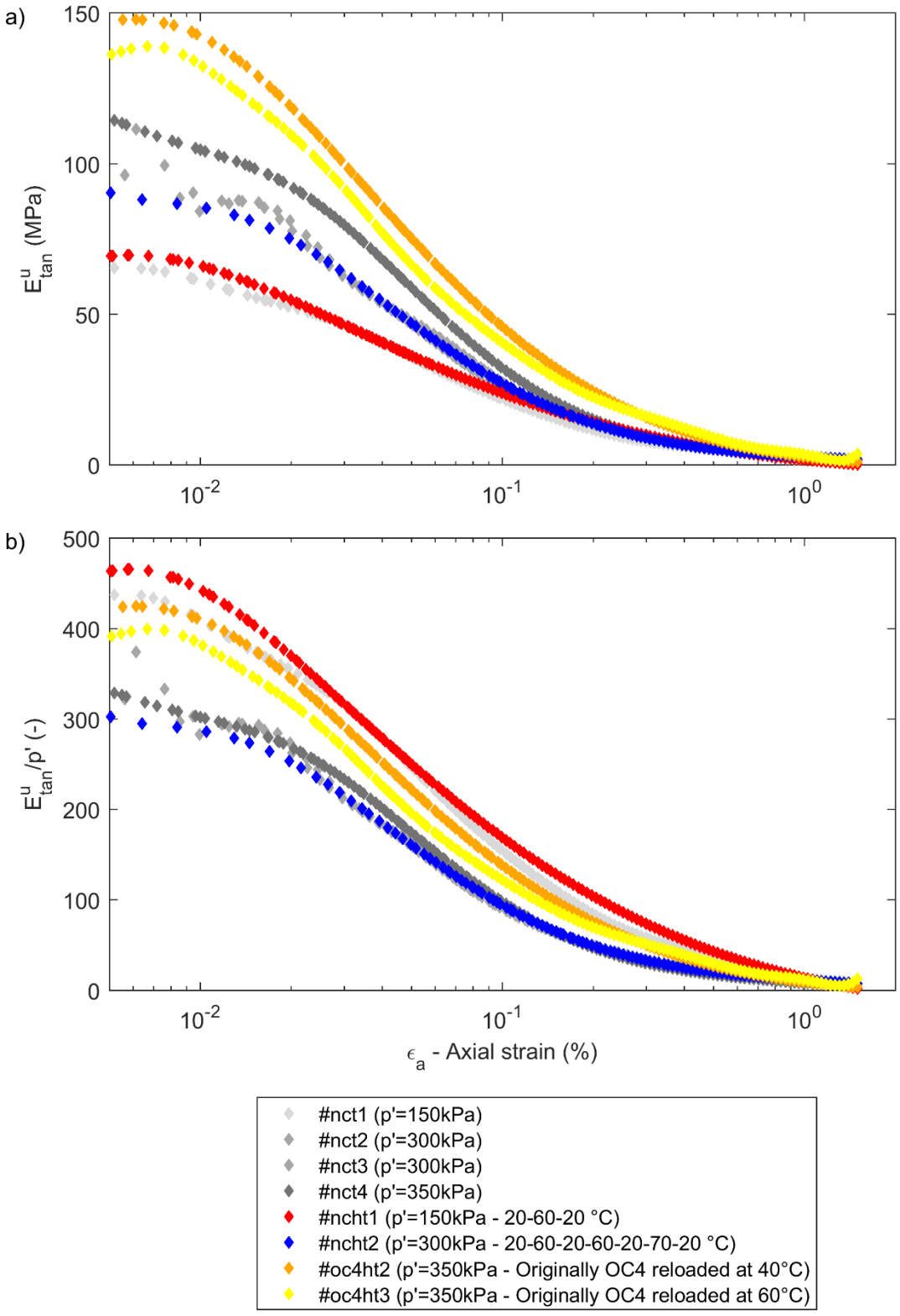

Figure 6.18 *Stiffness of the normally consolidated samples*

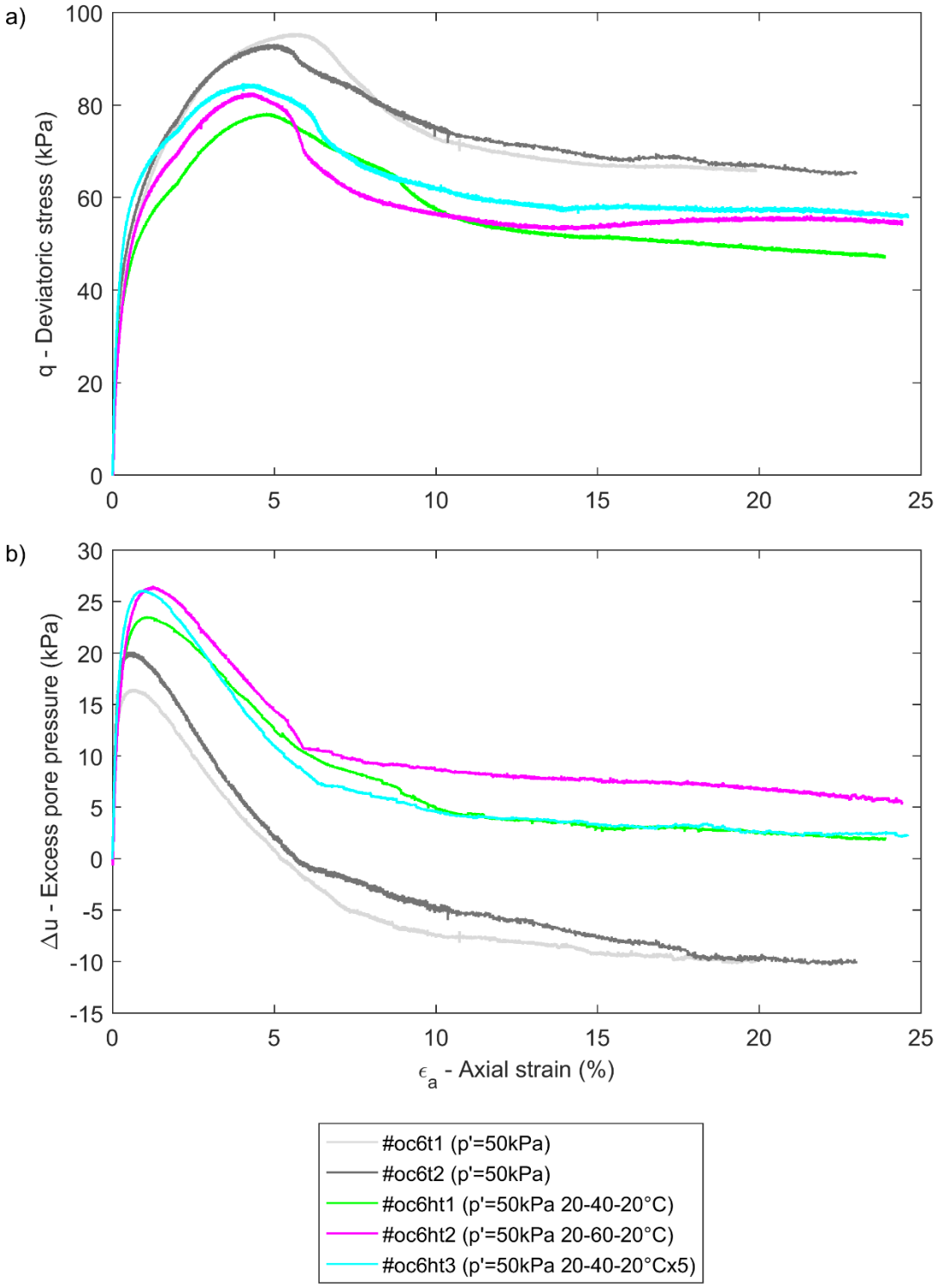

Figure 6.19 *Shearing data of the overconsolidated samples*

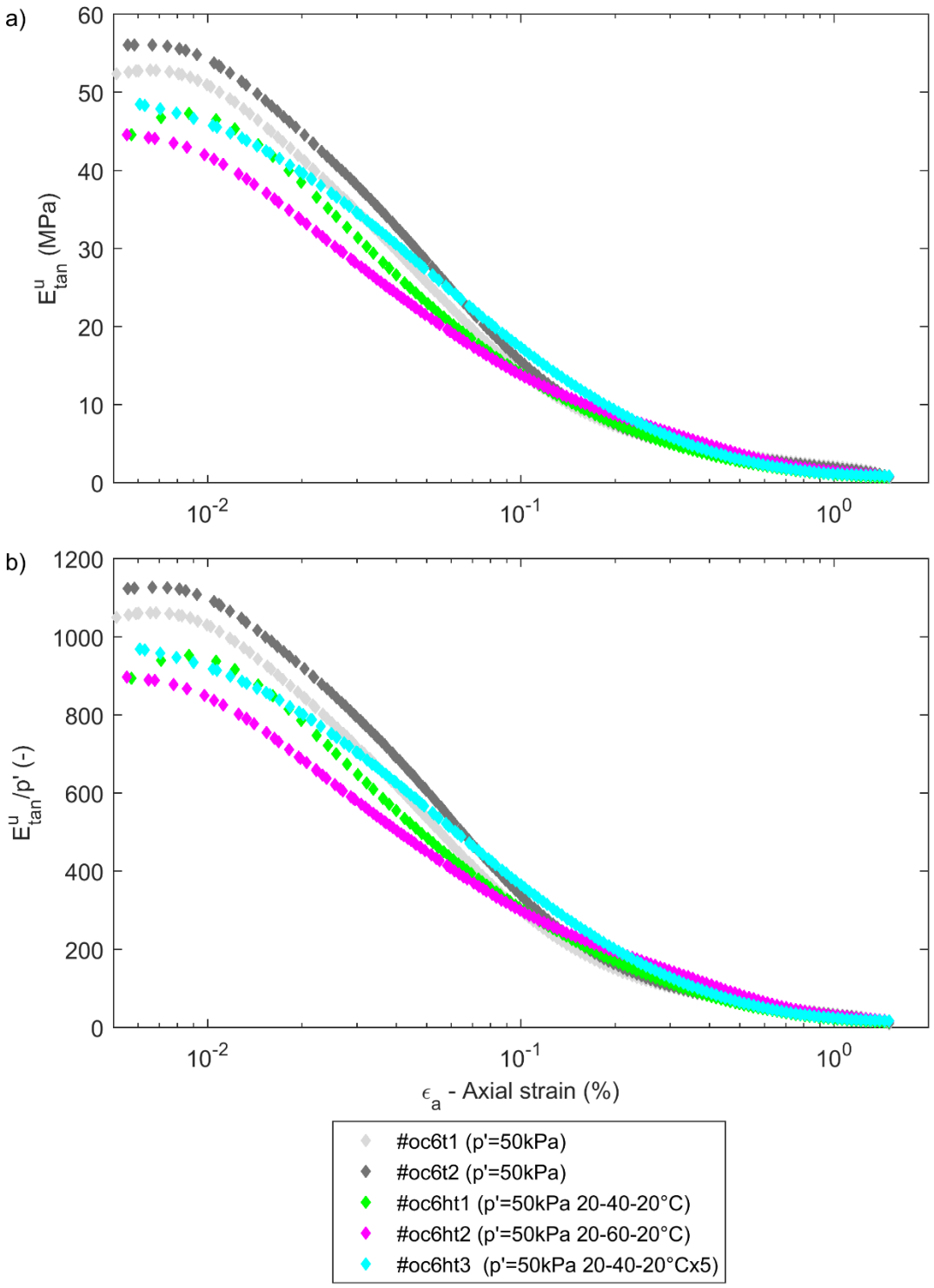

Figure 6.20 *Stiffness of the overconsolidated samples*

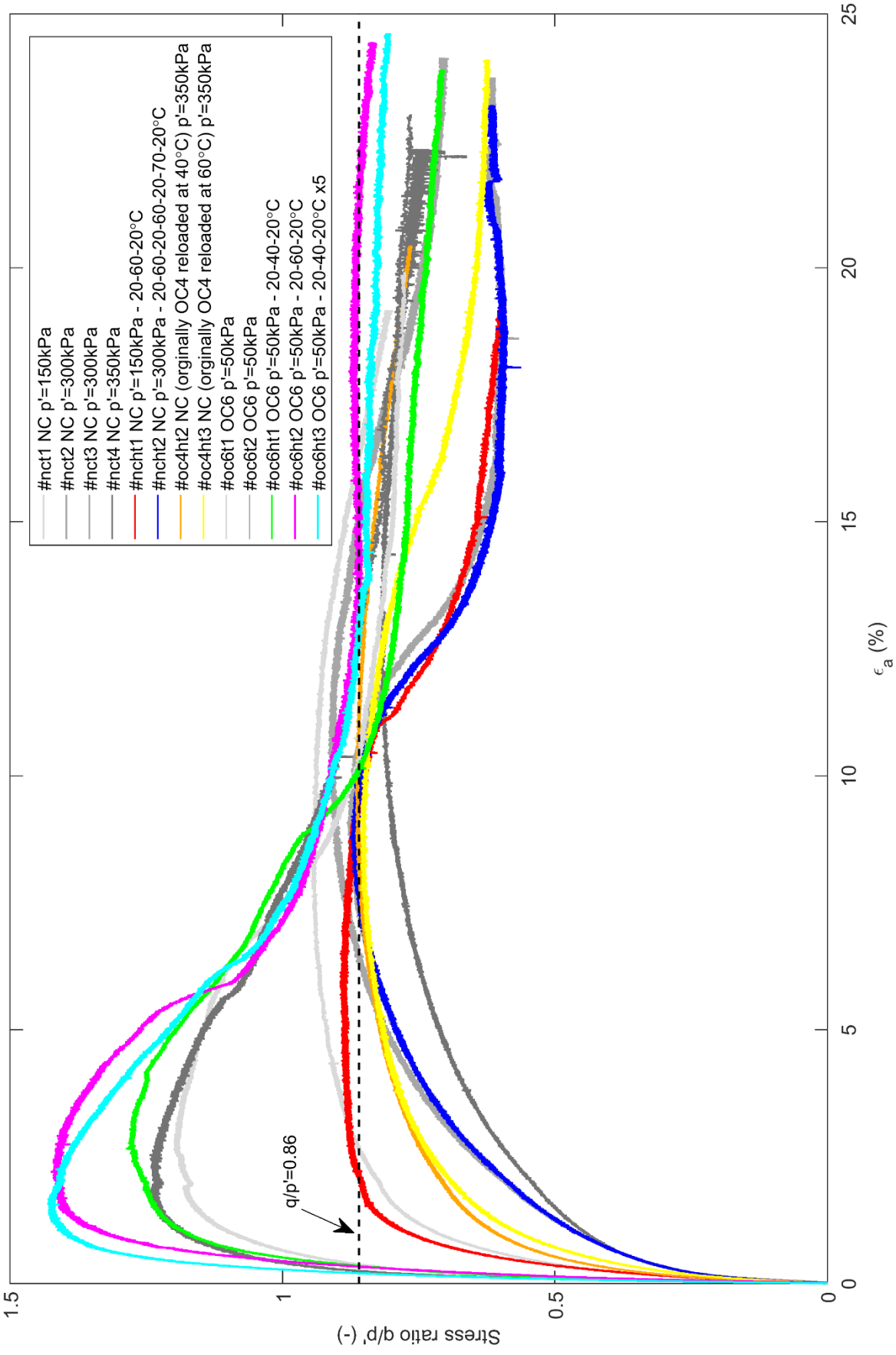

Figure 6.21 *Stress ratio evolution during shearing for all tests*

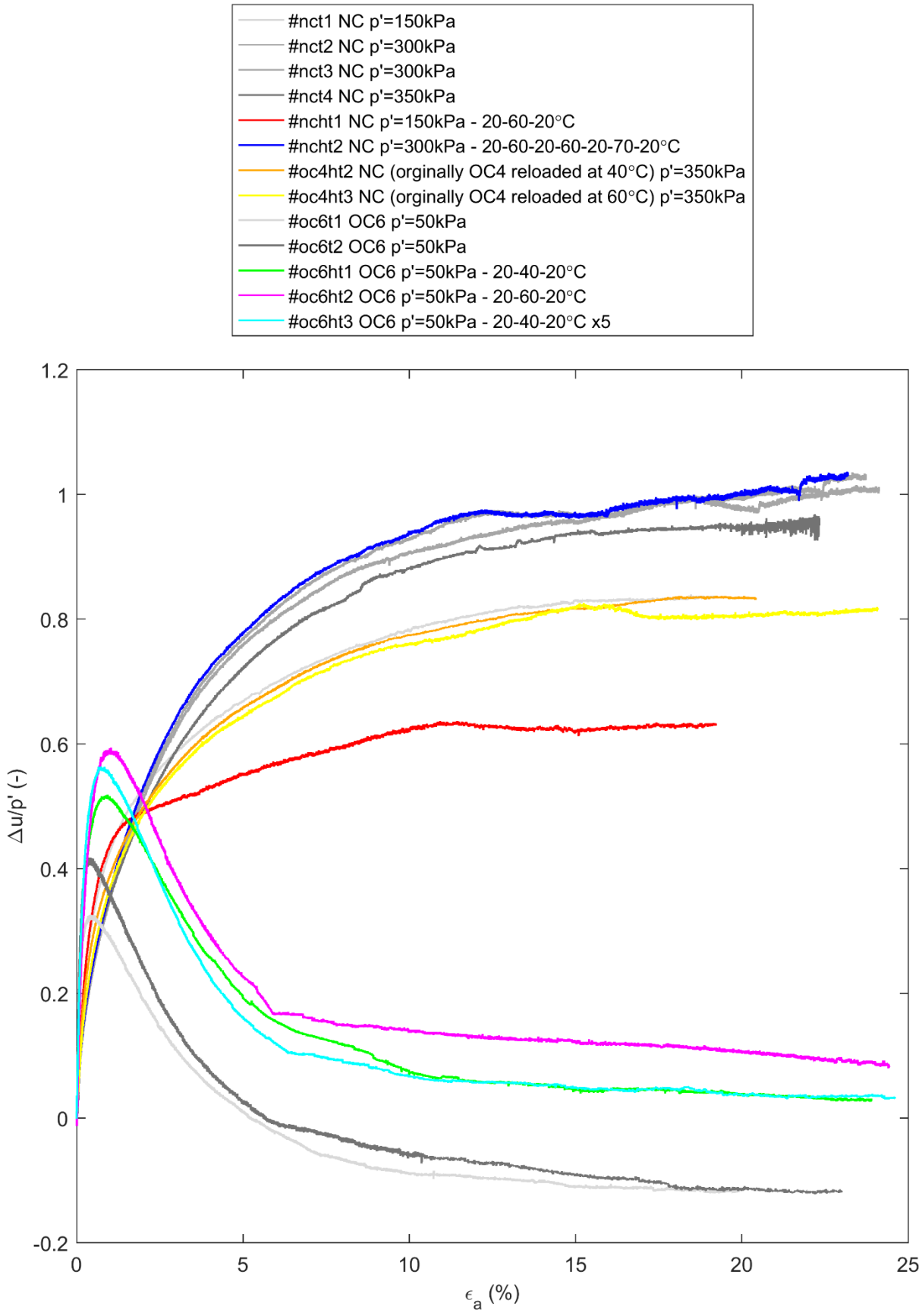

Figure 6.22 *Normalised excess pore pressure during shearing*

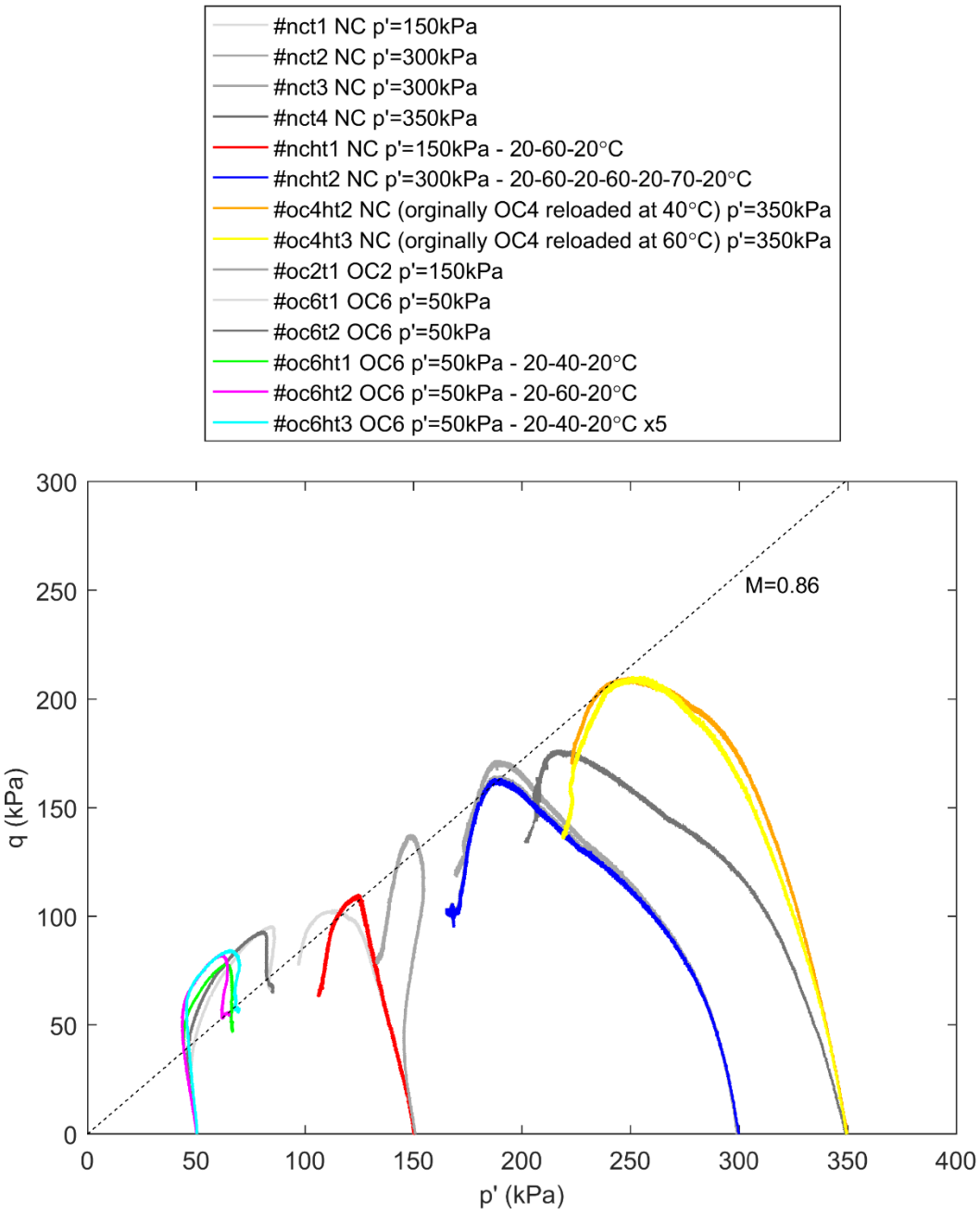

Figure 6.23 *Stress paths for all tests*

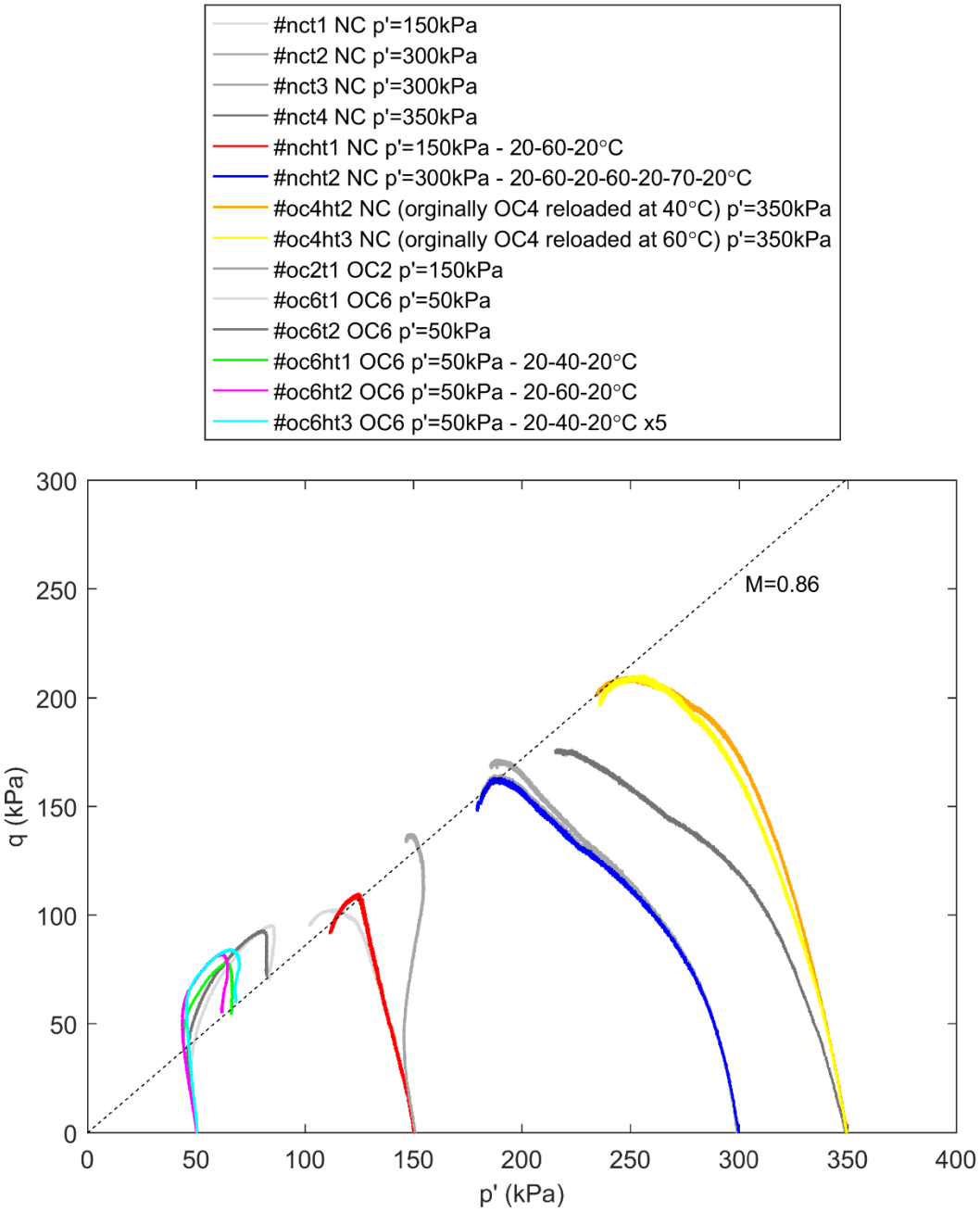

Figure 6.24 *Stress paths considering data up to 11% strain only*

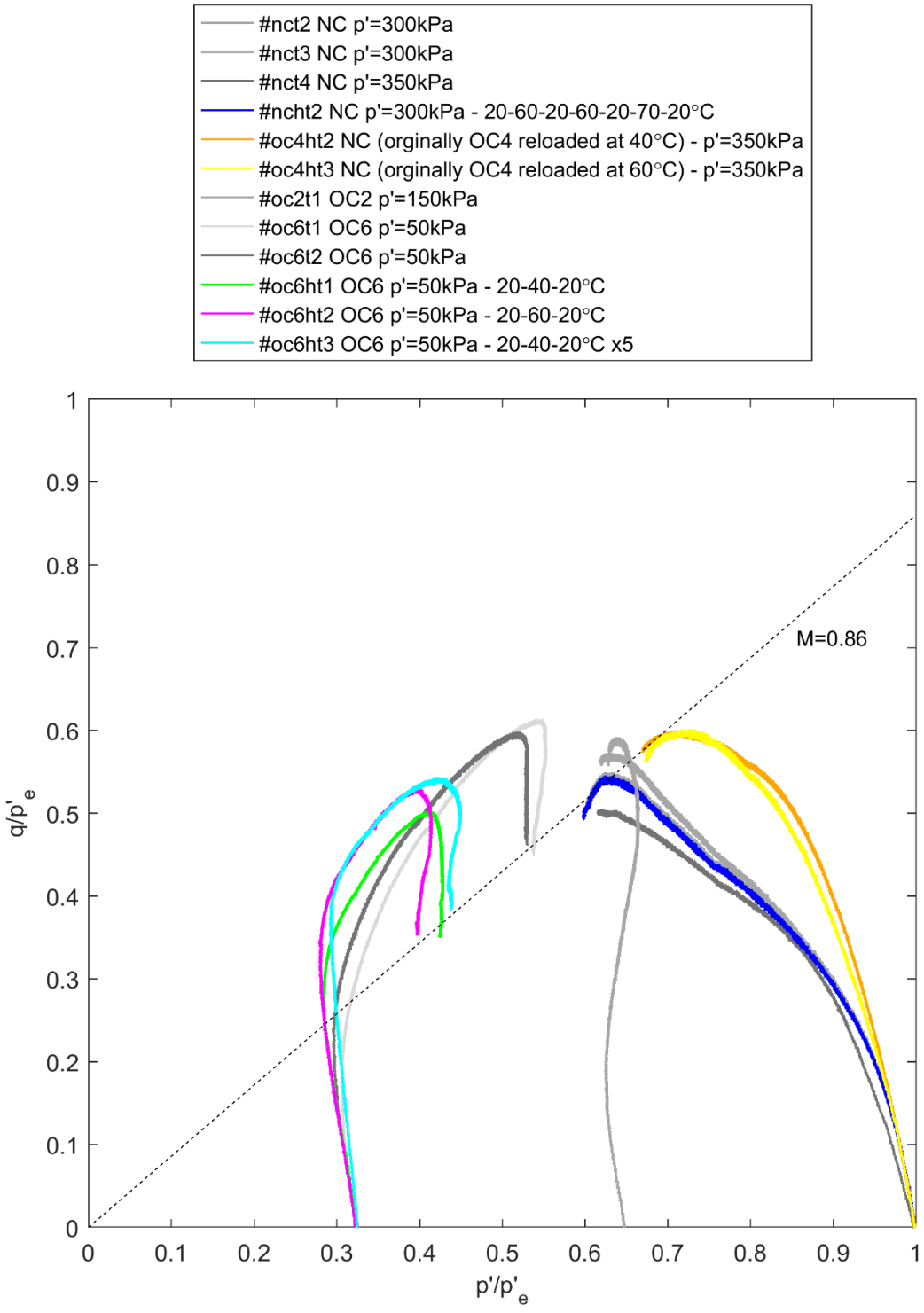

Figure 6.25 *Normalised stress paths considering data up to 11% strain only*

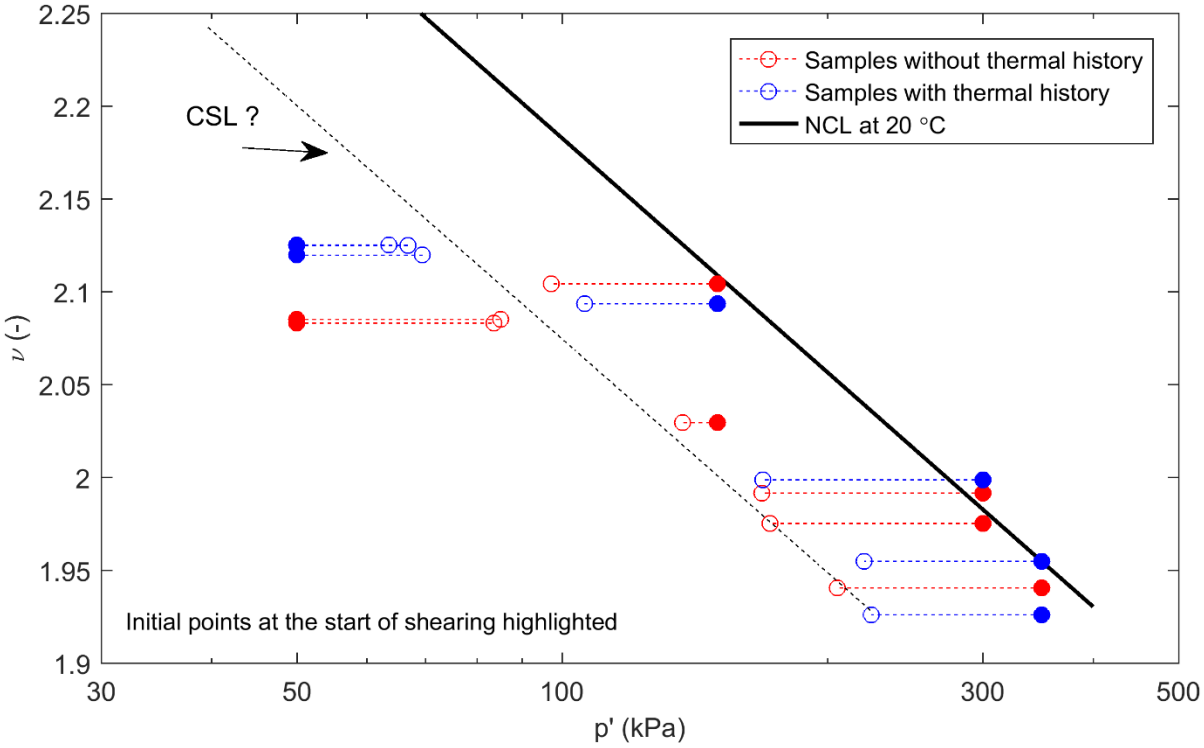

Figure 6.26 *Undrained shearing in the volumetric plane*

7. THERMAL PROPERTIES

7.1 Introduction

This chapter presents and discusses the results of the measurement of the thermal properties of reconstituted and intact London clay samples using the single needle and the dual-probe heat pulse techniques. The measured values of thermal conductivity, volumetric heat capacity and thermal diffusivity are compared to the predictions of several theoretical and empirical models.

7.2 Thermal conductivity

The experimental techniques of single needle and dual-probe heat-pulse tests for measuring the thermal conductivity (λ, in $Wm^{-1}K^{-1}$) of soils were presented in Chapter 5, together with their calibration and interpretation. This section presents the results of the thermal conductivity of the reconstituted and intact London clay samples using both techniques. A comparison is then made between the two sets of results, before assessing and discussing the thermal conductivity of London clay in terms of different modelling approaches.

7.2.1 Single needle test

As explained in Chapter 5, the thermal conductivity of the samples was measured in single needle tests using both the heating and cooling part of the temperature-time data series. A comparison between the thermal conductivities obtained with each section of the data is shown in Figure 7.1 with separate data points for intact and reconstituted samples. The solid black line represents an ideal result of $\lambda_{heating} = \lambda_{cooling}$, while the set of grey lines are contours representing the percentage deviation from the ideal result. Out of the 85 measurements shown for intact samples, the maximum differences in the thermal conductivity obtained using the cooling part of the data, compared to the heating part, are +8.71% and -5.34%, with on average +0.34% (s.d. 2.92%) higher thermal conductivities obtained using the cooling data. Likewise, out of the 46 measurements shown for reconstituted samples, the

maximum differences in thermal conductivity obtained using the cooling data, compared to the heating data, are +8.84% and -6.14% with an average of -0.40% (s.d. 3.46%). For both types of samples, the difference between the conductivity calculated from the heating and cooling parts of the temperature-time data is very small and either value can be considered appropriate.

The measured thermal conductivities for both reconstituted and intact samples are plotted against the porosity in Figure 7.2, showing individual measurements from heating, SN(h), and cooling SN(c), parts of each tests. On the other hand, Figure 7.3, displays the average conductivites for each sample and the corresponding range of measured values. The two plots also separate the direction of the single needle (SN) insertion in the sample, resulting in horizontal or vertical line heat sources as explained in Chapter 5. The information of the source of measurement is also provided in the figures: #CSx being the number of intact sample of London clay from the Hyde Park and #V&Ax the number of the reconstituted London clay sample from the V&A site, as listed in Table 5.7.

Two immediate observations arise from both figures: (a) a clear trend between thermal conductivity and porosity and (b) the influence of the direction of measurement. As the porosity of the sample increases (hence the relative volume fraction of the fluid phase), the conductivity decreases due to the different relative conductivities of the solid (~3 $Wm^{-1}K^{-1}$) and fluid (~0.6 $Wm^{-1}K^{-1}$) phases. For all samples studied, irrespective of the porosity, the thermal conductivity measured by inserting the needle vertically in the sample (and hence temperature radiating horizontally from it) is higher than when inserting it horizontally.

The average thermal conductivity of intact samples ranges from 1.22 to 1.33 $Wm^{-1}K^{-1}$ in the case of horizontal heat source measurements, and from 1.48 to 1.60 $Wm^{-1}K^{-1}$ in the case of a vertical heat source. The average scatter in the measurements of the conductivity in the intact samples is of ± 0.05 and ± 0.04 $Wm^{-1}K^{-1}$ for the vertical and horizontal heat source tests respectively. Sample #CS22 produces the lowest conductivities for both directions of measurement, while sample #CS16 produces the highest conductivity for a vertical heat

source and sample #CS44 for the horizontal heat source. Apart from sample #CS22 which has a distinctly higher porosity, the other six intact samples only cover a small range of porosities, between 0.398 in the case of #CS60 and 0.426 for #CS36, and the differences in the values measured between them cannot only be explained by the small differences in porosities. This becomes especially relevant in the case of samples #CS16 and #CS36, which despite being very similar in terms of porosity and water content present significant differences in the measured values of conductivity. Two reasons may explain these discrepancies: physical differences between the samples (mineralogy, particle size distribution), which will be later discussed, and experimental conditions. The latter can be caused by several factors: inevitable temperature drifts in the laboratory, poor contact between the soil and the needle if it is not coated in thermal grease, contact disturbance by pre-drilling the sample to ease needle insertion. The influence of laboratory temperature fluctuations can be minimised, as discussed in Chapter 5, if tests are performed in a controlled environment and only the portion of the cooling data of equal duration to the heating phase is considered for analysis.

In the case of reconstituted samples, given the wide range of porosities covered, between 0.435 (#V&At6) and 0.619 (#V&At1), the dependency of the thermal conductivity on the porosity becomes more obvious. Sample #V&At1 presents, as expected, the lowest thermal conductivities: 1.12 and 1.03 $Wm^{-1}K^{-1}$ for vertical and horizontal line heat source tests respectively; while sample #V&At6 presents the highest thermal conductivities: 1.49 and 1.30 $Wm^{-1}K^{-1}$. The samples of intermediate porosities further confirm the influence of porosity on the thermal conductivity. The average scatter in the measurements of the conductivity in the reconstituted samples is of ± 0.03 $Wm^{-1}K^{-1}$ for both directions of measurement. It is also interesting to note that the trend of the variation of thermal conductivity as a function of porosity in the reconstituted samples could predict the value of the thermal conductivity of intact samples reasonably well, for both directions of measurement.

7.2.2 Dual-probe heat-pulse test

The thermal conductivity of the reconstituted and intact London clay samples was also measured in dual-probe heat-pulse tests, using both the single point method and the nonlinear fit that involves the portion of the data that obeys $\Delta T(t) \geq 0.75T_m$ (where T_m is the maximum temperature rise in the monitoring needle). A comparison between the thermal conductivities obtained via the two methods is shown in Figure 7.4. It is clear that the measurements plot on both sides of the equality line, but are more concentrated above it, indicating higher values of λ interpreted with the weighted nonlinear fit method. Out of the 109 measurements shown for intact samples, the maximum differences in the thermal conductivity obtained using the nonlinear fit method, compared to the single point method, are +5.35% and -3.07%, with on average +1.32% (s.d. 1.61%) higher thermal conductivities obtained via the nonlinear fit method. Similarly, out of the 59 measurements shown for reconstituted samples, the maximum differences in thermal conductivity obtained using the nonlinear fit, compared to the simpler single point method, are +9.28% and -3.91% with an average of +1.99% (s.d. 2.09%).

In dual-probe heat-pulse tests, regardless of the analysis method used, the thermal conductivity is obtained by multiplying the other two "measured" thermal properties (volumetric heat capacity and thermal diffusivity), which are discussed in the subsequent sections of this Chapter. Discrepancies in the thermal conductivities obtained using both methods arise thus from discrepancies in the measurement of the other two properties and are significantly smaller than the measurement error as seen in the calibration tests performed in water-agar samples (Chapter 5, Table 5.6). The thermal conductivities reported in the following discussion and figures correspond to those obtained using the simpler single point method.

The results of these tests, plotted against the porosity of the sample as for the single needle tests, are shown in Figure 7.5, with all data points and in Figure 7.6, with just average values from each test and the respective range. As before, the two plots also separate the direction of the dual needle (DN) insertion in the sample, vertical or horizontal, with the latter being for all orientations of the two needles with repect to the horizontal plane as explained in Chapter

5. A very similar image to that of the single needle test arises: (a) influence of porosity; (b) direction of measurement; and (c) good agreement between reconstituted and intact samples. In the case of the intact samples, the lowest thermal conductivities for vertical and horizontal heat sources, 1.27 and 1.50 $Wm^{-1}K^{-1}$, are found in the more porous (0.460) sample, #CS22. The conductivities of the remaining six intact samples with porosities ranging from 0.398 to 0.426 vary between 1.56 and 1.63 $Wm^{-1}K^{-1}$ for a vertical heat source and between 1.32 and 1.36 $Wm^{-1}K^{-1}$ for a horizontal heat source. The average scatter of the measured conductivities in the intact samples is ± 0.05 and ± 0.06 $Wm^{-1}K^{-1}$ for the two directions of measurement respectively.

In the case of the reconstituted samples, the thermal conductivities range between 1.16 and 1.55 $Wm^{-1}K^{-1}$ in vertical heat source measurements, and between 1.13 and 1.35 $Wm^{-1}K^{-1}$ for horizontal heat source measurements. The average scatter of the measured conductivities in the reconstituted samples is ± 0.02 and ± 0.05 $Wm^{-1}K^{-1}$ for the two directions of measurement respectively. The small scatter reported for the vertical heat source measurements in reconstituted samples should be treated with caution as the number of measurements for such cases is very limited due to the size of those samples. The smaller 70 mm diameter limits the number of possible insertions of both single needle and dual-probe, that would not interfere with each other and would remain at an acceptable distance from the edge of the samples to avoid inducing additional errors, as discussed in section 5.4.

Additionally, the influence of the orientation of the monitoring needle with respect to the heating needle in the horizontal heat source measurements performed with the dual-probe is separately assessed in Figure 7.7 for the three orientations considered (0, 45 and 90°). No clear relationship between the value of the thermal conductivity and the orientation of the dual-probe can be established from the presented data.

7.2.3 Combined discussion

For the seven intact and six reconstituted samples of London clay, the averages of the measurements of thermal conductivity performed in the two heat source directions, and with two different instruments, are compared in Figure 7.8. For the seven intact samples (total of fourteen data points, one for each direction of measurement per sample), the thermal conductivity measured using the dual-probe is on average +3.43% (s.d. 2.19%) higher than the one measured using the single needle. Similarly, for the six reconstituted samples, the conductivities measured using the double needle are +3.82% (s.d. 2.07%) higher than when measured using the single needle. This consistent and small discrepancy within the two methods is of a smaller magnitude than the accuracy range (± 5%) of the sensors quoted by the manufacturer. As discussed in Chapter 5, the measurements from the dual-probe are unfactored, unlike those of the single needle, given that the results of the calibrations tests on water-agar fell well within the accuracy reported by the manufacturer and that a straight-forward application of a calibration factor is not possible due to the inter-dependency of the properties measured during the test. Given the assumptions in the derivation of the thermal properties from the dual-probe heat-pulse test (ignoring the finite length and diameter of the heat source), the unfactored value of conductivity was shown in Figure 5.16 to overestimate by about 1% the conductivity derived assuming a perfect cylindrical heat source. Nusier (2003) also report consistent higher conductivity values in the dual-probe heat-pulse tests than in the single needle for sandy and loam soils at different densities.

Proving the validity of both methods in determining the thermal conductivity of soils, two main observations arise from the measurements taken in both types of tests: (a) the influence of the sample porosity and the direction of measurement and (b) the reasonably good agreement between the reconstituted and intact samples.

Figure 7.9 shows the measured conductivities using both types of tests against additional soil parameters: water content, dry density and bulk density. Given that just saturated samples were tested and no substantial differences exist in the particle density (Table 4.3) between the

different samples, comparison to parameters such as gravimetric water content or density adds very little to the discussion of the results presented in terms of porosity. The main factor that explains the different conductivities across the range of intact and reconstituted samples tested is the relative volume proportions of solids and liquids and their relative thermal conductivities since $\lambda_s \gg \lambda_w$. In addition to this, minor factors such as small mineralogical composition variations between samples also play an effect on the thermal conductivity. For example, sample #CS18 presents a slightly higher thermal conductivity, particularly in the vertical direction than other samples with smaller porosities. This discrepancy could be explained by the smaller clay content (~55%) in this sample than average (~57.5%, Table Table 4.3), which could suggest a higher presence of highly conductive quartzitic minerals.

Figure 7.10 (single needle test) and Figure 7.11 (dual-probe heat-pulse test) show the thermal conductivity profiles with depth for the samples retrieved from the Hyde Park boreholes. No clear trend with depth can be identified and the variations of the thermal conductivity are simply explained by the relative volumes of the solids and fluid, which can be expressed by the porosity or a combination of the water content, density and specific gravity. The profile of water content with depth displays an inverted projection of the profile of thermal conductivity with depth. A decrease of water content with depth is matched by an increase in thermal conductivity, while an increase of water content with depth is matched by a decrease in thermal conductivity. The opposite is shown in the profile of density with depth, which takes the same shape as the thermal conductivity profiles. Only the single needle measurements of the deepest sample (#CS60) do not quite agree with these observations, which is also the sample which presents the biggest discrepancy between the conductivities measured by the two instruments, probably suggesting some minor experimental issues during such measurements. These could have been caused by the contact resistance between the needles and the sample since pre-drilling was necessary in this very stiff sample.

For both types of measurement of the thermal conductivity and types of sample, the thermal conductivity measured from a vertical heat source, with heat flowing in the radial horizontal

direction with respect to the soil cylinder, is always higher than the thermal conductivity measured from a horizontal heat source. This observation is illustrated in Figure 7.12 by plotting the ratio of the thermal conductivity measured with a vertical heat source to the one measured with a horizontal heat source ($\lambda_{vhs}/\lambda_{hhs}$) for the averages of the tests performed in each sample using the single needle and dual-probe heat-pulse tests. The anisotropy in thermal conductivity (i.e. the value of the ratio further away from unity) increases generally as the porosity decreases (dry density increases). For the reconstituted samples, the ratio $\lambda_{vhs}/\lambda_{hhs}$, is in the range of 1.03-1.09, in #V&At1 ($n = 0.574$), depending on the instrument used for its measurement, up to around 1.15 in the densest sample #V&At6 ($n = 0.435$). In the case of the intact samples, which have porosities between 0.398 and 0.460, comparable to the porosity of #V&At6, the densest reconstituted sample, the anisotropy is more pronounced ($\lambda_{vhs}/\lambda_{hhs}$= 1.17-1.26, with an average of 1.20) due to the distinct soil structure both at macro- and micro-level of the intact sample. This ratio is smaller in magtinude compared to other well-known anisotropic properties of London clay such as the hydraulic conductivity, however the range of possible thermal conductivities in soils is very limited (usually between 1 and 2.5 $Wm^{-1}K^{-1}$ in saturated clays). An accurate selection of the thermal conductivity is of great importance for the design of energy applications. Sanner et al. (2009) showed that differences as little as 0.2 $Wm^{-1}K^{-1}$ between estimated and real thermal conductivities can lead to significant extra costs even in small ground-source heat pump systems.

7.2.4 Modelling the thermal conductivity

Several models, as described in section 2.2.1, are able to predict the thermal conductivity of a saturated soil as a function of the conductivities of the solid and water phases and the relative proportions of each phases. They are reported here in Eq.[7.2]-[7.14]. The thermal conductivity of water, λ_w, can be taken as 0.607 $Wm^{-1}K^{-1}$, in these equations, which is its value at 25 °C. This is considered appropriate given that the tests were performed at a laboratory temperature of approximately 22 °C and the conductivities were measured during a 2-3 °C increase in the

soil's temperature. The thermal conductivity of the solid phase, λ_s, can be estimated using the weighted geometric mean of the thermal conductivities of the different minerals present in the sample (Eq.[7.1]) if their relative proportions are known. In this case, the averages of the mineralogical compositions from the XRD tests reported in Table 4.1 are used, together with the values reported in the literature for the thermal conductivities of the same minerals (and summarised in Table 2.1), to obtain a value of λ_s of 2.85 $Wm^{-1}K^{-1}$ for London clay:

$$\lambda_s = \prod_{i=1}^{n} \lambda_i^{w_i}$$
$$\lambda_s = 1.88^{0.30} \times 1.85^{0.26} \times 7.69^{0.23} \times 3.26^{0.07} \times 2.64^{0.05} \times 2.25^{0.05} \times 5.51^{0.03} \times 1.84^{0.01} = 2.85 \quad [7.1]$$

Although XRD analyses were performed only on the V&A material, it is reasonable to assume that a very similar mineralogical composition would be found in the Hyde Park samples, given the similarities in the results of the classification tests (particle density and clay content).

Thermal conductivity models:

- Parallel (λ_1) and series (λ_2) models and average of the two (λ_3):

$$\lambda_1 = (1-n)\lambda_s + n\lambda_w \quad [7.2]$$

$$\lambda_{2=} \left(\frac{1-n}{\lambda_s} + \frac{n}{\lambda_w} \right)^{-1} \quad [7.3]$$

$$\lambda_3 = \frac{\lambda_1 + \lambda_2}{2} \quad [7.4]$$

- Geometric mean - λ_4

$$\lambda_4 = \lambda_s^{(1-n)} \lambda_w^n \quad [7.5]$$

- Russell (1935) - λ_5

$$\lambda_5 = \lambda_s \left[\frac{n^{2/3} + (\lambda_s / \lambda_w)(1 - n^{2/3})}{n^{2/3} - n + (\lambda_s / \lambda_w)(1 + n - n^{2/3})} \right] \quad [7.6]$$

- Upper (λ_6) and lower (λ_7) bounds of Hashin and Shtrikman (1962)

$$\lambda_6 = \lambda_s + \frac{n}{\frac{1}{\lambda_w - \lambda_s} + \frac{1-n}{3\lambda_s}} \quad [7.7]$$

$$\lambda_7 = \lambda_w + \frac{n}{\frac{1}{\lambda_w - \lambda_s} + \frac{1-n}{3\lambda_w}} \quad [7.8]$$

- Nimick and Leith (1992) - λ_8

$$\lambda_8 = \lambda_7 \left[1 - \frac{3n(1-A)}{2 + A + n(1-A)} \right] \quad A = \frac{\lambda_6}{\lambda_7} \quad [7.9]$$

- Gori and Corasaniti (2004) - λ_9

$$\lambda_9 = \left[\frac{\beta - 1}{\lambda_w \beta} + \frac{\beta}{\lambda_w \left(\beta^2 - 1 \right) + \lambda_s} \right]^{-1} \quad \beta = \sqrt[3]{\frac{1}{1-n}} \quad [7.10]$$

- Hsu et al. (1995) - λ_{11} (taking $\gamma_c = 0.13$)

$$\lambda_{11} = \lambda_w \left[1 - \gamma_a^2 - 2\gamma_a\gamma_c + 2\gamma_a^2\gamma_c + \frac{\gamma_a^2\gamma_c^2}{1/\left(\frac{\lambda_s}{\lambda_w} \right)} + \frac{\gamma_a^2 - \gamma_a^2\gamma_c^2}{1 - \gamma_a + \left(\gamma_a / \frac{\lambda_s}{\lambda_w} \right)} + \frac{2\left(\gamma_a\gamma_c - \gamma_a^2\gamma_c \right)}{1 - \gamma_a\gamma_c + \left(\gamma_a\gamma_c / \frac{\lambda_s}{\lambda_w} \right)} \right] \quad [7.11]$$

$$n = 1 - (1 - 3\gamma_c^2)\gamma_a^3 - 3\gamma_c^2\gamma_a^2$$

- Kersten (1949) - λ_{12} (taking $G_s = 2.774$)

$$\lambda_{12} = \left[0.13 \log(w) - 0.288 \right] 10^{0.000625\rho_d}$$
$$\lambda_{12} = \left[0.13 \log\left(100 * \frac{n}{Gs(1-n)} \right) - 0.288 \right] 10^{0.625(Gs(1-n))} \quad [7.12]$$

- De Vries (1952) - λ_{13}

$$\lambda_{13} = \frac{n\lambda_w + F(1-n)\lambda_s}{n + F(1-n)} \quad F = \frac{1}{3} \sum_{a,b,c} \left[1 + \left(\frac{\lambda_s}{\lambda_w} - 1 \right) g_i \right]^{-1} \quad [7.13]$$

- Woodside and Messmer (1961) - λ_{14}

$$\lambda_{14} = (n-0.03)\lambda_w + (1-n+0.03)\left[\frac{1-n}{1-n+0.03}\lambda_s^{-1} + \frac{0.03}{1-n+0.03}\lambda_w^{-1}\right]^{-1} \quad [7.14]$$

where λ_s and λ_w are the thermal conductivities of the solid and water phases respectively and n is the porosity of the soil.

The predictions from the different theoretical and semi-empirical models listed above are plotted together with the experimental data in Figure 7.13 and Figure 7.14 for single needle tests, and Figure 7.15 for dual-probe heat-pulse tests. Figure 7.13 shows the model predictions over the full range of porosities, while Figure 7.14 and Figure 7.15 focus only on the tested range of porosities. The first observation is that all measurements plot within the limiting boundaries of the parallel, λ_1, and series, λ_2, conduction models. The vertical line heat source measurements are approximately half-way between these two models for both test methods. The horizontal line heat source measurements are closer to the series flow model again for both methods. None of the models considered captures well the thermal conductivity measured when inserting the needle horizontally. On the other hand, several models agree reasonably well with the experimental data on both intact and reconstituted samples, measured when inserting the needle vertically. All vertical line heat source measurements plot within the limits of Hashin and Shtrikman (1962), which represent the minimum, λ_7, and maximum, λ_6, values that a homogeneous, isotropic two-phase material can attain. In the case of vertical line heat source measurements performed with the single needle, the average of the parallel and series models, λ_3, and the model of Gori and Corasaniti (2004), λ_9, agree well with the experimental data from the reconstituted and intact samples. In the range of porosities of the intact samples, the geometric mean model, λ_4, and the models of Nimick and Leith (1992), λ_8 and De Vries (1952), λ_{13}, also plot reasonably close to the previous two (within 0.1 $Wm^{-1}K^{-1}$) and to the experimental data. In the case of the vertical dual-probe heat-pulse tests, with slightly higher measured λ than the single needle, the models of Nimick and Leith (1992), λ_8, and De Vries (1952), λ_{13}, agree well with the experimental data for both types of samples.

The models of Russell (1935), λ_5, Woodside and Messmer (1961), λ_{14}, and the upper bound of Hashin and Shtrikman (1962), λ_6, overpredict the thermal conductivity measured in both directions, while the model of Hsu et al. (1995), λ_{11}, plots between the measured conductivities in the two directions considered. Finally, the empirical model of Kersten (1949), λ_{12}, shows a very different trend from the experimental data and the rest of the models considered, as expected from the discussion in Chapter 2.

Given the clearly distinct trends in the values of thermal conductivity in the different measurement directions, it is clear that the thermal conductivity of both reconstituted and intact London clay cannot be modelled adequatedly with models that assume isotropic behaviour only; instead, expressions which can accommodate the anisotropy are needed.

As reviewed in Section 2.2.1, from the available models which consider the anisotropy in thermal conductivity, Abuel-Naga et al. (2008) model (λ_{10}, Eq.[7.15]) is a simple approach which considers a soil morphological parameter (Ω, $0 \leq \Omega \leq 1$) and two limiting scenarios: one where particles are perfectly oriented as parallel (λ_1, $\Omega = 1$) and the other where they are perpendicular (λ_2, $\Omega = 0$) to the direction of the heat flow.

$$\lambda_{10} = \Omega\lambda_1 + (1-\Omega)\lambda_2 \qquad [7.15]$$

Figure 7.16 and Figure 7.17 show the predicted values using Eq.[7.15] together with the experimental data points obtained by the single needle and dual-probe heat-pulse tests respectively. The values of the soil morphological parameter Ω are obtained by curve-fitting Eq.[7.15] to the experimental data. In the case of the single needle tests, the parameter Ω takes a value of 0.5327 and 0.4769 for the vertical heat source measurements taken in intact and reconstituted samples respectively, and of 0.1955 and 0.2806 for the horizontal heat source measurements on intact and reconstituted samples, respectively. In the dual-probe heat-pulse tests, the parameter Ω takes a value of 0.5802 and 0.5492 for intact and reconstituted samples, respectively, in the case of the vertical heat source measurements, and 0.2662 and 0.3398 for intact and reconstituted samples, respectively, for horizontal heat

source measurements. The higher values of the parameter Ω in all four cases in the dual-probe heat-pulse tests is explained by the higher conductivities measured using this method, compared to the single needle test.

It is clear from both figures that the measured thermal conductivities, from both intact and reconstituted samples, in both vertical and horizontal directions are very well predicted by their respective directional model λ_{10}. It is also worth noting that in both types of test, the parameter Ω has a more extreme difference between its magnitudes in the vertical and horizontal direction in the case of intact samples. This agrees well with the implied anisotropy ratio shown in Figure 7.12, which is also higher in the case of intact samples. A value of the parameter Ω close to zero would indicate that most particles are oriented perpendicular to the heat source direction, while a value close to one suggest that the preferred particle orientation is parallel to the heat source direction. Given the values of the soil morphological parameter in the modelled tests, it could be concluded that there is a preferred sub-horizontal particle orientation in both intact and reconstituted soil samples, more pronounced in the case of the intact samples (as per conceptual model in Figure 2.3).

7.2.5 Further discussion

a) Comparison with published values

On average, intact London clay samples (Figure 7.10 and Figure 7.11) have a thermal conductivity in the range of 1.54-1.58 $Wm^{-1}K^{-1}$, depending on the instrument used, when measured by applying the heat source vertically, and in the range of 1.28-1.33 $Wm^{-1}K^{-1}$ when measured by applying the heat source horizontally. Despite being one of the most commonly tested soils and of major importance to many fields of engineering geology and geotechnical engineering given the infrastructure development in the London area during the last two centuries, the studies of the thermal properties of London clay in the published literature are very scarce. Bloomer (1981) presented several single needle tests results on different clays in the United Kingdom, including five tests on London clay for which a thermal conductivity value of 2.45 ± 0.07 $Wm^{-1}K^{-1}$ is reported. This value is often quoted in the recent literature

related to ground source heat (e.g. Banks, 2008) and in the Thermal Pile Design Standard (GSHPA, 2012). The exact conditions of those samples (mineralogy, porosity, degree of saturation, particle density, and direction of measurement) as well as the relevant site information (depth, exact location), were not reported in Bloomer (1981) and many of those factors have been shown in this chapter to be of crucial importance. Midttomme et al. (1998) performed tests on London clay samples (porosity of 0.48) using a divided bar apparatus and the needle probe in two directions, parallel and perpendicular to the layering of the soil. Thermal conductivities of 1.19 and 0.83 $Wm^{-1}K^{-1}$ were found in the parallel and perpendicular measurements with the steady-state apparatus, while the results of the needle probe measurements, which were described as poor by the Authors, were 0.94 and 0.84 $Wm^{-1}K^{-1}$ respectively. The values from the two types of tests on London clay, and also on the rest of soils presented in Midttomme et al. (1998), are remarkably lower than those presented in the current chapter and should be treated with caution. More recently, Low et al. (2015) tested six different samples from different depths, although without reporting on the mineral composition, porosity nor particle density, using the single needle technique and a steady state method, known as the thermal cell, proposed by Clarke et al. (2008). The thermal conductivities reported vary between 0.92 and 1.49 $Wm^{-1}K^{-1}$ for the single needle tests, with a variability of ±13% on average between the five measurements taken in each sample, always inserting the needle vertically. The variability of those tests is significantly higher than the one presented in the current study (approximately ±3% on average), which could suggest that the samples are not very uniform, particularly the water content within the samples. The Authors raise concerns of sample disturbance and drying prior to testing, which could both explain the lower repeatability and lower thermal conductivity values of their study. In the case of the thermal cell, the measured conductivities range from 1.65 to 2.19 $Wm^{-1}K^{-1}$, higher than in the single needle tests. This difference is attributed to thermal losses in the cell, therefore overestimating the applied power and the observed moisture migration in the direction of heat flow and it is concluded that the needle technique is the preferred laboratory measurement of thermal conductivity. The current work constitutes the first comprehensive laboratory study of the

thermal conductivity of London clay using both intact and reconstituted samples, repeating several measurements for each direction of measurement in every sample using two types of instruments. The results of both intact and reconstituted samples are repeatable, accurate and consistent, and agree reasonably well with simple mixing models.

b) Applicability

The efficiency and cost effectiveness of the design of energy geostructures heavily relies on the accurate deteremination of the thermal conductivity of the soil. Sanner et al. (2009) showed that even for small-scale schemes erroneous design values of the thermal conductivity can cause significant costs. In the case of a small commercial ground source pump system with a capacity of 50 kW, an overestimate of the thermal conductivity of just 0.4 $Wm^{-1}K^{-1}$ can lead to increasing annual electricity costs in excess of 1000€ due to the reduction in the coefficient of performance of the system (extra consumption to match expected performance of the system).

Generally for ground-source heat pump applications, the use of a higher estimate of the thermal conductivity leads to an under-sizing of the heat exchange field, meaning that the circulating fluid temperatures will be lower than anticipated in the design, causing a reduction in the coefficient of performance of the heat pump which can no longer meet the heat load, increasing the electric power consumption. In extreme cases, it could lead to a total system failure of the heat pump. In the opposite scenario, with a lower estimate of the thermal conductivity of the ground, the borehole heat exchange field will be oversized. Despite not causing operational issues on the heat pump system, the oversized design leads to higher initial costs.

When considering the general applicability of the laboratory measurements of thermal conductivity, a similar discussion as the one on the measurement of permeability in the laboratory or in the field may arise. Laboratory tests provide a local measurement of conductivity on a small sized sample of soil and can offer an accurate image of the thermal properties provided that high quality sampling procedures are used, preventing moisture losses and significant disturbance. However, when dealing with large volumes of soil, major

features, such as fissures, non-homogeneity, layers of different materials may not be captured during sampling and affect the real in-situ conditions and global properties of the site. This is particularly relevant in the case where convective heat transfer effects are dominant in-situ (i.e. significant groundwater flow) which cannot be captured in laboratory tests. The thermal conductivity can be measured in the field by a thermal response test (TRT), a method developed in the 90s (Austin, 1998; Gehlin, 1998). The TRT involves circulating heated fluid at a constant power in a long and thin pilot borehole, analogous to an infinite line heat source, for a long time (>48 hours) and monitoring the temperature of the fluid with time. The borehole diameter, pipe configuration (size, material, geometrical arrangement) and filling material are specified in order to minimise the thermal resistance between the borehole wall and the fluid (Sanner et al., 2005). Contrary to laboratory measurements of intact samples, only a single thermal conductivity value is obtained for the whole soil mass and is affected by groundwater flow. Convective effects caused by water-filled fissures and highly permeable strata yield higher "apparent conductivities" in in-situ measurements compared to laboratory measurements (Gehlin, 2002). The applicability of the TRT for small-size schemes is a topic of ongoing discussion (Loveridge et al., 2015). TRT tests were originally conceived for long (>100 m) and thin borehole heat exchangers and thus most of the available rigs are set up to produce the power for standard tests for deep heat exchangers. The application of the same power for typical energy piles (15-20 m) may lead to significant problems due to overheating. Low et al. (2015), in addition to the laboratory tests, also performed a TRT which showed a ground conductivity value of 2.6 $Wm^{-1}K^{-1}$, which is much higher than measured during single needle tests on intact samples. The most likely source of error in this measurement is the large diameter of the pile used during the test, greater than recommended. Similarly, other sources of uncertainty reported by the Authors include the short length of the pile, non-uniformity of ground temperature prior to testing, and variability in the applied power. Finally, the value of the thermal conductivity in the ground may also differ from the measurement in the laboratory due to the effect of temperature in the thermal properties of the soil, particularly on thermal conductivity of water, as previously shown in Eq.[2.4]. Assuming the geometric

mean mixing model, a porosity of 0.4 and the values of λ_w at 10 °C (as a typical ground temperature) and 25 °C (as the temperature of the measurement in the laboratory), the laboratory measurement would over predict the conductivity in the field by 0.02 $Wm^{-1}K^{-1}$. This effect is very small, well within the accuracy margins of the instruments used for the measurement, and may be neglected.

Laboratory measurements of the thermal conductivity of soils using both the single needle and dual-probe heat-pulse tests may offer an inexpensive, and quick solution for the design of energy geostructures in the London area, if they are part of a site investigation which involves quality intact sampling and accurate profiling of the soil properties. Given the scarce literature on the topic, however, further coupled studies of laboratory and in-situ measurements are needed to expand the publicly available database of thermal properties, assess the natural variability of such properties and the representativeness of the values presented in this thesis.

7.3 Heat Capacity

7.3.1 Results

The volumetric heat capacity ($c\rho$, in $Jm^{-3}K^{-1}$) of the reconstituted and intact London clay samples was measured in the dual-probe heat-pulse tests using both the single point method and the nonlinear fit involving the portion of the data that obeys $\Delta T(t) \geq 0.75T_m$. A comparison between the heat capacities obtained using both methods is shown in Figure 7.18. Out of the 109 measurements reported on intact samples, the maximum differences in the heat capacity obtained using the nonlinear fit method compared to the single point method are +1.1% and -1.05%, with on average +0.45% (s.d. 0.33%) higher heat capacities obtained via the nonlinear fit method. Similarly, out of the 59 measurements reported on reconstituted samples, the heat capacity obtained using the nonlinear fit was higher in all cases with a maximum value of +1.48% and an average of +0.57% (s.d. 0.35%). The single point method, simpler and less computationally demanding than the nonlinear fit, is shown to produce very similar results, with the difference between the two methods being smaller than the general measurement

error, as discussed during the calibration tests in Chapter 5. In this section, the values and figures reported refer to the single point method measurements.

In a similar way as for the thermal conductivity, the results of the measurements of the volumetric heat capacity of the reconstituted and intact samples in both measurement directions are plotted against porosity in Figure 7.19, showing all data points. Figure 7.20 shows the average values and the corresponding ranges in both measurements directions. Given the very significant scatter in the measurements, no clear trend of the change in heat capacity with porosity can be observed initially. Similarly, by looking at the averages in both measurement directions, no clear signs of anisotropy could be identified as in the case of the thermal conductivity. This implies that the presentation of an average value of all measurements for each sample, irrespective of the measurement direction, would be appropriate, as shown in Figure 7.21. The variability between the different measurements made for each of the intact samples is very large, ±33% on average, raising important questions on the validity and accuracy of these measurements. The sample with more repeatable results, #CS22, presents a range of measurements of +18.8/-20.5 % from the average value, while #CS44 shows the largest variation with +67.7/-51.7 % from the average. In the case of reconstituted samples, this is reduced to ±11%, although with a smaller number of measurements per sample given the size constraint. Although some level of variability in the intact samples is expected given the natural variability and non-homogeneity of the samples, and some non-uniformities in the water content, the observed scatter is unacceptably high and cannot simply be attributed to the sample. In order to further investigate this issue, it is necessary to establish what would be reasonable results for this thermal property.

7.3.2 Discussion

The volumetric heat capacity of soils can be estimated by the summation of the individual components of volumetric heat capacity, as shown by Eq.[7.16] (Bristow, 1998).

$$(c\rho) = c_q \rho_q x_q + c_{rm} \rho_{rm} x_{rm} + c_w \rho_w x_w + c_a \rho_a x_a + c_o \rho_o x_o \qquad [7.16]$$

where ρ (in kgm^{-3}), c (in Jkg^{-1}K^{-1}) and x are the density, specific heat capacity and volume fractions respectively and the subscripts a, o, w, q and rm indicate air, organic matter, water, quartz and remaining minerals other than quartz. Assuming full saturation (c_w= 4.18 Jg^{-1}K^{-1}) of all samples and no presence of organic matter, taking the fraction of quartz (23%), reported from the XRD tests in Chapter 4 and its density and specific heat capacity (G_s = 2.66, c_q= 0.73 Jg^{-1}K^{-1}), and considering the remaining minerals as "clay minerals" (77%) and assuming typical clay properties (G_s = 2.8, c_{rm} = 0.88 Jg^{-1}K^{-1}), the volumetric heat capacity may be estimated as follows:

$$(c\rho) = (2.66\times997.5\times730\times0.23 + 2.8\times997.5\times880\times0.77)(1-n) + 997.5\times4180\times n$$

[7.17]

The predicted volumetric heat capacities are also plotted in Figure 7.21. The expected range of volumetric heat capacities for the range of porosities of the intact samples is between 3.04 and 3.18 MJm^{-3}K^{-1}, which taking into account the density of the samples, correspond to a range of specific heat capacities for intact London clay between 1.48 and 1.63 Jg^{-1}K^{-1}. Eq.[7.17] suggests that the volumetric heat capacity increases linearly with porosity from a minimum value of 2.47 MJm^{-3}K^{-1} at $n = 0$ up to a maximum value of 4.17 MJm^{-3}K^{-1} at $n = 1$, corresponding to the volumetric heat capacity of water at 25 °C. No measurement should therefore fall outside of these theoretical limits. This is unfortunately not met in most of the measurements made; there are several data points (in all tests except from #CS16, #V&At5, #V&At2 and #V&At1) and even test averages (#CS18, #CS36, #V&At6) or a whole test (#V&At4) which are outside the theoretical limits. In the case of the intact samples the averages of the measured volumetric heat capacities are within ±5% of the estimated values in samples #CS16, #CS44, #CS60, although with unacceptable scatter in some cases. The averages of the remaining samples is significantly lower than the estimated values, from 13% in the case of #CS30 up to 32.4% in the case of #CS18. In the case of the reconstituted samples, #V&At1, #V&At2 and #V&At5 averages are within ±5% of the estimated values; while

the average of #V&At3 is 20% lower than the prediction and, #V&At4 and #V&At4 measurements are more than 40% higher than the predictions.

These discrepancies are attributed to an error in the value assumed for the spacing between the two needles and used in the calculation, which is later confirmed by investigating the errors in the thermal diffusivity in the following section. The distance r is taken as 6 mm, which is the initial spacing of the needles in their untested, new condition. This distance is however very likely to change when the dual-probe is inserted in the soil, as some bending may occur, particularly when considerable force is required to push the device into stiff materials, as the ones used in this thesis. Given that multiple measurements are taken in the same soil sample, it is not surprising to see large scatter in the data, as the real spacing between the needles is unknown and is very likely to vary between insertions. Despite efforts undertaken to mitigate such errors, by pre-drilling holes in stiff samples before inserting the dual probes, the accuracy and consistency of measurements did not improve. Considering the error analysis performed in Figure 5.13, summarised numerically in Table 7.1, it becomes clear than large errors in the measurement of heat capacity can be induced by only slight changes in r during probe insertion. For example, bringing the probes together by just 0.5 mm during the insertion will lead to an overestimation of the volumetric heat capacity of nearly 20%. With time and repeated use, the probe assembly becomes looser and more likely to bend during insertion in a stiff material. It is therefore not surprising that the first measurements, performed with brand new probes in excellent state, which were also those made on the softer, less dense samples (#V&At1 and #V&At2) agree well with the predictions of the simple summation model described by Eq.[7.17]. Given the magnitude and likelihood of the error in these tests caused by bending of the probes, resulting in an uneven and unknown inter-probe spacing, the adequacy of this type instrument for measuring the heat capacity of stiff materials is questionable. This method seems to give very satisfactory results in soft and high water content materials such as in peats or slurries (Hanson et al., 2000), where inserting the needles is not likely to disturb the needle spacing.

7.4 Thermal diffusivity

7.4.1 Results

The thermal diffusivity (κ, expressed in m^2day^{-1} for convenience to the reader, given the small magnitude in the standard units of m^2s^{-1}) of the reconstituted and intact London clay samples was measured in the dual-probe heat-pulse tests using both the single point method and the nonlinear fit involving all of the measurements points that obey $\Delta T(t) \geq 0.75T_m$. A comparison between the thermal diffusivities obtained via the two methods is shown in Figure 7.22. Out of the 109 measurements reported on intact samples, the maximum differences in the thermal diffusivity obtained using the nonlinear fit method compared to the single point method are +4.65% and -3.67%, with on average +0.87% (s.d. 1.54%) higher thermal diffusivities obtained via the nonlinear fit method. Similarly, out of the 59 measurements reported on reconstituted samples, the maximum differences in thermal diffusivity obtained using the nonlinear fit compared to the simpler single point method are +7.94% and -4.34%, with an average of +1.41% (s.d. 2.04%). The differences between the two methods are more pronounced than in the case of the volumetric heat capacities and the main reason for this bigger discrepancy may be that a large source of error in the estimation of the diffusivity in the single point method is the error in the value of the maximum temperature rise recorded, as previously demonstrated in Figure 5.13. A flat peak or a peak resulting from measurement noise will affect the value of the single maximum temperature used in the single point method. This can be overcome by considering the whole area around the peak in the manner of the nonlinear fit method.

As for the rest of the thermal properties, the results of the thermal diffusivity are presented against the porosity of the sample in Figure 7.23, showing all data points, and Figure 7.24, showing averages in both measurement directions and their appropriate ranges. Significant scatter is present in the measurements, particularly in the case of the intact samples, although the influence of the direction of measurement is evident, unlike in the case of the volumetric heat capacity. As for the thermal conductivity, higher diffusivities are found when the line heat

source is vertical with respect to the soil cylinder. This is not shown in the case of samples #CS44 and #CS18, which seem to present higher diffusivities in the horizontal heat source measurements although the scatter in such measurements is unacceptably high, -47.8/+85.8 % in #CS18 and -48.7/+66.1% in the case of #CS44. In the case of the reconstituted sample, the scatter in the measurements is relatively small except for the horizontal heat source in sample #V&At3. From the experimental data in Figure 7.23, there is no clear trend in the influence of porosity on the thermal diffusivity of the samples, although it seems that reconstituted samples have smaller values than the intact ones.

7.4.2 Discussion

The thermal diffusivity, which is defined as the ratio of the thermal conductivity and volumetric heat capacity can be modelled by dividing the models used for these properties. To better represent the anisotropy in thermal conductivity, the mixing model of Abuel-Naga et al. (2008) is chosen, taking the averages of the morphological parameter Ω from the reconstituted and intact predictions in each direction (Figure 7.17, 0.5647 for a vertical line heat source and 0.3030 for a horizontal line heat source), while Eq.[7.17] is used for the volumetric heat capacity. The predictions of the thermal diffusivity are also plotted in Figure 7.24, and can be seen to slightly reduce with increasing porosity. For intact samples, the estimated thermal diffusivities for a vertical heat source would be within between 0.04533 and 0.04039 m^2day^{-1} (5.25E-7 – 4.67E-7 m^2s^{-1}); while for a horizontal heat source they would range from 0.03941 to 0.03496 m^2day^{-1} (4.56E-7 – 4.05E-7 m^2s^{-1}). The agreement between the models and the experimental data is not good for all samples and most of the discrepancy can be explained by the error in the spacing between the two probes. As shown in the error analysis performed in Table 7.1, significant errors in the measurement of the diffusivity may also arise from slight changes in the probe spacing. In this case, bringing the probes together by just 0.5 mm during the insertion will lead to an underestimation of the thermal diffusivity by about 15% compared to the overestimation of the volumetric heat capacity of nearly 20%. The explanation for the discrepancies seen on both the heat capacity and thermal diffusivity can be demonstrated by

looking individually at two samples: for instance, #CS36 and #V&At6. The average of volumetric heat capacity measured in those samples were -24.8% and +39% different from the model estimation (Figure 7.21). This would suggest, according to Table 7.1, that the real spacing between the probes in these tests were in the region of 6.9 and 5.1 mm respectively. Therefore the expected error in the thermal diffusivities would be an over prediction of around 33% for #CS36 and an under prediction of around -27% for #V&At6. Looking at the differences between the experimental data and the models shown in Figure 7.24, the measurements of thermal diffusivity in sample #CS36 are 34.5% and 33.2% higher than the models for the vertical and horizontal line heat sources respectively. In the case of sample #V&At6, the measured thermal diffusivities are 28% and 26.6% lower than those of the models, as suspected.

Therefore, it becomes clear that the sensitivity of the inter-probe spacing in the measurement of the volumetric heat capacity and thermal diffusivity explains the observed results of these two properties. Thus, the same conclusions on the adequacy of the dual-probe method for the determination of the thermal diffusivity of stiff clay samples apply here as in the case of the volumetric heat capacity. However, it is very important to note that the thermal conductivity, which is obtained from the dual-probe test by the product of the measured, and likely wrong, thermal diffusivity and volumetric heat capacity is not affected by the error caused by the changes in inter-probe spacing, which is cancelled by the product of the two. This was shown in the error analysis and by the good agreement of the measured thermal conductivities using the dual-probe and the singe needle test shown in this chapter.

7.5 Summary

This Chapter presents and discusses the results of an extensive laboratory study of the thermal properties of intact and reconstituted London clay samples using the single needle and dual-probe heat-pulse tests. The main conclusions of the study are briefly listed below:

- Both instruments, single needle and dual probe, are adequate for the measurement of the thermal conductivity and present good agreement between themselves, with differences smaller than their accuracy range. In the case of the single needle, both heating and cooling parts of the experimental data can be used for the derivation of the conductivity and in the case of the dual-probe, there are very little differences between the two analyses methods considered, making the simpler single-point method more attractive than the weighted nonlinear fit.
- The thermal conductivity of London clay is an anisotropic property, also influenced by the relative volumes of solids and water in the sample and cannot be simply modelled using conventional isotropic models. For the intact London clay samples, the average measured thermal conductivity is 1.54-1.58 $Wm^{-1}K^{-1}$, depending on the instrument used, when measured by applying the heat source vertically, and 1.28-1.33 $Wm^{-1}K^{-1}$ when measured by applying the heat source horizontally. There is no clear trend with depth, and variations between the samples can be explained by changes in the water content and density.
- Published detailed studies of the thermal properties of London clay are very scarce and raise several experimental issues. The possible reasons for the discrepancies between in-situ and laboratory measurements of thermal conductivity are discussed and further studies involving both types of measurement are recommended.
- The use of the dual-probe for the measurement of the volumetric heat capacity and thermal diffusivity in stiff materials is inadequate due to the very large errors induced by bending the probes during insertion, leading to an unknown inter-probe spacing. This error is however cancelled out in the measurement of the thermal conductivity. As a consequence of such error, there is an unacceptable scatter in the measurements.
- The volumetric heat capacity of the intact London clay samples can be estimated to be in the range of 3.04-3.18 $MJm^{-3}K^{-1}$ and the thermal diffusivity can be estimated to

be in the range of 0.04533-0.04039 m^2day^{-1} in the case of a vertical line heat source. and 0.03941-0.03496 m^2day^{-1} in the case of a horizontal line heat source.

Table 7.1 *Relative error in the measurement of the thermal diffusivity and volumetric heat capacity caused by changes in the probe spacing*

Real probe separation *r* (mm)	**Relative error in the volumetric heat capacity (%)**	**Relative error in the thermal diffusivity (%)**
4.6	70.13	-41.09
4.8	56.25	-35.86
5	44.00	-30.40
5.2	33.13	-24.72
5.4	23.45	-18.82
5.6	14.79	-12.69
5.8	7.01	-6.34
6	0.00	0.00
6.2	-6.35	7.02
6.4	-12.11	14.03
6.6	-17.36	21.27
6.8	-22.15	28.73
7	-26.53	36.42
7.2	-30.56	44.32
7.4	-34.26	52.45

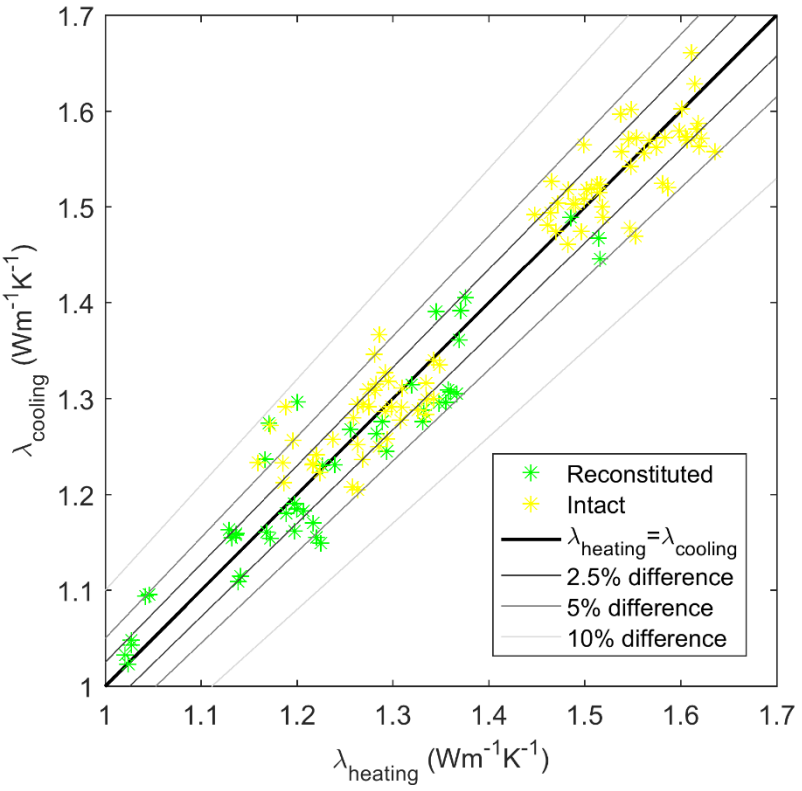

Figure 7.1 *Comparison of the thermal conductivities obtained using the heating and cooling parts*

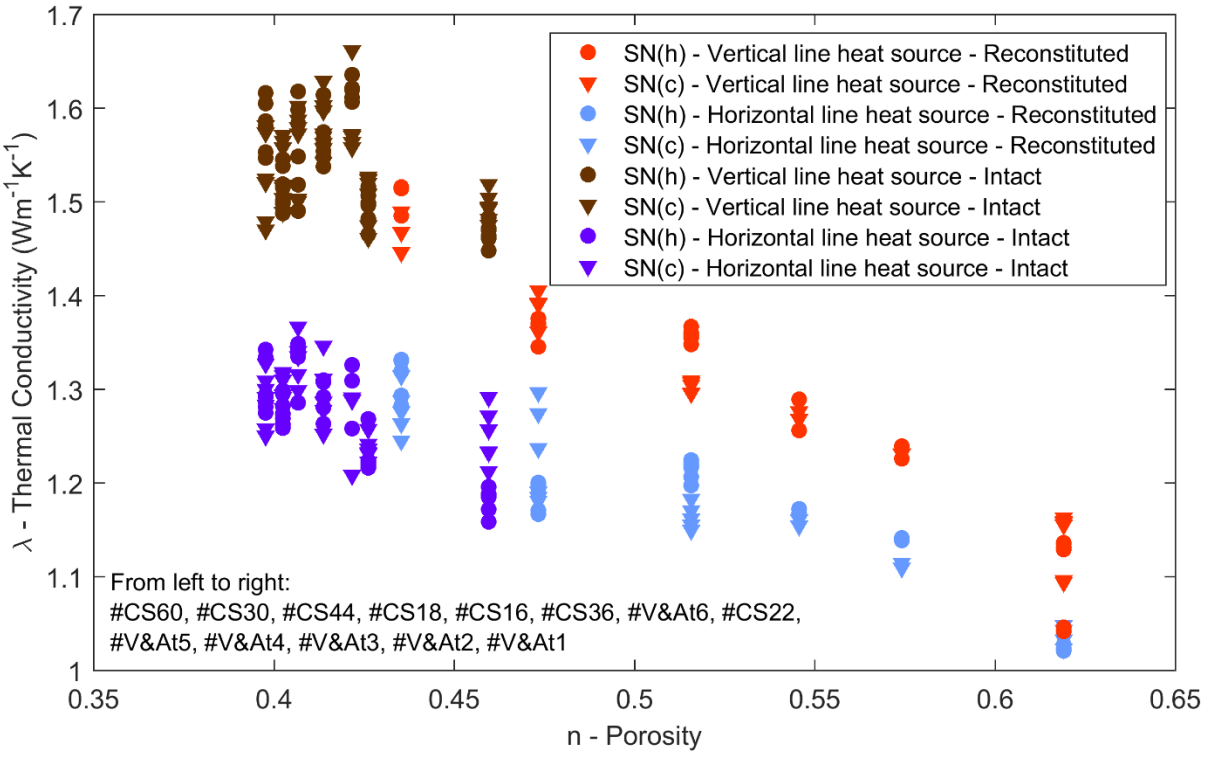

Figure 7.2 *Thermal conductivities measured in the single needle tests during heating (h) and cooling (c) (All points)*

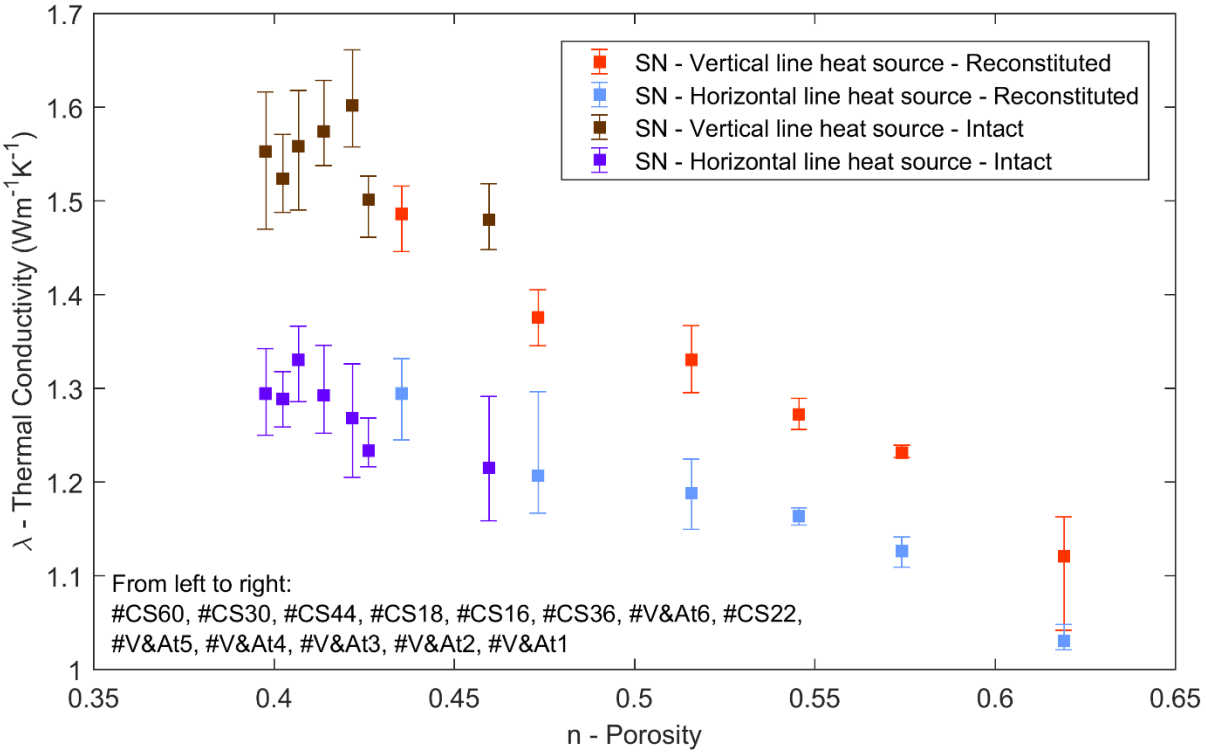

Figure 7.3 *Thermal conductivities measured in the single needle tests (ranges and averages)*

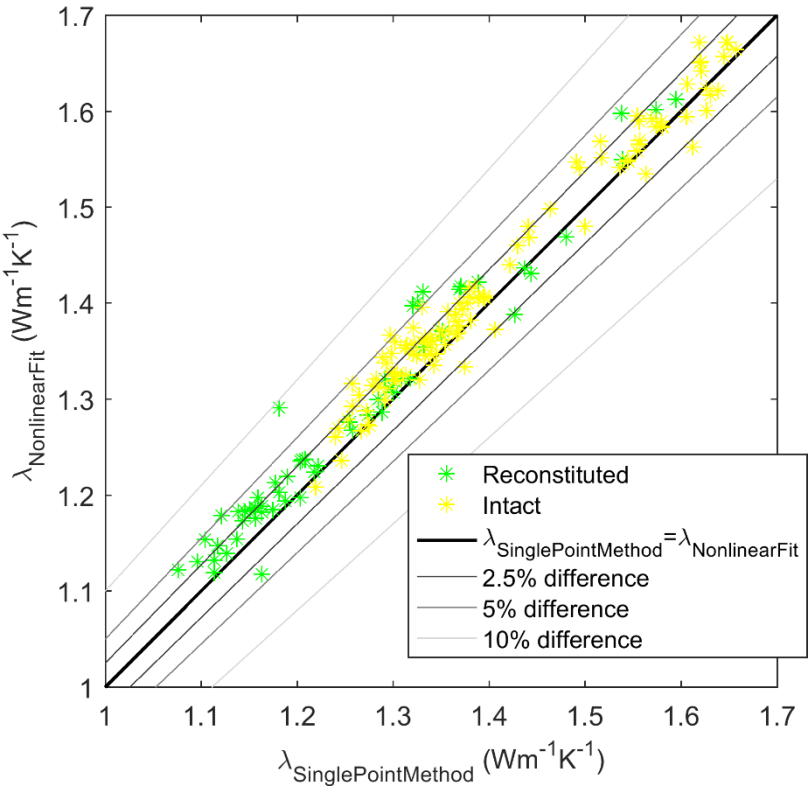

Figure 7.4 *Thermal conductivities obtained using the single point method and the nonlinear fit in dual-probe heat-pulse tests*

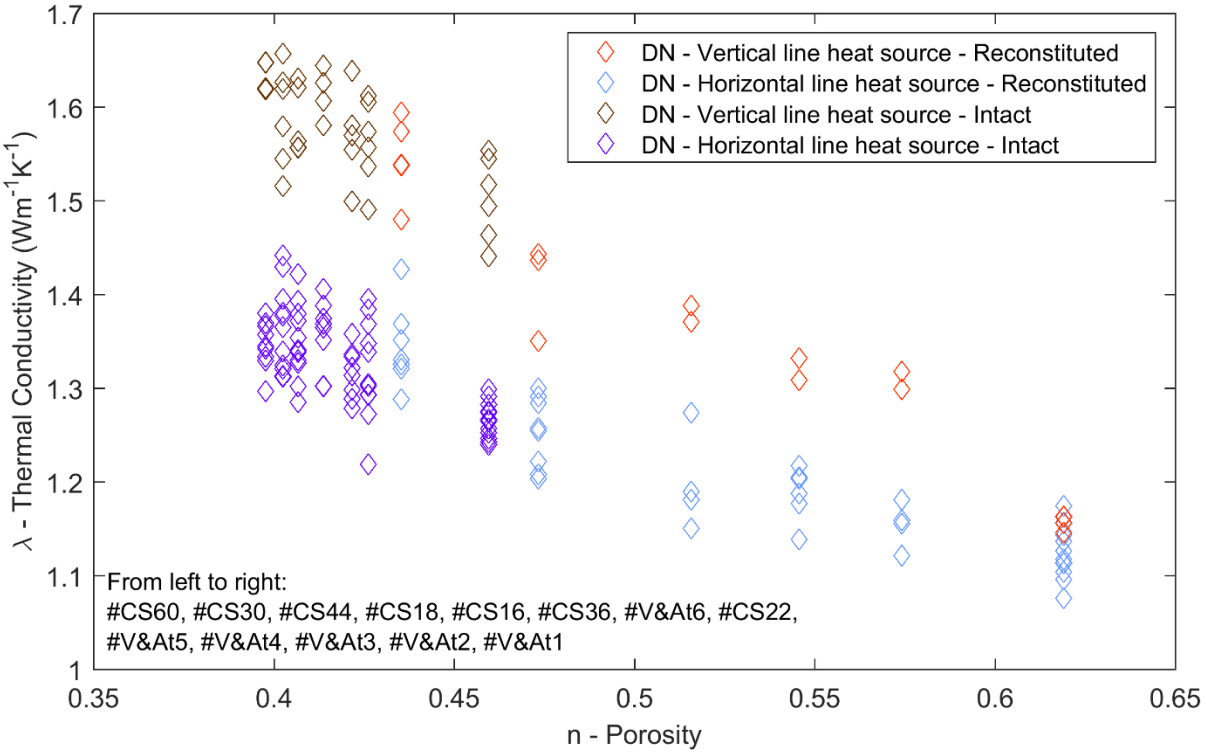

Figure 7.5 *Thermal conductivities measured in the dual-probe heat-pulse tests (All points)*

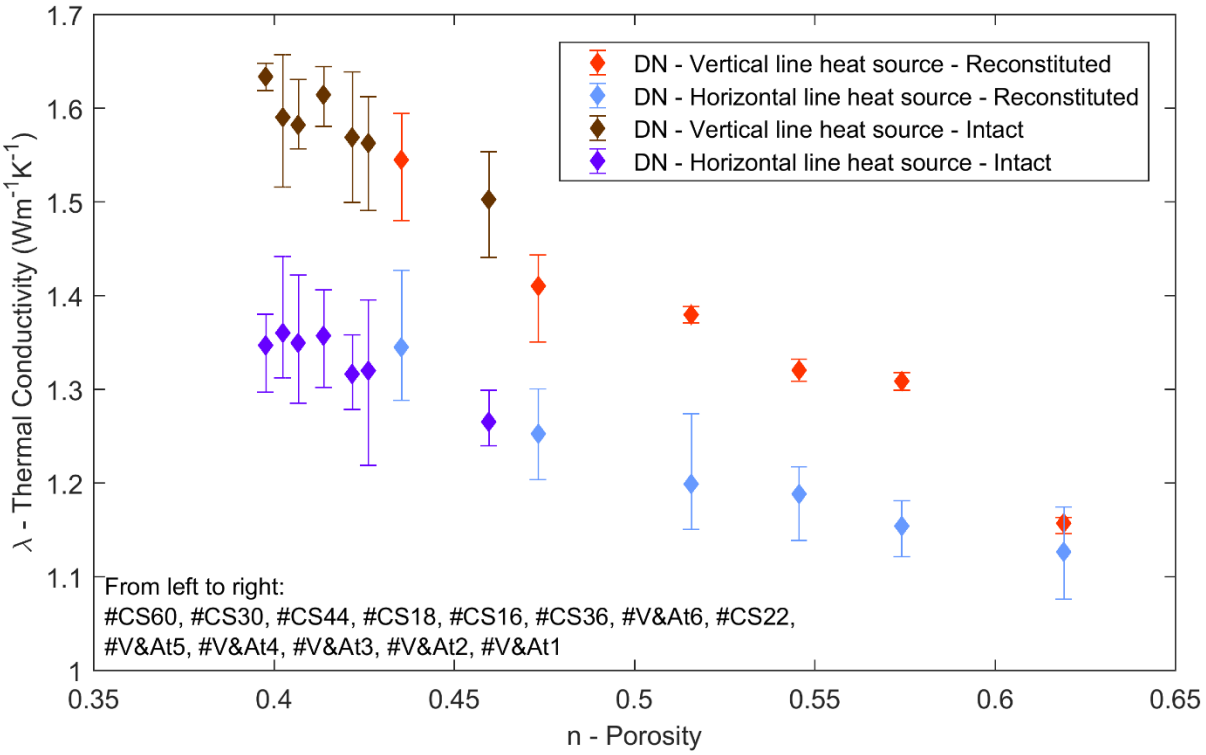

Figure 7.6 *Thermal conductivities measured in the dual-probe heat-pulse tests (ranges and averages)*

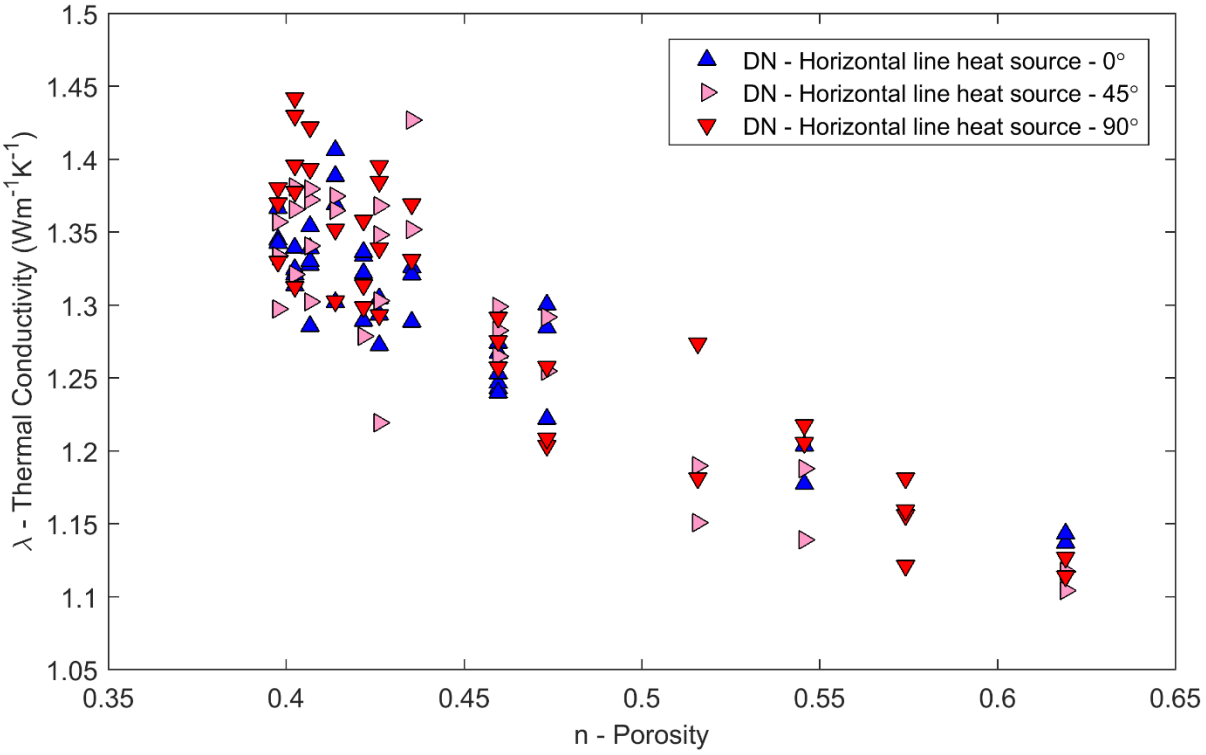

Figure 7.7 *Thermal conductivity measurements varying the orientation of the dual-probe*

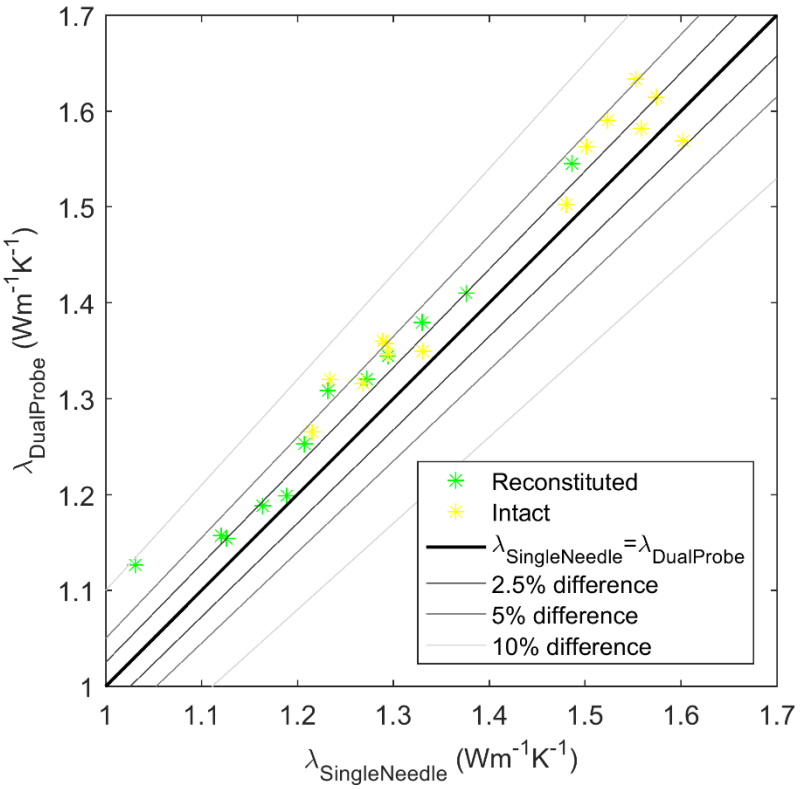

Figure 7.8 *Thermal conductivities obtained by the single needle test and the dual-probe heat-pulse test*

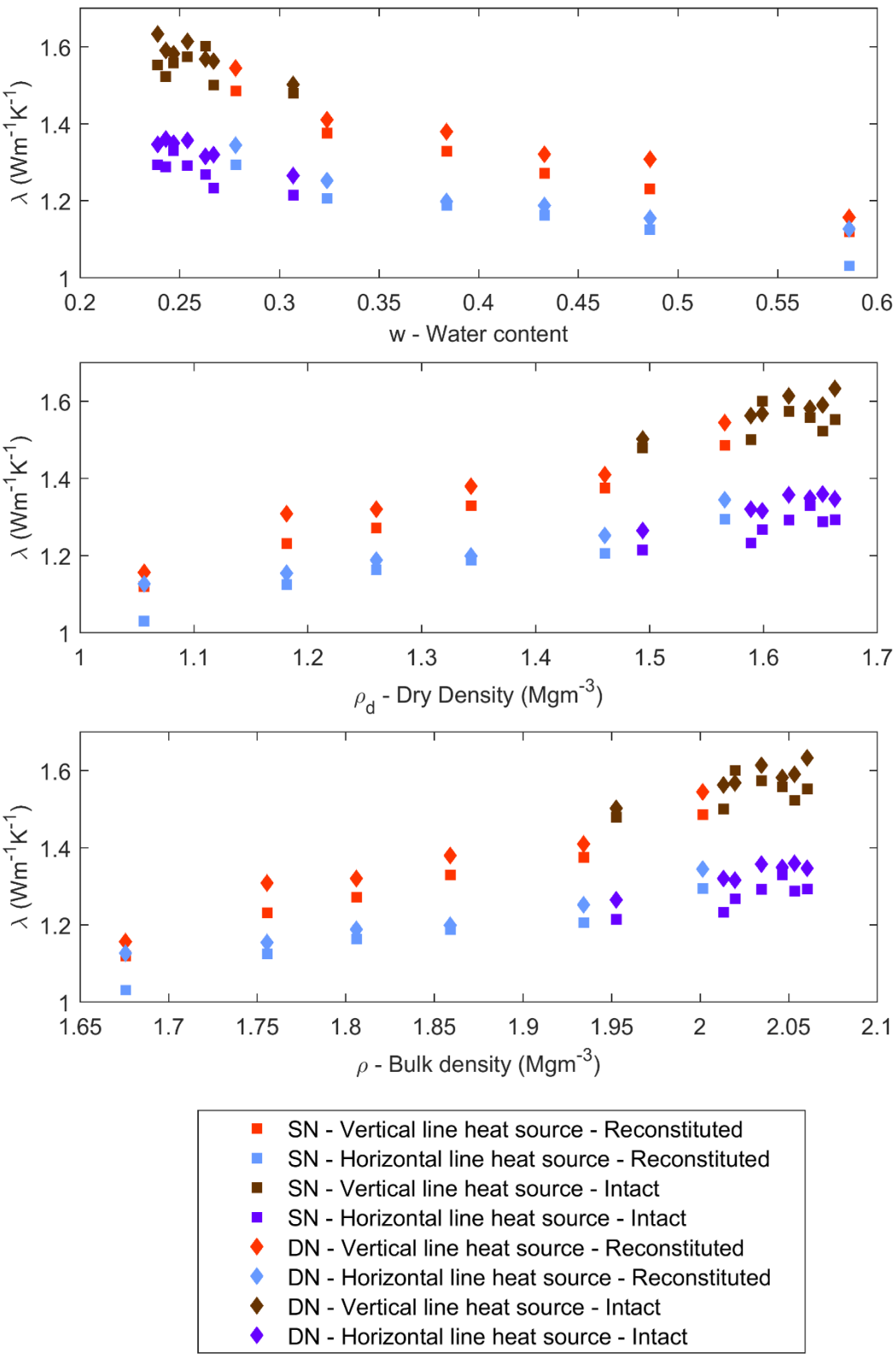

Figure 7.9 *Thermal conductivity as a function of water content and dry and bulk densities (average values only)*

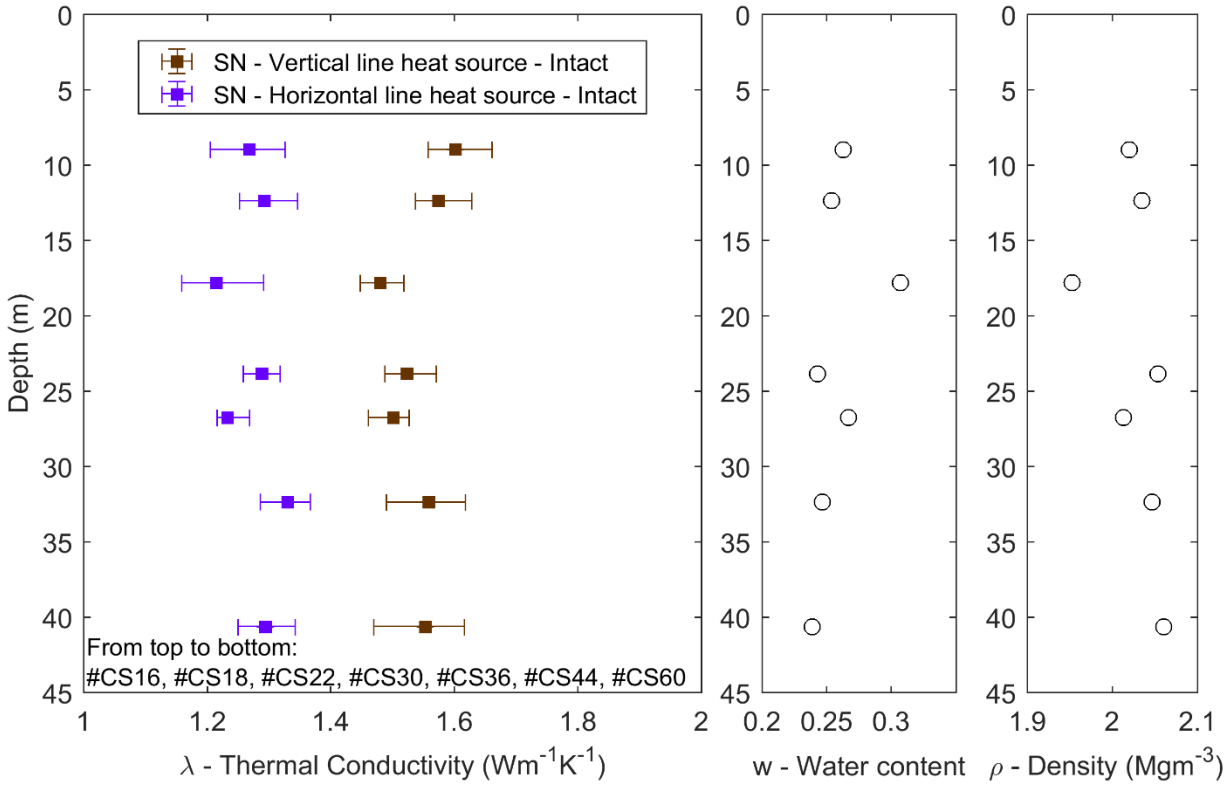

Figure 7.10 *Thermal conductivity profile with depth for intact samples (single needle tests)*

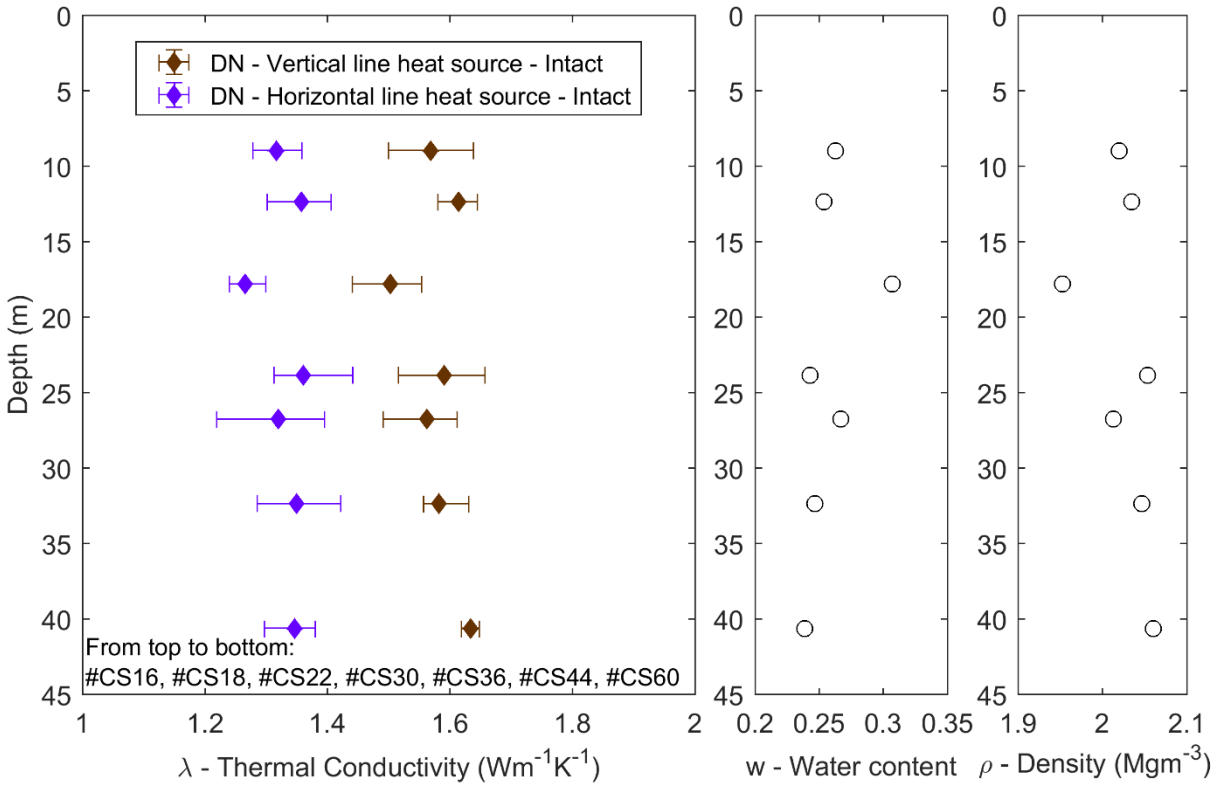

Figure 7.11 *Thermal conductivity profile with depth for intact samples (dual-probe heat-pulse tests)*

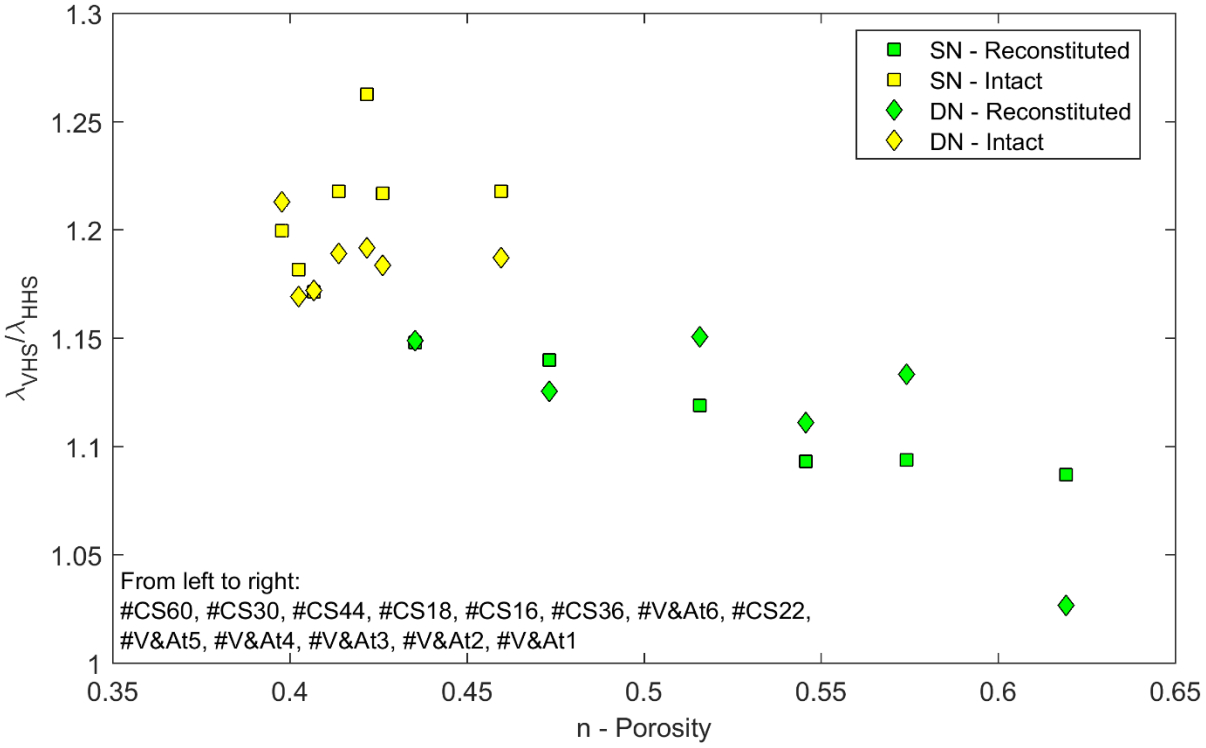

Figure 7.12 *Ratio of the thermal conductivities measured using a vertical heat source to a horizontal heat source for both types of probes*

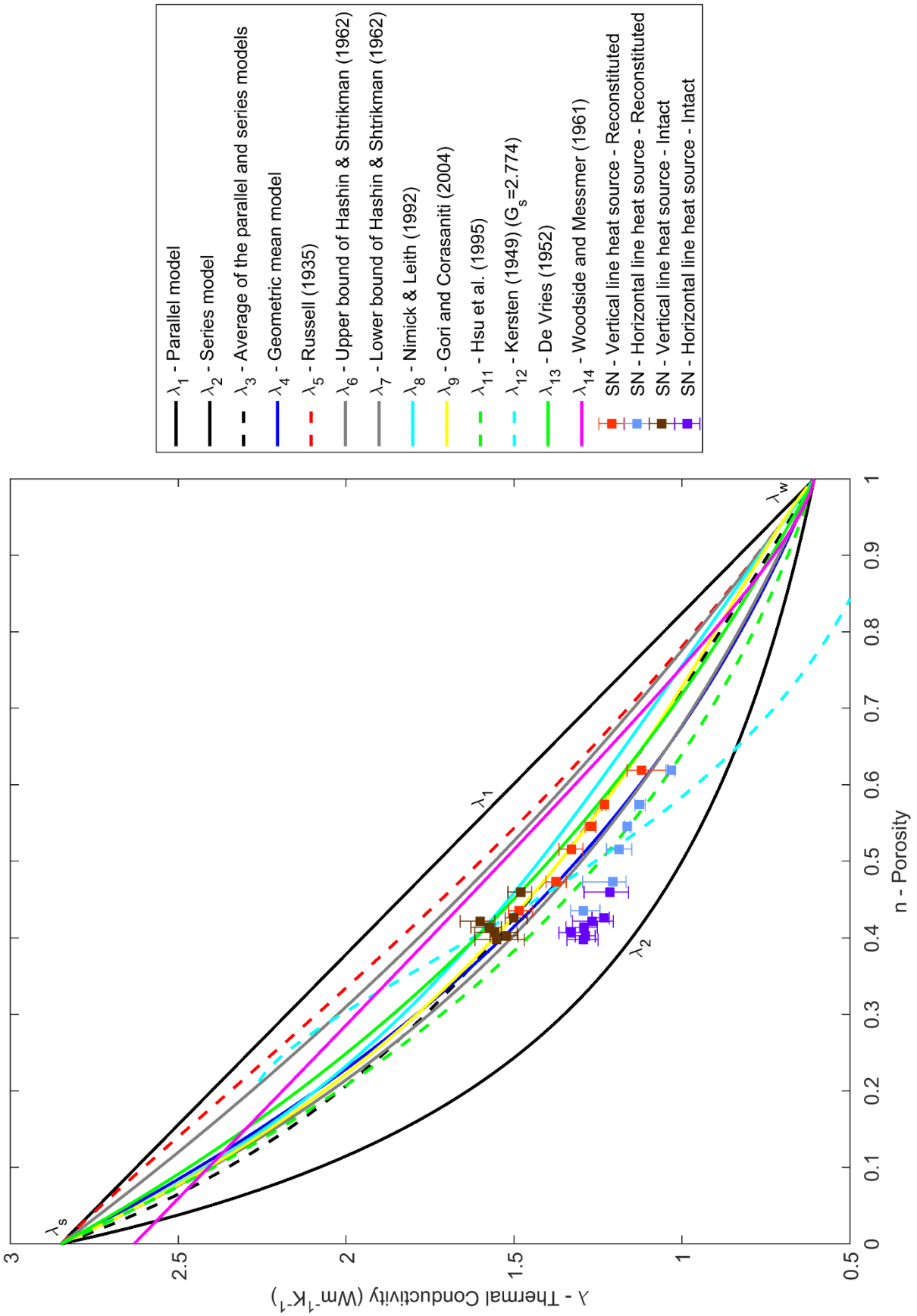

Figure 7.13 *Measured and predicted thermal conductivity values (single needle test)*

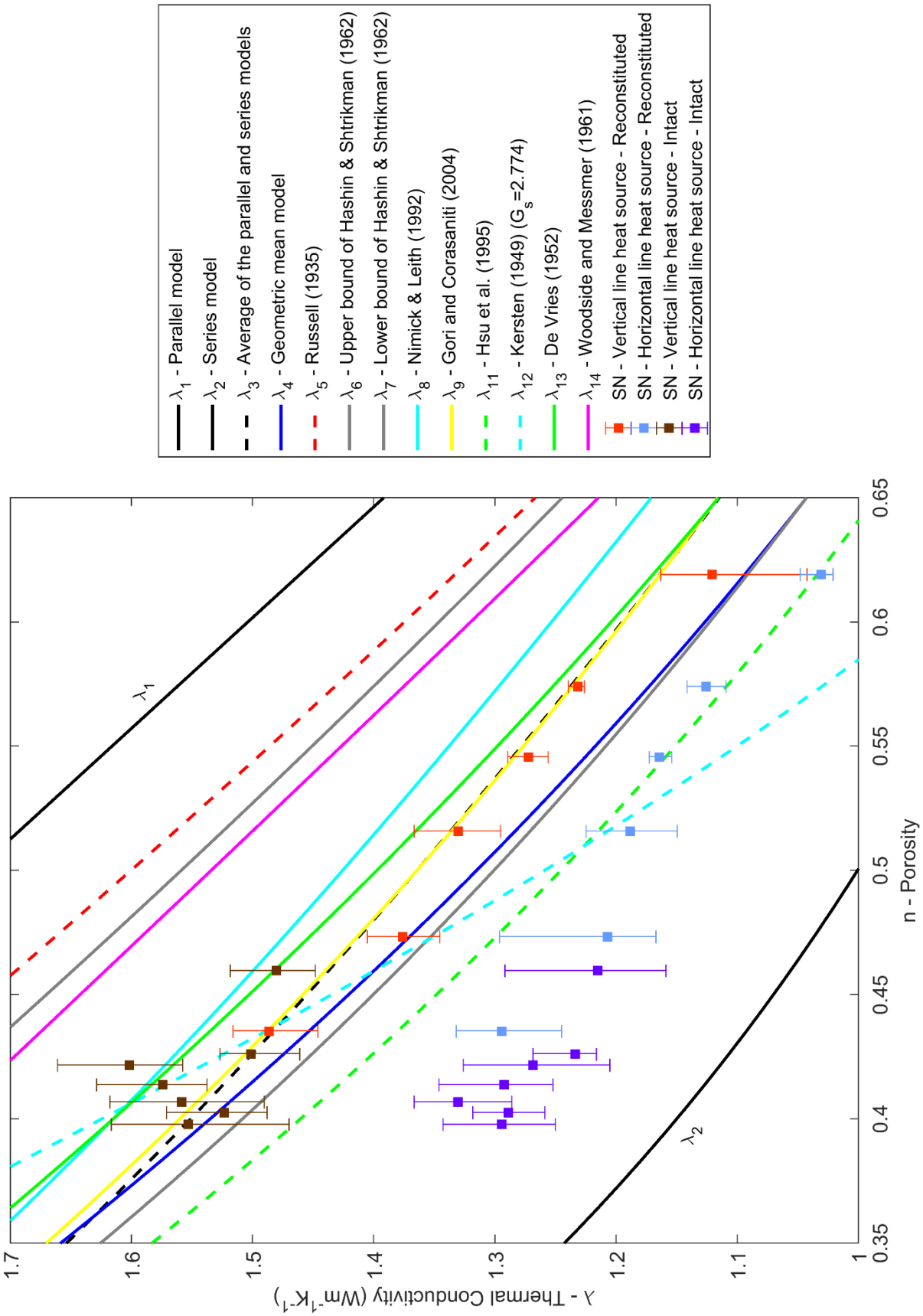

Figure 7.14 *Measured and predicted thermal conductivity values (single needle test, zoomed)*

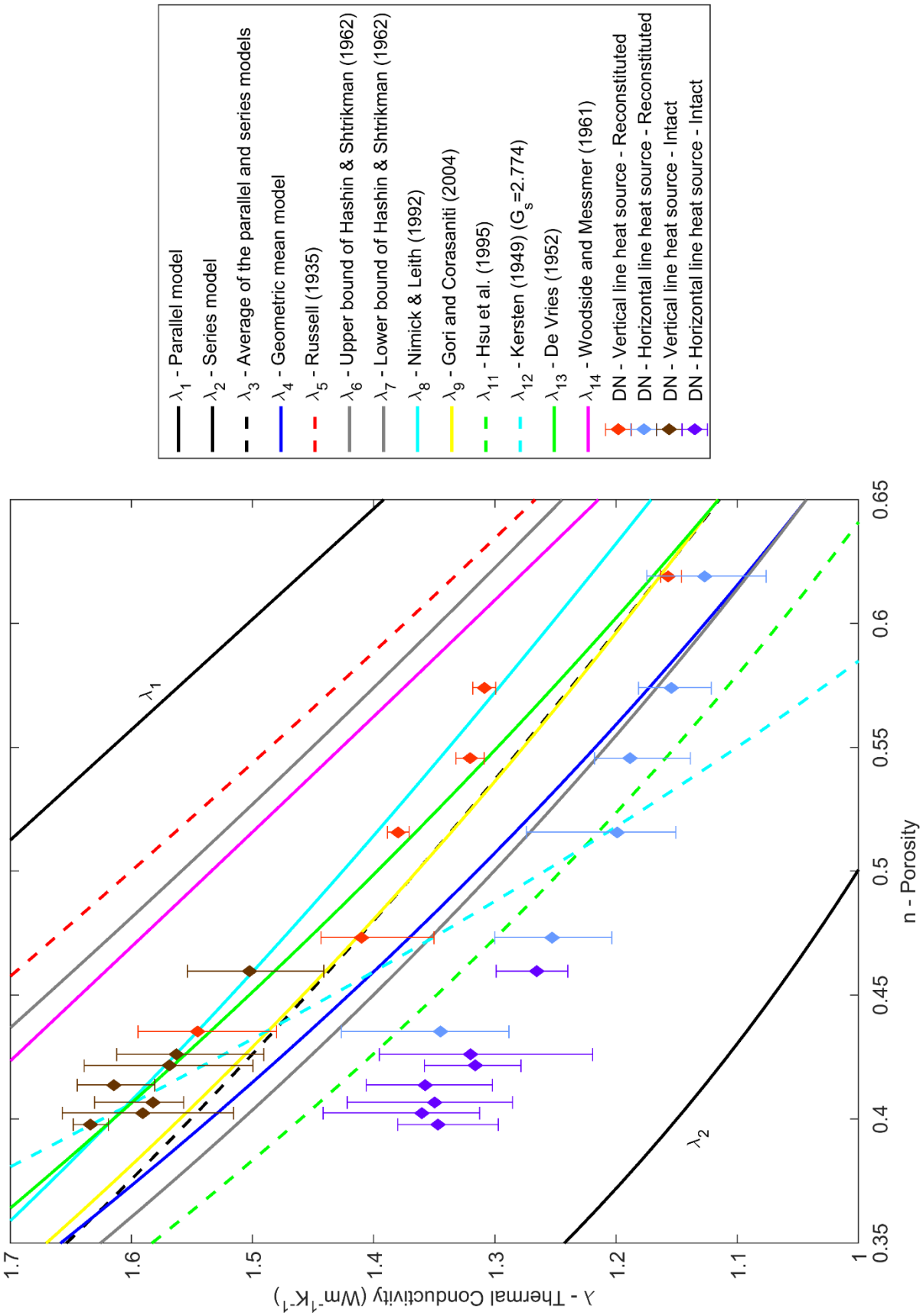

Figure 7.15 *Measured and predicted thermal conductivity values (dual-probe heat-pulse test)*

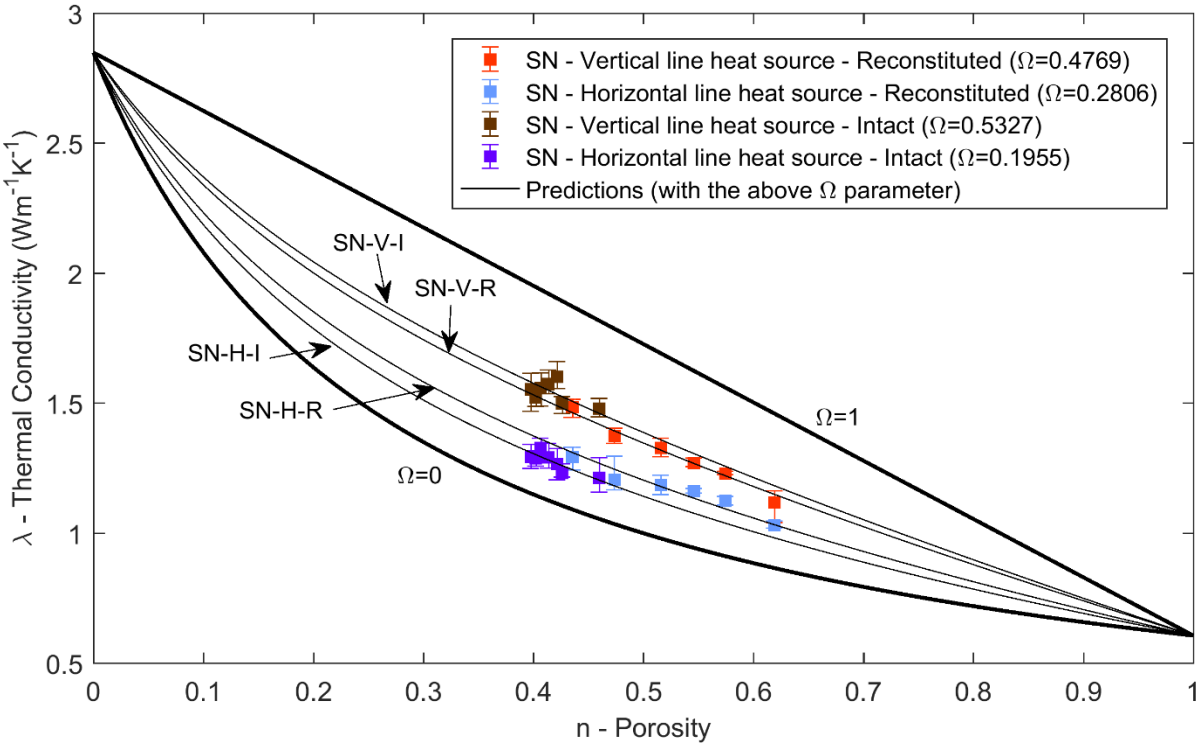

Figure 7.16 *Measured (single needle) and model prediction thermal conductivity results using Abuel-Naga et al., 2008)*

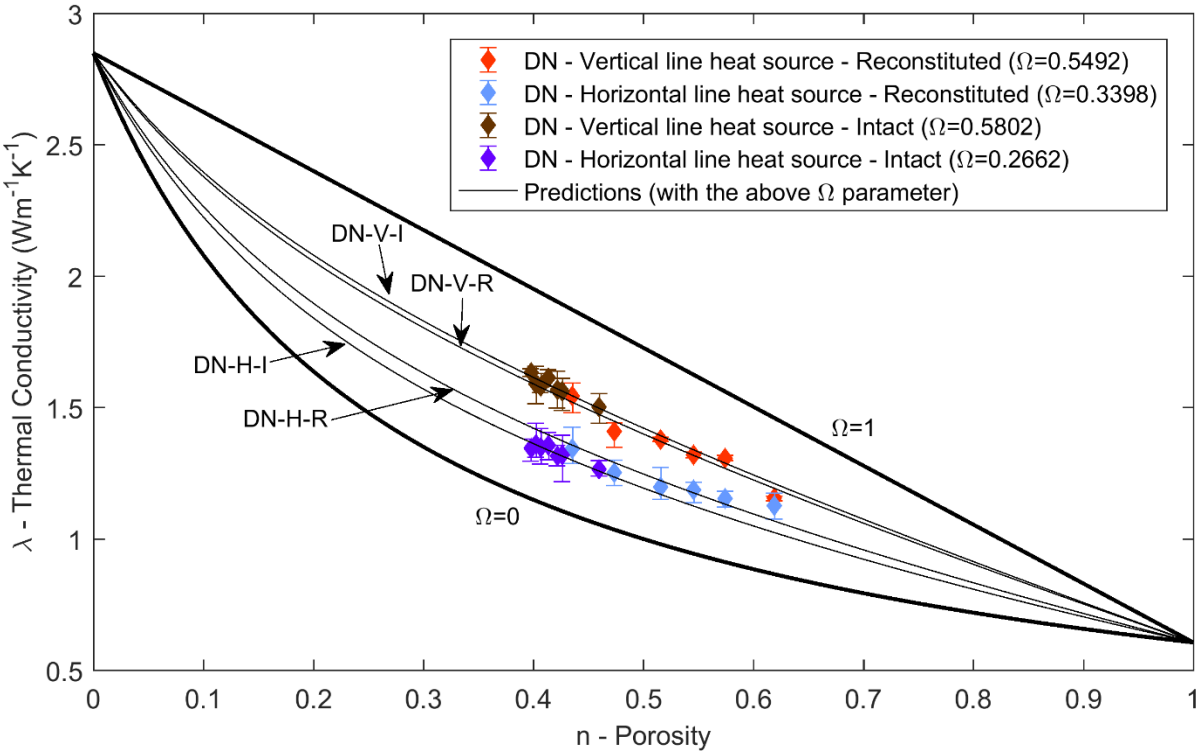

Figure 7.17 *Measured (dual-probe) and model prediction thermal conductivity results using Abuel-Naga et al., 2008)*

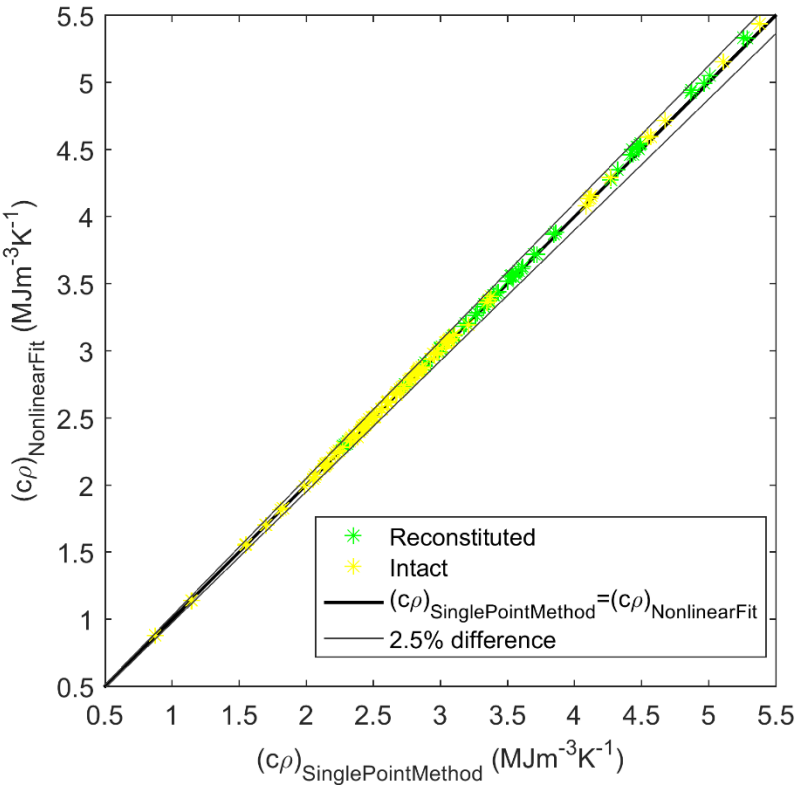

Figure 7.18 *Volumetric heat capacities obtained using the single point method and the nonlinear fit*

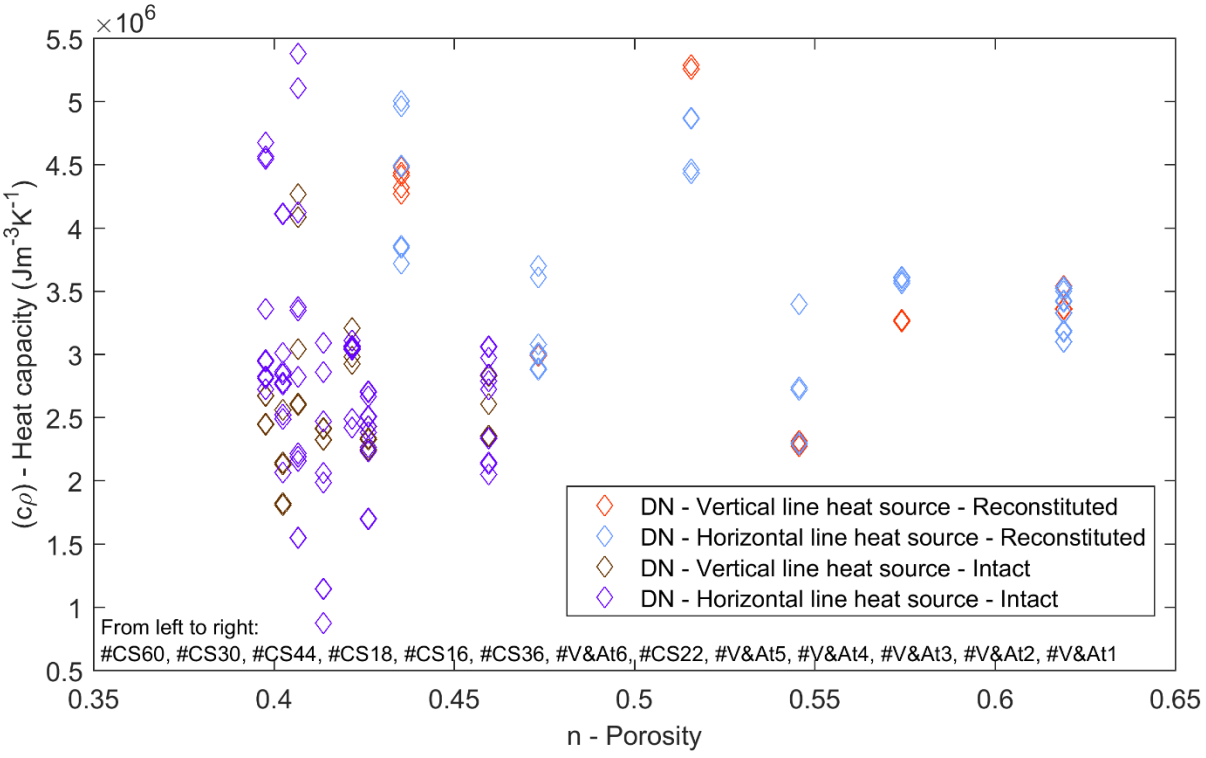

Figure 7.19 *Volumetric heat capacities measured in the dual-probe heat-pulse tests (All points)*

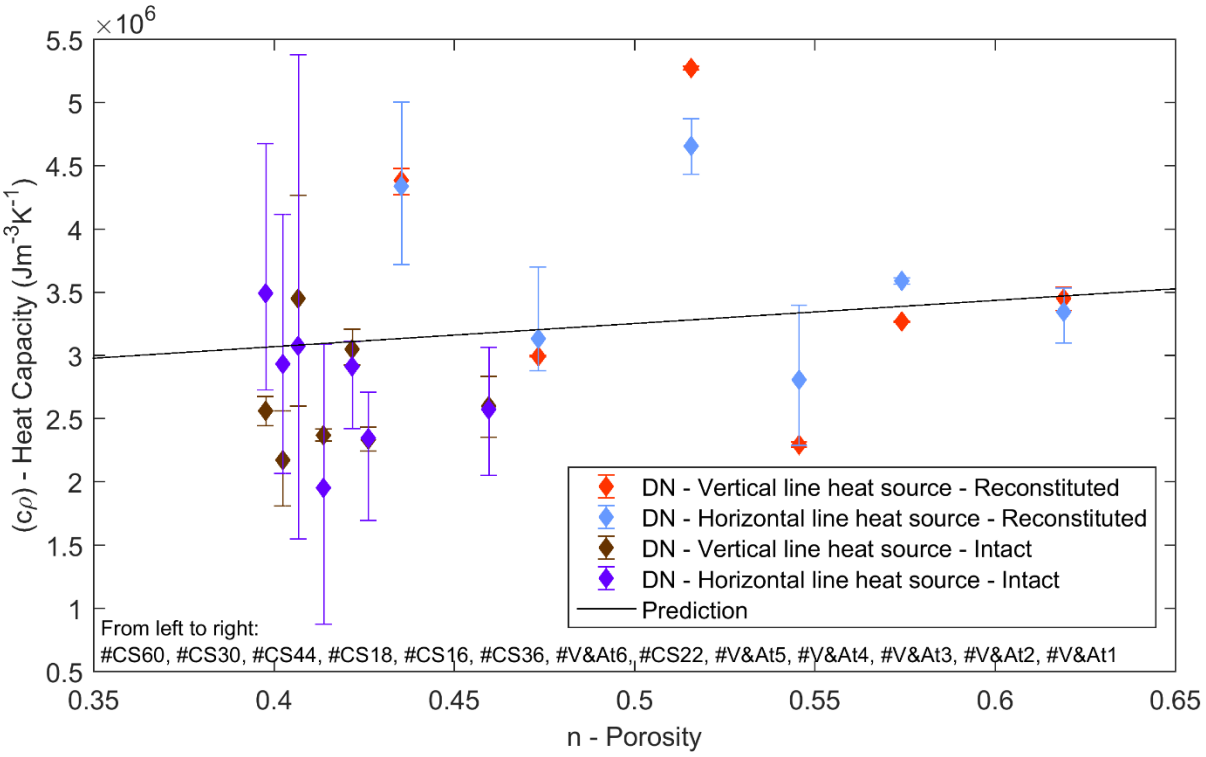

Figure 7.20 *Volumetric heat capacities measured in the dual-probe heat-pulse tests (ranges and averages for each direction of measurement) and predictions*

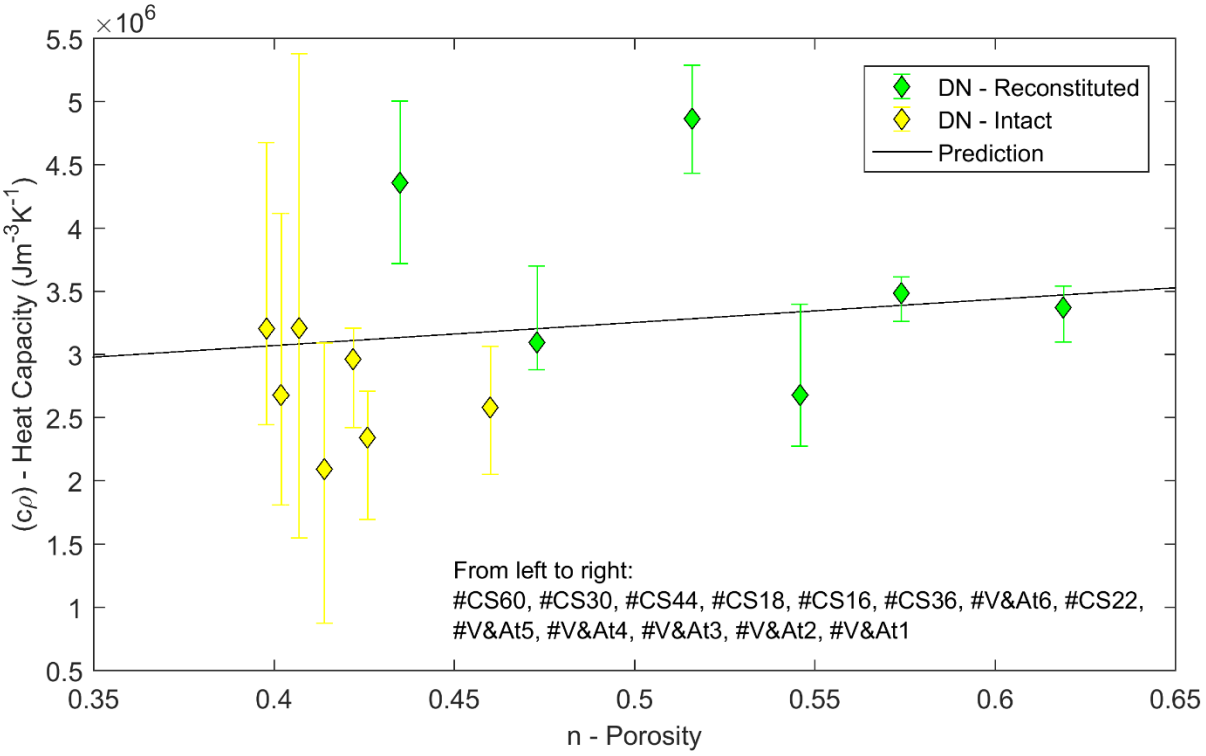

Figure 7.21 *Volumetric heat capacities measured in the dual-probe heat-pulse tests (ranges and global averages) and predictions*

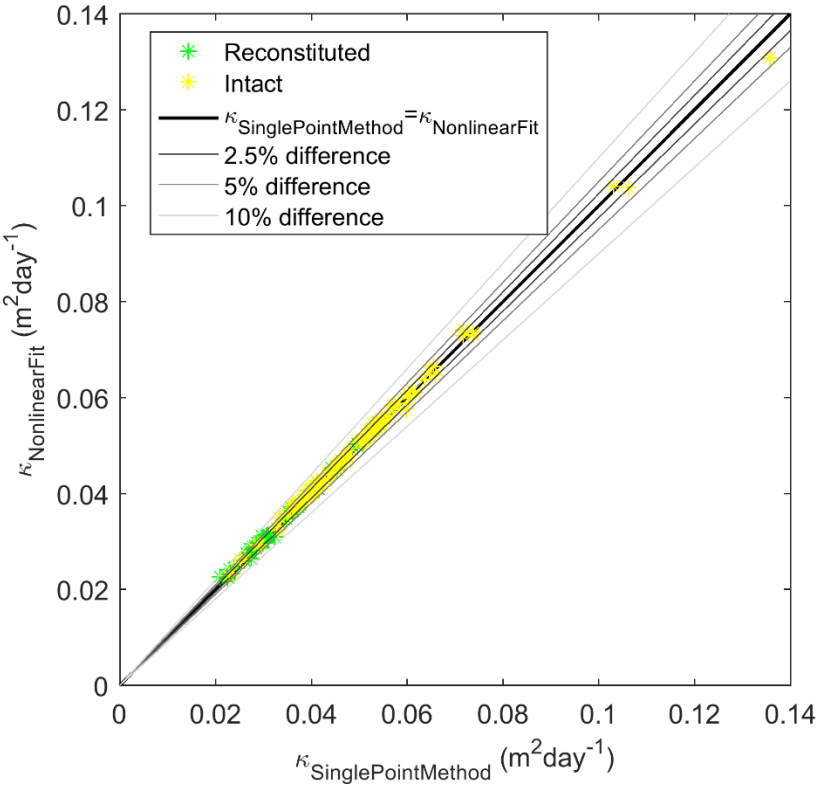

Figure 7.22 Thermal diffusivities obtained using the single point method and the nonlinear fit

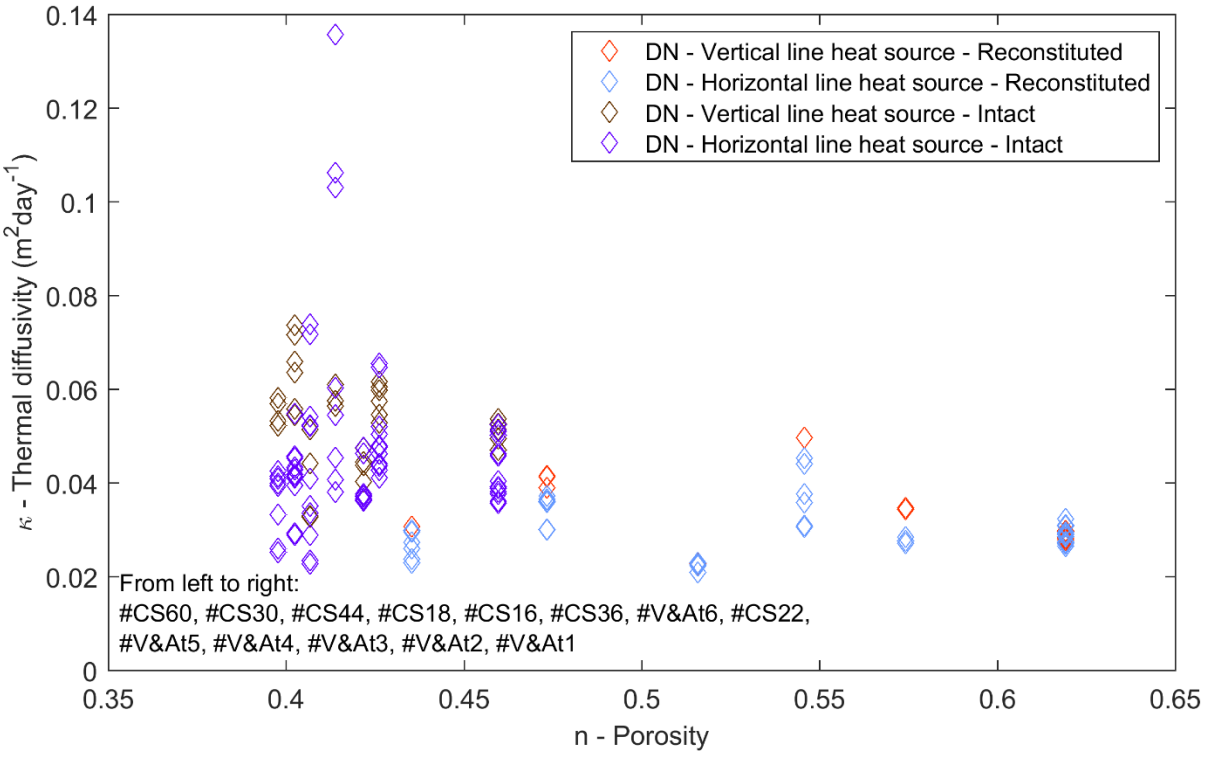

Figure 7.23 *Thermal diffusivities measured in the dual-probe heat-pulse tests (All points)*

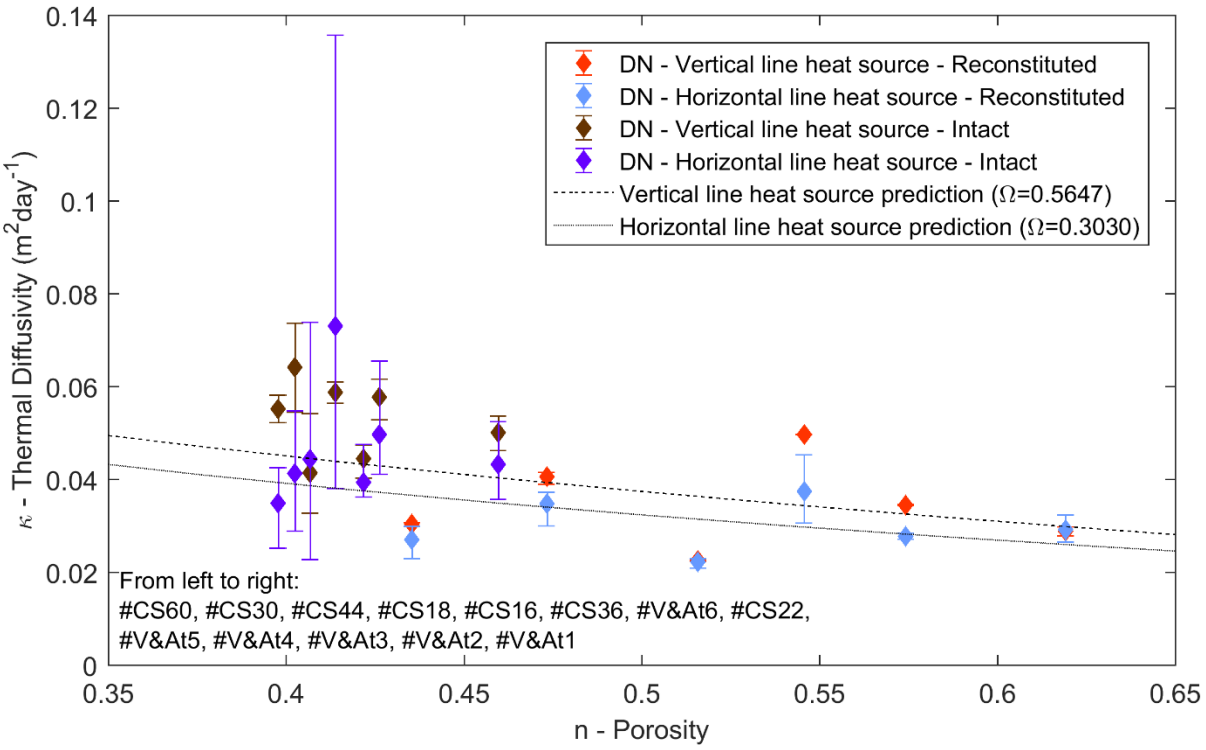

Figure 7.24 *Thermal diffusivities measured in the dual-probe heat-pulse tests (ranges and averages) and predictions*

8. CONCLUSIONS

The study of the thermo-hydro-mechanical behaviour of geomaterials is a growing field within the geotechnical research community, due to its importance to a wide range of contemporary civil engineering activities and applications which involve the ground as a heat source, heat sink or a medium for heat storage. This thesis presents an initial laboratory study of the thermo-mechanical behaviour and thermal properties of London clay, from which the following conclusions can be drawn.

Development of new experimental capabilities at Imperial College Geotechnics Laboratory

The adaption of conventional soil mechanics testing equipment such as the triaxial apparatus for thermo-hydro-mechanical tests presents several challenges, such as the control and measurement of the new variable, temperature, the performance of the different components at high temperature and the appropriate calibration of the different measuring devices for the thermal effects.

A new temperature-controlled apparatus, as a first piece of equipment in the Imperial College Geotechnics Laboratory capable of testing saturated soils at elevated temperatures, is presented in this thesis. It can apply confining pressures up to 800 kPa and temperatures ranging from ambient to 85 ºC. The thermal performance of the cell is thoroughly investigated focusing on the effect of heating rates, the measurement of the sample temperature and its uniformity and the thermal losses of the cell. The temperature sensor within the cell proved to be an accurate non-intrusive method to measure the sample temperature at steady state, which is found to be uniform throughout the sample. Critical aspects of the behaviour of the components (drainage system, internal instrumentation, membranes, etc.) are assessed, tested and improved until a satisfactory arrangement for the purposes of the testing programme of this thesis is found.

Additionally, the use of needle techniques for the measurement of the thermal properties is investigated, discussing the overlaying theory and potential sources of errors. The

experimental set-up developed for thermal tests using the single needle and dual-probe is presented, together with the calibration of its components.

Thermo-mechanical behaviour

A laboratory testing programme on London clay was conducted for the first time in order to study several aspects of its thermo-mechanical behaviour. Although the testing programme was limited due to the intricases involved with the development of the new cell and the duration of each test, it enabled the study of the thermally induced volume changes during heating and cooling and the influence of the stress level, stress history, number and amplitude of the temperature cycles. Additionally, the influence of temperature on the strength and stiffness of London clay samples at different stress levels and with different stress histories and compression behaviour was studied.

All samples contracted upon heating and expanded during cooling regardless of the stress history for the cases considered (normally and overconsolidated samples of reconstituted London clay) under drained conditions. Part of the contraction was not recoverable in the normally consolidated samples and its magnitude seemed to be independent of the stress levels (for the stress range considered) for the samples brought to the normally consolidated state at the same temperature. The reversible component during cooling in normally consolidated samples as well as the thermally-induced volume changes during heating in subsequent cycles were of a very similar magnitude as the thermal strains in overconsolidated samples. The application of multiple temperature cycles in both normally consolidated and overconsolidated samples did not seem to produce additional permanent strains in the soil. The measurements were also interpreted in terms of void ratio with similar findings: a reversible decrease in void ratio with increase in temperature and an additional permanent decrease in void ratio during the heating of normally consolidated samples. Another important aspect of the results is that for the range of temperatures considered (20-70 °C), the changes in volume and void ratio are very linear with temperature.

In terms of the compression behaviour, although the test data was not sufficient to establish clear trends, the apparent pre-consolidation pressure reduced with increasing temperature, the slope of the swelling line was found to be temperature independent and there are indications that the same applies for the normal compression line at different temperatures. Further testing to investigate this is recommended in the subsequent section.

These results present similitudes as well as discrepancies with published results on different clays, which are discussed in the thesis in terms of the nature of the measurement, interpretative framework and experimental conditions, as well as the proposed physical mechanisms. A key strength of the results presented here is their repeatability and the consistency in the sign and magnitude of the thermal volumetric strains. A main limitation of the study presented in this thesis, as well as of past studies of the thermo-mechanical behaviour of soils, is the indirect nature of the measurement of the thermal volumetric strains, as it relies on a number of assumptions in the interpretation of the results. A commonly used interpretative framework, originally presented by Campanella and Mitchell (1968) is thoroughly discussed, underlining discrepancies in the published literature on the values of the coefficient of thermal expansion of water, one of its key parameters, and proposing a new expression as a function of temperature and pressure based on the latest IAPWS formulation. The sensitivity of the framework to the chosen value of thermal expansion for the water is highlighted and could explain some discrepancies with past results where an erroneous value for this coefficient has been used. Moreover, the performance of the apparatus and adequacy of the methodology was ratified by performing drained heating and cooling on coarse sand, which agreed with the theoretical prediction.

Finally, undrained shearing performed on the samples exposed to thermal histories and on comparable samples of similar stress histories at ambient temperature, revealed several aspects of the influence of temperature on the strength and stiffness of the material. For the samples normally consolidated at ambient temperature, exposure to higher temperatures did not cause significant changes in terms of strength and stiffness. On the other hand, the

samples brought to a normally consolidated state at higher temperatures presented a higher stiffness and higher initial strength, and lower excess pore pressure during shearing than comparable samples without thermal history. In the case of the overconsolidated samples, exposure to temperature led to lower maximum mobilised deviatoric stress values, higher initial stress ratios, higher (and positive) excess pore pressures and lower stiffness. These effects became more pronounced with higher maximum temperature and increased number of temperature cycles. The stress ratio of all samples, with and without temperature history, seemed to converge at larger strains before the development of localised shear planes, suggesting that critical state conditions would be temperature-independent.

Thermal properties

The main heat transfer mechanism in saturated clays is heat conduction, which can be described by the thermal properties of the soil (thermal conductivity, volumetric heat capacity and thermal diffusivity). These properties depend on several characteristics of the soil such as the mineralogy, porosity, water content, density, degree of saturation, particle contact and packing geometry, fabric or structure.

An extensive testing programme was conducted using the two types of needles in order to investigate the thermal properties of reconstituted and intact London clay. Both instruments, single needle and dual probe, were considered adequate for the measurement of the thermal conductivity in the laboratory and presented good agreement between themselves, with differences smaller than their accuracy range. In the case of the single needle, both heating and cooling parts of the experimental data could be used for the derivation of the conductivity and in the case of the dual-probe, there were very small differences between the two analyses methods considered, making the simpler single-point method more attractive than the weighted nonlinear fit.

The thermal conductivity of saturated London clay was found to be an anisotropic property, influenced by the relative volumes of solids and water in the sample and the nature (mineralogy) of those solids. For the intact London clay samples, the average measured

thermal conductivity was 1.54-1.58 $Wm^{-1}K^{-1}$, depending on the instrument used, when measured by applying the heat source vertically, and 1.28-1.33 $Wm^{-1}K^{-1}$ when measured by applying the heat source horizontally. No clear trend of variation with depth was found, and variations between the samples could be explained by changes in the water content and density. Published detailed studies of the thermal properties of London clay are very scarce and raise several experimental issues, making the comparison of the results more difficult. The results of the reconstituted and intact samples were also modelled using several simple theoretical thermal conductivity mixing models, with some presenting a very good agreement with both types of samples in the vertical line heat source case.

The use of the dual-probe for the measurement of the volumetric heat capacity and thermal diffusivity in stiff materials was found inadequate due to the very large errors induced by bending the probes during insertion, mainly due to an unknown inter-probe spacing. As a consequence of such error, there was an unacceptable scatter in the measurements. This error was however cancelled out in the measurement of the thermal conductivity. The volumetric heat capacity of the intact London clay samples could be estimated to be in the range of 3.04-3.18 $MJm^{-3}K^{-1}$ and the thermal diffusivity could be estimated to be in the range of 0.04533-0.04039 m^2day^{-1} in the case of a vertical line heat source, and 0.03941-0.03496 m^2day^{-1} in the case of a horizontal line heat source.

8.1 Suggestions for future research

The suggestions for further research are split in this section into different components of the thermo-hydro-mechanical behaviour of geomaterials, focusing on the tested material, London clay.

Thermo-mechanical behaviour

When considering future testing programmes, the initial priority would be to overcome the current drawbacks of the new equipment, namely: the indirect nature of the thermal strain measurement and the inability of shearing at high temperature. The latter could be solved by

changes in the design of the equipment in order to accommodate an external load cell, appropriately insulated from the triaxial cell to avoid the issues reported in this thesis. Unlike submersible internal load cells, this external load cell would need to be calibrated for the frictional forces which will very likely change with temperature. Nonetheless, the more challenging issue remains the measurement of thermal strains for which the applicability of alternative methods needs to be investigated. As a first step, improvements in the system could be sought to improve the accuracy of the cell water measurements of volume change, which have been shown to be a reliable method of measurement in the literature. Additionally, novel measuring techniques such as fibre optic sensors could be introduced to the equipment after appropriate thermal investigation of there behaviour. Other types of measuring techniques such as laser displacement sensors or digital imaging techniques could be also investigated further although this would require significant design changes as the cell wall is currently made of steel, thus it is not transparent. Another aspect of the experimental set-up which could be improved is the application of drainage also at the top of the sample to reduce consolidation times particularly on low permeability material such as London clay. Equally, the installation of a mid-height pore water pressure sensor would be helpful in checking the pore pressure uniformity through the sample and to monitor the development of thermally-induced excess pore pressures.

Based on the results presented in this thesis, in order to expand on this initial characterisation of the thermo-mechanical behaviour of London clay, the following types of test are recommended:

- Heating and cooling cycle up to 60 °C at very low overconsolidation ratios, such as 1.25 and 2, to establish the size of the elastic domain where thermally-induced volume changes are not-permanent.
- Heating and cooling cycle up to 60 °C at a very high overconsolidation ratio, such as 12, to confirm the findings of recoverable thermally-induced contraction from samples tested at the “intermediate” overconsolidation range.

- More tests involving complex thermo-mechanical paths as those in samples #oc4ht2 and #oc4ht3 in order to fully understand the decrease of pre-consolidation pressure with temperature, a surface which could not be properly established from the two tests performed in this thesis. This would involve reloading from an intermediate overconsolidation state at high temperature up to much larger stresses than the previous maximum. In this thesis, a stress just 50 kPa greater than previous maximum was chosen, which did not allow for a clear determination of the compression line at high temperature. Given the lack of a clear trend in the findings of the decrease in pre-consolidation pressure with temperature, it is recommended to re-do the tests as well as consider other temperatures.
- An interesting finding of the present study was that the magnitude of the thermally-induced permanent contraction in normally consolidated soils seems to depend on the initial temperature at which the sample is mechanically loaded to its normally consolidated state. A further test is suggested to confirm this finding which involves isotropic consolidation up to 150 kPa at room temperature followed by heating steps of 10 °C under drained conditions and an increase in mean effective stress of 50 kPa before the next heating step. This would be done successively reaching 70 °C, which would occur under a mean effective stress of 350 kPa.
- Undrained shearing of all of the above at room temperature to extend the current shearing data and be able to establish clearer trends on the influence of temperature on the strength and stiffness of the material.
- Undrained shearing at high temperatures of samples with different stress histories.

This initial study of the thermo-mechanical behaviour of reconstituted London clay was limited to heating and cooling being performed under drained conditions at a unique “slow” rate. The influence of the heating rate and the behaviour with restricted drainage are aspects to consider in future tests. Another potential area for future research is the influence of anisotropy on the

thermally-induced volume changes since the material surrounding energy geostructures, such as thermo-active piles, would very likely be subjected to non-isotropic stress state conditions.

A further study to be conducted once a full benchmark characterisation of the behaviour of reconstituted material is attained would involve intact samples. Finally, another important aspect to consider in future work is the range of temperature in the experiments. A clear limitation of the current equipment is that temperatures below ambient cannot be applied to the samples. This includes the natural temperature of soils and parts of the temperature range covering the expected fluctuations caused by the circulation of warmer and colder fluids in energy geostructures.

In addition to the suggested studies looking at the thermo-mechanical behaviour of clays from a “macro-level”, it is also necessary to understand the physical and chemical processes which occur at a micro-level in the clay-water system in order to explain the observed phenomena during the tests. A possible initial study in this direction would be to perform a series of XRD analyses on wet hydrated samples, non-glycolated in a temperature and humidity controlled environment to determine the changes in basal spacing in the clay minerals with changes in temperature.

Thermo-hydraulic behaviour

An interesting and controversial aspect of thermo-hydro-mechanical behaviour of soils which was not studied in this thesis is the influence of temperature on the hydraulic conductivity of the material. This would require specifically-built equipment or adaptation of the current apparatus with shorter than usual samples to be able to apply a significant hydraulic gradient along the sample in order to achieve a measurable flow.

Thermal properties

Given the scarcity of published studies on the thermal properties of London clay, additional measurements of the properties of high-quality intact samples from different locations, depths and lithological units in the London basin would be necessary to establish a comprehensive

database, considering in all cases factors such as the mineralogy, water content, degree of saturation, or the direction of measurement, which were all seen to be of significant importance during the research conducted in this thesis. Further studies using needle techniques could also include more heat source directions, considering inserting the needle at different angles in the sample, in order to fully understand and model the anisotropy in the thermal conductivity.

A comprehensive study combining laboratory and field measurement of the conductivity, as well as numerical modelling of the thermal response tests to discuss the different interpretative techniques of the in-situ tests, would be of great use to further demonstrate the appropriateness of laboratory measurements of the thermal properties.

Finally from the point of view of the equipment development, it is necessary to investigate alternative designs for the dual-probe sensors, as well as improving pre-drilling procedures to avoid the very significant errors in the measurement of the thermal diffusivity and volumetric heat capacity caused by the difference between the estimated and real inter-probe spacings as a result of their insertion in stiff material, such as an intact heavily overconsolidated clay.

REFERENCES

Abramowitz, M. & Stegun, I. A. (1972) *Handbook of mathematical functions with formulas, graphs, and mathematical tables.* New York; Chichester, Wiley.

Abuel-Naga, H. M., Bergado, D. T., Bouazza, A. & Pender, M. J. (2009) Thermal conductivity of soft Bangkok clay from laboratory and field measurements. *Engineering Geology.* 105 (3–4), 211-219.

Abuel-Naga, H. M., Bergado, D. T. & Bouazza, A. (2008) Thermal Conductivity Evolution of Saturated Clay under Consolidation Process. *International Journal of Geomechanics.* 8 (2), 114-122.

Abuel-Naga, H. M., Bergado, D. T. & Lim, B. F. (2007a) Effect of temperautre on shear strength and yielding behaviour off soft Bangkok clay. *Soils and Foundations.* 47 (3), 423-436.

Abuel-Naga, H. M., Bergado, D. T. & Bouazza, A. (2007b) Thermally induced volume change and excess pore water pressure of soft Bangkok clay. *Engineering Geology.* 89 (1–2), 144-154.

Abuel-Naga, H. M., Bergado, D. T., Soralump, S. & Rujivipat, P. (2005) Thermal consolidation of soft Bangkok clay. *Lowland Technology International.* 7 (1), 13-21.

Ackerley, S. K., Standing, J. R. & Hosseini Kamal, R. (2016) A system for measuring local radial strains in triaxial apparatus. *Géotechnique.* 66 (6), 515-522.

Addis, M. A. (1987) *Mechanisms of sediment compaction responsible for field subsidence.* PhD thesis. Imperial College London, United Kingdom.

Aduda, B. (1996) Effective thermal conductivity of loose particulate systems. *Journal of Materials Science.* 31 (24), 6441-6448.

ASTM. (2014) *Standard Test Method for Determination of Thermal Conductivity of Soil and Soft Rock by Thermal Needle Probe Procedure.* D5334 − 14 edition.

Austin, W. A. (1998) *Development of an In Situ System for Measuring Ground Thermal Properties.* MSc Thesis. Oklahoma State University, USA.

Bailey, H. W. (2016) Personal Communcation.

Baldi, G., Hueckel, T., Peano, A. & Pellegrini, R. (1991) *Developments in modelling of thermo-hydro-geomechanical behaviour of Boom clay and clay-based buffer materials.* Luxembourg, Publications of the European Communities. Report number: 13365/2 EN.

Baldi, G., Hueckel, T. & Pellegrini, R. (1988) Thermal volume changes of the mineral water system in low-porosity clay soils. *Canadian Geotechnical Journal.* 25 (4), 807-825.

Baldi, G., Borsetto, M., Hueckel, T. & Tassoni, E. (1987) Thermally Induced Strains and Pore Pressure in Clays. In: H.Y. Fang (ed.) *Proc. 1st Int. Conf. on Environmental Geotechnics. Bethlehem (PA).* pp.391-402.

Banks, D. (2008) *An Introduction to Thermogeology: Ground Source Heating and Cooling.* Oxford, UK.

Banks, V. J., Bricker, S. H., Royse, K. R. & Collins, P. E. F. (2015) Anomalous buried hollows in London: development of a hazard susceptibility map. *Quarterly Journal of Engineering Geology and Hydrogeology.* 48 (1), 55-70.

Barry-Macaulay, D., Bouazza, A., Singh, R. M., Wang, B. & Ranjith, P. G. (2013) Thermal conductivity of soils and rocks from the Melbourne (Australia) region. *Engineering Geology.* 164 (0), 131-138.

Bergenstahl, L., Gabrielsson, A. & Mulabdic, M. (1994) Changes in soft clay caused by increases in temperature. *Proceedings of the XIII ICSMFE. India.* pp.1637-1640.

Berry, F. G. (1979) Late Quaternary scour-hollows and related features in central London. *Quarterly Journal of Engineering Geology.* 12 (1), 9-29.

Bish, D. L. & Post, J. E. (1989) *Modern powder diffraction.* Washington, D.C., Mineralogical Society of America.

Bishop, A. W. & Henkel, D. J. (1962) *The measurement of soil properties in the triaxial test.* 2nd edition. , Edward Arnold.

Bishop, A. W., Webb, D. L. & Lewin, P. I. (1965) Undisturbed Samples of London Clay from the Ashford Common Shaft: Strength–Effective Stress Relationships. *Géotechnique.* 15 (1), 1-31.

Bloomer, J. R. (1981) Thermal conductivities of mudrocks in the United Kingdoms. *Quarterly Journal of Engineering Geology.* 14 (4), 357-362.

Bourne-Webb, P. J., Amatya, B., Soga, K., Amis, T., Davidson, C. & Payne, P. (2009) Energy pile test at Lambeth College, London: geotechnical and thermodynamic aspects of pile response to heat cycles. *Geotechnique.* 59 (3), 237-248.

Brandl, H. (2006) Energy foundations and other thermo-active ground structures. *Geotechnique.* 56 (2), 81-122.

Brigaud, F. & Vasseur, G. (1989) Mineralogy, porosity and fluid control on thermal conductivity of sedimentary rocks. *Geophysical Journal International.* 98 (3), 525-542.

Bristow, K. L. (1998) Measurement of thermal properties and water content of unsaturated sandy soil using dual-probe heat-pulse probes. *Agricultural and Forest Meteorology.* 89 (2), 75-84.

Bristow, K. L., Bilskie, J. R., Kluitenberg, G. J. & Horton, R. (1995) Comparison of techniques for extracting soil thermal properties from dual- probe heat- pulse data. *Soil Science.* 160 (1), 1-7.

British Geological Survey. (2016) *The BGS Lexicon of Named Rock Units - London Clay Formation.* Available from: http://www.bgs.ac.uk/Lexicon/lexicon.cfm?pub=LC [Accessed 08/07/2016].

British Standard Institution. (1990) *BS 1377: 1990 - Methods of test for soils for civil engineering purposes.*

Burghignoli, A., Desideri, A. & Miliziano, S. (1995) Discussion of volume change of clays induced by heating. *Soils and Foundations.* 35 (1), 125-127.

Burghignoli, A., Desideri, A. & Miliziano, S. (1992) Deformability of clays under non-isothermal condtions. *Revista Italiana Di Geotechnica.* 4 227-236.

Burghignoli, A., Desideri, A. & Miliziano, S. (2000) A laboratory study on the thermomechanical behaviour of clayey soils. *Canadian Geotechnical Journal.* 37 (4), 764-780.

Burland, J. B. (1990) On the compressibility and shear strength of natural clays. *Géotechnique.* 40 (3), 329-378.

Burland, J. B., Rampello, S., Georgiannou, V. N. & Calabresi, G. (1996) A laboratory study of the strength of four stiff clays. *Géotechnique.* 46 (3), 491-514.

Busby, J., Lewis, M., Reeves, H. & Lawley, R. (2009) *Initial geological considerations before installing ground source heat pump systems.*

Campanella, R. G. & Mitchell, J. K. (1968) Influence of temperature variations on soil behaviour. *Journal of the Soil Mechanics and Foundation Division.* 94 (3), 709-734.

Campanella, R. G. & Mitchell, J. K. (1963) Creep studies in saturated clays. *ASTM-NRC of Canada, Symposium of Laboratory Shear Testing of Soils. September 1963, Ottawa, Canada.* pp.90-103.

Campbell, G. S., Calissendorf, C. & Williams, J. H. (1991) Probe for measuring soil specific heat using a heat-pulse method. *Soil Science Society of America Journal.* 55 291-293.

Carslaw, H. S. & Jaeger, J. C. (1959) *Conduction of heat in solids.* 2nd edition. Oxford, Clarendon Press.

Carslaw, H. S. & Jaeger, J. C. (1946) *Conduction of heat in solids.* 1st Edition edition. Oxford, Oxford University Press.

Cekerevac, C., Laloui, L. & Vulliet, L. (2005) A Novel Triaxial Apparatus for Thermo-Mechanical Testing of Soils. *Geotechnical Testing Journal.* 28 (2), 161-170.

Cekerevac, C. & Laloui, L. (2004) Experimental study of thermal effects on the mechanical behaviour of a clay. *International Journal for Numerical and Analytical Methods in Geomechanics.* 28 (3), 209-228.

Chandler, R. J. & Apted, J. P. (1988) The effect of weathering on the strength of London Clay. *Quarterly Journal of Engineering Geology.* 21 (1), 59-68.

Chandler, R. J., Willis, M. R., Hamilton, P. S. & Andreou, I. (1998) Tectonic shear zones in the London Clay Formation. *Géotechnique.* 48 (2), 257-270.

Chiu, S. (1996) *Behaviour of Normally Consolidated Clay at Elevated Temperature.* PhD Thesis. University of Sydney, Australia.

Cho, W. J., Lee, J. O. & Chun, K. S. (1999) The temperature effects on hydraulic conductivity of compacted bentonite. *Applied Clay Science.* 14 (1–3), 47-58.

Clarke, B. G., Agab, A. & Nicholson, D. (2008) Model specification to determine thermal conductivity of soils. *Proceedings of the Institution of Civil Engineers - Geotechnical Engineering.* 161 (3), 161-168.

Committee on Climate Change. (2016) *Next steps for UK heat policy.*

Côté, J. & Konrad, J. (2005) Thermal conductivity of base-course materials. *Canadian Geotechnical Journal.* 42 (1), 61-78.

Cui, Y. -., Le, T. T., Tang, A. M., Delage, P. & Li, X. L. (2009) Investigating the time-dependent behaviour of Boom clay under thermomechanical loading. *Géotechnique.* 59 (4), 319-329.

De Bruyn, D. & Thimus, J. -. (1996) The influence of temperature on mechanical characteristics of Boom clay: The results of an initial laboratory programme. *Engineering Geology.* 41 (1–4), 117-126.

De Freitas, M. H. & Mannion, W. G. (2007) A biostratigraphy for the London Clay in London. *Géotechnique.* 57 (1), 91-99.

De Vries, D. A. (1952) Thermal properties of soils. In: Van Wick, W. R. (ed.).*Physics of plant environment.* Amsterdam, North-Holland Publishing Company. pp. 210-235.

Del Olmo, C., Fioravante, V., Gera, F., Hueckel, T., Mayor, J. C. & Pellegrini, R. (1996) Thermomechanical properties of deep argillaceous formations. *Engineering Geology.* 41 (1–4), 87-102.

Delage, P., Cui, Y. J. & Tang, A. M. (2010) Clays in radioactive waste disposal. *Journal of Rock Mechanics and Geotechnical Engineering.* 2 (2), 111-123.

Delage, P., Sultan, N. & Cui, Y. J. (2000) On the thermal consolidation of Boom clay. *Canadian Geotechnical Journal.* 37 (2), 343-354.

Demars, K. R. & Charles, R. D. (1982) Soil volume changes induced by temperature cycling. *Canadian Geotechnical Journal.* 19 (2), 188-194.

Derjaguin, B. V., Karasev, V. V. & Khromova, E. N. (1986) Thermal expansion of water in fine pores. *Journal of Colloid and Interface Science,* 106, 586-587.

Dolinar, B. & Macuh, B. (2016) Determining the thickness of adsorbed water layers on the external surfaces of clay minerals based on the engineering properties of soils. *Applied Clay Science.* 123 279-284.

Duncan, J. M. & Seed, H. B. (1967) Corrections for strength test data. *Journal of the Soil Mechanics and Foundation Division ASCE.* 93 121-137.

Dusseault, M. B., Wang, Y. & Simmons, J. V. (1988) Induced stresses near a fire flood front. *AOSTRa J. Res.* 4 153-170.

Ellison, R. A. (2004) *Geology of London: special memoir for 1:50 000 geological sheets 256 (North London), 257 (Romford), 270 (South London) and 271 (Dartford) (England and Wales).* Nottingham, British Geological Survey.

Ermrich, M. & Opper, D. (2013) *XRD for the analyst. Getting acquainted with the principles.* , PANalytical.

Esch, D. C. (2004) *Thermal analysis, construction, and monitoring methods for frozen ground.* ASCE. Report number: TCCRE Monographs.

Farouki, O. (1981) *Thermal properties of soil.* USA Cold region research engineering laboratory. 81 (1) edition. Hannover, NH, USA.

Fei, Y. (2013) Thermal Expansion. In: Anonymous *Mineral Physics & Crystallography: A Handbook of Physical Constants.* , American Geophysical Union. pp. 29-44.

Fry, V. A. (2009) *Lessons from London: Regulation of open- loop ground source heat pumps in central London.*

Gale, I. (2005) *Ground source heat pumps: development of GeoReports for potential site characterisation, issue 1.2.* Keyworth, Nottingham, British Geological Survey.

Gangadhara Rao, M. & Singh, D. N. (1999) A generalized relationship to estimate thermal resistivity of soils. *Canadian Geotechnical Journal.* 36 (4), 767-773.

Gasparre, A. (2005) *Advanced laboratory characterisation of London clay.* PhD Thesis. Imperial College London.

Gehlin, S. (1998) *Thermal Response Test - In-situ measurements of thermal properties in hard rock.* Lic.thesis. Lulea University of Technology, Sweden.

Gehlin. S. (2002) *Thermal Response Test – Method Development and Evaluation.* PhD Thesis. Lulea University of Technology, Sweden.

Gens, A. (2010) Soil–environment interactions in geotechnical engineering. 47th Rankine lecture. *Geotechnique.* 60 (1), 3-74.

Gens, A., Vaunat, J., Garitte, B. & Wileveau, Y. (2007) In situ behaviour of a stiff layered clay subject to thermal loading: observations and interpretation. *Geotechnique.* 57 (2), 207-228.

Georgiannou, V. N. & Burland, J. B. (2001) A laboratory study of post-rupture strength. *Géotechnique.* 51 (8), 665-675.

Gori, F. & Corasaniti, S. (2004) Theoretical prediction of the thermal conductivity and temperature variation inside mars soil analogues. *Planetary and Space Science.* 52 (1–3), 91-99.

Graham, J., Tanaka, N., Crilly, T. & Alfaro, M. (2001) Modified Cam-Clay modelling of temperature effects in clays. *Canadian Geotechnical Journal.* 38 (3), 608-621.

GSHPA. (2012) *Thermal Pile Design, Installation & Materials Standards.* Issue 1.0

Hanson, J. L., Edil, T. B. & Yesiller, N. (2000) Thermal Properties of High Water Content Materials . In: Edil, T. B. & Fox, P. J. (eds.). *Geotechnics of High Water Content Materials.* West Conshohocken, PA, US, ASTM International. pp. 137-151.

Hanson, J. L., Neuhaeuser, S. & Yesiller, N. (2004) Development and calibration of a large-scale thermal conductivity probe. *Geotechnical Testing Journal.* 27 (4), 393-403.

Harris, W., White, C.N. (2008) X-ray Diffraction Techniques for Soil Mineral Identification. In: Ulery,A.L.,Drees, L.R. (ed.).*Methods of Soil Analysis Part 5—Mineralogical Methods.* , Soil Science Society of America.

Hashin, Z. & Shtrikman, S. (1962) A Variational Approach to the Theory of the Effective Magnetic Permeability of Multiphase Materials. *Journal of Applied Physics.* 33 (10), 3125-3131.

Head, K. H.,. (1998) *Manual of soil laboratory testing. Volume 3, Effective stress tests.* 3rd edition. Dunbeath, Whittles.

Henkel, D. J. & Gilbert, G. D. (1952) The Effect Measured of the Rubber Membrane on the Triaxial Compression Strength of Clay Samples. *Géotechnique.* 3 (1), 20-29.

Hight D.W., McMillan, F., Powell, J.J.M., Jardine, R.J., Allenou, C.P. (2003) Some characteristics of London Clay. In: Tan, T. S. (ed.).*Characterisation and Engineering Properties of Natural Soils, Volume 2.* , CRC Press. pp. 851-908.

Hooper, F. C. & Lepper, F. R. (1950) Transient heat flow apparatus for the determination of thermal conductivity. *Heating, Piping and Air Conditioning.* 22 (8), 129-134.

Horai, K. (1971) Thermal conductivity of rock-forming minerals. *Journal of Geophysical Research.* 76 (5), 1278-1308.

Houston, S. L., Houston, W. N. & Williams, N. D. (1985) Thermo- mechanical behavior of seafloor sediments. *Journal of Geotechnical Engineering.* 111 (11), 1249-1263.

Hsu, C. T., Cheng, P. & Wong, K. W. (1995) A Lumped- Parameter Model for Stagnant Thermal Conductivity of Spatially Periodic Porous Media. *Journal of Heat Transfer,.* 117 (2), 264-269.

Hueckel, T. & Baldi, G. (1990) Thermoplasticity of Saturated Clays: Experimental Constitutive Study. *Journal of Geotechnical Engineering.* 116 (12), 1778-1796.

Hueckel, T., François, B. & Laloui, L. (2009) Explaining thermal failure in saturated clays. *Geotechnique.* 59 (3), 197-212.

Hueckel, T. A. (1992) Water-mineral interaction in hygromechanics of clays exposed to environmental loads: a mixture-theory approach. *Canadian Geotechnical Journal.* 29 (6), 1071-1086.

Huggett, J. M. & Knox, R. W. O. (2006) Clay mineralogy of the Tertiary onshore and offshore strata of the British Isles. *Clay Minerals.* 41 (1), 5-46.

IAPWS (2007) *Revised Release on the IAPWS Industrial Formulation 1997 for the Thermodynamic Properties of Water and Steam. Available at www.iapws.org.*

Jackson, R. D. & Taylor, S. A. (1986) Thermal conductivity and diffusivity. In: Arnold Klute (ed.).*Methods of Soil Analysis: Part 1-Physical and Mineralogical Methods.* pp. 945-956.

Johansen, O. (1975) *Thermal conductivity of soils.* PhD Thesis. University of Trondheim, Norway.

Juza, M. (1966) *An equation of state water and steam. Steam tables in the critical region and in the range from 1000 to 100000 bars.* Prague, Czech Republic, Academia.

Kemp, C. J. & Wagner, D. (2006) *The mineralogy, geochemistry and surface area of mudrocks from the London Clay Formation of southern England.* Nottingham, UK, British Geological Survey. Report number: IR/06/060.

Kenney, T. C. (1966) *Shearing Resistance of Natural Quick Clays.* PhD Thesis. University of London, UK.

Kersten, M. S. (1949) *Laboratory research for the determination of the thermal properties of soils.* Unviersity of Minnesota, Research Laboratory Investigations, Engineering Experiment Station. Report number: Technical Report 23.

Khalili, N., Uchaipichat, A. & Javadi, A. A. (2010) Skeletal thermal expansion coefficient and thermo-hydro-mechanical constitutive relations for saturated homogeneous porous media. *Mechanics of Materials.* 42 (6), 593-598.

King, C. (1991) *Stratigraphy of the London Clay (Early Eocene) in the Hampshire Basin.* PhD Thesis. Kingston Polytechnic, UK.

King, C. (1981) The stratigraphy of the London Basin and associated deposits. *Tertiary Research Special Paper 6 (Backhuys, Rotterdam).*

Klug, H. P., Alexander, L. E. (1974) *X-ray diffraction procedures for polycrystalline and amorphous materials.* 2nd edition. New York, Wiley-Interscience.

Kluitenberg, G. J., Das, B. S. & Bristow, K. L. (1995) Error Analysis of Heat Pulse Method for Measuring Soil Heat Capacity, Diffusivity, and Conductivity. *Soil Science Society of America Journal.* 59 719-726.

Kukkonen, I. & Lindberg, A. (1995) *Thermal conductivity of rocks at the TVO investigation sites Olkiluoto, Romuvaara and Kivetty.* Nuclear Waste Commission of Finnish Power Companies. Report number: Report YJT-95-08.

Kuntiwattanakul, P. (1991) *Effect of high temperature on mechanical behaviour of clays.* PhD Thesis. Unversity of Tokyo, Tokyo, Japan.

Kuntiwattanakul, P., Towhata, I., Ohisi, K. & Seko, I. (1995) Temperature effects on undrained shear characteristics of clay. *Soils and Foundations.* 35 (1), 147-162.

La Rochelle, P. (1967) Membrane, drain, and area correction in triaxial test on soil samples failing along a single shear plane. *Proc. 3rd Pan-American Conf. on Soil Mechanics and Foundation Engineering.* pp.273-292.

La Rochelle, P., Leroueil, S., Trak, B., Blais-Leroux, L. & Tavenas, F. (1988) Observational approach to membrane and area corrections in triaxial tests. *Proc Symposium on Advanced Triaxial Testing of Soil and Rock. Louiseville, US.* pp.715-731.

Laloui, L. & Di Donna, A. (2013) *Energy Geostructures: Innovation in Underground Engineering.* , John Wiley & Sons, Inc.

Lambe, T. W. (1960) A Mechanistic Picture of Shear Strength in Clay. *ASCE Research Conference on Shear Strength of Cohesive Soils. Boulder, Colorado, US.* pp.503-532.

Leroueil, S. & Marques, M. E. S. (1996) Importance of strain rate and temperature effects in geotechnical engineering. *Proceedings of ASCE National Convention, Washington DC.*

Lingnau, B. E. (1993) *Consolidated Undrained-Triaxial Behavior of a Sand-Bentonite Mixture at Elevated Temperature.* PhD Thesis. The University of Manitoba, Manitoba, Canada.

Lingnau, B. E., Graham, J., Yarechewski, D., Tanaka, N. & Gray, M. N. (1996) Effects of temperature on strength and compressibility of sand-bentonite buffer. *Engineering Geology.* 41 (1–4), 103-115.

Loveridge, F. A., Olgun, C. G., Brettmann, T. & Powrie, W. (2015) Group thermal response testing for energy piles. In: Anonymous *Geotechnical Engineering for Infrastructure and Development.* , ICE Publishing. pp. 2595-2600.

Low, J. E., Loveridge, F. A., Powrie, W. & Nicholson, D. (2015) A comparison of laboratory and in situ methods to determine soil thermal conductivity for energy foundations and other ground heat exchanger applications. *Acta Geotechnica.* 10 (2), 209-218.

Martinez Calonge, D. (2013) *Development of a new high temperature triaxial apparatus.* MSc thesis. Imperial College London.

Martinez Calonge, D., Gawecka, K. A., Zdravkovic, L., Sim, W. W. & Taborda, D. M. G. (2015) Development of a new temperature-controlled triaxial apparatus for saturated

soils. In: Anonymous *Geotechnical Engineering for Infrastructure and Development.* , ICE Publishing. pp. 3219-3224.

Maxwell, J. C. (1873) A Treatise on Electricity and Magnetism. *Nature.* 7 (182), 478.

Mayor of London. (2004) *Green light to clean power, The Mayor's Energy Strategy.* Greater London Authority, UK.

McKinstry, H. (1965) Thermal expansion of clay minerals. *The American Mineralogist.* 12 212-222.

Met Office. (2017) *Climate data: London.* Available from: http://www.metoffice.gov.uk/public/weather/climate/gcpvpwgtg [Accessed 12/04/2017].

Midttomme, K., Roaldset, E. & Aagaard, P. (1998) Thermal conductivity of selected claystones and mudstones from England. *Clay Minerals.* 33 (1), 131-145.

Mitchell, J. K. (1993) *Fundamentals of Soil Behavior.* , John Wiley & Sons.

Mitchell, J. K. (1964) Shearing resistance of soils as a rate process. *Journal of the Soil Mechanics and Foundation Division ASCE.* 90 (1), 231-251.

Mitchell, J. K., McMillan, J. C., Green, S. L. & Sisson, R. C. (1982) Field testing of cable backfill systems. In: Anonymous *Underground Cable Thermal Backfill.* New York, Pergamon Press. pp. 19-33.

Mitchell, J. K. & Kao, T. C. (1978) Measurement of soil thermal resistivity. *Journal of Geotechnical Engineering.* 104 (10), 1307-1320.

Moore, D.M., Reynolds, R.C. (1997) *X-Ray Diffraction and the Identification and Analysis of Clay Minerals.* Second Edition edition. New York, Oxford University Press.

Morin, R. & Silva, A. J. (1984) The effects of high pressure and high temperature on some physical properties of ocean sediments. *Journal of Geophysical Research: Solid Earth.* 89 (B1), 511-526.

Moritz, L. (1995) *Geotechnical properties of clay at elevated temperatures.* Swedish Geotechnical Institute. Report number: 47.

Murayama, S. (1969) *Effects of Temperature and Heat on Engineering Properties of Soils.* Washington, D.C., Highway Research Board. Report number: Special Report 103.

Najorka, J. (2016) Personal Communication.

Nimick, F. B. & Leith, J. R. (1992) A model for thermal conductivity of granular porous media. *Journal of Heat Transfer.* 114 (2), 505-508.

Ochsner, T. E., Horton, R. & Ren, T. (2001) Simultaneous water content, bulk density, and air-filled porosity measurements with thermo-time domain reflectometry. *Soil Science Society of America Journal.* 65 1618-1622.

Plum, R. L. & Esrig, M. I. (1969) Some temperature effects on soil compressibility and pore water pressure. In: Anonymous *Effects of temperature and heat on engineering behaviour of soils.* Highway Research Board, Special Report 103 edition. pp. 231-242.

Pruß, A. & Wagner, W. (1995) A new equation of state for water as a candidate for the New Scientific Formulation of IAPWS. In: White, H. J. e. a. (ed.) *Physical Chemistry of Aqueous Systems: Meeting the Needs of Industry Proceedings of the 12th International Conference on the Properties of Water and Steam.* New York.

Pusch, R. & Carlsson, T. (1985) The physical state of pore water of na smectite used as barrier component*. Engineering Geology,* 21, 257-265.

Pusch, R. & Güven, N. (1990) Electron microscopic examination of hydrothermally treated bentonite clay. *Engineering Geology,* 28, 303-314.

Rees, S. W., Adjali, M. H., Zhou, Z., Davies, M. & Thomas, H. R. (2000) Ground heat transfer effects on the thermal performance of earth-contact structures. *Renewable and Sustainable Energy Reviews.* 4 (3), 213-265.

Ren, T., Noborio, K. & Horton, R. (1999) Measuring soil water content, electrical conductivity, and thermal properties with a thermo-time domain reflectometry probe. *Soil Science Society of America Journal.* 65 450-457.

Rietveld, H. M. (1969) A profile refinement method for nuclear and magnetic structures. *Journal of Applied Crystallography.* 2 (2), 65-71.

Romero, E., Gens, A. & Lloret, A. (2001) Temperature effects on the hydraulic behaviour of an unsaturated clay. *Geotechnical & Geological Engineering.* 19 (3-4), 311-332.

Russell, H. W. (1935) Principles of heat flow in porous insulation. *Journal of the American Ceramic Society.* 18 (1), 1-5.

Sanner, B., Mands E., Sauer, M. (2009) Economic aspects of thermal response test - advantages, technical improvements, commercial application. *Proceedings of International Conference of Thermal Energy Storage, Stockholm.*

Sanner, B., Hellstrom, G., Splitler, J. & Gehlin, S. (2005) Thermal Response Test – Current Status and World-Wide Application. *Proceedings World Geothermal Congress 2005. Antalya, Turkey.*

Sass, J. H., Stone, C. & Munroe, R. J. (1984) Thermal conductivity determinations on solid rock — a comparison between a steady-state divided-bar apparatus and a commercial transient line-source device. *Journal of Volcanology and Geothermal Research.* 20 (1), 145-153.

Savvidou, C. & Britto, A. M. (1995) Numerical and experimental investigation of thermally induced effects in saturated clay. *Soils and Foundations.* 35 (1), 37-44.

Shao, Y. X., Shi, B., Liu, C. & Gao, L. (2012) Experimental Study on Temperature Effect on Engineering Properties of Clayey Soils. *Advanced Materials Research.* 512-515 (Chapter 8: Energy Materials, Engineering Materials and Processing Technologies), 1905-1918.

Sherif, M. A. & Burrous, C. M. (1969) *Temperature effects on the unconfined shear strength of saturated, cohesive soils.* Highway Research Board Special Report;. Report number: 103.

Skempton, A. W. (1961) Horizontal stresses in an overconsolidated Eocene clay. *Proceedings of the 5th ICSMFE, Paris.* pp.351-357.

Skempton, A. W., Schuster, R. L. & Petley, D. J. (1969) Joints and Fissures in the London Clay at Wraysbury and Edgware. *Géotechnique.* 19 (2), 205-217.

Standing, J. R. & Burland, J. B. (2006) Unexpected tunnelling volume losses in the Westminster area, London. *Géotechnique.* 56 (1), 11-26.

Sultan, N., Delage, P. & Cui, Y. J. (2002) Temperature effects on the volume change behaviour of Boom clay. *Engineering Geology.* 64 (2–3), 135-145.

Tanaka, N., Graham, J. & Crilly, T. (1997) Stress-strain behaviour of reconstituted illitic clay at different temperatures. *Engineering Geology.* 47 (4), 339-350.

Tarnawski, V. R., Leong, W. H., Gori, F., Buchan, G. D. & Sundberg, J. (2002) Inter-particle contact heat transfer in soil systems at moderate temperatures. *International Journal of Energy Research.* 26 (15), 1345-1358.

Tinham, B. (2007) *Cooling the tube.* Rail Engineering. Nov-Dec edition. Plant Engineer.

Toby, B. H. (003) R factors in Rietveld analysis: How good is good enough? *Powder Diffraction.* 21 (1), 67-70.

Toll, D. (1999) A Data Acquisition and Control System for Geotechnical Testing. In: Kumar, B. & Topping, B. H. V. (eds.) *Computing Developments in Civil and Structural Engineering.* Edinburgh pp.237-242.

Towhata, I., Kuntiwattanakul, P., Seko, I. & Ohisi, K. (1993) Volume changes of clays induced by heating as observed in consolidation tests. *Soils and Foundations.* 33 (4), 170-183.

Van der Held, E. F. M. & Van Drunen, F. G. (1949) A method of measuring the thermal conductivity of liquids. *Physica.* 15 (10), 865-881.

van Olphen, H. (1977) *An introduction to clay colloid chemistry.* 2nd Edition edition. New York, US, John Wiley & Sons.

Vargas, W. L. & Mccarthy, J. J. (2001) Heat conduction in granular materials. *AIChE Journal.* 47 (5), 1052-1059.

Wan, M. S. P. & Standing, J. R. (2014) Field measurement by fully grouted vibrating wire piezometers. *Proceedings of the Institution of Civil Engineers - Geotechnical Engineering.* 167 (6), 547-564.

Wechsler, A. E. (1966) *Development of thermal conductivity probes for soils and insulations.* Cold Regions Research and Engineering Laboratory (U.S.) Engineer Research and Development Center (U.S.). Report number: CRREL Technical Report 182.

Woodside, W. & Messmer, J. H. (1961) Thermal Conductivity of Porous Media. I. Unconsolidated Sands. *Journal of Applied Physics.* 32 1688-1699.

Yong, R. N., Taylor, S. A. & Warkentin, B. P. (1962) Swelling pressures of sodium montmorillonite at depressed temperatures. *11th National Conference on Clay and Clay Minerals. Ottawa, Canada.* pp.268-281.

Yu, B. & Cheng, P. (2002) Fractal models for the effective thermal conductivity of bidispersed porous media. *Journal of Thermophysics and Heat Transfer.* 16 (1), 22-29.

Zhang, N., Yu, X. & Pradhan, A. (2017) Application of a thermo- time domain reflectometry probe in sand- kaolin clay mixtures. *Engineering Geology.* 216 98-107.

APPENDIX

The MATLAB scripts to adcquire and visualize the data during the single needle and dual-probe heat-pulse tests are presented here.

A-1 Single needle test

```
if exist('s')
disp('Serial port found, closing and deleting');
fclose(s);
clear s;
end

clear;
Open_Port;        % Serial Port is opened

% misc variables
SAMPLES     = 2000;     % Number of samples for system to run for
DELAY       = 00;       % Delay between samples

% Variables sought are as follows:
CURRENT     = zeros(SAMPLES,1);   % Current through heater network (AMPERES)
POWER       = zeros(SAMPLES,1);   % Power Consumed by heater (WATTS)
R_THERM     = zeros(SAMPLES,1);   % Resistance in thermistor (OHMS)
TEMPERATURE = zeros(SAMPLES,1);   % Temperature (DEG C)
TIMER       = zeros(SAMPLES,1);   % Time axis in (SECONDS)

% Voltage measurements are as follows:
V_THERM_SINGLE    = zeros(SAMPLES,1);   % voltage across thermistor
V_HEATER_SINGLE   = zeros(SAMPLES,1);   % across heater
V_DIVIDER         = zeros(SAMPLES,1);   % across thermistor divider
V_SENSE_SINGLE    = zeros(SAMPLES,1);   % through current sensing network

% Constants are as follows:
R_SENSE     = 60;     % Ohms
R_HEATER    = 69.9;   % Ohms
R_DIVIDE    = 10000;  % Ohms

figure
a = plot(TIMER,TEMPERATURE);
xlabel('Time in seconds'); % x-axis label
ylabel('Temperature in celsius'); % y-axis label
a.XDataSource = 'tempx';
a.YDataSource = 'tempy';

tic;

for i = 1:SAMPLES
 fprintf(s,'%s\r'  ,'RL1,6'); % SEND READ COMMAND TO MSL
 pause(0);

 INPUT = fscanf(s, '%s'); %RESPONSE READ FROM MSL UNIT
 eval(['CELLINPUT = {' INPUT '}']);
 PARSEDINPUT = cell2mat(CELLINPUT)*10^(-6);

 V_DIVIDER(i)            = PARSEDINPUT(1);
 V_THERM_SINGLE(i)       = PARSEDINPUT(2);
 V_HEATER_SINGLE(i)      = PARSEDINPUT(4);
 V_SENSE_SINGLE(i)       = PARSEDINPUT(6);

 %COEFFICIENTS FOR THERMISTOR (CALIBRATION EQ.[3.1])
 a=0.00119739029096315;
 b=0.000222535369400142;
 c=1.17294439771075e-7;
 CURRENT(i) = V_SENSE_SINGLE(i)/R_SENSE;
 POWER(i) = (CURRENT(i).^2).*R_HEATER;
```

```
 R_THERM(i)=((V_THERM_SINGLE(i)*R_DIVIDE)/(V_DIVIDER(i)-
V_THERM_SINGLE(i)));
 TEMPERATURE(i) = 1./(a + b.*log(R_THERM(i)) + c.*(log(R_THERM(i))).^3)-
273.15;
 TIMER(i) = toc;
 tempx = TIMER(1:i);
 tempy = TEMPERATURE(1:i);
 refreshdata;
 pause(DELAY);
end
Close_Port;     %Serial Port is closed
```

A-2 Dual-probe heat-pulse test

```
if exist('s')
disp('Serial port found, closing and deleting');
fclose(s);
clear s;
end
Open_Port;        % Serial Port is opened
% misc variables
SAMPLES     = 1600;   % Number of samples for system to run for
DELAY       = 00;    % Delay between samples
% Variables sought are as follows:
CURRENT     = zeros(SAMPLES,1);   % Current through heater network (AMPERES)
POWER       = zeros(SAMPLES,1);   % Power Consumed by heater (WATTS)
R_THERM     = zeros(SAMPLES,1);   % Resistance in thermistor (OHMS)
TEMPERATURE = zeros(SAMPLES,1);   % Temperature (DEG C)
TIMER       = zeros(SAMPLES,1);   % Time axis in (SECONDS)
% Voltage measurements are as follows:
V_SENSE_DOUBLE = zeros(SAMPLES,1);% voltage through current sensing network
V_HEATER_DOUBLE   = zeros(SAMPLES,1);   % across heater
V_THERM_DOUBLE    = zeros(SAMPLES,1);   % across thermistor
V_DIVIDER         = zeros(SAMPLES,1);   % across thermistor divider
% Constants are as follows:
R_SENSE     = 5.553;     % Ohms measured with curent source and voltmeter
R_HEATER    = 37.5;      % Ohms
R_DIVIDE    = 10000;     % Ohms
figure
a = plot(TIMER,TEMPERATURE);
xlabel('Time in seconds'); % x-axis label
ylabel('Temperature in celsius'); % y-axis label
a.XDataSource = 'tempx';
a.YDataSource = 'tempy';
tic;
for i = 1:SAMPLES
 fprintf(s,'%s\r'  ,'RL1,7'); % SEND READ COMMAND TO MSL
 pause(0.1);
 INPUT = fscanf(s, '%s'); %RESPONSE READ FROM MSL UNIT
 eval(['CELLINPUT = {' INPUT '}']);
 PARSEDINPUT = cell2mat(CELLINPUT)*10^(-6);
 V_SENSE_DOUBLE(i)      = PARSEDINPUT(7);
 V_HEATER_DOUBLE(i)     = PARSEDINPUT(5);
```

```
 V_THERM_DOUBLE(i)       = PARSEDINPUT(3);
 V_DIVIDER(i)            = PARSEDINPUT(1);
% COEFFICIENTS FOR THERMISTOR (CALIBRATION EQ.[3.1])
 a=0.00112981312073147;
 b=0.000231975301614012;
 c=8.49451966313391e-8;
 CURRENT(i) = V_SENSE_DOUBLE(i)/R_SENSE;
 POWER(i) = (CURRENT(i).^2).*R_HEATER;
 R_THERM(i)        =        abs((V_THERM_DOUBLE(i)*R_DIVIDE)/(V_DIVIDER(i)-
V_THERM_DOUBLE(i)));
 TEMPERATURE(i) = 1./(a + b.*log(R_THERM(i)) + c.*(log(R_THERM(i))).^3)-
273.15;
 V_TEMP_RATIO(i) = V_THERM_DOUBLE(i)/V_DIVIDER(i);
 TIMER(i) = toc;
 tempx = TIMER(1:i);
 tempy = TEMPERATURE(1:i);
 refreshdata;
 pause(DELAY);
end

Close_Port;       %Serial Port is closed
```

A-3 Open port (Open_port)

```
s = serial('COM4');
set(s,'BaudRate',9600,'StopBits',1,'terminator', 13);
fopen(s);

% SENDS INTIALISE COMMAND TO MSL
```

A-4 Close port (Close_port)

```
fclose(s);
delete(s);
clear s;
```